Exhumation Processes at Orogenic Syntaxes: Insights from the Cascadia Subduction Zone (USA)

Dissertation
der Mathematisch-Naturwissenschaftlichen Fakultät
der Eberhard Karls Universität Tübingen
zur Erlangung des Grades
eines Doktors der Naturwissenschaften
(Dr. rer. nat.)

vorgelegt von

Lorenz Michel

aus Dachau

Tübingen
– 2019 –

Gedruckt mit Genehmigung der Mathematisch-Naturwissenschaftlichen Fakultät der Eberhard Karls Universität Tübingen

Tag der mündlichen Prüfung	23.07.2019
Dekan	Prof. Dr. Wolfgang Rosenstiel
1. Berichterstatter	Prof. Todd Ehlers
2. Berichterstatter	PD Dr. Christoph Glotzbach
3. Berichterstatter	apl. Prof. Dr. Edward Sobel

Abstract

The topography of mountain ranges or orogens results from the interaction between two oppositely directed processes: (1) rock uplift and (2) denudation. Eventually this leads to exhumation of rocks at the Earth's surface. During the last two decades a large debate arose in the geoscience community, how tectonics and climate impact the uplift, denudation and exhumation of rocks, and whether feedbacks and interactions between tectonic and climatic processes exist during mountain building. The Olympic Mountains, situated at the Cascadia Subduction Zone (CSZ) in the northwestern USA, have been introduced as a textbook flux steady-state mountain range, whereby the tectonic/accretionary influx has been balancing the denudational outflux since 14 Ma. By providing new low-temperature thermochronometric ages and results from thermo-kinematic modelling this thesis aims at better understanding the evolution of the Olympic Mountains and of mountain building processes in general.

Overall 111 new thermochronometric ages have been obtained. The observed pattern of thermochronometer ages requires a spatially variable pattern of exhumation rates and the highest exhumation rates coincide with the high-elevation, central part of the orogen. This focusing of exhumation is tectonically controlled, because the Olympic Mountains are located in an orogenic syntaxis, where the subducting oceanic plate is bent, causing a lower angle of subduction below the Olympic Mountains. Furthermore, exhumation varies temporally, related either to changes in the tectonic parameters (decrease in plate convergence rate at 6 Ma) or climatic framework (increased glacial erosion due to the onset of Plio-Pleistocene glaciation at 2–3 Ma). Because no equivalent increase in rock uplift balances the observed increase in exhumation caused by glacial erosion, a reduction in topography on the western side of the orogen is plausible. An independent calculation of the denudational outflux out of the orogen as well as the accretionary influx into the mountain range indicates that the orogen is in flux steady-state on long timescales (i.e., 14 Myr). However, Plio-Pleistocene glaciation could have elicited perturbations of the flux steady-state on shorter timescales. A comparison of the pattern of exhumation from this thesis with published datasets of denudation and rock uplift corroborates that most permanent deformation is focused in the central part of the orogen. However, the present-day signal from GPS stations in the western part of the Olympic Mountains reflects elastic deformation of the seismic earthquake cycle, because free slip is restricted on the shallow, locked part of the subduction interface of the CSZ. The deeper part of the subduction interface displays a more complex pattern of slip and visco-plastic flow could initiate permanent deformation in the overriding crust. Ultimately that process would produce the elevated topography of the Olympic Mountains.

In summary, this thesis reveals a complex and temporally non-steady history of the Olympic Mountains. Both tectonics and climate play an important role in the evolution of the orogen, and in particular Plio-Pleistocene glaciation has a profound effect on the shape of the mountain range. The combination of observations from datasets integrating on both long-term and short-term timescales might also contribute to a better understanding of the seismic hazard of the Cascadia Subduction Zone.

Zusammenfassung

Die Topographie von Gebirgsketten resultiert aus dem Zusammenwirken von zwei entgegen gerichteten Prozessen: (1) Gesteinshebung und (2) Denudation. Letztendlich führt dieser Vorgang zur Exhumierung von Gesteinen an die Erdoberfläche. Während der letzten zwei Jahrzehnte wurde in den Geowissenschaften eine intensive Debatte darüber geführt, wie Tektonik und Klima die Hebung, Denudation und Exhumierung von Gesteinen beeinflussen und ob Rückkopplungen sowie ein Zusammenwirken zwischen tektonischen und klimatischen Prozessen während der Gebirgsbildung existieren. Die an der Kaskaden Subduktionszone in den nordwestlichen USA gelegenen Olympic Mountains wurden als klassisches Beispiel für ein Gebirge eingeführt welches im Fluss Gleichgewicht steht, wobei der tektonische bzw. akkretionäre Zufluss den denudierten Abfluss seit 14 Ma ausgleicht. Das Ziel der vorliegenden Doktorarbeit ist es, zu einem besseren Verständnis der Entwicklung der Olympic Mountains und von Gebirgsbildungsprozessen im Allgemeinen beizutragen. Hierfür werden neue Niedrig-Temperatur Thermochronometer Alter und Ergebnisse von thermo-kinematischen Modellierungen bereitgestellt.

Insgesamt konnten 111 neue Thermochronometer Alter bestimmt werden. Um das beobachtete Muster der Thermochronometer Alter zu erklären wird ein räumlich variables Muster der Exhumierungsraten benötigt und der Ort der höchsten Exhumierungsraten überlappt mit der höchsten Topographie im Zentrum des Gebirges. Diese Bündelung der Exhumierung ist tektonisch bedingt, da die Olympic Mountains in einer orogenen Syntaxe liegen. Hierbei ist die subduzierte, ozeanische Platte gekrümmt, was zu einem flacheren Subduktionswinkel unter den Olympic Mountains führt. Des weiteren ist die Exhumierung zeitlich variabel, was entweder durch Änderungen in den tektonischen Rahmenbedingungen (eine Abnahme der Platten Konvergenzrate vor 6 Ma) oder klimatischen Rahmenbedingungen (eine Zunahme von glazialer Erosion in Folge des Einsetzens der Plio-Pleistozänen Vereisung vor 2–3 Ma) bedingt ist. Da kein entsprechender Anstieg der Gesteinshebung den durch die glaziale Erosion hervorgerufenen Anstieg der Exhumierung ausgleicht, ist eine Verringerung der Topographie auf der westlichen Seite des Gebirges wahrscheinlich. Die unabhängig voneinander berechneten Mengen des denudierten Abflusses aus dem Gebirge heraus sowie des akkretionären Zuflusses in das Gebirge hinein verdeutlichen, dass das Gebirge im Fluss Gleichgewicht steht, zumindest auf lange Zeitskalen (über 14 Myr) hin betrachtet. Allerdings könnte die Plio-Pleistozäne Vereisung eine Störung des Fluss Gleichgewichts auf kürzeren Zeitskalen verursacht haben. Der Vergleich des Exhumierungsmusters dieser Arbeit mit publizierten Datensätzen der Denudation und der Gesteinshebung bestätigt, dass die meiste permanente Verformung in der Mitte des Gebirges konzentriert ist. Das heutige Signal von GPS Stationen auf der Westseite der Olympic Mountains spiegelt jedoch die elastische Deformation im Rahmen des Erdbeben Zyklus wider, da auf dem oberen, verriegelten Teil der Plattengrenze der Kaskaden Subduktionszone keine freie Bewegung möglich ist. Die tieferen Teile der Plattengrenze weisen ein deutlich komplexeres Bewegungsmuster auf und viskos-plastisches Fließen könnte permanente Deformation in der überliegenden Kruste verursachen. Dieser Prozess würde letztendlich die erhöhte Topographie der Olympic Mountains verursachen.

Zusammenfassend verdeutlicht diese Doktorarbeit eine komplexe und zeitlich nicht beständige Geschichte der Olympic Mountains. Sowohl Tektonik als auch Klima spielen eine wichtige Rolle während der Entwicklung des Gebirges und insbesondere die Plio-Pleistozäne Vereisung hat einen erheblichen Einfluss auf die Gestalt des Orogens. Die Kombination von Datensätzen, die sowohl über lange als auch über kurze Zeitskalen integrieren, könnte auch zu einem verbesserten Verständnis der Erdbebengefahr der Kaskaden Subduktionszone beitragen.

Acknowledgments

Working on my PhD project during the past four and a half years was a long (and sometimes tedious) endeavor. Many people helped and supported me during that time and the following lines are an attempt to acknowledge most of these.

First of all I like to thank my two supervisors Todd and Christoph for their ongoing support and advise during the entire project. Whenever I had a question (and I had a lot), encountered a problem or got stuck in a scientific dead end, the two of you helped me out. Todd – thanks a lot for letting me be part of your EXTREME project and for giving me the chance to work in such an amazing place like the Olympic Mountains. I very much enjoyed it, learned a lot and benefited from countless discussions with you about thermochronometry, modelling and science. Christoph – thanks for generously sharing your knowledge and expertise in thermochronometry and modelling. Without your help in measuring my thermochronometry samples, the thesis would not have been possible.

Byron, thank you so much for being my field buddy in the Olympics – together we survived the jungle, resisted several torrential downpours and warded off attacks by sneaky rodents. These nine weeks were an unforgettable experience and you kind of introduced important parts of American culture to me. You also always had an open ear, if I needed to discuss any problem during my PhD, answered many of my dumb questions and readily shared your knowledge.

Fieldwork in the Olympics would also not have been possible without the generous support by the NPS staff of the Olympic National Park. In particular this accounts for Jerry Freilich and William Baccus; M. Beazly also removed a severe obstacle in the Quinault valley.

The Earth Surface Dynamics group was a lively and inspiring environment to work in and countless discussions during group seminars or coffee talks provided valuable insights. Doing fieldwork in the Atacama Desert of Peru was kind of the opposite of doing fieldwork in the Olympics. Jess – thanks for taking me with you as your field assistant to such an interesting place. Sarah introduced me to the secrets and pitfalls of fission-track dating and took over the tricky task of dating these nasty Olympic sandstones with apatite fission-track. Max – the posh-coffee ceremony was sorely missed during the end of the PhD project. Thanks also to my office mates for tolerating the chaos of my workspace and my moods! Assistance during treating rock samples by Doro, Martina, Dagmar and various HiWis laid the foundation for many parts of this work. Willi provided invaluable help in solving many of the Pecube bugs and problems that I encountered. Claudia and Beate helped to survive the bureaucratic jungle during the past years, such that in the end I even managed to correctly fill out the “Dienstreiseantrag” and get reimbursed with the “Reisekostenabrechnung”.

And what would be the world without friends? Thanks for all the support, climbing, various enjoyable meals, emptied beers, rounds of Kniffel, discussions about life and advice during the time. This pertains both to the Tübingen crew (Luise, Emilio, Holger, Verena, Phillip, Luisa, Jasmin) and people from other places (Jonathan, Theresa, Eric, Martin, Christoph, Basti, Christian).

The thesis addresses mountain ranges. Besides the scientific insights I could obtain on mountains during the past four and a half years, I was fortunate to spend several unique and very rewarding moments out there in the mountains. Thanks a lot to all my friends, who joined me on these trips! In particular summiting Mt. Olympus together with Holger and Byron was kind of the peak of the entire field work.

Contents

List of Figures

List of Tables

Chapter 1

Introduction

Mountain ranges or orogens are the result of the interaction between deeply rooted tectonic processes (endogenic processes) and processes acting at the Earth's surface (exogenic processes). Characteristic features of active mountain ranges include elevated and rugged topography, steep relief, extreme climatic conditions and ongoing deformation.

Despite having been a focus of geoscientific research for over two centuries, many processes which contribute to the evolution of orogens still remain elusive and are part of ongoing research. Particularly the interplay and possible feedbacks between endogenic and exogenic processes is a contentious topic in the geoscience community.

However, mountain ranges have a profound impact on many aspects of the earth system (e.g., climate, evolution of species) and human life, and therefore need to be better understood. This thesis aims at contributing to a better understanding of the processes involved in the formation and evolution of mountain ranges by investigating the Olympic Mountains, located in an orogenic syntaxis at the Cascadia Subduction Zone.

The structure of the thesis is as follows: The first chapter is intended as introductory chapter and provides background information on mountain building processes in general as well as on the study area in particular. Furthermore, the methods applied in the thesis (thermochronometric dating, thermo-kinematic modelling) are briefly described. The second chapter states the hypothesis and research questions that are addressed. The results and discussion on these are reported in chapter three, in the form of manuscripts that are either published, accepted for publication or under preparation. The fourth chapter summarizes the outcomes, revisits the hypotheses and provides suggestions for future work.

1.1 Mountain ranges – A general introduction

The next two sections first briefly outline some of the impacts mountain ranges have both on humans and on the earth system. After that, an introduction to some key concepts behind mountain building is given, as well as a summary on which processes are responsible for mountain building and how these processes are investigated by geoscientists.

1.1.1 Impact of mountain ranges on humankind and the earth system

During the history of humankind, the rugged topography and impressive relief developed between mountain tops and valley bottoms acted as natural barrier for unrestricted traffic and migration. Nonetheless, following the retreat of the ice masses at the end of the last glacial maximum, the European Alps were quickly colonized by human settlements and the flat valley bottoms show evidence of agriculture starting at the Early to Middle Neolithicum about 5000–7000 years before Present (Schmidl et al., 2005; Colombaroli et al., 2013). However, the partly hostile environment of mountain areas in terms of climate, natural hazards and remoteness often placed a threshold on further, flourishing development of mountain villages, compared to settlements in the foreland or on the flat valley bottoms of mountain ranges. In the case of the European Alps these circumstances along with other disadvantages led to the impoverishment and depopulation of many smaller mountain villages in the Italian and French Alps during the late 19th and mid 20th century (Bätzing, 2002).

Meanwhile, humans have discovered mountains in terms of their recreational potential, so that mountain villages and their surroundings often serve as important tourist destinations. Because mountain ranges are often located in tectonically active areas, are capable of receiving large amounts of precipitation and display a steep relief, they are prone to natural hazards like earthquakes, rock fall, debris flows or avalanches, making them a particularly vulnerable habitat. Nonetheless, the gravitational potential offered by the steep relief is also often used for generation of electricity by hydrodynamic power.

Besides their impact on humankind, the natural barrier represented by mountain ranges also affects other parts of the earth system. The evolution of species has shown to be impacted by the development of mountain ranges, whereby the genetic pool of species is affected by the restricted exchange between populations on the different sides of evolving mountain ranges (e.g., Hoorn et al., 2010, 2013; Craw et al., 2015).

The absence or presence of mountain chains influences the movement of air masses within the Earth's atmosphere (Kasahara et al., 1973), which can strongly impact the local climate and weather (e.g., Molnar et al., 2010). For instance, the absence of an east-west trending mountain chain in North America allows arctic air masses to ingress far south, whereas tropical air masses can reach far north, causing weather extremes like blizzards or tornadoes (Häckel, 2016). Furthermore, the north-south trending Rocky Mountains in North America are also responsible for the contrasting winter climates between North America and Europe, because they interfere with the atmospheric circulation (Seager et al., 2002).

Orographic precipitation (i.e., the rise of moist air masses on one side of an orogen and the descent of dry air on the other side, Banta, 1990) creates precipitation gradients of up to a magnitude decrease in the amount of precipitation between the windward and leeward side of mountain chains (Roe, 2005), which ultimately leads to strong climatic gradients. Examples for this include Asia, where a strong gradient exists between the Himalayan foreland/high mountain regions and the Tibetan Plateau (Bookhagen & Burbank, 2010), South America, where the Andean Cordillera creates strong gradients between the Amazonian lowlands and the Altiplano/western side of the Cordillera (e.g., Garreaud et al., 2009), or New Zealand, where precipitation is focused on the western side of the Southern Alps (e.g., Griffiths & McSaveney, 1983; Willett, 1999).

Greenhouse gases like CO_2 play a pivotal role in controlling the global climate. Weathering of silicate rocks consumes CO_2 and removes it from the atmosphere, having an important control on the global climate (Berner et al., 1983). The formation of mountain chains by tectonic processes exposes fresh, unweathered silicate rocks at the Earth's surface, which in turn could be responsible for Cenozoic climate change due to the CO_2 drawback from the atmosphere by weathering (Molnar & England, 1990; Raymo & Ruddiman, 1992). So besides possible effects on local or regional climate, the formation and evolution of mountain ranges also has significant implications for the global climate.

Furthermore, mountains also have an important control on river networks and hence influence the development of watersheds of entire continents. Drainage divides between large river systems are often located within mountainous areas, and river incision or processes like drainage capture and river reversal can be a direct response to tectonic processes in mountains. Prominent examples include the evolution of the Tsangpo-Yarlung river in the Eastern Himalaya (e.g., Finnegan et al., 2008; Wang et al., 2014; Seward & Burg, 2008), the evolution of the Amazon river system in South America (e.g., Hoorn et al., 1995; Shephard et al., 2010), or the evolution of the Central European river system of Rhine, Rhone and Danube (e.g., Ziegler & Fraefel, 2009; Kuhlemann & Rahn, 2013; Yanites et al., 2013; Olariu et al., 2018).

1.1.2 Exploring the evolution of mountain ranges

As a summary of the above paragraphs, orogens have a profound impact on various aspects of the earth system and human life. But what are the actual mechanisms that contribute to the shape and evolution of active mountain chains and how can these be investigated? The following paragraphs aim at providing a brief outline of several concepts and terms behind mountain building processes. However, because the focus of the thesis is to determine the spatial extent and possible temporal variations in deformation and exhumation in an active moun-

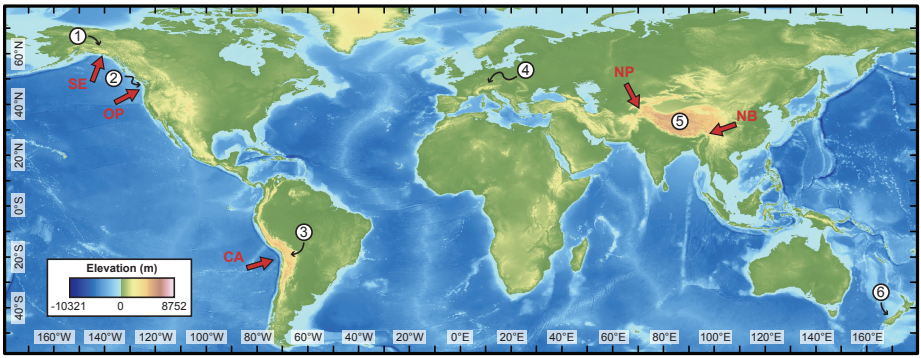

Figure 1.1: Topography of the Earth. Orogens referred to in the text are (1) St. Elias Range in Alaska/Canada, (2) Olympic Mountains, (3) Andes, (4) European Alps, (5) Himalaya, and (6) Southern Alps of New Zealand. The red arrows indicate the location of plate corners/orogenic syntaxes, which include St. Elias (SE), Olympic Mountains (OP), the central Andes (CA), Nanga Parbat (NP) and Namche Barwa (NB).

tain range, only aspects relevant for this thesis are further outlined. Many other concepts and disciplines behind the investigation of mountain building processes (as for instance paleoaltimetry, sedimentary analysis) or observations from extensional settings are of course important, but the following lines do not further elaborate on these.

Although characteristic features of orogens like elevated topography can also be the result of extensional processes or the interaction of mantle plumes with the earth's crust, this thesis focuses on processes at convergent plate margins. At convergent margins, orogens are the result of orogenesis, where compression due to the tectonic forces lead to intra-plate shortening, crustal thickening and surface uplift (e.g., Kearey et al., 2009). Currently, many active mountain ranges are located at the Earth's various convergent margins (Figure 1.1), which can be further divided into oceanic-continental collisional settings (e.g., the Andes, Olympic Mountains) or in continent-continent collisional settings (e.g., European Alps, Himalaya). Mountain building processes can be directly investigated at these actively deforming mountain ranges, which are characterized by for instance elevated topography and increased seismicity. On the other hand, important information can also be obtained from the deeply eroded parts of formerly active mountain ranges, as for instance in the European remnants of the Variscan or Caledonian Orogens. The roots of these inactive mountain ranges offer valuable insights into ductile deformation processes, high temperature/pressure metamorphism and associated magmatism.

When investigating mountain belts, terms like surface uplift, rock uplift and exhumation are widely applied. However, as noted by England & Molnar (1990), these terms are often used in a misleading or erroneous way. So, in the following parts of the thesis, these terms will be defined according to England & Molnar (1990) and used in that sense. The elevated topography as observed in active mountain ranges requires surface uplift (displacement of the earth's surface with respect to the geoid), but obtaining actual measures of surface uplift is a difficult undertaking. Rock uplift refers to the displacement of rock with respect to the geoid and can be determined by geodetic methods. Exhumation describes the displacement of rocks with respect to the Earth's surface, and either occurs through denudation, normal faulting or ductile thinning (Ring et al., 1999). Hence, methods measuring the amount of denudation yield an estimate of exhumation. The three parameters are interrelated to each other, because surface uplift = rock uplift – exhumation. Considering also the respective time over which crustal and surface processes occur, yields an equation linking surface uplift rate (dz/dt), rock uplift rate (U) and exhumation rate ($\dot{E}$):

$$\frac{dz}{dt} = U - \dot{E} \tag{1.1}$$

In case no surface uplift, the topography is temporally invariant, which is referred to as topographic steady state (e.g., Willett & Brandon, 2002). Therefore, the rock uplift rate equals the exhumation rate, and measurements from one of the parameters can be interpreted as a measure of the other.

To quantitatively constrain rock uplift and exhumation rates, proxies or methods directly measuring the respective parameter are employed. However, one caveat to the direct comparison between the different methods is, that these often integrate over different timescales, i.e., they represent short-term measures of 10^1–10^3 years or long-term measures of 10^4–10^6 years. Geodetic methods like leveling campaigns or global positioning system (GPS) surveys provide direct measurements of rock uplift (e.g., Friedrich et al., 2003; Krogstad et al., 2016), usually integrating not longer than over a few decades. The geomorphic analysis of landscapes also provides clues on the processes responsible for the formation of these landscapes, because rivers record dynamic processes of landscapes (Willett et al., 2014) such that the analysis of river profiles can be used to obtain rock uplift rates from timescales of up to several 10^7 years (e.g., Pritchard et al., 2009; Glotzbach, 2015). Applying cosmogenic nuclide dating as for instance ^{10}Be dating allows to directly measure denudation rates at the Earth's surface (e.g., von Blanckenburg, 2005; von Blanckenburg & Willenbring, 2014; Granger & Schaller, 2014). This method usually has integration timescales of 10^3–10^5 years. Thermochronometric cooling ages record the cooling of rock samples during

exhumation and pinpoint the cooling through a certain temperature (the closure temperature of the respective thermochronometric system). If the closure temperature of the respective thermochronometer system and the evolution of the geothermal gradient are known, exhumation rates can be obtained from cooling ages (e.g., Braun, 2005; Fox et al., 2014; Willett & Brandon, 2013). Thermochronometric dating has integration timescales of 10^6–10^7 years, providing long-term estimates of exhumation and denudation.

As outlined above, various methods exist in order to quantitatively constrain the evolution of orogens. This thesis investigates the exhumation history of the Olympic Mountains. In order to have a better sense how the exhumation of this particular mountain range compares with other orogens, it is useful to have a rough sense of the magnitude and extent of exhumational processes. In general, exhumation rates are variable between different mountain ranges, depending on the governing processes of denudation or rock uplift. For instance, an extreme end member are the western, central Andes, which display very low denudation due to the arid climate (e.g., Starke et al., 2017; Madella et al., 2018). Hence, that part of the Central Andes is one of the most slowly exhuming active orogens on Earth, and exhumation rates can be less than 0.1 km/Myr over several millions of years (Avdievitch et al., 2018). On the other hand, in places where denudation is more efficient as is the case in the Namche Barwa syntaxis or parts of the New Zealand Alps (Figure 1.1), exhumation rates can exceed values of 5 km/Myr and these places are some of the fastest exhuming orogens on Earth (e.g., Lang et al., 2016; Enkelmann et al., 2011, 2015; Jiao et al., 2017). Exhumation is not only variable between different orogens, but also within single orogens strong spatial gradients in exhumation can be observed (Reiners et al., 2003; Thiede & Ehlers, 2013; Lease et al., 2016; Enkelmann et al., 2017; Jiao et al., 2017), depending for instance on the local distribution of precipitation. Furthermore, temporal variations in exhumation can also occur during the lifespan of an orogen, if the parameters responsible for exhumation like tectonics or climate are temporally not steady (e.g., Carrapa et al., 2003; Glotzbach et al., 2011; Adams et al., 2015; Lease et al., 2016; Enkelmann et al., 2017; Jiao et al., 2017).

1.2 From case studies to general concepts – Introducing the Olympic Mountains

Many of the concepts and aspects described in section 1.1.1 and section 1.1.2 are general concepts behind orogen formation, but were originally obtained from case studies of e.g., the European Alps, the Himalaya or the St. Elias range. Because mountain building processes are governed by forces like tectonics, climate or gravity that are not restricted to single orogens, it is common practice to gen-

eralize the findings of case studies from a specific orogen and to transfer these ideas and concepts to other orogens. Following that approach, this thesis aims at contributing to a better understanding of mountain building processes by using the Olympic Mountains as a case study. In the following sections, the study area is introduced in more detail by providing background information on the Cascadia Subduction Zone and the Olympic Mountains.

1.2.1 The Cascadia Subduction Zone

The Olympic Mountains, located in Washington State (USA), are part of the Cascadia Subduction Zone. Today, this subduction zone extends along the North American West Coast from 40° N to 51° N (Figure 1.2a). Just north of Vancouver Island, the subduction zone terminates in a transform fault (the Queen Charlotte Fault), and in the south offshore the Californian coast, the subduction zone terminates in the Mendocino Triple Junction. Along most of the margin, the Juan de Fuca Plate is subducting below the North American continent, and at the northern and southern end two further micro plates (Explorer Plate, Gorda Plate; Figure 1.2b) are involved in the subduction. The present-day configuration of the subduction zone and the modern volcanism of the Cascades Arc was initiated at around 40 Ma, after accretion of the Coast Range Terrane (Brandon & Vance, 1992; du Bray & John, 2011). This terrane (often also referred to as Siletzia) represents a large magmatic, oceanic plateau, which can be traced along the margin from southern Vancouver Island to southern Oregon (Wells et al., 2014; Eddy et al., 2017; Phillips et al., 2017).

At present, the convergence angles and rates vary along the subduction margin (Figure 1.2a), and at the latitude of the Olympic Mountains subducting and overriding plates converge with rates of 34 mm/yr (Doubrovine & Tarduno, 2008). The age of the oceanic crust at the deformation front is young and varies between ~6 Ma and ~9 Ma (Figure 1.2b; Wilson, 1993). Due to the young and warm oceanic crust, the buoyancy of the subducting slab is high, causing a flat subduction angle at the Cascadia Subduction Zone, compared to other subduction zones worldwide. The down-going slab displays a complex three-dimensional geometry below the Olympic Peninsula and southern Vancouver Island (Figure 1.2b), because a bend in the slab (with the axis of the bend approximately parallel to the dip direction of the slab) results in a locally flatter angle of subduction compared to areas north or south (Crosson & Owens, 1987; McCrory et al., 2012).

The young and warm oceanic crust has also important implications for the earthquake hazard of this subduction zone. In general, the Cascadia Subduction Zone is capable of producing strong, devastating earthquakes, involving partial or entire rupture of the margin (e.g., Wang et al., 2013; Wang & Tréhu, 2016) and the last known earthquake occurred AD 1700, corresponding to a moment

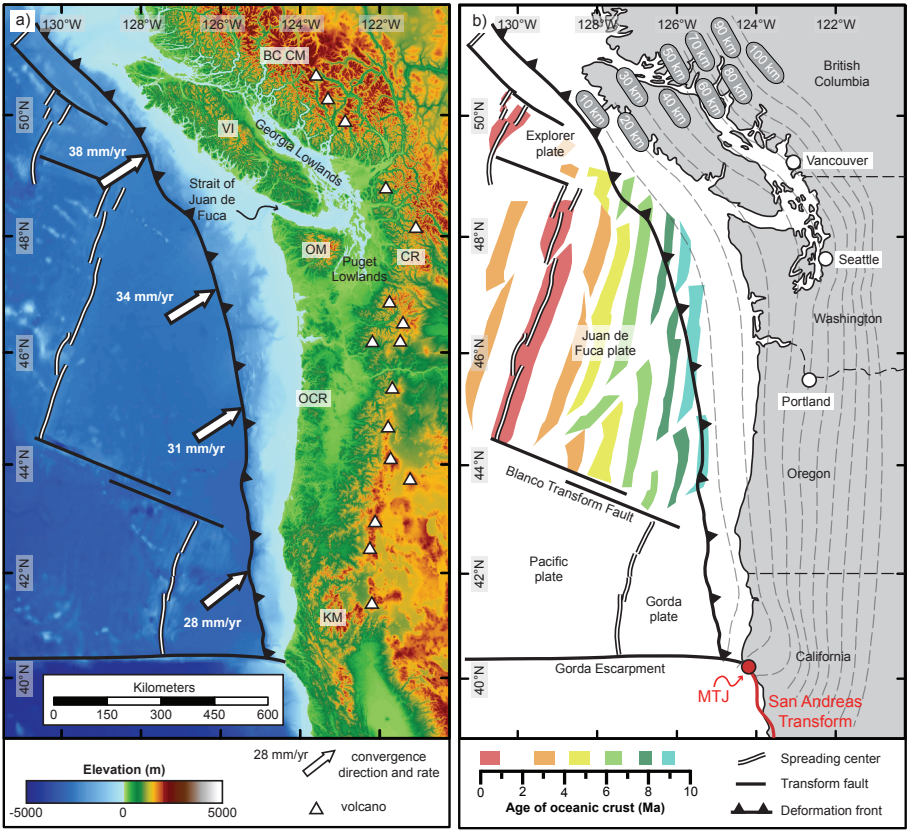

Figure 1.2: Maps of the Cascadia Subduction Zone displaying **(a)** the general topography. Areas of elevated topography referred to in the text are indicated with abbreviations, comprising (from north to south) the British Columbia Coast Mountains (BC CM), Vancouver Island (VI), the Olympic Mountains (OM), the Cascade Range (CR), the Oregon Coast Range (OCR), and the Klamath Mountains (KM). White triangles denote volcanoes of the Cascade arc with Pleistocene/Holocene activity (du Bray & John, 2011). The arrows correspond to the present-day convergence direction and rate at the deformation front, as derived from Doubrovine & Tarduno (2008). **(b)** Detailed tectonic features and plates involved in the subduction, the color coding corresponds to the age of the oceanic crust (Wilson, 1993). Dashed, gray lines correspond to contour lines of the top of the subducted slab at depth (in 10 km intervals), taken from the Slab1.0 model (McCrory et al., 2012). MTJ = Mendocino Triple Junction.

magnitude ~9.0 quake (Satake et al., 2003). An important constraint for the hazard assessment of future earthquakes is the width of the locked or seismogenic zone, which is widely disputed at the Cascadia Subduction Zone (e.g., Hyndman & Wang, 1993; Burgette et al., 2009; Hyndman, 2013; Bruhat & Segall, 2016; Wang & Tréhu, 2016).

The locked zone corresponds to the area, where free slip on the plate interface between the overriding and subducting plate is restricted due to the high friction between the two plates, leading to the accumulation of elastic strain between two earthquakes (interseismic period). The buildup of elastic strain in the interseismic period can be observed in GPS or leveling data, because coastal areas show an upwards displacement (e.g., Hyndman, 2013). Finally, this process leads to the initiation of a megathrust earthquake and the release of the accumulated, elastic strain during the coseismic period. This sequence of interseismic and coseismic period is known as the seismic cycle, which is particularly long at the Cascadia Subduction Zone (300–500 years, Wang & Tréhu, 2016).

Most models for hazard assessment assume that all elastic deformation accumulated during the interseismic period is recovered coseismically, implying that no permanent deformation occurs (e.g., Hyndman, 2013; Burgette et al., 2009; McCaffrey, 2009). However, recent work has indicated, that during the seismic cycle viscoelastic deformation should also be considered, which is capable of producing permanent deformation (Li et al., 2015). Refining the current understanding of elastic and viscoelastic deformation and how these affect the width of the locked zone are important for the seismic hazard assessment of the Cascadia Subduction Zone.

A novel discovery in the early 2000s by Dragert et al. (2001) was that at Cascadia, slip occurred on plate interface outside the seismogenic zone without any associated seismicity (also called a silent or slow slip event, SSE). After detection that SSEs are not completely silent and are accompanied by non-volcanic tremor, these events were introduced as episodic tremor and slip (ETS, Rogers & Dragert, 2003). The exact bearing of ETS is a matter of active and the expression of ETS can be different between subduction zones. However, a better understanding of the impact of ETS on the width of the seismogenic zone has implications for the seismic hazard of a subduction zone (e.g., Vidale & Houston, 2012; Wang & Tréhu, 2016; Bürgmann, 2018).

At Cascadia, the occurrence of tremor is localized in a narrow band along the subduction zone, roughly corresponding to the location of the subducted slab at depths of 30–40 km (Wang & Tréhu, 2016). A particular focus of tremor and slow slip is located below the southern end of Vancouver Island and the Olympic Peninsula, as well as beneath the Klamath Mountains in northern California (Schmidt & Gao, 2010; Wells et al., 2017). Single events do not affect the entire margin but

are spatially restricted and usually last for days to weeks (e.g., Schmidt & Gao, 2010). Slip and tremor propagate from the initiation of the single event along the plate interface (Dragert & Wang, 2011; Wech & Creager, 2011), but the exact propagation speed and direction can display complex behavior (e.g., Houston et al., 2011; Wech & Bartlow, 2014). The displacement at the Earth's surface related to ETS can be measured with GPS, and the horizontal displacement is directed opposite to the plate convergence direction (i.e., to the SW) and the vertical displacement is directed upwards (e.g., Schmidt & Gao, 2010; Bruhat & Segall, 2016).

1.2.2 The Olympic Mountains

Compared to the surroundings, the Olympic Mountains form an isolated block of elevated topography with its highest summit Mt. Olympus towering 2430 m above the nearby Pacific Ocean (Figure 1.2a and 1.3a). In the north, the Strait of Juan de Fuca separates the Olympic Peninsula from Vancouver Island, with it's highest point Golden Hinde (2195 m) located 250 km to the north-west of Mt. Olympus. To the east, the Puget Lowlands separate the Olympic Mountains from the Cascade Mountain Range, where elevations can be higher than 3000 m. In the south, the Oregon Coast Range extends along the coast, but never reaches elevations in excess of 1250 m. This pattern is in accordance with the topographic features of fore arc high (Vancouver Island, Olympic Mountains, Oregon Coast Range), fore arc low (Georgia and Puget Lowlands) and volcanic arc (Cascades Mountains) commonly observed at subduction zones (Figure 1.2).

The Olympic Mountains are an actively deforming orogen, as evidenced by present-day GPS data (e.g., McCaffrey, 2009; Bruhat & Segall, 2016) and Holocene seismicity (Wilson et al., 1979; Barnett et al., 2015; Nelson et al., 2017; Delano et al., 2017). Geologically, the accretionary wedge of the Cascadia Subduction Zone is exposed onshore within the Olympic Mountains and comprises flysch sediments of Eocene to Miocene age (which have been off-scraped from the subducting oceanic plate) with minor intercalations of basaltic rocks (Tabor & Cady, 1978; Brandon et al., 1998). The Hurricane Ridge Fault (HRF) separates the accretionary wedge from the surrounding Coast Range Terrane (Figure 1.3b), which predominantly consists of ~50 Ma old basaltic rocks (Eddy et al., 2017) besides minor sediments of Eocene age (Tabor & Cady, 1978; Eddy et al., 2017). In general, the metamorphic overprint of the sandstones and shales from the accretionary wedge is low, but increases from the coast towards the interior of the mountain range, reaching lower greenshist facies (Tabor & Cady, 1978). Locally, the basalts of the Coast Range Terrane can reach blueshist facies overprint (Hirsch & Babcock, 2009). Because the interior part of the Olympic Mountains offers only poor outcrop conditions, the internal structure of the accretionary

wedge is difficult to constrain, but Brandon et al. (1998) grouped it into Coastal, Upper and Lower Olympic Structural Complex (Figure 1.3b), based on available faults, lithology and apatite fission-track ages.

From a climatic viewpoint, the Olympic Mountains form the first barrier for incoming, moist air masses from the Pacific Ocean. Hence, there is a strong gradient in precipitation developed across the mountain range, where mountainous areas close to Mt. Olympus receive up to 6000 mm/yr of precipitation, while the much drier east side receives <1000 mm/yr (Figure 1.3c). The spatial distribution and the large amount of precipitation also impacted the development of glaciers. Although the currently existent glaciers are only a puny leftover from the past major glaciation and are vanishing rapidly (e.g., Riedel et al., 2015), the mountain range was intensely shaped by glacial processes. Particularly on the western side of the orogen, alpine glaciers incised deeply into the topography (e.g., Adams & Ehlers, 2017; Montgomery & Greenberg, 2000; Montgomery, 2002), forming wide valleys like Hoh, Elwha, Queets and Quinault (Figure 1.3a), and lobes of piedmont glaciers almost reached the Pacific Ocean (Thackray, 2001). The Cordilleran Ice Sheet (one of North America's major ice shields) surrounded the Olympic Mountains in the north (covering large parts of Vancouver Island and the continental shelf) and in the east, shaping the Puget Lowlands (Booth et al., 2003; Clague & James, 2002). Dating the onset of alpine glaciation in the Olympics is non-trivial due to the deeply weathered glacial deposits, but is thought to have occurred at ~2 Ma (Easterbrook, 1986).

The Olympic Mountains have been the location for several studies applying thermochronometry (Batt et al., 2001; Brandon & Vance, 1992; Brandon et al., 1998; Garver & Brandon, 1994; Stewart & Brandon, 2004), cosmogenic nuclide dating (Belmont et al., 2007; Adams & Ehlers, 2018) or geomorphic techniques (Pazzaglia & Brandon, 2001; Adams & Ehlers, 2017; Delano et al., 2017) in order to investigate the evolution of this mountain range. Hence, a large collection of data is available, in particular of thermochronometric ages consisting of apatite and zircon fission track ages with minor apatite (U-Th)/He ages (Figure 1.3d). Based on the interpretation of the thermochronometric ages, exhumation of the Olympic Mountains commenced at around 18 Ma (Brandon & Vance, 1992; Brandon et al., 1998) and since ~14 Ma the mountain range is thought to be in flux steady-state (Batt et al., 2001; Brandon et al., 1998; Pazzaglia & Brandon, 2001). Highest exhumation rates (1.0 km/Myr) are reported on the western side of the range, and exhumation rates are lower (<0.3 km/Myr) at the coast (Figure 1.3d; Brandon et al., 1998). Based on the metamorphic overprint of the sandstones, a crucial role during uplift of the Olympic Mountains is assigned to the bend in the subducting slab below the mountain range, which is interpreted to be the result of extension in the Basin and Range Province starting at ~16 Ma (Brandon

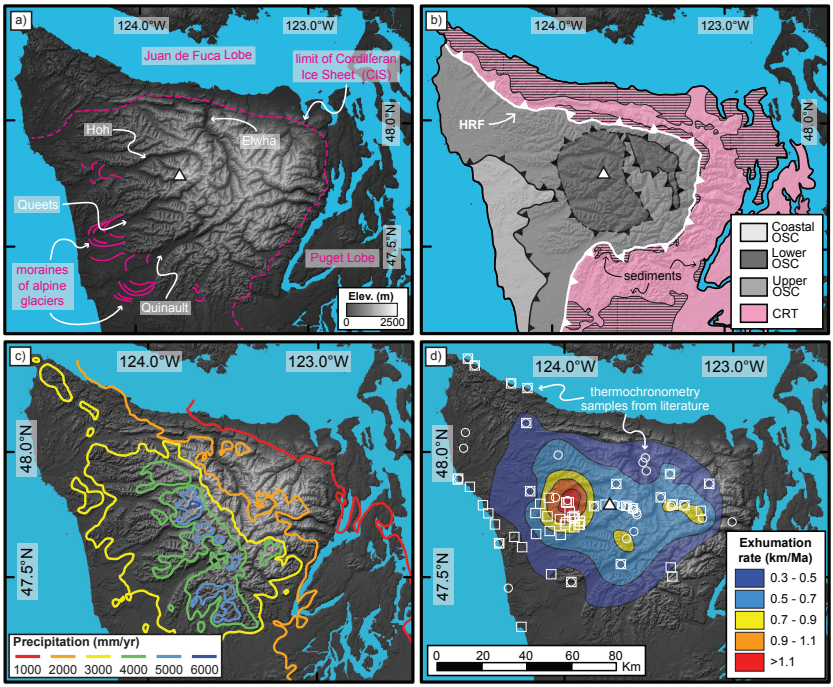

Figure 1.3: (a) Topography of the Olympic Mountains, indicating the location of Mt. Olympus (white triangle) and major valleys (Hoh, Elwha, Queets, Quinault). Pink lines correspond to Quaternary features, like the extent of alpine glaciers and the Cordilleran Ice Sheet (CIS), which surrounded the Olympic Mountains in the north and east and can be divided into the Juan de Fuca and Puget lobes. Extent of alpine glaciers after Tabor & Cady (1978) and of the CIS after Porter (1964). **(b)** Geological and structural map, showing the distribution of rocks from the accretionary wedge (OSC=Olympic Structural Complex) and the surrounding Coast Range Terrane (CRT), separated by the Hurricane Ridge Fault (HRF). Map is based on Tabor & Cady (1978) and Brandon et al. (1998). **(c)** Precipitation pattern across the Olympic Peninsula, taken from the PRISM dataset (`http://prism.oregonstate.edu/`). **(d)** Map of exhumation rates as suggested by Brandon et al. (1998) along with the location of published thermochronometry ages (Brandon & Vance, 1992; Garver & Brandon, 1994; Brandon et al., 1998; Batt et al., 2001; Stewart & Brandon, 2004). Squares denote zircon fission-track ages, circles denote apatite fission-track ages. Apatite (U-Th/He) ages also exist for eleven samples (not indicated on map). The map of exhumation rates is based on the inversion of apatite fission-track ages.

& Calderwood, 1990). Topographic analysis and denudation rates derived from cosmogenic nuclides support the hypothesis that the bend in the subducted slab is important for shaping the Olympic Mountains (Adams & Ehlers, 2017, 2018).

1.3 Background for methods applied in the thesis

As introduced in section 1.1.2 many tools like thermochronometric dating or cosmogenic nuclide dating as well as geodetic methods can be utilized to investigate mountain building processes. In this thesis, thermochronometric dating of rock samples along with thermo-kinematic modelling of thermochronometric cooling ages is applied, to better understand the exhumation history of the Olympic Mountains. A brief introduction to the theoretical background behind these two methods is given in section 1.3.1 and 1.3.2, respectively.

Furthermore, different published datasets are used in order to investigate the flux steady-state balance of the Olympic Mountains or to better understand the mechanisms behind deformation. These include published thermochronometric ages, denudation rates from cosmogenic nuclides, sedimentary data from offshore drill cores as well as offshore seismic data and GPS-based observations. A summary of these datasets is provided in section 1.3.3.

1.3.1 Thermochronometry

The discovery of radioactivity and radioactive decay chains in the late 19th and early 20th century (e.g., Rutherford & Soddy 1903a,b; Rutherford 1905) laid the foundation for radiometric dating. Since then, radiometric dating has become a widely used tool in the geosciences allowing to determine absolute ages of geological processes. Radiometric dating is based on the exponential decay of radioactive parent isotopes into stable daughter isotopes, whereby the number of daughter isotopes (N_d) is linked to the number of parent isotopes (N_p) by the decay constant λ and the evolved time (t) via

$$N_d = N_p(e^{\lambda t} - 1) \tag{1.2}$$

After reformulation, equation 1.2 yields the general age equation used in radiometric dating:

$$t = \frac{1}{\lambda} \ln \left(\frac{N_d}{N_p} + 1 \right) \tag{1.3}$$

Radiometric dating is performed on certain minerals, which contain sufficient radioactive parent nuclides and retain the daughter nuclides. If the decay constant is known and the amount of daughter and parent nuclides within a given

mineral can be determined, an age can be calculated using equation 1.3. Various isotope systems exist for different minerals, and these can be grouped in methods applied in geochronology (e.g., U-Pb dating of zircon or apatite, Sm-Nd dating of garnet) and thermochronometric methods like Ar-Ar dating of micas or feldspar, (U-Th)/He dating of apatite or zircon (AHe and ZHe) or fission-track dating of apatite and zircon (AFT and ZFT).

AHe and ZHe dating is based on the measurement of accumulated He atoms within apatite and zircon mineral grains, which are formed from α-particles as part of the decay chain of U and Th to Pb (and in the case of apatite also of Sm to Nd). The total amount of produced ^{4}He equals the sum from the single, contributing isotopes, where the respective production of ^{4}He is governed by the decay constant λ of the respective isotope

$$^{4}\mathrm{He} = 8^{238}\mathrm{U}(e^{\lambda_{238}t}-1)+7^{235}\mathrm{U}(e^{\lambda_{235}t}-1)+6^{232}\mathrm{Th}(e^{\lambda_{232}t}-1)+^{147}\mathrm{Sm}(e^{\lambda_{147}t}-1) \quad (1.4)$$

With that equation, an AHe or ZHe age can be calculated, if the amount of ^{4}He and the respective parent isotopes is measured. To do so, single crystals of either apatite or zircon are in a first step analyzed for their He content and in a second step for their U/Th/Sm content. A diagram outlining the entire procedure inherent to (U-Th)/He dating is displayed in Figure 1.4. Before a final AHe or ZHe age can be calculated, the measured amount of He needs to be corrected, because the kinetic energy of α-particles is high and single α-particles are ejected over a distance of up to 20 μm in a mineral grain, leading to potential He loss at the mineral grain boundaries (Farley et al., 1996; Farley, 2002). The correction is known as the Ft-correction and depends on the grain size and grain shape fo a crystal. In (U-Th)/He dating of bedrock samples, usually 3–7 single grains are analyzed and a mean sample age is calculated from the single grain ages.

Besides the decay of U, Th and Sm to table daughter products, which is utilized in (U-Th)/He dating, ^{238}U can also undergo spontaneous fission, whereby the unstable ^{238}U nucleus is split into two fragment nuclei and 2–3 neutrons (Tagami & O'Sullivan, 2005). The fragment nuclei have high kinetic energies, are expelled from the site of fission and cause damage to the surrounding crystal lattice due to their positive electric charge. These damage zones are termed fission-tracks, are typically several microns long and can be made visible for identification with a microscope by etching the crystals. Counting these fission-tracks as "daughter products" forms the basis of fission-track dating, whereby fission-tracks accumulate in a crystal with increasing time.

Fission-track dating of apatite (AFT) or zircon (ZFT) is performed on mineral mounts, where the respective minerals are embedded in epoxy or teflon in a first step. The following steps involved in counting the fission-tracks and calculating an age are summarized in Figure 1.4. The fission-tracks in the host minerals ap-

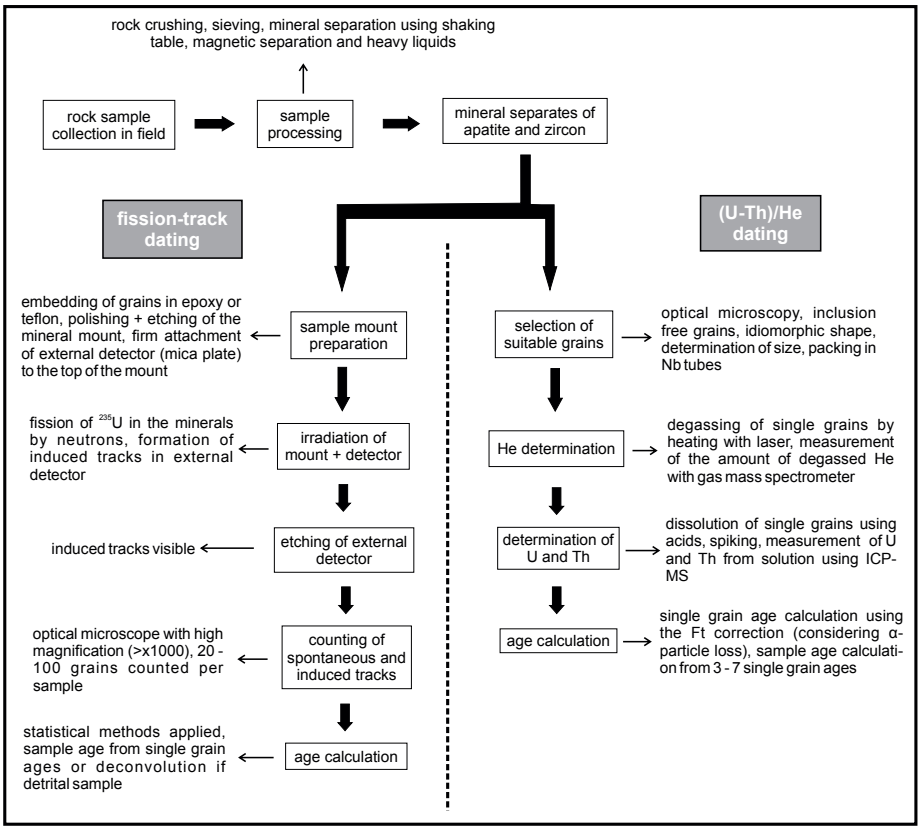

Figure 1.4: Diagram illustrating the steps involved in obtaining thermochronometric cooling ages, starting from taking rock samples in the field to calculating the final ages for fission-track and (U-Th)/He dating of apatite or zircon (AFT, ZFT, AHe, ZHe, respectively).

atite or zircon are termed spontaneous fission-tracks, and the number of counted tracks corresponds to the amount of produced daughter products in terms of equation 1.3. In order to determine the amount of parent products (so the ^{238}U content), U can either be measured using laser-ablation or estimated with an external detector (a sheet of mica), which is firmly attached to the surface of a mineral mount. The external detector method (EDM) capitalizes on the induced fission of ^{235}U within the host minerals by thermal neutron irradiation in a nuclear reactor. Here, fission of ^{235}U leads to formation of induced fission-tracks in the mica sheet that can then be counted after etching of the mica sheets, yielding the amount of parent products via the known and constant ratio of ^{238}U and ^{235}U. A fission-track age can be obtained via

$$t = \frac{1}{\lambda_D} \ln \left(\frac{1}{137.88} \frac{\lambda_D}{\lambda_F} \frac{N_s}{N_i} \sigma_F \phi \right) \tag{1.5}$$

where λ_D and λ_F, respectively, correspond to the constants of decay and fission of ^{238}U, N_s and N_i refer to the counted number of spontaneous and induced fission-tracks, σ_F corresponds to the cross section of induced fission for ^{235}U and ϕ is the thermal neutron flux within the nuclear reactor. Around 20 grains are usually dated for fission-track analysis and uncertainties on the single grain ages are very high. Statistical methods are applied in order to check, whether the single grain ages belong to the same age population, which is then interpreted to correspond to the sample's fission-track age (Galbraith, 2005). If a sample is detrital, hence the single grain ages can belong to different grain age populations, about 100 grains need to be dated and the grain age distribution can be decomposed in the respective age populations (Brandon, 1992).

After successful analysis, an age can be readily calculated from the measured amount of parent and daughter nuclides using for instance equation 1.3 or modified versions like equation 1.4 or 1.5. However, during the interpretation of thermochronometric ages it is important to take into account that the retention of daughter nuclides in the considered minerals after decay is subject to diffusion. Diffusion itself is strongly temperature dependent via an Arrhenius relationship

$$D = D_0 \exp \left(-\frac{E_a}{RT} \right) \tag{1.6}$$

where diffusion D depends on the frequency factor D_0, the activation energy E_a, the gas constant R and the temperature T. For most geochronologic methods (e.g., U-Pb dating of zircon), the diffusion of the daughter isotopes is negligibly small even at high temperatures, hence an age obtained from geochronologic dating is usually interpreted to correspond to the formation age of a particular

sample. For instance, a zircon U-Pb age of a granitic sample corresponds to the crystallization age of this granite.

Contrary to that, the diffusivity of the considered daughter isotopes in thermochronometry is high, and the obtained age corresponds to a cooling age. Figure 1.5a summarizes the evolution of the daughter/parent nuclide ratio during cooling, as for instance occurs while a rock sample is exhumed to the surface. Initially, the temperature is high and no daughter isotopes are retained, because the loss by diffusion outpaces the production by radioactive decay (open system). In case of AHe or ZHe this implies that no ^{4}He produced by the decay of U or Th is retained within the minerals due to the diffusional loss. For AFT or ZFT, this means that no fission-tracks are retained within the host minerals, because all damage created to the crystal lattice by the spontaneous fission of ^{238}U is annealed. As time progresses and sufficient cooling has occurred, the accumulation of daughter isotopes starts (but diffusional loss still occurs) and when a sample has cooled below the blocking temperature, all daughter isotopes are retained and the parent/daughter ratio evolves linearly with time (closed system, Figure 1.5a). This range of temperatures between onset of accumulation and complete retention is known as the partial retention zone (PRZ). Strictly speaking, the ages obtained with thermochronometric dating record the entire time interval of the PRZ.

However, because it is difficult to relate a cooling age obtained from thermochronometric dating to a temperature interval (the PRZ), Dodson (1973) introduced the concept of a closure temperature T_c. Here, an apparent cooling age can be interpreted to represent cooling below a discrete temperature, the closure temperature (Figure 1.5). For the case of steady cooling, Dodson (1973) defined the closure temperature as

$$T_c = \frac{E_a}{R \ln(A\tau D_0/a^2)} \tag{1.7}$$

where A is a numerical constant, a corresponds to the diffusion domain (usually the grain size of a dated mineral) and τ relates T_c to the cooling rate ($\dot{T}$) and is given by

$$\tau = \frac{RT_c^2}{E_a \dot{T}} \tag{1.8}$$

Therefore, contrary to geochronology, an age obtained from thermochronometric dating does not reflect the formation age of a rock sample but represents an (apparent) cooling age. However, this has also the benefit that the cooling paths of rock sample can be reconstructed.

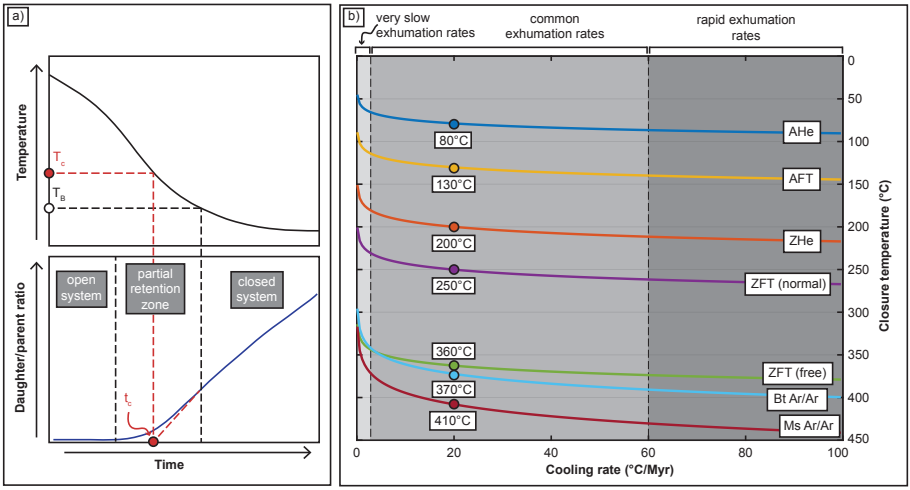

Figure 1.5: (a) Sketches illustrating the concept behind a closure temperature, showing the evolution of temperature with time (top panel), as well as the evolution of the daughter/parent nuclide ratio (bottom panel). If the temperature is too high, all daughter isotopes are lost by diffusion (constant ratio, open system behavior). When sufficient cooling has occurred, accumulation of daughter nuclides starts, however the change in parent/daughter nuclide ratio is non-linear, due to partial loss by diffusion (partial retention zone). When cooling below the blocking temperature T_B has occurred, all daughter isotopes are retained and the daughter/parent ratio evolves linearly (closed system). The closure temperature T_c corresponds to the temperature at the apparent closure time (t_c), which is obtained by extrapolating the linear daughter/parent ratio onto the time axis. Sketch after Dodson (1973) and Braun et al. (2006). **(b)** Closure temperature estimates of common thermochronometer systems calculated for a range of cooling rates, using the parameters given in Ehlers (2005). The grey areas illustrate, in which setting the respective cooling rates could be found, for instance very slow cooling in shields (or after cessation of tectonic activity), intermediate cooling rates as found in many areas of active tectonics, and very rapid cooling as can be found in some orogens (e.g., Southern Alps of New Zealand or the Namche Barwa syntaxis, Figure 1.1). For a cooling rate of 20°C/Myr, the respective closure temperatures are indicated in white boxes, and assuming a geothermal gradient of 20°C/km this would correspond to the expected closure temperatures for an exhumation rate of 1 km/Myr.

Inspecting equations 1.7 and 1.8 shows that the closure temperature depends on the cooling rate, grain size and the kinetics of diffusion (as contained in the diffusional parameters D_0 or E_a). The kinetic parameters differ between the various thermochronometer systems and can be obtained from laboratory measurements (e.g., Farley, 2000; Reiners et al., 2004; Ketcham et al., 1999; Rahn et al., 2004). However, the kinetic parameters for a single system can also vary, depending on the properties of the respective mineral like its composition (e.g., Green et al., 1985; Ketcham et al., 1999; Brandon et al., 1998) or radiation damage caused by α-decay (e.g., Nasdala et al., 2001; Rahn et al., 2004; Flowers et al., 2009; Guenthner et al., 2013). Figure 1.5b displays the respective closure temperature estimates as a function of cooling rate for various thermochronometer systems including apatite and zircon (U-Th)/He (AHe and ZHe), apatite and zircon fission-track (AFT and ZFT), and biotite and muscovite Ar-Ar. Lower closure temperatures are obtained for very slow cooling rates, as might be the case for slowly eroding areas like cratonic shields.

In order to provide an estimate of which temperature range can be constrained with the four thermochronometer systems applied in the thesis (AHe, AFT, ZHe, ZFT), the respective closure temperatures (80°C, 130°C, 200°C and 250°C) are indicated in Figure 1.5b, assuming a cooling rate of 20°C/Myr. Such a cooling rate corresponds to an exhumation rate of 1 km/Myr, if a geothermal gradient of 20°C/km is assumed. However it is important to remember that the calculated closure temperatures are only valid in the case of steady cooling, i.e., if variations in cooling rate occur during cooling through the PRZ, then a numerical approximation for the closure temperature has to be used (Braun et al., 2006).

1.3.2 Thermo-kinematic modelling

During exhumation, rocks experience cooling on their path from the hotter interior of the earth to the cooler surface. The thermal structure of the Earth's crust can be imagined as a series of isotherms, which correspond to lines (in two dimensions) or planes (in three dimensions) of equal temperature, similar to contour lines of equal elevation (Figure 1.6). As described in section 1.3.1, thermochronometers record the time, when a rock cooled below a certain temperature, the closure temperature of the respective thermochronometric system. By using the time of cooling recorded by the thermochronometer and the closure temperature, a cooling rate for a rock can be calculated. Hence, thermochronometry allows to put quantitative constraints on the cooling paths of rocks. However, for many geological problems it is of particular interest not only to know the cooling rate of a rock, but to know how fast it emerged to the surface (so to quantify its exhumation rate). Therefore, it is necessary to constrain how the thermal structure of the Earth's crust is evolving through time.

The thermal structure of the crust is governed by the transport of heat from the mantle to the surface, which is controlled mainly by heat conduction and heat advection, and to a minor amount by the production of heat within the crust due to the decay of radioactive elements. Fourier's law states that conductive heat flow (q) occurs due to a temperature gradient (ΔT) over a distance l, affected by the thermal conductivity (k)

$$q = k\frac{\Delta T}{l} \tag{1.9}$$

The heat flux equals the heat released within a given time over an area and can be measured at the Earth's surface. This would allow calculating the temperature gradient (also called the geothermal gradient), if the thermal conductivity of a rock is known. By using the calculated geothermal gradient, cooling rates obtained from thermochronometry could be converted into exhumation rates.

However, the subsurface temperature field is a transient feature, depending on the respective contributions from heat conduction, heat advection and heat production. Hence, the geothermal gradient is variable with time, which has to be considered for the interpretation of thermochronometry data, because for example the concept of the closure temperature (Equation 1.7) only applies for the case of a steady cooling rate. The three-dimensional heat-conduction equation (Fowler, 2005) describing the variation of temperature with time is

$$\frac{\partial T}{\partial t} = \frac{k}{\rho c_P}\nabla^2 T + \frac{A}{\rho c_P} \tag{1.10}$$

Here, the contributions of the conduction of heat (controlled by the physical properties of thermal conductivity k, density ρ and heat capacity c_P) and the contribution of heat production by the decay of radioactive elements (A, heat production rate per volume) is considered, and ∇ is the Nabla-Operator, as defined by

$$\nabla = \frac{\partial}{\partial x} + \frac{\partial}{\partial y} + \frac{\partial}{\partial z} \tag{1.11}$$

For most rocks on Earth, the thermal conductivity is low. Hence, it takes many millions of years to disturb a given temperature field by for instance the heat released by an intrusion or a change in the mantle heat flux, if heat transport occurs solely by conduction of heat.

On the other hand, heat advection, so the transport of heat by the movement of particles as occurs during exhumation, is a much more efficient heat transport mechanism (Figure 1.6). Equation 1.10 provides sensible estimates of the subsurface temperature field for very slow exhumation rates (e.g., < 0.1 mm/yr, Braun et al., 2006). If the exhumation rates are higher as is the case for most

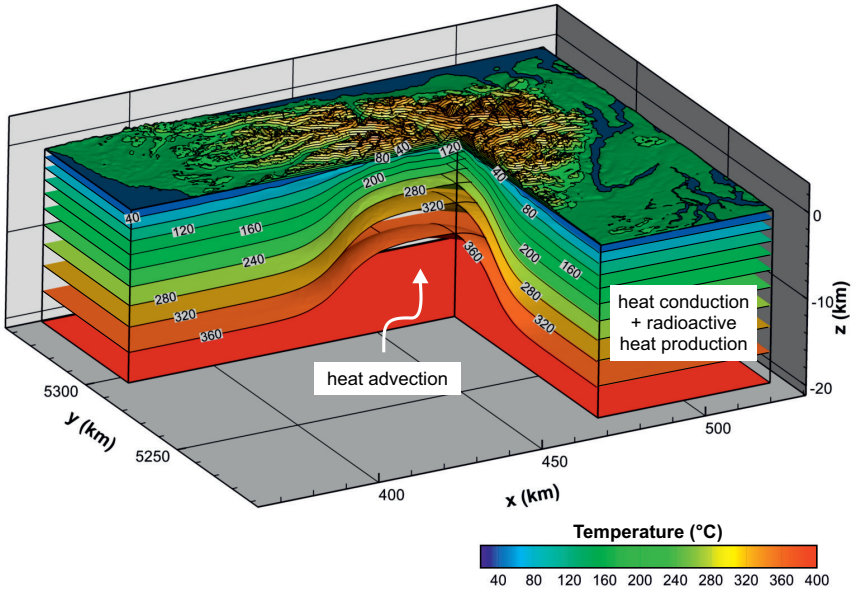

Figure 1.6: Results from a thermo-kinematic model, showing the 3-dimensional, thermal structure below the Olympic Mountains, which is affected by contributions from heat conduction, heat production by radioactive decay and heat advection. The upward deflection of isotherms (lines of equal temperature) in the center of the Olympic Mountains is the result of the dominance of heat advection in this area, caused by locally faster exhumation rates compared to areas close to the coast. The vertical axis of the diagram is exaggerated by a factor of 2.

active mountain ranges, then also the effect of heat advection has to be taken into account. Therefore equation 1.10 needs to be modified to include the heat advective term (Fowler, 2005), yielding

$$\frac{\partial T}{\partial t} = \frac{k}{\rho c_P}\nabla^2 T + \frac{A}{\rho c_P} - \dot{E}\frac{\partial T}{\partial z} \tag{1.12}$$

That equation considers only displacement of particles in the z direction towards the surface of the Earth ($\dot{E}$, the exhumation rate). If also velocities in other directions are considered, equation 1.12 needs to be modified correspondingly.

Besides the effect of heat conduction and heat advection, another important parameter controlling the near surface thermal structure of the crust is the topography (Stüwe et al., 1994; Mancktelow & Grasemann, 1997). Isotherms are deflected upwards below topographic highs and downwards below topographic lows (Figure 1.6). In general, this effect depends on the wavelength and amplitude of the considered features and decreases exponentially with depth and particularly low-temperature isotherms are affected. Hence, the effect of topography has to be considered for thermochronometer systems with low closure temperatures (e.g., AHe), because for a constant exhumation rate cooling is faster below valleys compared to mountain tops. On the other hand, this effect can also be used in order to constrain changes in the topography of landscapes (e.g., House et al., 1998, 2001; Braun, 2002; Ehlers et al., 2006).

In order to interpret cooling histories derived from thermochronometric cooling ages and to provide quantitative constraints on exhumation, a thermo-kinematic model is applied in this thesis. Pecube is a 3D finite-element, thermo-kinematic model, which solves the partial-differentials of equation 1.12 considering the contributions of topography, heat conduction, heat advection and production of heat on the subsurface temperature field (Braun, 2003; Braun et al., 2006, 2012). For a given kinematic field, the model calculates particle paths from the time-dependent location of particles and predicts thermochronometric cooling ages for particles at the surface, based on their thermal histories. Because the closure temperature of a thermochronometer system depends on the cooling rate, which can be transient due to the effects of exhumation, Pecube uses a numerical solution of Equation 1.7.

Pecube requires the user to define the kinematic field, physical properties of rocks and the topography, in order to calculate time-temperature histories (Figure 1.7). From that, modeled ages are predicted and can be compared to thermochronometer ages from actual samples. Several options exist to explore temporal variations in exhumation or changes in topography. The user can run forward-model simulations with pre-defined exhumation histories where he defines the exhumation pattern as well as the timing and magnitude of changes in

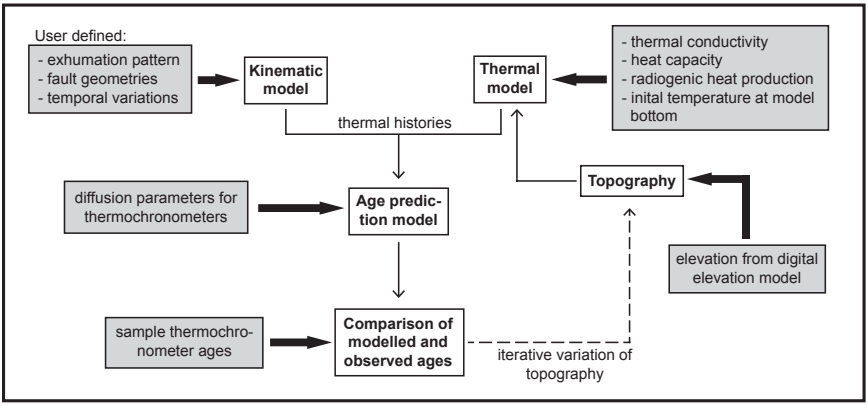

Figure 1.7: Diagram illustrating the work flow of the thermo-kinematic model Pecube (Braun, 2003), which allows to explore possible exhumation histories. Based on the prescribed parameters, thermal histories are calculated and thermochronometer ages are predicted, which are finally compared to observed thermochronometer ages. The iterative topography variation allows to reconstruct the paleotopography of landscapes (Olen et al., 2012). Grey boxes indicate input parameters that need to be specified by the user.

exhumation, and the viability of a particular exhumation history is assessed by comparing modelled and observed ages. These simulations are run in three dimensions, include the effect of topography and are suitable for a large dataset of thermochronometric cooling ages, but are time-consuming and generally require a rough a-priori knowledge of possible exhumation scenarios. The user can also capitalize on the built-in Monte-Carlo algorithm, which allows to explore a large range of possible exhumation scenarios (i.e., thousands of simulations) for a single sample with no a-priori knowledge of the exhumation history (e.g., Adams et al., 2015; Thiede & Ehlers, 2013). However, these simulations are only performed in one dimension for a single column of rock, but due to the large number of simulations a robust, statistical estimate of the temporal evolution of exhumation is derived. The approach is particularly useful for samples, which are dated with multiple thermochronometer systems. Another option allows to reconstruct changes in topography for a given exhumation scenario, where Pecube iteratively varies the topography within the three-dimensional model geometry, until the misfit between modeled and observed ages is minimized (Olen et al., 2012). This option is particularly useful to evaluate the erosive potential of glaciers on landscapes.

In the thesis, the forward modelling approach is utilized in order to reconstruct the large scale, spatial pattern of exhumation in the Olympic Mountains, based on the comparison between modelled and observed thermochronometer ages distributed over the entire Olympic Peninsula. Furthermore the thesis aims at resolving the location of changes in topography from the forward models. For samples with three to four available thermochronometer ages the Monte-Carlo approach is used in order to estimate possible temporal variations in exhumation rate. However, although this approach is well-suited to resolve temporal variations, the spatial resolution of the obtained exhumation history is limited to the respective sample site.

1.3.3 Published datasets used in this thesis

Besides generating new data by using thermochronometric dating and thermo-kinematic modelling, the thesis capitalizes on the plethora of published datasets that are available for the Olympic Mountains. Abundant thermochronometric data for AHe, AFT and ZFT are available (Brandon & Vance, 1992; Brandon et al., 1998; Stewart & Brandon, 2004), in particular on the western side of the Olympic Mountains (see Figure 1.3d). These thermochronometric ages are included in the thermo-kinematic models. Denudation rates derived from cosmogenic nuclide dating (Adams & Ehlers, 2018) are available for the Olympic Mountains and are compared with exhumation rates from this work. During the International Ocean Drilling Program, three marine drill cores were drilled into the sediments blanketing the Juan de Fuca Plate, yielding information on the sediment thickness and sedimentation rates offshore the Olympic Peninsula (Kulm et al., 1973; Su et al., 2000; Westbrook et al., 1994). Along with information from offshore seismic data (Adam et al., 2004; Booth-Rea et al., 2008; Han et al., 2016), these constraints are used to estimate the accretionary influx into the Olympic Mountains. Furthermore, GPS velocities, the GPS-derived vertical displacement due to episodic tremor and slip (Bruhat & Segall, 2016) as well as the available distribution of tremor (`https://pnsn.org/tremor`) due to episodic tremor and slip yields constraints on the deformation of the Olympic Mountains on timescales of decades.

Chapter 2

Scope of the thesis - evaluated hypotheses

The previous chapter aimed at providing an overview of mountain building processes in general and introduced the study area and methods. As indicated, the main objective of the thesis is to contribute to a better understanding of processes involved in mountain building. This overarching objective is framed around the following five hypotheses and scientific questions, which are addressed in the thesis:

① **If the plate geometry plays an important role in focusing deformation in mountain ranges, then a focused pattern of exhumation rates should be observed within orogenic syntaxes.**

② **If changes in the tectonic conditions or climate affect the evolution of orogens, then an increase in exhumation rates should be caused by an increase in plate convergence rate or the onset of Plio-Pleistocene glaciation.**

③ **If the denudational outflux out of an orogen is increased by glacial erosion, then the flux steady-state balance of an orogen should be disturbed unless the accretionary influx increases by the same amount.**

④ **If the effects of viscoelastic deformation during the seismic cycle permanently deform landscapes, then these effects should be detectable with methods measuring deformation over different timescales.**

⑤ **If glacial erosion is capable of significantly lowering the elevation of mountain ranges, then a concomitant increase in exhumation rate must occur.**

The intention of the current chapter is to elaborate in more detail on these five hypotheses and to provide additional background information. The actual results of the thesis and the discussion about the results are presented in chapter 3.

2.1 Effect of the plate geometry on mountain building

Some of the highest exhumation rates on Earth (>5 km/Myr) are documented for the Nanga Parbat and Namche Barwa areas of the greater Himalaya region

and the St. Elias region in Alaska (Enkelmann et al., 2011, 2015; Lang et al., 2016). These regions (Figure 1.1) are traditionally referred to as good examples of the tectonic aneurysm model (Figure 2.1a), where high exhumation rates are the result of a coupling between climate, erosion and tectonics (e.g., Zeitler et al., 2001; Enkelmann et al., 2009; Koons et al., 2013). Focused and rapid erosion by rivers or glaciers results in exhumation of warmer rocks from greater depths. Because that process perturbs the stress and thermal field, the crust is locally weakened, which creates a feedback and leads to more exhumation, finally focusing deformation and exhumation of rocks.

However, Nanga Parbat, Namche Barwa and St.Elias are also located in oroclines or orogenic syntaxes. Orogenic syntaxes can be found, where the concave segments of plate boundaries intersect, creating a convex, upward bend of the plate in the intersection of the segments (Mahadevan et al., 2010; Bendick & Ehlers, 2014). Based on numerical simulations Bendick & Ehlers (2014) showed that bending the down-going plate results in mechanical stiffening and formation of a rigid indenter, which in turn creates focused deformation and rapid exhumation in the overriding plate (Figure 2.1b). Nettesheim et al. (2018) expanded the simulations of Bendick & Ehlers (2014) by also incorporating surface processes. Their observations emphasize the importance of the plate geometry in focusing exhumation and deformation, but also indicate that efficient erosional processes are required in order to exhume rocks.

So both the tectonic aneurysm and the rigid indenter model elicit focused deformation and exhumation of rocks. However, the driving mechanism differs between the two concepts, because in the tectonic aneurysm model surface processes control the focusing of exhumation, whereas in the rigid indenter model focusing of exhumation is controlled by the plate geometry.

At the Cascadia Subduction Zone, a bend in the down-going slab (Figure 1.2b) and lower angle of subduction compared to areas north or south is well documented below the Olympic Mountains (Brandon & Calderwood, 1990; Crosson & Owens, 1987; McCrory et al., 2012). A locally flatter angle of subduction is required to create the mechanical stiffening of a rigid indenter. Hence, the Olympic Mountains are ideally suited to validate the model predictions from Bendick & Ehlers (2014) and Nettesheim et al. (2018) and to investigate the first hypothesis:

If the plate geometry plays an important role in focusing deformation in mountain ranges, then a focused pattern of exhumation should be observed within orogenic syntaxes.

The effect of plate geometry on exhumation and evolution of the Olympic Mountains is investigated by means of low-temperature thermochronometric dating

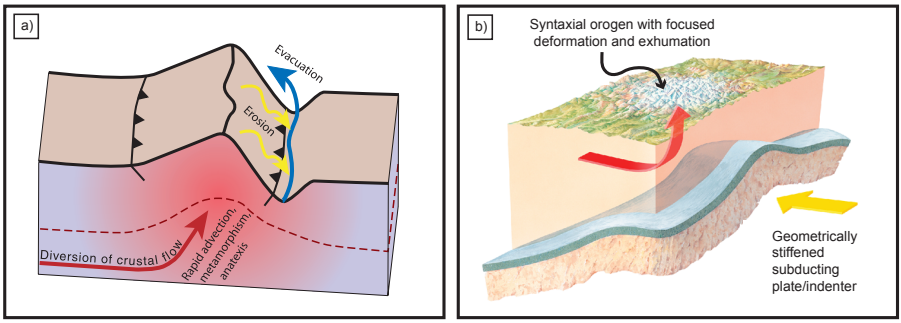

Figure 2.1: Competing models for explaining focused deformation and exhumation of rocks, **(a)** tectonic aneurysm model, where localized, strong erosion at the surface (e.g., by a river) results in focused exhumation of hot material, locally weakening the crust. This creates a positive feedback, leading to more exhumation. Taken from Zeitler et al. (2001). **(b)** Rigid indenter model, where the plate geometry plays a pivotal role, because a bend in the subducting plate creates a mechanical stiffening and the resulting indenter focuses deformation and exhumation in the overriding plate. Modified from Bendick & Ehlers (2014).

(predominantly apatite and zircon (U-Th)/He) and thermo-kinematic modelling of new and existing (Brandon & Vance, 1992; Brandon et al., 1998; Stewart & Brandon, 2004) thermochronometer ages.

2.2 Effects of climate and tectonics on mountain building

Molnar & England (1990) suggested possible feedbacks between late Cenozoic cooling, denudation and uplift of mountain ranges. Since then, the contribution of processes like tectonics, erosion, and climate on the development of mountain ranges (e.g., the formation of topography and relief) and possible feedbacks between these processes (Figure 2.2) has been an ongoing debate among geoscientists (e.g., Whipple, 2009; Champagnac et al., 2012). The importance of tectonics on parameters like topography or distribution of denudation and a response of climate to tectonics (rather than a response of tectonics to climate) has been proposed by various studies (e.g., Robert et al., 2011; Godard et al., 2014; Wang et al., 2014; Adams et al., 2015; Lease et al., 2016; van der Beek et al., 2016).

However, based on model predictions, a strong impact of surface processes on the style and deformation of mountain ranges is expected (e.g., Beaumont et al., 1992; Avouac & Burov, 1996; Willett, 1999; Whipple & Meade, 2006).

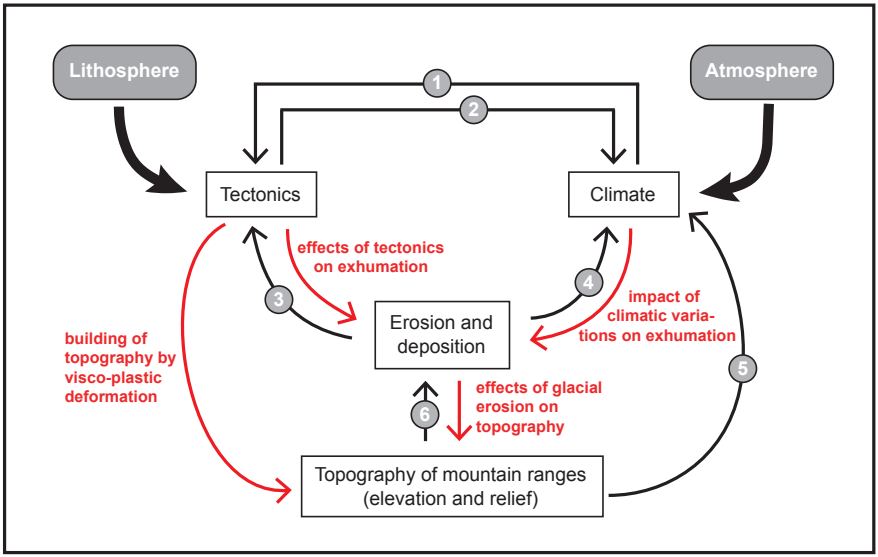

Figure 2.2: Sketch illustrating possible links and feedbacks between tectonics, denudation, climate and topography, which correspond to an interplay between endogene (lithosphere) and exogene (atmosphere) processes. Links investigated in this thesis are highlighted in red. Further links include (1) the isostatic loading or unloading of the lithosphere by climate, (2) the effect of e.g. volcanism on climate, (3) the modification of the pattern of deformation by erosion, (4) the effect of erosion on climate by carbon burial and weathering, (5) the interference of topography with the atmospheric circulation or orographic precipitation, (6) the effect of hill slopes on erosion. Figure is modified from Champagnac et al. (2012), for further description of the described links see their publication.

Various studies have documented the importance of climate in governing surface processes like fluvial or glacial erosion, and how this influences the development of mountain ranges (e.g., Reiners et al., 2003; Ehlers et al., 2006; Grujic et al., 2006; Egholm et al., 2009; Whipple, 2009; Thomson et al., 2010; Glotzbach et al., 2013; Lease & Ehlers, 2013; Enkelmann et al., 2015; Georgieva et al., 2019). Nevertheless, in particular the impact of Cenozoic cooling and Plio-Pleistocene glaciation is a contentious topic, where a world-wide increase in denudation and sedimentation rates is either supported (e.g., Zhang et al., 2001; Herman et al., 2013; Herman & Champagnac, 2016) or viewed critically (e.g., Willenbring & von Blanckenburg, 2010; Willenbring & Jerolmack, 2016; Schildgen et al., 2018).

The Olympic Mountains offer a good opportunity to explore the contributions of both climate and tectonics to the evolution of a mountain range. A strong gradi-

ent in precipitation exists across the range (Figure 1.3c) and it has been intensely affected by Plio-Pleistocene glaciation (Figure 1.3a, Montgomery & Greenberg, 2000; Montgomery, 2002; Adams & Ehlers, 2017; Porter, 1964). As outlined in section 2.1, the plate geometry (and hence the tectonics) could contribute to the evolution. Furthermore, the convergence rate between the subducting Juan de Fuca plate and the North American plate can be reconstructed over time using the plate reconstruction model of Doubrovine & Tarduno (2008). Given these circumstances, the Olympic Mountains offer the possibility to investigate the second hypothesis:

> **If changes in the tectonic conditions or climate affect the evolution of orogens, then an increase in exhumation rates should be caused by an increase in plate convergence rate or the onset of Plio-Pleistocene glaciation.**

For that, exhumation rate histories are reconstructed from thermochronometric cooling ages (in particular from samples dated with multiple thermochronometer systems). Possible variations in exhumation rates are compared to the onset of Plio-Pleistocene glaciation and to variations in the plate convergence rate, as derived from the plate reconstruction model of Doubrovine & Tarduno (2008).

2.3 Possible disturbance of steady-state mountain ranges

Steady-state, which implies a balance between opposingly-directed processes like rock uplift and exhumation, is a concept widely employed in order to investigate mountain ranges, because it allows to infer parameters that are otherwise difficult to constrain (e.g., exhumation rates from thermochronometry can be interpreted as rock uplift rates). In general four types of steady-state can be discerned (Willett & Brandon, 2002), but this thesis focuses on topographic steady-state and flux steady-state. If a landscape is in topographic steady-state, then the topography is invariant, because exhumation equals rock uplift (so no surface uplift occurs). Flux steady-state corresponds to the balance between the influx into an orogen (by accretion of sediment or rock) and the outflux out of an orogen (by denudation).

Although steady-state is often assumed and forms the basis of many modeling studies (e.g., Willett, 1999; Whipple & Meade, 2006), there is ample field evidence that exhumation rates in orogens are varying through time (e.g., Carrapa et al., 2003; Glotzbach et al., 2011; Adams et al., 2015; Lease et al., 2016; Georgieva et al., 2019). Variations in exhumation both impact topographic steady-state (i.e., if a change in exhumation is not associated with a commensurate change in rock uplift, then the topography changes), and flux steady-state, be-

cause a variation in exhumation corresponds to a variation in denudation, directly impacting the flux balance.

The Olympic Mountains serve as a text book example for a steady-state mountain range, because they have been interpreted to be in flux steady-state for 14 Myr (Batt et al., 2001; Pazzaglia & Brandon, 2001). Steady exhumation rates have been proposed, based on the inversion of apatite fission-track ages (Brandon et al., 1998). However, the previous studies did neither consider the impact of Plio-Pleistocene glaciation on topography or exhumation (impacting the outflux), nor did they consider possible temporal variations of parameters governing the influx into the mountain range (like sediment thickness or plate convergence rate). Given that the Olympic Mountains were heavily glaciated during the Plio-Pleistocene (Adams & Ehlers, 2017; Montgomery, 2002; Porter, 1964) and the offshore sediment thickness increased during the Quaternary (e.g., Adam et al., 2004), both the denudational outflux and the accretional influx seem to be temporally variable. Hence, the thesis re-investigates the flux steady-state balance of the Olympic Mountains and the third hypothesis addressed is:

If the denudational outflux out of an orogen is increased by glacial erosion, then the flux steady-state balance of an orogen should be disturbed unless the accretionary influx increases by the same amount.

For that purpose, an improved knowledge of the spatial pattern of exhumation and temporal evolution of exhumation is obtained by using multiple thermochronometer systems, which provides constraints on the denudational outflux. The accretionary influx is estimated from constraints of the offshore sediment thickness (e.g., Adam et al., 2004; Han et al., 2016; Su et al., 2000; Westbrook et al., 1994) along with the temporal evolution of the plate convergence rate, taken from the plate reconstruction model of Doubrovine & Tarduno (2008).

2.4 Timescale dependence of observations

As described in section 1.1.2, observations from methods like geodesy, dating of river terraces, cosmogenic nuclide dating or thermochronometry provide valuable insights into the evolution of mountain belts. The integration timescale of these methods, i.e., the timespan on which an obtained rock uplift rate or denudation rate is acting, is different, lasting from decades (geodesy), to 10^3–10^5 years (cosmogenic nuclides) or to 10^6–10^7 years (thermochronometry). An important question is whether present-day, short-term observations (e.g., GPS velocities or the displacement on a fault during an earthquake) are representative of processes involved in the long-term development and deformation of mountain ranges.

However, studies comparing results from methods with different integration timescales with each other often report discrepancies between short-term and

long-term observations (e.g., Friedrich et al. 2003; Finnegan et al. 2014; Niemi & Clark 2018; Ramírez-Herrera et al. 2018). This might be due to the fact that mechanisms responsible for deformation have a strong timescale dependence, i.e., that single events involved in deformation have variable magnitudes or occur erratically. Hence, long-term observations record more events and provide better statistics compared to short-term observations.

Furthermore, it is important to consider what type of deformation the signal of the respective method is capturing. As briefly outlined in section 1.2.1, the seismic cycle corresponds to the time between two major earthquakes at a subduction zone and is characterized by the accumulation of strain during the interseismic period, which is then released coseismically. Many studies using geodetic, short-term methods assume their signal to record the accumulation of elastic (recoverable) strain during the seismic cycle (e.g., Burgette et al., 2009; Bruhat & Segall, 2016; Hyndman, 2013; Krogstad et al., 2016). On the other hand, recent work has highlighted that in addition to elastic deformation, viscoelastic deformation plays an important role during the seismic cycle (e.g., Li et al., 2015). Hence, the short-term signal records both the elastic and viscoelastic (permanent) parts of deformation. Long-term estimates of deformation like exhumation rates derived from thermochronometry or cosmogenic nuclide based denudation rates have the benefit that they integrate over 100s to 1000s of seismic cycles. Therefore, the signal from these methods provides a measure of the cumulative amount of permanent deformation, without the elastic component. A separation of the short-term signal in both the elastic and permanent parts of deformation should allow a direct comparison between short-term and long-term methods. The fourth hypothesis of the thesis focuses on this problem:

If the effects of viscoelastic deformation during the seismic cycle permanently deform landscapes, then these effects should be detectable with methods measuring deformation over different timescales.

This hypothesis is tested by considering and comparing various short-term and long-term datasets. Located at the Cascadia Subduction Zone, the Olympic Mountains and surrounding areas are monitored by a dense GPS-station network, which allows to obtain continuous GPS timeseries. Additionally, the GPS-derived, vertical displacement due to episodic tremor and slip (ETS) is available (Bruhat & Segall, 2016). The occurrence and distribution of tremor events due to ETS is obtained from the Pacific Northwest Seismic Network (`https://pnsn.org/tremor`). Denudation rates from cosmogenic nuclides (Adams & Ehlers, 2018) are combined with new estimates of exhumation rates from this thesis, covering integration timescales of decades over millennia to millions of years.

2.5 Effects of glacial erosion on the topography of orogens

The present-day topography of mountain ranges is the result of an interplay between earth surface and deep-seated processes. As outlined in section 2.3 temporally invariant, steady topography is a fundamental assumption in many studies investigating mountain building processes (e.g., Willett & Brandon, 2002). Hence, constraining how processes like river incision or glacial erosion affect the temporal evolution of topography could give insights into the accuracy of this assumption and is facilitated by applying low-temperature thermochronometry and thermo-kinematic modelling (e.g., House et al., 1998, 2001; Braun, 2003; Ehlers et al., 2006; van der Beek et al., 2009; Olen et al., 2012; McDannell et al., 2018).

Particularly glaciers are known to be efficient agents of erosion that can rapidly incise into landscapes, remove mass, and significantly overprint the pre-glacial landscape (Shuster et al., 2005; Ehlers et al., 2006; Mitchell & Montgomery, 2006; Egholm et al., 2009; Valla et al., 2011; Steer et al., 2012). The efficacy of glacial erosion depends on parameters like the sliding velocity or the temperature at the bottom of the glacier (e.g., Yanites & Ehlers, 2012, 2016), and in general glacial erosion appears to be highest close to the equilibrium line altitude (ELA) of a glacier (Brozović et al., 1997; Egholm et al., 2009; Herman et al., 2011; Sternai et al., 2011; Steer et al., 2012).

The Olympic Mountains experienced intense glaciation during the Plio-Pleistocene (Figure 1.3a), and alpine glaciers significantly overprinted the landscape (Thackray, 2001; Montgomery & Greenberg, 2000; Montgomery, 2002; Adams & Ehlers, 2017). Especially the area to the west of Mt. Olympus was affected by valley widening and deepening (Montgomery & Greenberg, 2000), which also corresponds to the area of lowest ELA within the Olympic Peninsula (Porter, 1964). Given these circumstances, the fifth hypothesis evaluated in this thesis is:

> **If glacial erosion is capable of significantly lowering the elevation of mountain ranges, then a concomitant increase in exhumation rate must occur.**

This is facilitated by dating new rock samples with low-temperature thermochronometry, in particular with AHe, since this thermochronometer system has the lowest closure temperature and is particularly sensitive to variations in topography. Based on the new and published AHe ages (Batt et al., 2001), thermo-kinematic modelling using Pecube is deployed, in order to evaluate an increase in exhumation rate with the onset of Plio-Pleistocene glaciation and possible effects on the topography.

Chapter 3

Scientific results

All hypotheses addressed in this thesis have been outlined in the previous chapter. The following sections contain the main scientific results of the thesis, which are used to address the hypotheses. The observations and discussion on these are presented either as published or accepted manuscripts, or manuscript which are in preparation. Where available, a supplement file is presented after each manuscript, which provides the raw data or additional information for the respective manuscript. Data tables containing detailed information like single grain analyses from thermochronometry can be found in the appendix at the end of the thesis.

3.1 Tectonic and climatic contributions to focused exhumation

3.1.1 Declaration on contributions to joint work

The following section of the dissertation has been published and is available online under `https://doi.org/10.1130/G39881.1`. The full citation is:

Michel, L., Ehlers, T. A., Glotzbach, C., Adams, B. A. and Stübner, K. (2018). Tectonic and glacial contributions to focused exhumation in the Olympic Mountains, Washington, USA. Geology, 46(6), 491–494.

The original manuscript is provided in section 3.1.2 and the original electronic supplement file is provided in section 3.1.3. The data tables presented online together with the electronic supplement are provided in the appendix (Section A), containing the single grain ages from apatite and zircon (U-Th)/He dating, respectively.

Five authors contributed to the work presented in the paper: Lorenz Michel (LM), Todd Ehlers (TE), Christoph Glotzbach (CG), Byron Adams (BA) and Konstanze Stübner (KS). A summary of the respective contributions is provided in Table 3.1. The detailed contributions are as follows: TE developed the overall idea of testing the Olympic Mountains for the rigid indenter model and the idea

Table 3.1: Summary of contribution to joint work for the paper "Tectonic and glacial contribution to focused exhumation in the Olympic Mountains, Washington, USA.", indicating the average fraction of work of the respective author in percent. The paper has successfully been published in April 2018.

Author	Position	Scientific ideas (in %)	Data generation (in %)	Analysis and Interpretation (in %)	Paper writing (in %)
LM	[1]	55	60	70	65
TE	[2]	30	5	10	10
CG	[3]	10	25	10	10
BA	[4]	5	5	10	10
KS	[5]	0	5	0	5

was further developed by LM (including the quaternary overprint). LM, TE and BA performed fieldwork. LM performed the sample treatment, mineral separation and selected apatite and zircon minerals for thermochronometric dating. CG performed most of the analytic work involved in (U-Th)/He dating, with help from KS and LM. The thermo-kinematic modeling (Pecube) was performed by LM, with input from TE, BA and CG. Analysis and interpretation of the results was done by LM with contributions from TE, CG and BA. LM drafted the first version of the manuscript along with all figures and during further writing/review TE, CG, and BA gave most of the following input during writing. During peer review, three reviewers commented on the manuscript.

3.1.2 Paper: "Tectonic and glacial contribution to focused exhumation in the Olympic Mountains, Washington, USA."

THE GEOLOGICAL SOCIETY OF AMERICA®

Tectonic and glacial contributions to focused exhumation in the Olympic Mountains, Washington, USA

Lorenz Michel, Todd A. Ehlers*, Christoph Glotzbach, Byron A. Adams, and Konstanze Stübner
Department of Geosciences, University of Tübingen, Tübingen 72074, Germany

ABSTRACT

Tectonics and climate are major contributors to the topographic evolution of mountain ranges. Here, we investigate temporal variations in exhumation due to the onset of Pleistocene glaciation in the Olympic Mountains (Washington State, USA). We present 29 new apatite and zircon (U-Th)/He ages (AHe and ZHe), showing a decrease in ages toward the interior of the mountain range for both thermochronometric systems. Young AHe ages (<2 Ma) can be found on the western side and the interior of the mountain range. Thermokinematic modeling of sample cooling ages suggests, that ZHe ages can be explained by an ellipse-shaped exhumation pattern with lowest/highest rates of ~0.25 and 0.9 km/m.y. These rates are interpreted as tectonically driven rock uplift, where the pattern of rates is governed by the shape of the subducted plate. However, the youngest AHe ages require a 50–150% increase in exhumation rates in the past 2–3 m.y. This increase in rates is contemporaneous with Pliocene-Pleistocene alpine glaciation of the orogen, indicating that tectonic rock uplift is perturbed by glacial erosion.

INTRODUCTION

The evolution of mountain topography (e.g., relief, mean elevation) is sensitive to variations in climate and tectonics that modulate the efficiency of various surface processes (e.g., Whipple, 2009). The onset of Pleistocene glaciation is hypothesized to have increased orogen exhumation rates, and significantly modified topography (e.g., Brocklehurst and Whipple, 2002; Ehlers et al., 2006; Valla et al., 2011; Glotzbach et al., 2013; Herman et al., 2013). Advances in low-temperature thermochronology and thermal modeling enable the quantification of spatial and temporal variations in exhumation (e.g., Braun, 2003). Here we test the hypothesis that enhanced Pleistocene glacial erosion can perturb the flux steady state of an orogen by increasing the erosional flux over million-year time scales.

We evaluate this hypothesis through an application to the tectonically active and glaciated Olympic Mountains located in Washington State, USA (Fig. 1A). This orogen is the exhumed portion of the Cascadia Subduction zone accretionary wedge (Tabor and Cady, 1978). Previous studies have suggested that exhumation rates have been largely constant since ca. 14 Ma, and that the orogen is in flux steady state, where accretionary and erosional fluxes are balanced (Brandon et al., 1998; Batt et al., 2001; Pazzaglia and Brandon, 2001). Largely unexplored in previous work is the potential transient effect of Pleistocene glaciation on the orogen-wide exhumation.

Here we complement previous work with new apatite and zircon (U-Th)/He ages (AHe and ZHe, respectively) from the Olympic Mountains (Fig. 1B) and compare them to predicted thermokinematic model ages to discriminate between different exhumation histories.

BACKGROUND

At the Cascadia subduction zone, the Juan de Fuca plate subducts beneath the North American plate and displays a three-dimensional (3-D) bend beneath the Olympic Mountains (Fig. DR1a in the GSA Data

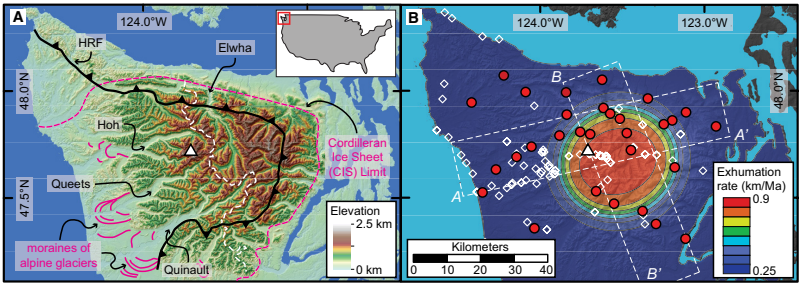

Figure 1. A: Map of the Olympic Peninsula (Washington State, USA) showing topographic features: major river valleys (Elwha, Hoh, Queets, Quinault) are denoted. White triangle shows location of Mount Olympus (2428 m asl), and white dashed line corresponds to the range divide. Quaternary features (location of CIS is after Porter, 1964) and the location of Hurricane Ridge fault (HRF) are indicated. B: Exhumation rate pattern used for our modeling approach. Open symbols are previously published samples (see Fig. DR3 [see footnote 1] for information on thermochronometer system and age). Red circles represent new data reported in this study. Swath profiles perpendicular and parallel to the range divide (A-A′ and B-B′, respectively) used for comparing sample and model ages are outlined by white boxes.

*E-mail: todd.ehlers@uni-tuebingen.de

GEOLOGY, June 2018; v. 46; no. 6; p. 491–494 | GSA Data Repository item 2018161 | https://doi.org/10.1130/G39881.1 | Published online 6 April 2018

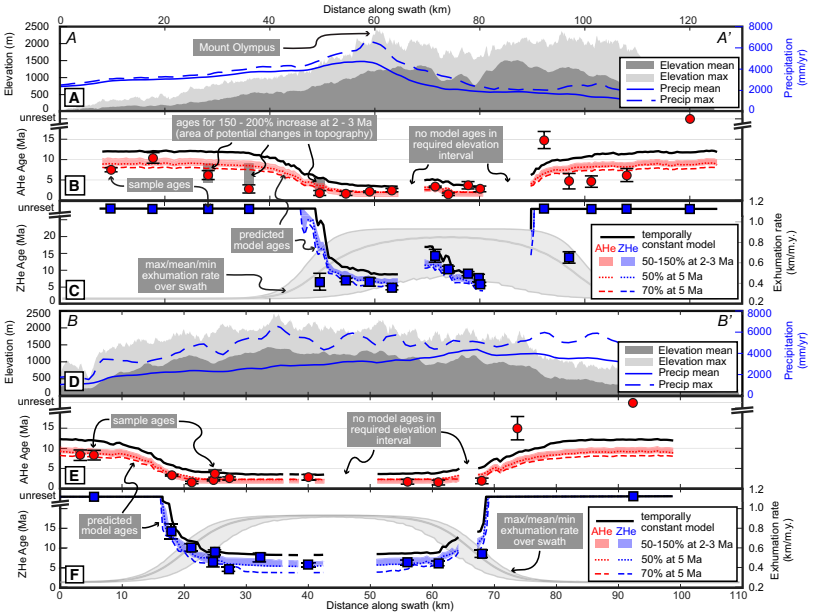

Figure 2. Swath profiles perpendicular (*A-A'*, panels A–C) and parallel (*B-B'*, panels D–F) to the range divide; see Figure 1B for location. A and D show elevation and precipitation across the range; precipitation is from the PRISM data set (http://prism.oregonstate.edu). Apatite (U-Th)/He (AHe; B and E) and zircon (U-Th)/He (ZHe; C and F) samples (circles/squares) and model ages (lines/envelopes) are shown, together with exhumation rates (gray envelopes). At the respective position of the swath, predicted model ages correspond to the mean age calculated from model results within the swath (from an elevation interval of 200–500 m). Black line corresponds to a model run with temporally constant exhumation rates, whereas the red and blue envelopes encompass the range of solutions from transient simulations, where rates were increased by 50–150% at 2 or 3 Ma relative to the constant simulation. Results from earlier increase histories (50% or 70% at 5 Ma) are also shown. In B, gray boxes denote the range of modeled ages at the location of three samples (OP1527, OP1529, and OP1532) for an exceptionally strong increase (150–200% at 2 and 3 Ma). This could also be the area of changes in topography. Exhumation rates are taken from the temporally constant model run and correspond to mean (central gray line) and max/min (gray envelope) values within the swath. A comparison of literature apatite fission-track and zircon fission-track ages with modeled ages can be found in Figure DR9 (see footnote 1).

Repository[1]). The mountain range is dominated by two tectonostratigraphic units, which are separated by the Hurricane Ridge fault (HRF; Fig. 1; Fig. DR1b). The footwall represents the actual accretionary wedge, consisting of Eocene to Miocene marine sandstones and siltstones accreted to North America (Tabor and Cady, 1978; Brandon et al., 1998).

During the Pleistocene, alpine glaciers incised deep, wide valleys (e.g., Hoh, Queets, Quinault, and Elwha valleys; see Fig. 1A), locally forming piedmont-style glaciers approaching the Pacific Ocean (Thackray, 2001; Montgomery, 2002; Adams and Ehlers, 2017). Furthermore, the Cordilleran Ice Sheet surrounded the orogen in the north and east (Booth et al., 2003). Although the highest point (Mount Olympus, 2428 m) is located to the west of the range divide, most of the high topography is located east of the Elwha valley (Figs. 1A and 2). A strong gradient in modern precipitation exists, where the west side of the range receives 3–6 m/yr compared to the drier east (1–3 m/yr; see Fig. 2A and Fig. DR1c). Linked to the precipitation gradient, the Pleistocene equilibrium line altitude (ELA) increases from 1000 m on the west side of the divide to 1800 m on the east (Fig. DR1d).

Sedimentary rocks often contain thermochronometric age populations controlled by bedrock cooling histories. Burial and heating of sedimentary rocks (e.g., during metamorphism or subduction) reset thermochronometers, directly relating them to the exhumation of the collected bedrock sample. During exhumation, samples cool and pass through their closure temperatures: ~240 °C for zircon fission-track (ZFT), ~180 °C for ZHe, ~100–120 °C for apatite fission-track (AFT), and ~60–70 °C for AHe (Reiners and Brandon, 2006). Published thermochronometer ages for the Olympic Mountains are compiled in Figure DR3. Young AFT ages (2.3–3.9 Ma) are present on the western side of the mountain range, but the only four reset ZFT samples (13–14 Ma) are located to the east of Mount Olympus. Youngest AHe ages (2.0–2.5 Ma) can be found in the vicinity of Mount Olympus. High exhumation rates of 1 km/m.y. are suggested on the west

[1]GSA Data Repository item 2018161, supplementary figures, details about methods and modeling, and analytical results (in Excel tables), is available online at http://www.geosociety.org/datarepository/2018/ or on request from editing@geosociety.org.

side of the range (Fig. DR1e), which then decrease toward zero near the coast of the peninsula (Brandon et al., 1998; Pazzaglia and Brandon, 2001).

NEW THERMOCHRONOMETER DATA

We collected 30 bedrock samples for (U-Th)/He thermochronometric dating at an elevation of ~400 m (Fig. 1B; Fig. DR2). This equal-elevation sampling approach allows for direct comparison of ages, without the need to correct ages for different sample elevation. Twenty-nine (29) of these samples yielded datable apatite crystals (e.g., suitable crystal shape, no inclusions) and 27 samples were selected for ZHe dating. A map of AHe and ZHe ages (Fig. DR3), a description of analytical methods, and data tables are provided in the Data Repository.

Reset AHe ages (27 samples) range from 15.0 to 1.5 Ma, but two samples at the east coast contain un-reset ages (Fig. DR3). Eleven samples are younger than or equal to the onset of glaciation (ca. 2–3 Ma), which are all located to the west of the Elwha valley. Only 14 samples have reset ZHe ages (4.8–14.3 Ma), and they are all located in the deeply incised valleys within the high-topography part of the range. The youngest ZHe ages (4.8 Ma and 5.9 Ma for samples OP1533 and OP1515, respectively) can be found in the headwaters of the Hoh and Elwha valleys.

Swath profiles of our data perpendicular (A-A′) and parallel (B-B′) to the range divide are shown in Figure 2 (for location, see Fig. 1B). In both swath profiles, AHe and ZHe ages decrease or change from un-reset to reset toward the center of the range. For swath B-B′, the high-topography part of the range overlaps with the area of young cooling ages (kilometers 20 and 70 of the swath). However, in swath A-A′, the area of reset ZHe samples and young AHe ages (<2.5 Ma) is offset from the highest topography and shifted toward the west.

THERMOKINEMATIC NUMERICAL MODELING

Converting thermochronometric ages into exhumation histories requires estimation of the geothermal gradient over time. For this, we use the 3-D thermokinematic model Pecube (Braun, 2003), integrated with previous ages and our new thermochronometer ages. Although the importance of frontal accretion and horizontal velocities in the Olympic Mountains has been explored by previous studies (Batt et al., 2001), we only consider vertical movement in our model simulations. Further details and discussion about the justification of this approach, as well as explanations about the modeling, can be found in the Data Repository.

Our thermokinematic model uses the present-day topography of the Olympic Mountains as input. Following Brandon et al. (1998), we start exhumation and development of topography at 18 Ma, and reach a steady state at 14 Ma. Orogens situated in an orogenic syntaxis (like the Olympic Mountains) are predicted to show a "bull's eye" pattern of exhumation (Bendick and Ehlers, 2014). Therefore, we choose an ellipse-shaped exhumation pattern for our model simulations (Fig. 1B), matching mean elevation and relief (Fig. DR7), which are suggested to correlate with rock uplift (Adams and Ehlers, 2017). The ellipse pattern is defined by a minimum rate at the edge of the ellipse and a maximum rate at the centroid of the ellipse. Our first objective is to find a spatial pattern of constant, long-term exhumation rates. To achieve this, we vary the location and size of the ellipse, and the gradient in exhumation rates, to minimize the misfit between modeled and observed ages (from literature and our data) with a reduced χ^2-test (Fig. DR6). Our second objective is to test the hypothesis that the exhumation rates increased in Pliocene-Pleistocene times due to enhanced glacial erosion. To thoroughly investigate plausible increase scenarios, we take the preferred ellipse from the previous step and increase the rate of the entire model domain each at six different time steps by seven different magnitudes. From the resulting 42 combinations, we find the best-fit time and magnitude by comparing our and published ages with the modeled ages using a reduced χ^2-test (results are shown in Figure DR8 and Table DR5). Finally, for comparison with our new data, modeled ages are extracted along the swaths A-A′ and B-B′ (Fig. 1B) from elevations between 200 and 500 m and displayed in Figure 2.

Our preferred ellipse for temporally steady exhumation rates has diameters of 70–60 km and the centroid of the ellipse is located in the core of the mountain range. Rates of 0.25 km/m.y. are found at the edges and increase to 0.9 km/m.y. in the center (Fig. 1B). Using this ellipse and keeping the rates constant throughout the entire model duration results in ages (black solid lines in Figs. 2B, 2C, 2E, and 2F) reproducing the general age pattern for AHe and ZHe. Abrupt changes in modeled ages (particularly for ZHe) are caused by the strong gradient in exhumation rates. However, for constant-rate models, the modeled AHe ages are anomalously old compared to observed ages, indicating that an increase in rates is required. We find a wide variety of transient exhumation histories, where rate increases occurred between 10 and 2 Ma. These transient exhumation histories produce improved statistical fits to the data (total χ^2 values of 50–54; Fig. DR8) than the constant-rate simulations (lowest total χ^2 value of 66; Fig. DR6). A timeline summarizing possible exhumation histories from our transient simulations is shown in Figure 3.

DISCUSSION AND CONCLUSIONS

Our new data and modeling allow us to resolve the long-term spatial pattern of exhumation in the Olympic Mountains and to identify an increase in exhumation that occurred around the same time as the onset of Pliocene-Pleistocene glaciation. The strong spatial gradient in thermochronometer ages (e.g., Fig. 2) requires a proportional spatial gradient in exhumation, and our best-fit model suggests an elliptical exhumation pattern with minimum and maximum rates of 0.25 and 0.9 km/m.y. While the range of exhumation rates agrees with previous findings (Brandon et al., 1998; Pazzaglia and Brandon, 2001), our spatial pattern of exhumation rates is different. The highest exhumation rates occur in the high, rugged core of the range, encompassing the headwaters of Hoh, Queets, Quinault, and Elwha rivers (Fig. 1B), as also suggested by Adams and Ehlers (2017) based on topographic analysis. We interpret that the general ellipse-shaped exhumation pattern is imposed by the geometry of the subducted plate, similar to other syntaxial orogens with focused exhumation (Bendick and Ehlers, 2014; Falkowski and Enkelmann, 2016; Lang et al., 2016). The required bending of the subducted plate and slab convexity is well known in the Olympic Mountains (e.g., Crosson and Owens, 1987; see also Fig. DR1a).

A temporally constant exhumation rate may explain the observed cooling ages of higher-closure-temperature systems (AFT, ZHe, ZFT), but transient exhumation histories provide much better statistical fits for ZHe, and for the AHe ages. The χ^2-test also reveals that there is no unique exhumation history solution, and several transient scenarios produce equally good fits (Fig. DR8). Generally speaking, the older the increase in rates is, the smaller is the required amount of increase (e.g., 30–50% rate increase at 7 Ma compared to 100–150% at 2 Ma). In the absence of other

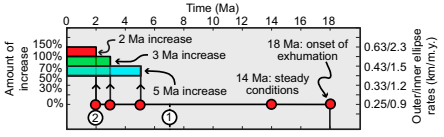

Figure 3. Timeline of our preferred transient model simulations, whose model ages are depicted in Figure 2. Left *y*-axis indicates the magnitude of increase in comparison to the constant rate, and the right *y*-axis corresponds to the actual values of exhumation rates. Events related to glaciation are (1) onset of glaciation in the Coast Mountains of British Columbia (Canada) at ca. 7 Ma (Ehlers et al., 2006), and (2) onset of glaciation in the Olympic Mountains at ca. 2 Ma (Easterbrook, 1986).

tectonic or climate mechanisms that might increase exhumation rates at older times (e.g., >5 Ma), increased erosion due to glaciation during the Pliocene-Pleistocene is the most plausible mechanism for explaining the young increase scenarios at 2–3 Ma with an increase in rates by 50–150%. These transient scenarios (colored envelopes in Figs. 2B and 2E) result in AHe ages that are 2–4 Ma younger compared to constant-rate predictions, thereby improving the fit to observed ages. However, temporal constraints for the onset of alpine glaciation in the Olympic Mountains are ambiguous, and areas nearby experienced glaciations earlier than 2–3 Ma (Fig. 3). Indeed, an earlier increase in exhumation at 4 or 5 Ma (but with a smaller magnitude) is permissible (colored dashed lines in Figs. 2B, 2C, 2E, and 2F). The ELA corresponds to the area of most effective glacial erosion (e.g., Montgomery, 2002) and is lowest on the western side of the range (Fig. DR1d). Thus, the effect of glacial erosion on exhumation is expected to be strongest on the west side of the mountain range. Here, the AHe ages from three samples (OP1527, OP1529, and OP1532) support this hypothesis and locally suggest an increase in rates by 150–200% at 2–3 Ma (gray zones in Fig. 2B). This area could also have experienced a glacial-related change in topography, causing younger AHe ages (e.g., Ehlers et al., 2006). Other reasons that might explain a mismatch between modeled and observed ages include a deviation from the assumed, perfect ellipse-shaped exhumation pattern or an even more complex transient exhumation history.

In conclusion, the Olympic Mountains are the product of both spatial and temporal variations in exhumation rates. While the spatial pattern of exhumation is governed by the tectonic setting, the temporal variation was caused by Pliocene-Pleistocene glaciation. The magnitude of exhumation rate increase is similar to other neighboring orogens influenced by Pleistocene glaciation (e.g., Ehlers et al., 2006). Given our observed temporal increase in rates, and the increase in material flux and the change in deformational style of the wedge during the Quaternary (Adam et al., 2004), the proposed flux steady state of the mountain range (Batt et al., 2001) is questionable.

ACKNOWLEDGMENTS

This work was supported by a European Research Council (ERC) Consolidator Grant (615703) to Ehlers. We thank Holger Sprengel, Bill Baccus, Jerry Freilich, Roger Hoffman, and the Olympic National Park rangers for their help and assistance during field work. We thank Mark Quigley for editorial handling of the manuscript, and Doug Burbank, Jim Spotila, and an anonymous reviewer for constructive reviews.

REFERENCES CITED

Adam, J., Klaeschen, D., Kukowski, N., and Flueh, E., 2004, Upward delamination of Cascadia Basin sediment infill with landward frontal accretion thrusting caused by rapid glacial age material flux: Tectonics, v. 23, TC3009, https://doi.org/10.1029/2002TC001475.

Adams, B.A., and Ehlers, T.A., 2017, Deciphering topographic signals of glaciation and rock uplift in an active orogen: A case study from the Olympic Mountains, USA: Earth Surface Processes and Landforms, v. 42, p. 1680–1692, https://doi.org/10.1002/esp.4120.

Batt, G.E., Brandon, M.T., Farley, K.A., and Roden-Tice, M., 2001, Tectonic synthesis of the Olympic Mountains segment of the Cascadia wedge, using two-dimensional thermal and kinematic modeling of thermochronological ages: Journal of Geophysical Research: Solid Earth, v. 106, p. 26731–26746, https://doi.org/10.1029/2001JB000288.

Bendick, R., and Ehlers, T.A., 2014, Extreme localized exhumation at syntaxes initiated by subduction geometry: Geophysical Research Letters, v. 41, p. 5861–5867, https://doi.org/10.1002/2014GL061026.

Booth, D.B., Troost, K.G., Clague, J.J., and Waitt, R.B., 2003, The Cordilleran Ice Sheet, *in* Gillespie, A.R, et al., eds., The Quaternary Period in the United States: Developments in Quaternary Sciences: v. 1, p. 17–43, https://doi.org/10.1016/S1571-0866(03)01002-9.

Brandon, M.T., Roden-Tice, M.K., and Garver, J.I., 1998, Late Cenozoic exhumation of the Cascadia accretionary wedge in the Olympic Mountains, northwest Washington State: Geological Society of America Bulletin, v. 110, p. 985–1009, https://doi.org/10.1130/0016-7606(1998)110<0985:LCEOTC>2.3.CO;2.

Braun, J., 2003, Pecube: a new finite-element code to solve the 3D heat transport equation including the effects of a time-varying, finite amplitude surface topography: Computers & Geosciences, v. 29, p. 787–794, https://doi.org/10.1016/S0098-3004(03)00052-9.

Brocklehurst, S.H., and Whipple, K.X., 2002, Glacial erosion and relief production in the Eastern Sierra Nevada, California: Geomorphology, v. 42, p. 1–24, https://doi.org/10.1016/S0169-555X(01)00069-1.

Crosson, R.S., and Owens, T.J., 1987, Slab geometry of the Cascadia Subduction Zone beneath Washington from earthquake hypocenters and teleseismic converted waves: Geophysical Research Letters, v. 14, p. 824–827, https://doi.org/10.1029/GL014i008p00824.

Easterbrook, D.J., 1986, Stratigraphy and chronology of quaternary deposits of the Puget Lowland and Olympic Mountains of Washington and the Cascade Mountains of Washington and Oregon: Quaternary Science Reviews, v. 5, p. 145–159, https://doi.org/10.1016/S0277-3791(86)80014-2.

Ehlers, T.A., Farley, K.A., Rusmore, M.E., and Woodsworth, G.J., 2006, Apatite (U-Th)/He signal of large-magnitude accelerated glacial erosion, southwest British Columbia: Geology, v. 34, p. 765–768, https://doi.org/10.1130/G22507.1.

Falkowski, S., and Enkelmann, E., 2016, Upper-crustal cooling of the Wrangellia composite terrane in the northern St. Elias Mountains, western Canada: Lithosphere, v. 8, p. 359–378, https://doi.org/10.1130/L508.1.

Glotzbach, C., van der Beek, P., Carcaillet, J., and Delunel, R., 2013, Deciphering the driving forces of erosion rates on millennial to million-year timescales in glacially impacted landscapes: An example from the Western Alps: Journal of Geophysical Research: Earth Surface, v. 118, p. 1491–1515, https://doi.org/10.1002/jgrf.20107.

Herman, F., Seward, D., Valla, P.G., Carter, A., Kohn, B., Willett, S.D., and Ehlers, T.A., 2013, Worldwide acceleration of mountain erosion under a cooling climate: Nature, v. 504, p. 423–426, https://doi.org/10.1038/nature12877.

Lang, K.A., Huntington, K.W., Burmester, R., and Housen, B., 2016, Rapid exhumation of the eastern Himalayan syntaxis since the late Miocene: Geological Society of America Bulletin, v. 128, p. 1403–1422, https://doi.org/10.1130/B31419.1.

Montgomery, D.R., 2002, Valley formation by fluvial and glacial erosion: Geology, v. 30, p. 1047–1050, https://doi.org/10.1130/0091-7613(2002)030<1047:VFBFAG>2.0.CO;2.

Pazzaglia, F.J., and Brandon, M.T., 2001, A fluvial record of long-term steady-state uplift and erosion across the Cascadia forearc high, western Washington State: American Journal of Science, v. 301, p. 385–431, https://doi.org/10.2475/ajs.301.4-5.385.

Porter, S.C., 1964, Composite Pleistocene snow line of Olympic Mountains and Cascade Range, Washington: Geological Society of America Bulletin, v. 75, p. 477–482, https://doi.org/10.1130/0016-7606(1964)75[477:CPSLOO]2.0.CO;2.

Reiners, P.W., and Brandon, M.T., 2006, Using thermochronology to understand orogenic erosion: Annual Review of Earth and Planetary Sciences, v. 34, p. 419–466, https://doi.org/10.1146/annurev.earth.34.031405.125202.

Tabor, R.W., and Cady, W.M., 1978, The structure of the Olympic Mountains, Washington: Analysis of a subduction zone: U.S. Geological Survey Professional Paper 1033, 38 p.

Thackray, G.D., 2001, Extensive early and middle Wisconsin glaciation on the western Olympic Peninsula, Washington, and the variability of Pacific moisture delivery to the northwestern United States: Quaternary Research, v. 55, p. 257–270, https://doi.org/10.1006/qres.2001.2220.

Valla, P.G., Shuster, D.L., and van der Beek, P.A., 2011, Significant increase in relief of the European Alps during mid-Pleistocene glaciations: Nature Geoscience, v. 4, p. 688–692, https://doi.org/10.1038/ngeo1242.

Whipple, K.X, 2009, The influence of climate on the tectonic evolution of mountain belts: Nature Geoscience, v. 2, p. 97–104, https://doi.org/10.1038/ngeo413.

Manuscript received 9 November 2017
Revised manuscript received 8 March 2018
Manuscript accepted 18 March 2018

Printed in USA

3.1.3 Supplement for "Tectonic and glacial contribution to focused exhumation in the Olympic Mountains, Washington, USA."

Electronic supplement to:

Tectonic and Glacial Contributions to Focused Exhumation in the Olympic Mountains, USA

Lorenz Michel, Todd A. Ehlers *, Christoph Glotzbach, Byron A. Adams, Konstanze Stübner
Department of Geosciences, University of Tübingen, Tübingen, 72074, Germany
** Corresponding Author, todd.ehlers@uni-tuebingen.de*

DR1. ADDITIONAL BACKGROUND INFORMATION

The modern configuration of the Cascadia subduction zone formed during subduction of the Juan de Fuca plate beneath North America since the latest Eocene (Brandon and Vance, 1992). At present, the convergence rate between both plates reaches 34 km/Ma at the latitude of the Olympic Mountains (Doubrovine and Tarduno, 2008). The Olympic Mountains represent the aerially exposed part of the accretionary wedge (Tabor and Cady, 1978), whereas to the north beneath Vancouver Island and to the south beneath the Oregon Coast Range the wedge can only be found offshore (see Figure DR1a). A peculiar feature of the Cascadia subduction zone is a bend in the subducted slab beneath the Olympic Mountains (Figure DR1a). The wavelength of this bend and the resulting curvature of the slab differ, depending on which data set is used. Crosson and Owens (1987) provide a data set, where the wavelength is close to the size of the Olympics, whereas in a more recent model for slab geometry (Hayes et al., 2012; McCrory et al., 2012) the bend has a longer wavelength, so that the curved part of the slab also lies beneath the southern tip of Vancouver Island.

The Olympic Mountains consist of two tectono-stratigraphic units (see Figure DR1b), separated by a thrust fault (the Hurricane Ridge Fault, HRF): the Coast Range Terrain (CRT) and the Olympic Structural Complex (OSC). The CRT represents the upper plate and consists of Eocene aged basaltic rocks overlain and intercalated with sedimentary rocks of Eocene to Miocene age (Tabor and Cady, 1978; Eddy et al., 2017). The origin of these Eocene aged partly marine basaltic rocks is disputed (plume-derived plateau vs. back-arc volcanics), but recent studies suggest them to represent an oceanic plateau (Phillips et al., 2017; Eddy et al., 2017). For a full discussion on this point we refer the interested reader to Phillips et al. (2017). Contrary to that, the OSC dominantly consists of marine turbidite sequences or slate of Eocene to Miocene age and minor basaltic lenses, which are interpreted as the actual accretionary wedge (Tabor and Cady, 1978; Brandon et al., 1998). The OSC can be further divided in the three subunits coastal, upper and lower OSC (Brandon et al., 1998). Rocks with the youngest depositional ages (Miocene) can be found in the coastal OSC. In general, the metamorphic overprint of the rocks from the OSC is low, increases from west to east and the highest metamorphic overprint is found in the center of the range in the area neighboring the HRF (Tabor and Cady, 1978).

The strong orographic rainshadow effect in the Olympics is shown in Figure DR1c. Areas on the western side of the mountain range receive 5000 – 6000 mm/yr of precipitation, whereas the eastern part of the range is much drier and partly receives < 1000 mm/yr of precipitation.

The Olympics were strongly impacted by glacial processes. The Cordilleran Ice Sheet (CIS) advanced from the Coast Mountains in British Columbia down to the latitude of the Olympic Mountains several times during the Pleistocene (Easterbrook, 1986), and the Juan de Fuca and Puget lobe surrounded the range in the north and east/south east, respectively (Porter, 1964, see Figure DR1d). Due to the presence of the CIS it is difficult to reconcile the extent of alpine glaciation on the northern and eastern side of the peninsula, because alpine ice streams merged with the CIS or deposits from alpine glaciers were destroyed by later advances of the CIS. Contrary to that, the western side of the peninsula offers well preserved glacial deposits (Figure 1a in the main text), suggesting that piedmont-style alpine glaciers initiating in the headwaters of Hoh, Quinault or Queets valleys almost advanced to the Pacific ocean (Thackray, 2001). Similar to the distribution of rainfall, the equilibrium line altitude ELA

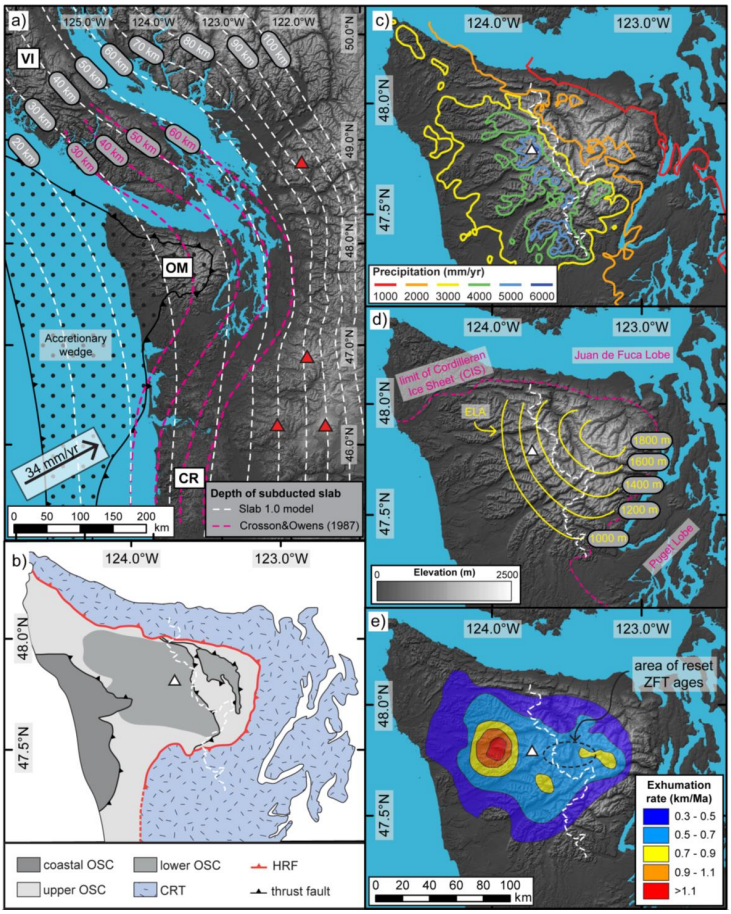

Figure DR1: *(a) Overview of the Cascadia subduction zone at the latitude of the Olympic Mountains, convergence velocity of 34 mm/yr from Doubrovine and Tarduno (2008), dashed lines show the location of the top of the subducted slab at depth, Slab1.0 is based on McCrory et al. (2012), note that McCrory et al. (2012) refer to the top of the slab as the top of the oceanic igneous crust, whereas Crosson and Owens (1987) refer to it as the oceanic Moho, red triangles denote active volcanoes, VI = Vancouver Island, OM = Olympic Mountains, CR = Coast Range. (b) Structure of the Olympics, based on Tabor and Cady (1978) and Brandon et al. (1998), OSC = Olympic Structural Complex, CRT = Coast Range Terrain, HRF = Hurricane Ridge Fault. (c) Precipitation pattern from the PRISM data set (www.prism.oregonstate.edu). (d) Extent of the Cordilleran Ice Sheet and location of the equilibrium line altitude (ELA) on the peninsula, after Porter (1964). (e) Exhumation rate pattern as derived from the inversion of AFT data (Brandon et al., 1998), area of reset ZFT ages is based on Brandon and Vance (1992). In all panels, the white triangle and the thin white dashed line denote the location of Mt. Olympus or the range divide, respectively.*

shows a strong spatial gradient (Figure DR1d) and increases from 1000 m on the western side to 1800 m on the eastern side (Porter, 1964).

It is difficult to exactly determine, when Pleistocene glaciation initiated in the Olympic Mountains. The oldest, preserved remnants from the CIS in the area were found south of Seattle (Easterbrook, 1986) and belong to the Orting drift. They are believed to be ~2 Ma old, however, due to the magnetic polarization of the deposits, they could be deposited anytime between 0.78 and 2.48 Ma. Remnants of older alpine, glaciations are scarce within the Olympic Mountains, but deeply weathered glacial deposits on the western peninsula are believed to be of the same age as the Orting drift (Easterbrook, 1986). A marine drill core (OPD leg 168, at 48°N, 200 km offshore from Vancouver Island) shows a transition from deep sea sedimentation to turbidity current derived sedimentation at 1.7 Ma (Underwood et al., 2005). This could indicate increased turbidity current activity due to higher sediment supply, caused by increased glacial erosion. Generally, the offshore sedimentation increased significantly during the Quaternary and even led to a change in deformation of the accretionary wedge (e.g. Adam et al., 2004)

The exhumation rate pattern suggested by Brandon et al. (1998) based on inversion of their AFT data suggests fastest exhumation rates (>1.0 km/Ma) at the confluence of the north and south fork Hoh rivers (see Figure DR1e). Lower rates (~0.7 km/Ma) prevail in the center of the range. However, the only area of reset zircon fission track ages (13 – 14 Ma) is to the east of Mt. Olympus (Brandon and Vance, 1992).

DR2. THERMOCHRONOMETRIC DATING

DR2.1 Details for sampling

Where possible, we preferred sandstone to siltstone/slate while sampling. The collected sandstones vary in color, grain size and mineral composition (especially in feldspar, mica and lithics content). Location of the samples within the Olympics is shown in Figure DR2, coordinates and elevation together with the final ages for each sample can be found in table DR1. A map of ages is shown in Figure DR3.

DR2.2 Analytical procedure for thermochronometric dating

Common mineral separation techniques involving density and magnetic separation are applied to get apatite and zircon separates. Mineral grains are hand-picked under air in the thermochronology labs at the University of Tübingen using a Leica microscope. Euhedral, inclusion-free grains are selected and packed in Nb-tubes. Especially for apatite this often proofs to be difficult due to the detrital nature of the rocks. Hence, sometimes smaller but well-shaped grains (<70 µm) are packed. Apatite and zircon grains are analyzed in the thermochronology labs at the University of Tübingen and the further measurement procedure follows Stübner et al. (2016) and is described there. Parameters for Ft-correcting the AHe and ZHe ages are taken from Farley (2002) and Hourigan et al. (2005), respectively. The approach used for solving the (U- Th)/He age equation follows the method of Meesters and Dunai (2005). For each sample, 3 – 5 grains are dated for AHe and three grains for ZHe. Data for the single grain analyses for apatite and zircon are reported in excel-tables DR2 and DR3, respectively.

To calculate the sample ages from the single grain ages, we use the Helioplot software package (Vermeesch, 2010). However, we do not use the recommended central age as sample age, but instead use the arithmetic mean age. In our case, the errors for the central age are very large for some samples, which is probably caused by the very different composition of the mineral grains in these detrital samples. This effect is also enhanced by the small number of mineral grains that we only date per sample (n=3 – 5). As uncertainty Helioplot states the standard error (1SE), which we then use to calculate the standard deviation (1SD) that is reported in our data table.

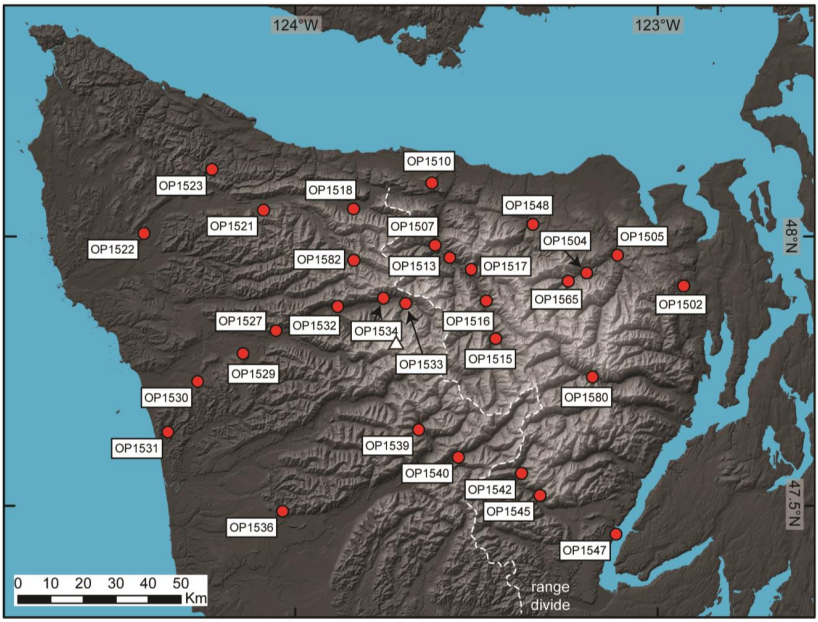

***Figure DR2**: Samples collected for this study and their location on the Olympic Peninsula. White triangle denotes location of Mt. Olympus.*

In general, the geologic uncertainty that is inherent in (U-Th-Sm)/He dating is larger than the analytic uncertainty, which results in very different and overdispersed single grain ages within one sample. This geologic uncertainty is caused by overseen inclusions in the mineral grains, radiation damage or factors that affect the Ft-correction (e.g. grain shape, strong U/Th-zonation). As further complication in our case, it is possible, that a sample is not fully reset and the mineral grains still record a signal from the source region of the sandstones, as is the case with published AFT and ZFT data for the study area (Brandon and Vance, 1992; Brandon et al., 1998). Likewise, this creates problems using common methods for outlier detection. Our approach for determining, whether the range in single grain ages is caused by the geologic uncertainty or by the unreset/partially reset nature of the sample is as follows.

First, samples that only contain single grain ages older than the onset of exhumation in the Olympics (18 Ma, Brandon et al., 1998) or where the single grain ages are similar to/older than the depositional age of the sample (see table DR1) are considered unreset. Samples, which pass this first test, are checked, whether they still show a large spread in single grain ages and if grains do not overlap within 2SD of their respective analytic uncertainty, the particularly old or young grains are considered as possible outliers. However, due to our small number of grains dated per sample (3 – 5), we can not discern between fully reset, partially reset or multiply reset samples (e.g. Brandon et al., 1998).

Table DR1: Overview of the samples, providing coordinates, AHe ages, ZHe ages and depositional age of the samples (depositional age after Brandon et al. (1998); Tabor and Cady (1978)). nd = not determined.

Sample	North (°)	East (°)	Elevation (m)	AHe age (Ma)	AHe 1SD (Ma)	ZHe age (Ma)	ZHe 1SD (Ma)	probable depositional age	
OP1502	47.90796	-122.92804	325	unreset	-	unreset	-	late Eocene	40 - 34 Ma
OP1504	47.93233	-123.19509	675	4.6	1.4	unreset	-	lower - middle Eocene	55 -43 Ma
OP1505	47.96524	-123.11056	314	6.2	1.6	unreset	-	lower - middle Eocene	55 -43 Ma
OP1507	47.98305	-123.61359	453	3.3	0.2	14.3	1.9	Eocene	34 - 55 Ma
OP1510	48.09852	-123.62231	273	8.3	1.2	unreset		upper Eocene - Oligocene	37 - 24 Ma
OP1513	47.96015	-123.57273	402	1.5	0.3	10.2	1.0	Eocene	34 - 55 Ma
OP1515	47.81031	-123.44630	537	2.8	0.7	5.9	0.5	early Eocene	34 - 55 Ma
OP1516	47.88040	-123.47196	426	nd	-	7.7	1.1	late Oligocene - early Miocene	26 - 20 Ma
OP1517	47.93891	-123.51376	423	3.7	0.9	9.0	0.6	late Oligocene - early Miocene	26 - 20 Ma
OP1518	48.05061	-123.83886	223	8.6	1.5	nd	-	lower - middle Eocene	55 - 43 Ma
OP1521	48.04832	-124.08702	390	2.0	0.4	unreset	-	Eocene	55 - 34 Ma
OP1522	48.00530	-124.41620	367	9.1	0.9	unreset	-	late Oligocene - early Miocene	26 - 20 Ma
OP1523	48.12315	-124.22835	363	6.8	1.1	nd	-	upper Eocene - Oligocene	37 - 24 Ma
OP1527	47.82500	-124.05184	280	2.8	1.0	unreset	-	late Oligocene - early Miocene	26 - 20 Ma
OP1529	47.78265	-124.14257	343	6.2	1.1	unreset	-	late Oligocene - early Miocene	26 - 20 Ma
OP1530	47.73081	-124.26813	221	10.4	1.3	unreset	-	early - middle Miocene	20 - 14 Ma
OP1531	47.63659	-124.34966	50	7.5	0.5	unreset	-	early - middle Miocene	20 - 14 Ma
OP1532	47.87025	-123.88135	323	1.8	0.6	6.6	2.5	late Oligocene - early Miocene	26 - 20 Ma
OP1533	47.87572	-123.69427	430	2.5	0.4	4.8	0.6	late Oligocene - early Miocene	26 - 20 Ma
OP1534	47.88536	-123.75552	475	2.1	0.2	6.5	1.2	late Oligocene - early Miocene	26 - 20 Ma
OP1536	47.48917	-124.03370	390	7.5	0.8	unreset	-		
OP1539	47.64151	-123.65870	446	2.1	0.6	6.8	0.4	late Oligocene - early Miocene	26 - 20 Ma
OP1540	47.59012	-123.54913	367	1.5	0.6	6.2	0.6	late Oligocene - early Miocene	26 - 20 Ma
OP1542	47.56001	-123.37533	450	1.9	0.7	8.6	0.9	early Eocene (?)	
OP1545	47.51918	-123.32442	390	15.0	2.9	nd	-	lower - middle Eocene	55 - 43 Ma
OP1547	47.44632	-123.11424	11	unreset	-	unreset	-	Oligocene - lower Miocene	34 - 21 Ma
OP1548	48.02186	-123.34295	407	14.8	2.1	unreset	-	Oligocene (upper Eocene)	34 -24 Ma
OP1565	47.91644	-123.24616	720	4.7	1.9	13.8	1.7	Eocene	34 - 55 Ma
OP1580	47.73972	-123.17929	509	5.0	1.2	10.0	1.5	Eocene	34 - 55 Ma
OP1582	47.95595	-123.83732	578	1.7	0.5	7.1	0.5	late Oligocene - early Miocene	26 - 20 Ma

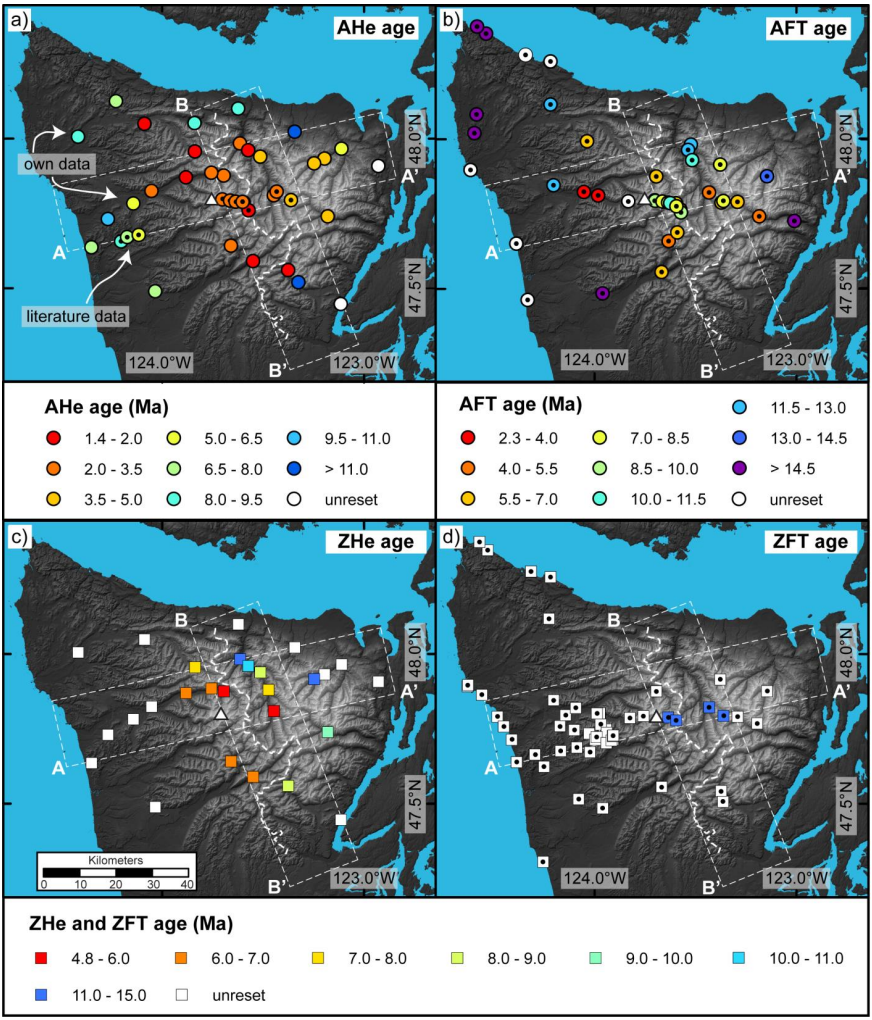

Figure DR3: *Compiled map of the thermochronometry data available for the Olympic Mountains. AHe and ZHe are from this work, literature AHe data are taken from Batt et al. (2001), AFT is from Brandon et al. (1998) and ZFT from Brandon and Vance (1992) and Stewart and Brandon (2004). Note that our data are collected at an equal elevation of 400 m, whereas the literature data are not. The white dashed line denotes the range divide and the white triangle Mt. Olympus, respectively. White boxes outline the swaths parallel and perpendicular to the range divide.*

The detrital nature of our sandstone samples, and linked to this the poor sample quality and different chemical composition of single grains likely also impacts the reproducibility of measured ages. For the analyzed apatites the mean standard deviation is ~21% (1 sigma, 27 samples, 92 dated grains, outlier grains and grains from unreset samples excluded). For the dated zircon grains the mean standard deviation is ~13 % (1 sigma, 14 samples, 34 dated grains, outlier grains and grains from unreset samples excluded). The poor reproducibility for our AHe ages is probably also linked to the very low He content of many grains, which is caused by the young age of many samples and the partly volcanic origin of apatite grains (these contain low amounts of U and Th and hence He). High uncertainties of up to 30% for apatite single grains from young samples supports this hypothesis. Comparison with the reproducibility of standards measured in the thermochronology labs of the University of Tübingen (for Durango apatite 6%, n=24; for Fish Canyon Tuff zircons 6%, n=21) indicates that indeed our observed reproducibility is likely caused by the nature of our samples and not by analytical issues.

DR3. DETAILS FOR THERMO-KINEMATIC MODELING

DR3.1 General setup for the models

For our numerical modeling purpose we use the 3D thermo-kinematic model Pecube-D (e.g. Whipp et al., 2009; McQuarrie and Ehlers, 2015), which allows to calculate thermochronometric cooling ages from time-temperature paths and compare these modeled ages with our data. The model domain encompasses almost the entire Olympic Peninsula (120 km x 140 km, see Figure DR 4) and the depth of the model is 20 km, which corresponds to the minimum thickness of the accretionary wedge beneath the Olympic Mountains (e.g. Davis and Hyndman, 1989). Further model parameters are summarized in table DR4. For elevation, we use the present day topography, which is derived from a 10 m digital elevation model and downscaled, so that the final resolution of the model is 500 m. In order to better recognize modeled, unreset ages, we initiate our models at 50 Ma. Following Brandon et al. (1998), we start exhumation at 18 Ma and reach steady state at 14 Ma, which implies steady, present-day topography for the remaining model duration. This seems counterintuitive, because glaciation significantly impacted the topography of the mountain range. However, considering changes in topography within the model requires knowledge of the pre-glaciation topography, which we are not able to provide. So in order to reduce the model complexity and to not use unconstrained parameters, we keep the topography constant.

DR3.2 Vertical-velocity-only models

DR3.2.1 Constant, long-term exhumation rates

Spatial variations in exhumation rates in the Olympic Mountains have already previously been reported for the Olympic Mountains (Brandon et al., 1998; Batt et al., 2001). Hence, we explored which pattern best explains the observed ages from our study (AHe and ZHe) and the literature data (AHe, AFT and ZFT). We run our models only considering vertical velocities and use an elliptic shaped exhumation pattern (for discussion of horizontal velocities see section DR3.3). Maximum exhumation rates are defined in the inner ellipse and minimum rates (“background rates”) outside of the ellipse (see Figure DR4). Pecube interpolates smoothly between these two values, to get the further values. Furthermore, in order to reconstruct transient changes in exhumation in the Olympic Mountains with onset of Pleistocene glaciation, we use a two-step approach.

First, in order to estimate the best long-term exhumation history, we use constant rates throughout the entire model duration and try to find the best-fit ellipse in terms of location, size and rates. The location and size of the ellipse are assessed by the general pattern of reset/unreset ages. The most appropriate rates for the ellipse are found by using a reduced χ^2-test. We perform runs with five different

Table DR 4: List of parameters used for the Pecube modeling.

Parameter	Value	Source
thermal conductivity	1.83 W $m^{-1}K^{-1}$	average value for six drill cores in sediment material in the shelf offshore from Vancouver Island (Lewis et al., 1988)
Specific heat capacity	1200 J $kg^{-1}K^{-1}$	
crustal density	2700 kg m^{-3}	
mantle density	3200 kg m^{-3}	
temperature at the base of the model	400 °C	extrapolation to greater depths from temperature estimates based on heat flow measurements on the shelf (Hyndman et al., 1990; Hyndman and Wang, 1993; Booth-Rea et al., 2008)
temperature at sea level	8 °C	
atmospheric lapse rate	6.69 °C km^{-1}	
crustal heat production	0.77 µW m^{-3}	average value from drill cores on the shelf offshore from Vancouver Island (Lewis and Bentkowski, 1988)

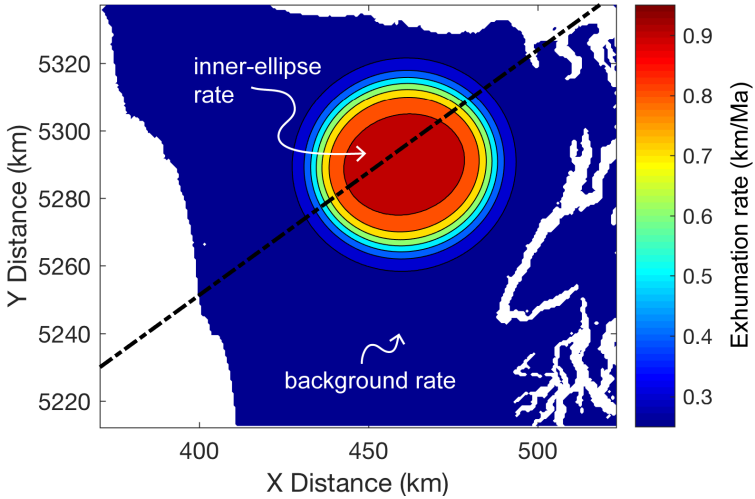

Figure DR4: *Elliptic exhumation rate pattern used for our model runs. Rates are defined outside of the ellipse (background rates), where they are lowest and in the inner ellipse, where they are highest. The pattern and values shown (0.25 to 0.9 mm/yr) are for our preferred constant rate ellipse. Rates for the horizontal model runs (section DR3.3) were extracted along the black, dashed line. Offshore above the ocean exhumation rates are set to zero.*

inner ellipse rates (0.8, 0.9, 1.0, 1.2, 1.4 km/Ma) and six different background rates (0.1, 0.2, 0.25, 0.3, 0.4, 0.5 km/Ma). At first we look at the distribution of single χ^2-values for each sample and each model run in order to get an overview of how well the models reproduce the ages. The χ^2-value gives information about the misfit between predicted (τ_m) and observed ages (τ_o with uncertainty σ_o):

$$\chi^2 = \left(\frac{\tau_o - \tau_m}{\sigma_o}\right)^2$$

In order to also assign an uncertainty to unreset samples and include them in the χ^2-test, we use an "arbitrary" uncertainty of 10%. Following Adams et al. (2015) we also apply this approach to reset samples and either use the actual uncertainty or use the 10%, whichever is greater. Furthermore, because Pecube can not discern between fully and partially reset samples, we exclude all AFT and ZFT samples from the data set that do not show concordant ages. Figure DR5 displays the range of observed χ^2-values for each thermochronometric system. Generally the misfit for AFT and ZFT is smaller (χ^2<100) compared to AHe or ZHe, where the χ^2-values can be as high as 10^4 and can display a range of several magnitudes for some samples. Samples that have these very high χ^2-values are likely candidates that can distort and bias a reduced χ^2-analysis. Hence, we excluded several samples from the further analysis. This includes samples OP1521 and OP1582 for AHe (sample number 14 and 33 in Figure DR5), and samples OP1532, OP1542 and OP1582 for ZHe (sample number 16, 22 and 27 in Figure DR5). One reason why these samples show particularly high χ^2-values could be that the true shape of the exhumation rate pattern deviates from the imposed perfectly ellipse-shaped pattern.

So we use a total of 31 AHe, 14 AFT, 24 ZHe and 45 ZFT ages for our reduced χ^2-analysis. For the respective thermochronometer system, the reduced χ^2-value is defined as the sum of the single χ^2-values from each sample divided by the number of samples (n):

$$\chi^2_{reduced} = \frac{1}{n-2}\sum\left(\frac{\tau_o - \tau_m}{\sigma_o}\right)^2$$

The resulting reduced χ^2-values for assessing the best-fit ellipse are displayed in Figure DR6 and give information about the goodness of fit for the respective combination of outer/inner ellipse rates. Comparing the best-fit suggestions (outlined by the red box in the subpanels in Figure DR6) for the four thermochronometer systems shows that very different combinations of outer/inner ellipse rates are suggested for each thermochronometer system (e.g. 0.25/1.2 for ZHe vs. 0.25/0.8 for AFT vs. 0.5/1.2 for AHe). This indicates that there is likely no single constant exhumation rate history fitting all thermochronometer systems equally well. Thus, simply adding the reduced χ^2-values from each system to a total χ^2-value could lead to a biased combination of outer/inner rates (e.g. this approach would favor 0.25/1.2 km/Ma, giving an almost perfect fit for ZHe, but significantly misfiting AHe and to a minor amount AFT and ZFT). Furthermore, high rates in the inner ellipse (>1.0 km/Ma) result in ZFT ages that are much too young, compared to their unreset age or to the four partly reset ZFT ages (modeled ages of 5 – 10 Ma vs. 13 – 14 Ma for the reset samples). Choosing a high value in the inner ellipse results already in a very good fit for ZHe with constant exhumation rates (e.g. a reduced χ^2-value of 1 – 2). However, a later increase in rates (which is suggested by the bad fit of constant rate models for AHe) would lead to very young ZHe ages and again decrease the reduced χ^2-values for ZHe.

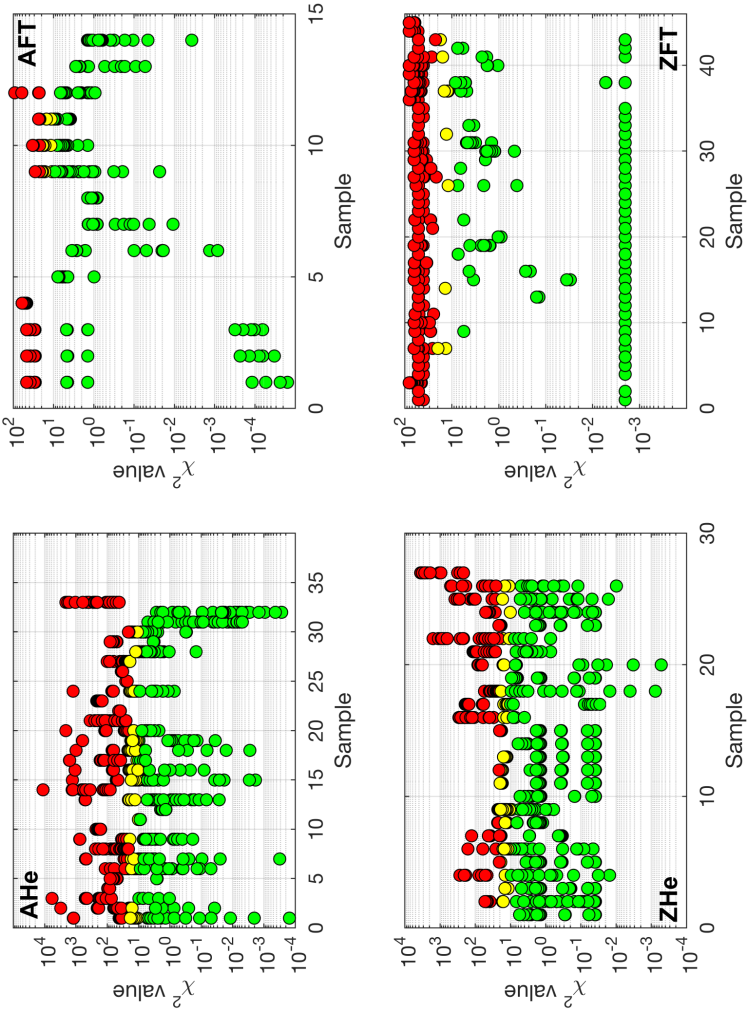

Figure DR5: *Range of χ^2-values for AHe, AFT, ZHe and ZFT from investigating the best-fit ellipse in terms of inner ellipse rate and background rate. Each point corresponds to the outcome from one single model run, so in total 30 points are shown for each sample (5 inner ellipse rates and 6 background rates give 30 possible combinations). The color coding corresponds to the goodness of fit: green symbols χ^2<10, yellow χ^2 between 10 and 20, red χ^2>20. In general the AHe and ZHe ages are more difficult to fit and their χ^2-values can have a range of several orders of magnitude. Some AHe and ZHe samples have high χ^2-values (χ^2>1000) and are particularly difficult to fit, hence we excluded them from the further reduced χ^2-analysis. This includes samples 33 and 14 for AHe, and 27, 22 and 16 for ZHe. Note that the y-axes are logarithmic.*

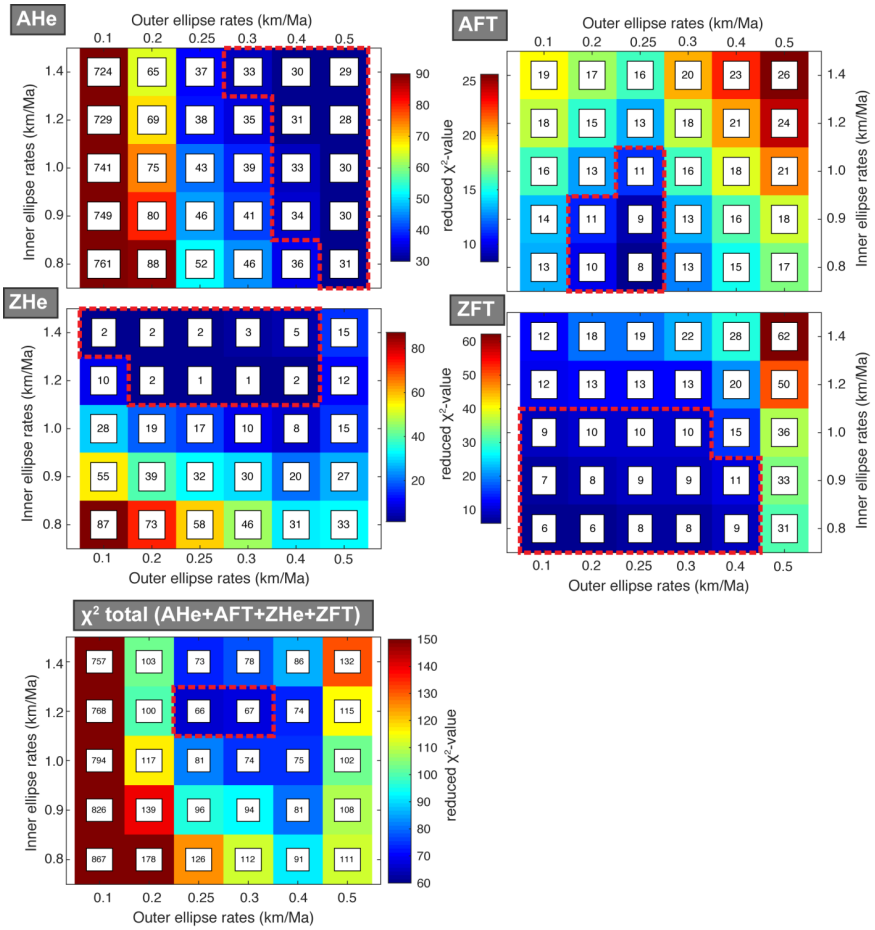

Figure DR6: *Results from finding the best-fit constant rates for the ellipse, showing the reduced χ^2-values for AHe, AFT, ZHe, ZFT and the sum of all systems from our reduced χ^2-test runs. We performed model runs with five different erosion rates in the inner ellipse and six different background/outer ellipse erosion rates. Best fit solutions for each system are indicated by red boxes, note that the best-fit combinations of inner/outer ellipse rates differ significantly for the different thermochronometer systems. The colorbar is different for each subpanel.*

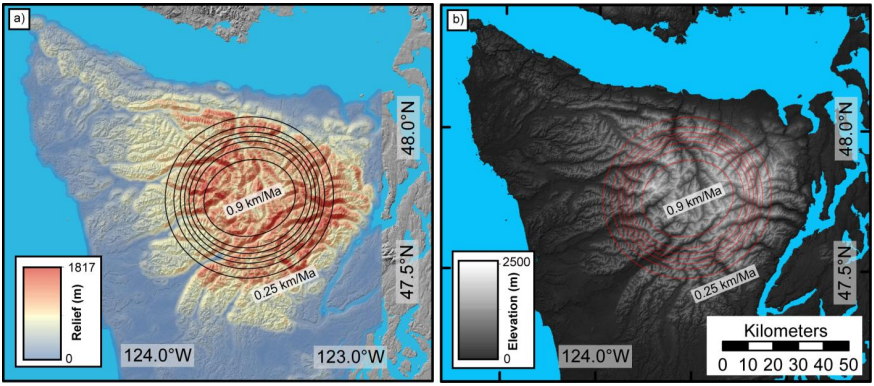

Figure DR7: *Maps of a) relief (calculated for a moving circle of 3 km diameter) and b) elevation compared to our best-fit ellipse pattern. Both areas of high relief and elevation are contained within our ellipse pattern.*

To conclude, due to the afore mentioned points we argue for an inner ellipse rate that is not too high and picked rates of 0.25/0.9 km/Ma for our preferred constant-rate ellipse. This combination is strongly favored by AFT and ZFT (each have reduced χ^2-values of 9), and if rates are increased within the transient model runs for the 0.25/0.9 km/Ma ellipse, the total χ^2-values are also lower (~50 for best-fit transient models, see below) compared to the 0.25/1.2 km/Ma ellipse suggested by the total χ^2-values (66). Different from Brandon et al., (1998) we do not locate the center of our ellipse on the western side (see Fig. DR1e), but in the central high topography part of the mountain range. Here, highest rock uplift rates are suggested to correlate with mean elevation and relief (Adams and Ehlers, 2017). Our proposed ellipse pattern matches both relief and mean elevation, where areas of highest relief and elevation are contained within the ellipse (Fig. DR7)

DR3.2.2 Transient model runs

In a second step, we use these best-estimate long-term exhumation rates (0.25 - 0.9 km/Ma) in order to explore transient model runs, where the exhumation rate is increased. This is centered around the question, whether Pleistocene glaciation, which undoubtedly affected the topography in the Olympics (e.g. Montgomery and Greenberg, 2000; Montgomery, 2002; Adams and Ehlers, 2017), also had an influence on the exhumation of the mountain range.

Considering transient model runs adds more parameters to the model space that could be variable and that need to be explored. Hence, we try to find the best timing of increase in rates as well as increase amount by again using a reduced χ^2-test. For this we consider six times of increase (1, 2, 3, 5, 7 and 10 Ma) and seven increase amounts (10, 30, 50, 70, 100, 150 and 200%, all measured relative to the best-fit ellipse rate of 0.25/0.9 km/Ma), resulting in 42 possible increase histories. Values from the reduced χ^2-test for each thermochronometer system and the total reduced χ^2-value (sum of all systems) for each increase history are shown in Figure DR8, where the best-fit solutions with the lowest χ^2-values are outlined by red boxes. Transient model runs with increasing exhumation rates lead to a much better fit of

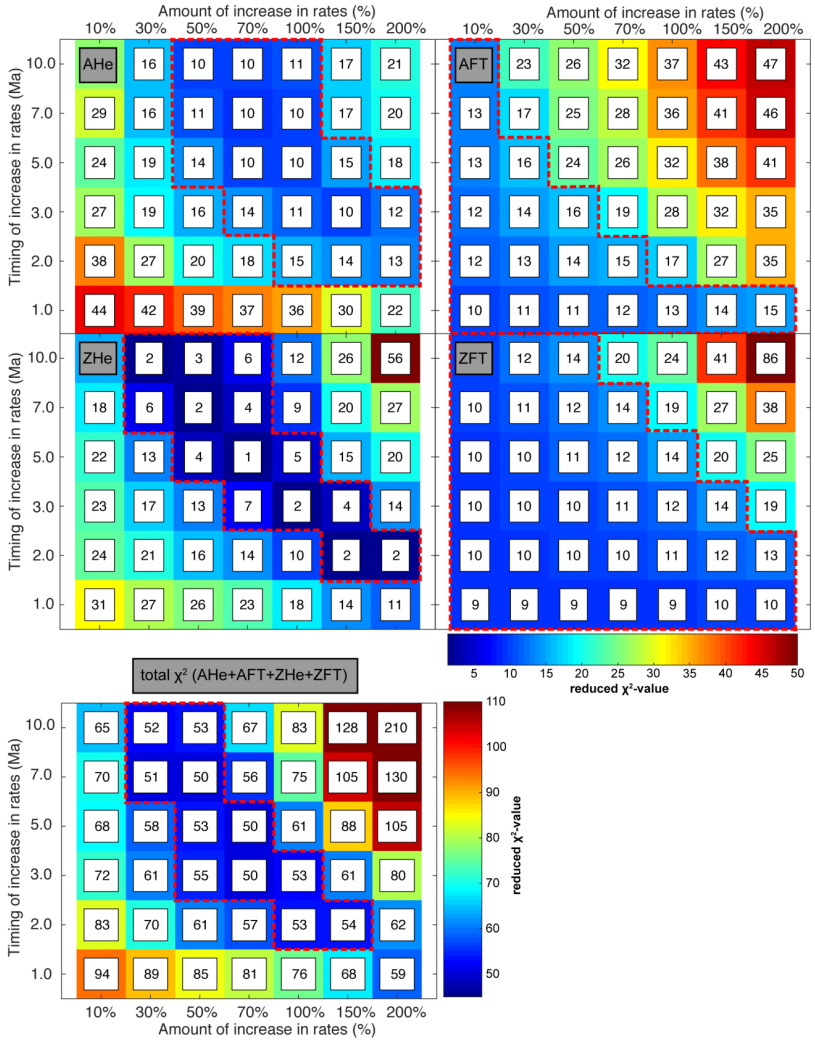

Figure DR8: *Results from finding the best-fit transient model run, where the timing of an increase in exhumation rates (6 different times) and the magnitude of increase (7 different amounts) are varied, giving a total of 42 possible combinations. Shown are the reduced χ^2-values for AHe, AFT, ZHe, ZFT and the sum of the four systems. Best-fit solutions are outlined by red boxes in each subpanel. This indicates, that several increase histories equally well fit the data, e.g. an earlier increase requires a smaller amount, compared to a later increase with higher increase in exhumation rate. The amount of increase is measured relative to the best fit ellipse, which has rates of 0.25/0.9 km/Ma.*

AHe ages (reduced χ^2-values of 10 – 15 compared to 29 – 34 for constant models, see Figures DR6 and DR8). Furthermore, ZHe now also shows a much better fit (reduced χ^2-values of 1 – 7, compared to 32 for the constant 0.25/0.9 model run). Reduced χ^2-values for AFT and ZFT do slightly increase for the transient model runs, probably because the modeled ages for unreset samples become even younger with increased rates. In summary, the total reduced χ^2-value for the transient models (50 – 55) is lower than for the best-fit constant rate model (66) and suggests that an increase in exhumation rate is required to explain the observed ages. However, this also shows that there is a non-unique solution and that several exhumation histories give an equally good fit (Figure DR8): at 2 Ma 100 – 150% increase, at 3 Ma 50 – 100% increase, at 5 Ma 50 – 70% increase and at 7 or 10 Ma 30 – 50% increase. So the earlier the timing of increase, the smaller is the required amount of increase in rates. A summary of our preferred simulations can be found in table DR 5.

Although the model suggests that an increase in rates could happen at different times, there also needs to be an increase mechanism preserved in the geological record at this particular time step, to make this timing of increase geologically feasible. To our knowledge, there is no mechanism between 5 – 10 Ma, that could result in an increase in exhumation rates, e.g. the subduction zone geometry is thought to be in its present day geometry since the latest Eocene (Brandon and Vance, 1992), exhumation of the Olympic Mountains started already at 18 Ma (Brandon et al., 1998), and no significant change in climate has been proposed for this period. On the other hand, Pleistocene glaciation shaped the Olympic Mountains, both by alpine glaciers (see e.g. Figure 1 in the main paper) and the Cordilleran Ice Sheet (Figure DR1d). So Pleistocene glaciation is a mechanism readily at hand and has been invoked as a reason for changes in exhumation on a world-wide scale (e.g. Herman et al., 2013), but also local studies in other orogens suggest a strong impact of Pleistocene glaciation, e.g. in the Coast Mountains of British Columbia (Ehlers et al., 2006), St. Elias Range of Alaska (e.g. Berger et al., 2008) or the European Alps (e.g. Glotzbach et al., 2013).

The exact onset of alpine glaciation in the Olympic Mountains is difficult to determine (see discussion in chapter DR1), hence we also collected information about Pleistocene glaciation in nearby areas in order to present a possible time frame for glaciation. Onset of alpine glaciation in the Olympics could be as old as 2 Ma (Easterbrook, 1986) and is close to the proposed onset of northern hemisphere glaciation at 2.7 Ma (Haug et al., 2005). However, glaciation commenced as early as 7 – 8 Ma in the BC Coast Mountains (Clague, 1989; Ehlers et al., 2006), only 400 km north of the Olympics. Given these time constraints, we believe that 2 to 3 Ma are plausible timings for increasing exhumation rates and picked these times and the suggested increase amounts (at 2 Ma 100 – 150% increase, at 3 Ma 50 – 100% increase) as our preferred transient model solutions. Our proposed range of increasing rates by 50 – 150% is also in accordance with results from the BC Coast Mountains (Ehlers et al., 2006) and would correspond to an ellipse with outer/inner rates of 0.38/1.4 – 0.63/2.3 km/Ma. Furthermore, a peak in glacial erosion at 1.8±0.2 Ma in the BC Coast Mountains (Shuster et al., 2005) suggests, that the effect of glacial erosion on exhumation can be temporally variable, and hence offering a range of increase times and amounts is geologically meaningful.

In order to finally compare sample ages with model ages (Figures 2b,c,e,f in the main paper), we use the following approach. Model ages from the preferred transient model runs are extracted along the swaths A/A' and B/B', both with a width of 30 km. For better comparison with our equal elevation data (collected at ~400 m), these model ages are filtered for elevations between 200 and 500 m in a next step and the mean ages are calculated for each increment of the swath from the filtered ages. Finally, the colored envelopes in Figure 2b,c,e,f represent the range of ages derived from the five preferred transient model runs and are compared to the constant model run with the 0.25/0.9 km/Ma ellipse (black, solid lines in Figure 2b,c,e,f). For reference, the results for an earlier increase in rates (50 and 70% at 5 Ma) are also displayed, and given the uncertainty with onset of glaciation in the Olympics, the effect of glaciation commencing at this time would still produce ages observed in the Olympics.

Table DR 5: Summary of our preferred transient thermo-kinematic simulations from Figure DR8.

Amount of increase relative to constant rate	Outer/Inner ellipse rates (km/Ma)	Onset times for an increase in rates				
		2 Ma	3 Ma	5 Ma	7 Ma	10 Ma
Initial constant rate	0.25/0.9					
10%	0.28/1.0	-	-	-	-	-
30%	0.33/1.2	-	-	-	X	X
50%	0.38/1.4	-	X*	X*	X	X
70%	0.43/1.5	-	X*	X*	-	-
100%	0.5/0/1.8	X*	X*	-	-	-
150%	0.63/2.3	X*	-	-	-	-

Notes: X = Respective increase at respective time yields best-fit simulation.
- = Respective increase at respective time did not yield a best-fit simulation
* = Results from simulations are displayed in Figure 2.

As elaborated in chapter DR1, both precipitation and the location of the equilibrium line altitude (ELA) show strong west to east gradients within the Olympics (Figures DR1c,d) and the ELA is lowest on the west side. Because the ELA corresponds to the area of most effective glacial erosion (e.g. Montgomery, 2002), the effect of glacial erosion on the exhumation rate is also expected to vary spatially in the Olympics. This is already partly reflected by the range of viable increase amounts of our models (50 – 150%). But particularly samples on the western side of the range (OP1527, OP1529, OP1532) still have AHe ages that are younger than ages predicted by our preferred transient model runs. So locally an increase by 150 – 200% or even more could explain the observed, young AHe ages (see range of predicted ages for this amount of increase in Figure 2b).

We do not include the literature data in our swath profiles of Figure 2, because direct comparison between our own data and the published literature data is hampered, due to the different (non-constant elevation) sampling approach. Our own samples were collected at an equal elevation of ~400 m allowing for direct comparison between the samples (where the effect of topography on thermochronometric ages does not have to be considered). On the other hand, the literature samples were collected at elevations between sea level and 2400 m. Nevertheless, we use the fully reset AFT ages in our χ^2-approach in order to assess the goodness of fit for our transient model runs (Figure DR8). Furthermore we provide a comparison of literature AFT and ZFT ages to modeled ages along the swaths in Figure DR9, where we considered literature samples from elevations between 0 and 600 m asl (to make these swaths comparable to Figure 2). However, not many samples are available within this elevation range. The observed fit of sample to modeled ages is not as good as for our own AHe and ZHe data, particularly AFT ages seem to be too old. Several reasons could account for that. All of our and literature samples collected in the Olympic Mountains are sandstones and are hence detrital in nature, if they have not been subducted deep enough and heated to reset them. For their AFT ages this leads Brandon et al. (1998) to discern between fully reset (single age peak, younger than depositional age of sample), partially reset (several peaks, one age peak younger than depositional age), multiply reset (several age peaks, all younger than depositional age) and detrital samples (all peaks older than depositional age). The distribution of the different sample types is not correlated with their spatial occurrence, because fully, partially and multiply reset samples can all be found in the interior of the mountain range. This

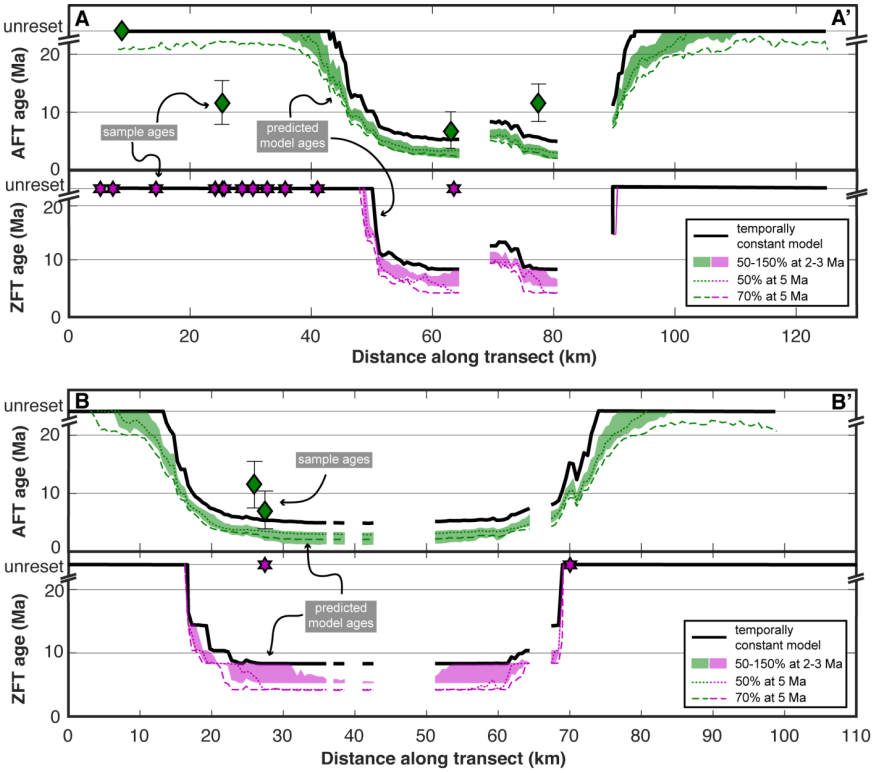

Figure DR9: *Literature AFT/ZFT ages (symbols) and modeled AFT/ZFT ages along the swath profiles A-A' and B-B'. Literature data are taken from an elevation interval between 0 and 600 m asl, to make the analysis comparable to our own equal elevation data. Model ages are taken from an elevation interval between 200 – 500 m. For location of the swaths see Figure 1b, AHe/ZHe ages together with elevation/precipitation can be found in Figure 2. Note: only fully reset or unreset literature samples are considered.*

clearly indicates that the resetting process is variable from sample to sample. Due to the different kinetics of the AHe, AFT and ZHe systems differences in the resetting behavior for these systems seem to be plausible. This could partly account for the better fit of AHe and ZHe ages to our models, compared to AFT, especially since modeled ages within Pecube are treated as fully reset ages. Furthermore, the quality of some of the sandstone samples from the Olympics can be poor and can cause analytical difficulties. E.g. for some of their fully reset samples Brandon et al. (1998) were able to report only 9 – 13 grains, although usually 20 grains should be dated for AFT dating purposes. Finally, one further aspect that could result in a good fit of AHe and ZHe but a bad fit of AFT ages is another variation in exhumation rates besides our proposed increase at 2 Ma like a decrease in rates after samples cooled through the closure temperature of ZHe and subsequent stronger increase. This further complication of cooling histories should be addressed in future work.

To conclude, transient models with various timings and amounts of increase in exhumation rates give a good fit to the observed thermochronometric cooling ages in the Olympic Mountains. However, there are also other factors that are not included in our modeling approach, but that can explain the still observed mismatch between modeled ages and sample ages. First, the increase in rates (which is interpreted as the impact of glaciers) seems to be spatially (and temporally) variable. Second, the shape of the exhumation rate pattern could be different from the assumed perfect ellipse shape and explain some of the excluded, 'outlier' samples (e.g. samples OP1521 and OP1582), too. A possible reduction in topography, e.g. due to Pleistocene glaciation (Ehlers et al., 2006), was also not included in the model. And the exhumation history could be even more complicated, where exhumation rates increase or decrease additionally to the imposed 2 – 3 Ma.

DR3.3 Horizontal velocity models

In a previous study the horizontal velocity component additional to the vertical velocity component was considered in a modeling approach as well (Batt et al., 2001). For this model, a cross section through the accretionary wedge is assumed, starting at the offshore deformation front and extending to the east coast of the Olympic Peninsula. Sedimentary material derived from the subducting slab can enter the accretionary wedge either via frontal accretion or underplating. Batt et al. (2001) concluded that ~90% of the sediment needs to be frontally accreted (and hence a high horizontal velocity component is required) in order to explain their observed age pattern of AHe, AFT and ZFT.

However, there are several reasons why we believe that the contribution of horizontal velocities in the Olympics is less important than previously suggested. First the approach of Batt et al. (2001) is questionable. They base their model on a predefined erosion rate function, which governs the vertical velocity field (and hence the rock uplift). Although the rates of the function are variable from model to model run (in order to explore the best-fitting rates), the shape of the function stays constant. This erosion rate function is determined from uplifted river terraces at the west coast (Pazzaglia and Brandon, 2001) and long-term exhumation rates from inversion of AFT ages (Brandon et al., 1998). These AFT-derived exhumation rates are based on a 1D thermo-kinematic model, but do not consider the proposed effect of horizontal velocities (e.g. the protracted cooling history due to longer travel paths) or possible changes of rates with time. So simply based on the shape of the function, highest erosion rates are always observed 20 – 30 km from the western coastline. Due to the fact that this corresponds also to the area of high horizontal velocities (generally speaking the horizontal velocities decrease from west to east), a strong interplay between horizontal and vertical velocities can always be expected for these models.

Second, the equation stated for the vertical velocity in Batt et al. (2001) contains a mistake, because their derivative of the horizontal velocity is not correct (it is missing a $\eta v_c h_0$ term). Although a full derivation of horizontal and vertical velocities is beyond the scope of this paper (see e.g. Batt et al., 2001; Pazzaglia and Brandon, 2001), we reformulate the corrected equation for the vertical velocity component,

$$w(x,z) = \alpha\left(\dot{\varepsilon}(x) - \frac{z\,\dot{\varepsilon}(x)}{h(x)} - z\cdot\tan\phi\cdot\left(\frac{\eta v_c h_0 - \int_0^x \dot{\varepsilon}(x)}{h^2(x)}\right)\right) + (1-\alpha)\,\dot{\varepsilon}(x)$$

where the vertical velocity *w(x,z)* at place x and z in the wedge is calculated based on the erosion rate at the surface $\dot{\varepsilon}(x)$, thickness of the wedge *h(x)*, angle of subduction ϕ, the incoming sediment material (product of sediment porosity η, subduction velocity v_c and sediment thickness h_0). The factor α is the ratio between frontal accretion and sedimentary underplating (so if α=1 all sediment is frontally accreted). The formula for the horizontal velocity in Batt et al. (2001) is correct,

$$u(x) = \alpha\left(\frac{\eta v_c h_0 - \int_0^x \dot{\varepsilon}(x)}{h(x)}\right)$$

with the underlying assumption that horizontal velocities do not vary with depth but only in x-direction. Examining this equation shows that the horizontal velocity is highest for 100% frontal accretion (α=1) and zero, if only underplating occurs (α=0).

Using these two equations and the values given in table DR6, we also perform model runs in Pecube with both horizontal and vertical velocities. However, these model runs are highly simplified compared to our model runs described in chapter DR3.2: they neither include topography, nor do they consider an increase in rates at 2 – 10 Ma. Furthermore, the model follows a cross section across the Olympic Peninsula parallel to the subduction direction (with a bearing of 54°, for the trace of the cross section see Figure DR4). We derive the integral of the erosion rate by integrating over our preferred elliptic exhumation rate pattern (from the constant rate model run) along the cross section. Using the derived integral and the values listed in table DR6, we calculate the horizontal and vertical velocities along the cross section with a matlab script (using the above equations) and put these values back in Pecube. The resulting pattern of ages is depicted in Figure DR10. A high α-value (i.e. high horizontal velocities) generates AHe and ZHe ages that are too old compared to the observed ages, because it basically shifts the area of reset ages further to the east. For the α=0 model run sample ages are often younger than the model ages (particularly on the west side), which is probably related to the increase in rates at around 2 – 3 Ma due to Pleistocene glaciation. We did not include this increase in our horizontal model runs.

All the points mentioned above lead us to the conclusion, that for our chosen exhumation rate pattern a high horizontal velocity (meaning a high amount of frontal accretion) is not necessary to explain the observed age pattern in the Olympic Mountains for the AHe and ZHe thermochronometer systems we consider. This is also in accordance with seismic studies showing that sedimentary underplating is taking place in the Olympics (Calvert et al., 2011). Hence, our approach to model an increase in exhumation rates at Plio-Pleistocene time using a model that only considers vertical movement seems to be viable. However, we acknowledge the possibility that horizontal motion may be significant for higher temperature thermochronometers (e.g. ZFT) that integrate over longer time scales and distances.

Table DR 6: Additional list of parameters used for the horizontal velocity runs.

Parameter	Value	Source
incoming sediment thickness	2.5 km	approximate value offshore from the Olympic Peninsula (Booth-Rea et al., 2008)
subduction velocity	34 km/Ma	calculated plate velocity of the down going Juan de Fuca plate at the latitude of the Olympics (Doubrovine and Tarduno, 2008)
sediment porosity	27 %	taken from Batt et al. (2001)
angle of subduction	10°	average value of the present day angle of subduction for the Cascadia subduction zone at the latitude of the Olympics (Davis and Hyndman, 1989)

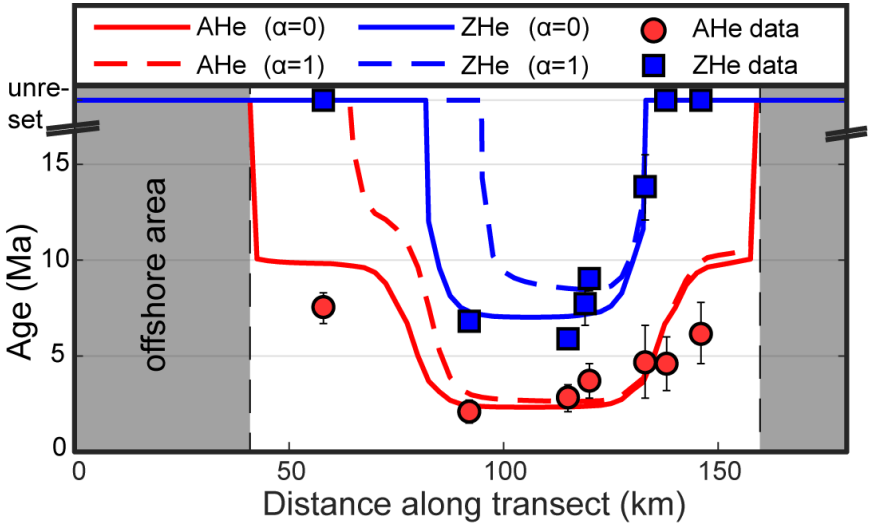

***Figure DR10**: Modeled and observed AHe and ZHe ages from 2D kinematic model simulations extracted along a profile across the Olympic Peninsula (see Fig. DR4 for location). Note that in offshore regions no exhumation is defined within the model, hence all ages are unreset. The α-value corresponds to the amount of material that is frontally accreted in the wedge (α=1, 100% frontal accretion with maximum horizontal velocity; α=0, 100% underplating with no horizontal velocity). A large horizontal velocity component predicts anomalously old cooling ages for both AHe and ZHe.*

REFERNCES

Adam, J., Klaeschen, D., Kukowski, N., and Flueh, E., 2004, Upward delamination of Cascadia Basin sediment infill with landward frontal accretion thrusting caused by rapid glacial age material flux: Tectonics, v. 23, doi: 10.1029/2002TC001475.

Adams, B.A., and Ehlers, T.A., 2017, Deciphering topographic signals of glaciation and rock uplift in an active orogen: a case study from the Olympic Mountains, USA: Earth Surface Processes and Landforms, doi: 10.1002/esp.4120.

Adams, B.A., Hodges, K.V., Whipple, K.X., Ehlers, T.A., van Soest, M.C., and Wartho, J., 2015, Constraints on the tectonic and landscape evolution of the Bhutan Himalaya from thermochronometry: Late Cenozoic Evolution of Bhutan: Tectonics, v. 34, p. 1329–1347, doi: 10.1002/2015TC003853.

Batt, G.E., Brandon, M.T., Farley, K.A., and Roden-Tice, M., 2001, Tectonic synthesis of the Olympic Mountains segment of the Cascadia wedge, using two-dimensional thermal and kinematic modeling of thermochronological ages: Journal of Geophysical Research: Solid Earth, v. 106, p. 26731–26746, doi: 10.1029/2001JB000288.

Berger, A.L., Gulick, S.P.S., Spotila, J.A., Upton, P., Jaeger, J.M., Chapman, J.B., Worthington, L.A., Pavlis, T.L., Ridgway, K.D., Willems, B.A., and McAleer, R.J., 2008, Quaternary tectonic response to intensified glacial erosion in an orogenic wedge: Nature Geoscience, v. 1, p. 793–799, doi: 10.1038/ngeo334.

Booth-Rea, G., Klaeschen, D., Grevemeyer, I., and Reston, T., 2008, Heterogeneous deformation in the Cascadia convergent margin and its relation to thermal gradient (Washington, NW USA): Tectonics, v. 27, doi: 10.1029/2007TC002209.

Brandon, M.T., Roden-Tice, M.K., and Garver, J.I., 1998, Late Cenozoic exhumation of the Cascadia accretionary wedge in the Olympic Mountains, northwest Washington State: Geological Society of America Bulletin, v. 110, p. 985–1009, doi: 10.1130/0016-7606(1998)110<0985:LCEOTC>2.3.CO;2.

Brandon, M.T., and Vance, J.A., 1992, Tectonic evolution of the Cenozoic Olympic subduction complex, Washington State, as deduced from fission track ages for detrital zircons: American Journal of Science, v. 292, p. 565–636, doi: 10.2475/ajs.292.8.565.

Calvert, A.J., Preston, L.A., and Farahbod, A.M., 2011, Sedimentary underplating at the Cascadia mantle-wedge corner revealed by seismic imaging: Nature Geoscience, v. 4, p. 545–548, doi: 10.1038/ngeo1195.

Clague, J.J., 1989, Quaternary Geology of the Canadian Cordillera, *in* Fulton, R.J. ed., Quaternary Geology of Canada and Greenland, Ottawa, Geological Survey of Canada, Geology of Canada 1, p. 17–96.

Crosson, R.S., and Owens, T.J., 1987, Slab geometry of the Cascadia Subduction Zone beneath Washington from earthquake hypocenters and teleseismic converted waves: Geophysical Research Letters, v. 14, p. 824–827, doi: 10.1029/GL014i008p00824.

Davis, E.E., and Hyndman, R.D., 1989, Accretion and recent deformation of sediments along the northern Cascadia subduction zone: Geological Society of America Bulletin, v. 101, p. 1465–1480.

Doubrovine, P.V., and Tarduno, J.A., 2008, A revised kinematic model for the relative motion between Pacific oceanic plates and North America since the Late Cretaceous: Journal of Geophysical Research, v. 113, doi: 10.1029/2008JB005585.

Easterbrook, D.J., 1986, Stratigraphy and chronology of quaternary deposits of the Puget Lowland and Olympic Mountains of Washington and the Cascade Mountains of Washington and Oregon: Quaternary Science Reviews, v. 5, p. 145–159, doi: 10.1016/0277-3791(86)90180-0.

Eddy, M.P., Clark, K.P., and Polenz, M., 2017, Age and volcanic stratigraphy of the Eocene Siletzia oceanic plateau in Washington and on Vancouver Island: Lithosphere, v. 9, p. 652–664, doi: 10.1130/L650.1.

Ehlers, T.A., Farley, K.A., Rusmore, M.E., and Woodsworth, G.J., 2006, Apatite (U-Th)/He signal of large-magnitude accelerated glacial erosion, southwest British Columbia: Geology, v. 34, p. 765–768.

Farley, K.A., 2002, (U-Th)/He Dating: Techniques, Calibrations, and Applications: Reviews in Mineralogy and Geochemistry, v. 47, p. 819–844, doi: 10.2138/rmg.2002.47.18.

Glotzbach, C., van der Beek, P., Carcaillet, J., and Delunel, R., 2013, Deciphering the driving forces of erosion rates on millennial to million-year timescales in glacially impacted landscapes: An example from the Western Alps: Journal of Geophysical Research: Earth Surface, v. 118, p. 1491–1515, doi: 10.1002/jgrf.20107.

Haug, G.H., Ganopolski, A., Sigman, D.M., Rosell-Mele, A., and others, 2005, North Pacific seasonality and the glaciation of North America 2.7 million years ago: Nature, v. 433, p. 821.

Hayes, G.P., Wald, D.J., and Johnson, R.L., 2012, Slab1.0: A three-dimensional model of global subduction zone geometries: SLAB1.0 3D SUBDUCTION GEOMETRY: Journal of Geophysical Research: Solid Earth, v. 117, p. n/a-n/a, doi: 10.1029/2011JB008524.

Herman, F., Seward, D., Valla, P.G., Carter, A., Kohn, B., Willett, S.D., and Ehlers, T.A., 2013, Worldwide acceleration of mountain erosion under a cooling climate: Nature, v. 504, p. 423–426, doi: 10.1038/nature12877.

Hourigan, J.K., Reiners, P.W., and Brandon, M.T., 2005, U-Th zonation-dependent alpha-ejection in (U-Th)/He chronometry: Geochimica et Cosmochimica Acta, v. 69, p. 3349–3365, doi: 10.1016/j.gca.2005.01.024.

Hyndman, R.D., and Wang, K., 1993, Thermal constraints on the zone of major thrust earthquake failure: The Cascadia Subduction Zone: Journal of Geophysical Research: Solid Earth, v. 98, p. 2039–2060, doi: 10.1029/92JB02279.

Hyndman, R.D., Yorath, C.J., Clowes, R.M., and Davis, E.E., 1990, The northern Cascadia subduction zone at Vancouver Island: Seismic structure and tectonic history: Canadian Journal of Earth Sciences, v. 27, p. 313–329.

Lewis, T.J., and Bentkowski, W.H., 1988, Potassium, Uranium and Thorium Concentrations of Crustal Rocks: a Data File: Geological Survey of Canada, Open File, 1–165 p.

Lewis, T.J., Bentkowski, W.H., Davis, E.E., Hyndman, R.D., Souther, J.G., and Wright, J.A., 1988, Subduction of the Juan de Fuca Plate: Thermal consequences: Journal of Geophysical Research: Solid Earth, v. 93, p. 15207–15225, doi: 10.1029/JB093iB12p15207.

McCrory, P.A., Blair, J.L., Waldhauser, F., and Oppenheimer, D.H., 2012, Juan de Fuca slab geometry and its relation to Wadati-Benioff zone seismicity: JDF SLAB GEOMETRY AND WBZ SEISMICITY: Journal of Geophysical Research: Solid Earth, v. 117, p. n/a-n/a, doi: 10.1029/2012JB009407.

McQuarrie, N., and Ehlers, T.A., 2015, Influence of thrust belt geometry and shortening rate on thermochronometer cooling ages: Insights from thermokinematic and erosion modeling of the Bhutan Himalaya: GEOMETRY, RATES, AND MODELED COOLING AGES: Tectonics, v. 34, p. 1055–1079, doi: 10.1002/2014TC003783.

Meesters, A.G.C.A., and Dunai, T.J., 2005, A noniterative solution of the (U-Th)/He age equation: Geochemistry, Geophysics, Geosystems, v. 6, doi: 10.1029/2004GC000834.

Montgomery, D.R., 2002, Valley formation by fluvial and glacial erosion: Geology, v. 30, p. 1047–1050, doi: 10.1130/0091-7613(2002)030<1047:VFBFAG>2.0.CO;2.

Montgomery, D.R., and Greenberg, H.M., 2000, Local relief and the height of Mount Olympus: Earth Surface Processes and Landforms, v. 25, p. 385–396.

Pazzaglia, F.J., and Brandon, M.T., 2001, A fluvial record of long-term steady-state uplift and erosion across the Cascadia forearc high, western Washington State: American Journal of Science, v. 301, p. 385–431.

Phillips, B.A., Kerr, A.C., Mullen, E.K., and Weis, D., 2017, Oceanic mafic magmatism in the Siletz terrane, NW North America: Fragments of an Eocene oceanic plateau? Lithos, v. 274–275, p. 291–303, doi: 10.1016/j.lithos.2017.01.005.

Porter, S.C., 1964, Composite Pleistocene snow line of Olympic Mountains and Cascade Range, Washington: Geological Society of America Bulletin, v. 75, p. 477–482.

Shuster, D.L., Ehlers, T.A., Rusmoren, M.E., and Farley, K.A., 2005, Rapid Glacial Erosion at 1.8 Ma Revealed by 4He/3He Thermochronometry: Science, v. 310, p. 1668–1670, doi: 10.1126/science.1118519.

Stewart, R.J., and Brandon, M.T., 2004, Detrital-zircon fission-track ages for the “Hoh Formation”: implications for late Cenozoic evolution of the Cascadia subduction wedge: Geological Society of America Bulletin, v. 116, p. 60–75.

Stübner, K., Drost, K., Schoenberg, R., Böhme, M., Starke, J., and Ehlers, T.A., 2016, Asynchronous timing of extension and basin formation in the South Rhodope core complex, SW Bulgaria, and northern Greece: Tectonics, v. 35, p. 136–159, doi: 10.1002/2015TC004044.

Tabor, R.W., and Cady, W.M., 1978, The structure of the Olympic Mountains, Washington: Analysis of a subduction zone: US Govt. Print. Off., v. 1033.

Thackray, G.D., 2001, Extensive Early and Middle Wisconsin Glaciation on the Western Olympic Peninsula, Washington, and the Variability of Pacific Moisture Delivery to the Northwestern United States: Quaternary Research, v. 55, p. 257–270, doi: 10.1006/qres.2001.2220.

Underwood, M.B., Hoke, K.D., Fisher, A.T., Davis, E.E., Giambalvo, E., Zuhlsdorff, L., and Spinelli, G.A., 2005, Provenance, Stratigraphic Architecture, and Hydrogeologic Influence of Turbidites on the Mid-Ocean Ridge Flank of Northwestern Cascadia Basin, Pacific Ocean: Journal of Sedimentary Research, v. 75, p. 149–164, doi: 10.2110/jsr.2005.012.

Vermeesch, P., 2010, HelioPlot, and the treatment of overdispersed (U–Th–Sm)/He data: Chemical Geology, v. 271, p. 108–111, doi: 10.1016/j.chemgeo.2010.01.002.

Whipp, D.M., Ehlers, T.A., Braun, J., and Spath, C.D., 2009, Effects of exhumation kinematics and topographic evolution on detrital thermochronometer data: Journal of Geophysical Research, v. 114, doi: 10.1029/2008JF001195.

3.2 Temporal variations of exhumation and steady-state orogens

3.2.1 Declaration on contributions to joint work

The following section of the dissertation contains a manuscript that has been submitted and is accepted for publication in the journal *Earth Surface Dynamics - Discussion*, entitled "How steady are steady-state mountain belts? – a re-examination of the Olympic Mountains (Washington State, USA)". It is an open review process journal, hence the initial version of the submitted manuscript can be accessed online under `https://doi.org/10.5194/esurf-2018-65`. The most-recent versions during peer-review of the submitted manuscript and the electronic supplement are provided in section 3.2.2 and section 3.2.3, respectively. Supplementary data tables containing the single grain ages of AHe, ZHe, AFT and ZFT are provided in the appendix (Section B).

Five authors contributed to the work presented in the manuscript: Lorenz Michel (LM), Christoph Glotzbach (CG), Sarah Falkowski (SF), Byron Adams (BA) and Todd Ehlers (TE). A summary of the respective contributions is provided in Table 3.2. The detailed contributions are as follows: LM developed the idea of re-investigating steady-state of the Olympic Mountains by refining the influx calculation and using cross sections. This basic idea was expanded by contributions from CG, BA, TE and SF. LM, TE and BA performed fieldwork and collected samples. LM performed the sample treatment, mineral separation and selected apatite and zircon minerals for thermochronometric dating. SF prepared mineral mounts for apatite and zircon fission-track dating (AFT, ZFT). SF performed the AFT dating and LM performed ZFT dating, respectively, and the interpretation of fission-track ages was done by SF and LM. CG performed most of the analytic work involved in (U-Th)/He dating, with minor help from LM. The thermo-kinematic modeling (Pecube) was performed by LM, with input from BA, TE and CG. Analysis and interpretation of the results was done by LM, CG, BA, SF and TE. LM drafted the first version of the manuscript along with all figures. During further writing and development of the manuscript, the manuscript received comments from BA, SF, CG and TE. During peer review, two reviewers commented on the manuscript.

Table 3.2: Summary of the contribution to joint work for the paper "How steady are steady-state mountain belts? – a re-examination of the Olympic Mountains (Washington State, USA)", indicating the average fraction of work of the respective author in percent. The manuscript has been accepted for publication in February 2019.

Author	Position	Scientific ideas (in %)	Data generation (in %)	Analysis and Interpretation (in %)	Paper writing (in %)
LM	[1]	70	60	65	65
CG	[2]	15	20	15	10
SF	[3]	5	15	10	10
BA	[4]	5	5	5	10
TE	[5]	5	0	5	5

3.2.2 Manuscript: "How steady are steady-state mountain belts? – a re-examination of the Olympic Mountains (Washington State, USA)."

How steady are steady-state mountain belts? – a re-examination of the Olympic Mountains (Washington State, USA)

Lorenz Michel[1], Christoph Glotzbach[1], Sarah Falkowski[1], Byron A. Adams[1,2], Todd A. Ehlers[1]

[1]Department of Geosciences, University of Tübingen, Tübingen, 72074, Germany
[2]School of Earth Sciences, University of Bristol, Bristol, BS8 1RJ, United Kingdom

Correspondence to: Todd A. Ehlers (todd.ehlers@uni-tuebingen.de)

Abstract. The Olympic Mountains of Washington State (USA) represent the aerially exposed accretionary wedge of the Cascadia Subduction Zone and are thought to be in flux steady-state, whereby the mass outflux (denudation) and influx (tectonic accretion) into the mountain range are balanced. We use a multi-method approach to investigate how temporal variations in the influx and outflux could affect previous interpretations of flux steady-state. This includes analysis of published and new thermochronometric ages for (U-Th)/He dating of apatite and zircon (AHe and ZHe, respectively) and fission track dating of apatite and zircon (AFT and ZFT, respectively), 1D thermo-kinematic modelling of thermochronometric data, and independent estimates of outflux and influx.

In total, we present 61 new AHe, ZHe, AFT, and ZFT thermochronometric ages from 21 new samples. AHe ages are generally young (<4 Ma), and, in some samples, AFT ages (5–8 Ma) overlap with ZHe ages (7–9 Ma) within uncertainties. Thermo-kinematic modelling shows that exhumation rates are temporally variable, with rates decreasing from >2 km/Myr to <0.3 km/Myr around 5–7 Ma. With the onset of Plio-Pleistocene glaciation, exhumation rates increased to values >1 km/Myr. This demonstrates that the material outflux is varying through time, requiring a commensurate variation in influx to maintain flux steady-state. Evaluation of the offshore and onshore sediment record shows that the material influx is also variable through time and that the amount of accreted sediment in the wedge is spatially variable. This qualitatively suggests that significant perturbations of steady-state occur on shorter timescales (10^5–10^6 yr), like those created by Plio-Pleistocene glaciation. Our quantitative assessment of influx and outflux indicates that the Olympic Mountains could be in flux steady-state on long timescales (10^7 yr).

1 Introduction

The assumption of a balance between opposing processes has allowed geoscientists to use proxy measurements (like denudation rates) to constrain difficult to measure variables like rock uplift. This has given rise to the concept of steady-state landscapes or mountain ranges. Likewise, a steady-state (i.e., a mass balance) is commonly one of the boundary conditions in modelling studies investigating the evolution and dynamics of orogens in response to changes of other boundary conditions like climate or tectonic fluctuations (e.g., Batt et al., 2001; Stolar et al., 2007; Whipple and Meade, 2006; Willett, 1999). Two main types of steady-state are often used to interpret mountain building processes (e.g., Willett and Brandon, 2002): (1) Topographic steady-

state, where the topography is invariant, because rock uplift and horizontal motion of material is balanced by denudation, and (2) flux steady-state, where the material influx (by accretion of sediment and rock) is balanced by the material outflux (by denudation) from a mountain range. The assumption of steadiness is both spatial- and timescale-dependent so that for a given timescale, steadiness might only be achieved on a large, orogen-wide spatial scale, due to the spatial averaging of single processes acting on a small scale (e.g., catchment-wide sediment discharge vs. orogen-wide sediment discharge). Furthermore, a possible perturbation of steady-state is sensitive to the timescale it takes for orogens to respond to variations in crustal deformation or a change in climate. If the timescales required for a change in the influx and outflux are significantly different from each other, a deviation from steady-state is likely.

Likewise, studies from different orogens worldwide suggest strong variations in denudation and exhumation on million-year timescales. These variations can be linked to changes in the tectonic conditions (e.g., Adams et al., 2015; Lease et al., 2016), internal dynamics of drainage basins (e.g., Willett et al., 2014; Yanites et al., 2013), changes in the magnitude of precipitation (e.g., Lease and Ehlers, 2013; Whipple, 2009), or the onset of glaciation (e.g., Berger et al., 2008; Bernard et al., 2016; Ehlers et al., 2006; Glotzbach et al., 2013; Gulick et al., 2015; Herman et al., 2013; Herman and Brandon, 2015; Lease et al., 2016; Thomson et al., 2010; Thomson et al., 2013; Valla et al., 2011; Yanites and Ehlers, 2012).

Based on thermo-kinematic modelling of thermochronometric cooling ages, the Olympic Mountains, USA, (Fig. 1a) have been proposed to be in flux steady-state since ca. 14 Ma (Batt et al., 2001; Brandon et al., 1998). The approach of these studies was to assume flux steady-state along a two-dimensional profile across the Olympic Peninsula as a precondition in order to derive the kinematics of the model from the balance between accretionary influx (governed by the thickness of accreted sediment and plate convergence rate) and denudational outflux (as set by exhumation rates). Because the cooling ages can successfully be modelled with the used kinematics, the mountain range is then interpreted to be in flux steady-state. However, possible temporal variations in parameters like sediment thickness, plate convergence rate or exhumation rates were not considered in these studies. Likewise, the impact of Plio-Pleistocene glaciation on the flux steady-state hypothesis has not been considered yet, although the range was extensively incised by glaciers (Adams and Ehlers, 2017; Montgomery, 2002; Montgomery and Greenberg, 2000; Porter, 1964) and experienced significant changes in climate conditions over the past 3 Myr (Mutz et al., 2018). Numerical modelling studies investigated the mechanics of the wedge by either considering fluvial erosion (Stolar et al., 2007) or glacial erosion (Tomkin and Roe, 2007). A significant response of the orogenic wedge to glaciation was suggested (Tomkin and Roe, 2007) and recent studies proposed that exhumation rates in the Olympic Mountains increased due to Plio-Pleistocene glacial erosion (Herman et al., 2013; Michel et al., 2018). Resulting high sedimentation rates during the Quaternary increased the sediment thickness on the oceanic plate and seem to have caused a change in the deformational style of the offshore part of the wedge (Adam et al., 2004).

In this study, we test the hypothesis of flux steady-state in the Olympic Mountains, considering variations in both the material influx and outflux. First, we test the temporal steadiness of exhumation rates from bedrock

cooling histories with a 1D thermo-kinematic model, capitalizing on new samples which have been dated with three to four thermochronometers (apatite and zircon (U-Th)/He and fission-track data; AHe, ZHe, AFT, and ZFT, respectively). Second, instead of assuming flux steady-state as a precondition, we attempt to estimate both the accretionary influx and denudational outflux independently from each other. We particularly consider possible temporal variations in parameters affecting both fluxes by using published data of the off- and onshore sediment records, and exhumation rates from thermochronometry. With our new thermochronometry data we reveal a previously undetected temporal variation in exhumation rates due to a change in the tectonics (a reduction in plate convergence rates that resulted in a decrease in exhumation rate), as well as the previously reported increase in exhumation rates related to the Plio-Pleistocene glaciation (reflecting a change in climate). Similarly, both material influx and outflux are temporally variable, especially during the Quaternary. A quantitative comparison between both fluxes suggests that the Olympic Mountains could be in flux steady-state over longer timescales (e.g., 10^7 yr), if a three-dimensional geometry is considered.

2 Background

2.1 Geology and glacial history of the Olympic Mountains

At present, the Juan de Fuca Plate subducts obliquely with respect to the overriding North American Plate (Fig. 1a) at 34 mm/yr at the latitude of the Olympic Mountains (Doubrovine and Tarduno, 2008). The forearc high of the subduction zone comprises (from north to south) Vancouver Island, the Olympic Mountains and the Oregon Coast Range, and lies west of a forearc low (e.g., Georgia Lowlands, Puget Lowlands) and the active volcanic arc (Fig. 1a). Seismic imaging suggests a flatter subduction angle beneath southern Vancouver Island and the Olympic Mountains (Hayes et al., 2012; McCrory et al., 2012), compared to areas in the north and south (Fig. 1a). The modern configuration of the subduction zone was established by the latest Eocene (e.g., Brandon and Vance, 1992) after accretion of the Coast Range Terrane to the North American continent (Fig. 1c). This terrane represents a large oceanic plateau and extends from the southern tip of Vancouver Island to Oregon (Eddy et al., 2017; Phillips et al., 2017; Wells et al., 2014).

The accretionary wedge of the subduction zone is exposed onshore within the Olympic Mountains (Fig. 1a) and is composed of Eocene–Miocene flysch (Brandon et al., 1998; Tabor and Cady, 1978). This part of the mountain range is known as the Olympic Structural Complex (Brandon et al., 1998) and is separated from the surrounding Coast Range Terrane by the Hurricane Ridge thrust fault (HRF; Fig. 1c), a major discontinuity traceable in seismic surveys (e.g., Clowes et al., 1987; Calvert et al., 2011). Minor sedimentary rocks of Eocene age (Eddy et al., 2017; Tabor and Cady, 1978) are contained within the Coast Range Terrane besides the predominant ~50 Ma old marine and subaerial basaltic rocks (Eddy et al., 2017). Exhumation of the range commenced at 18 Ma and since 14 Ma, the orogen is supposed to be in flux steady-state (Batt et al., 2001; Brandon et al., 1998; Pazzaglia and Brandon, 2001).

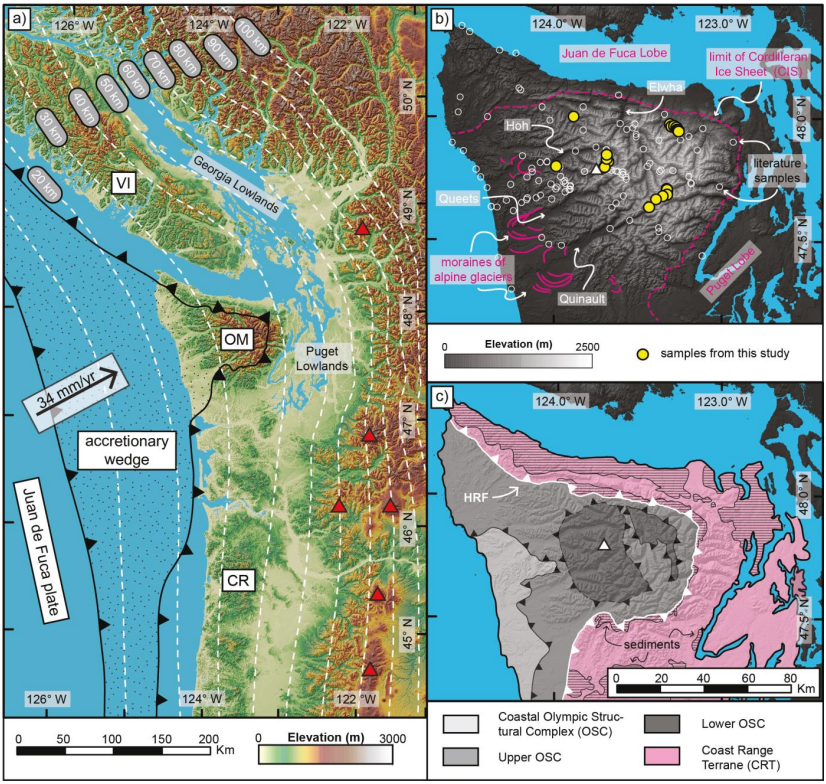

Figure 1: a) Overview map of the Cascadia Subduction Zone, showing the extent of the accretionary wedge. White dashed lines are contour lines for the top of the subducted oceanic plate from the Slab1.0 model (Hayes et al., 2012; McCrory et al., 2012), the black arrow indicates the present-day convergence rate and direction at the latitude of the Olympic Mountains (Doubrovine and Tarduno, 2008), red triangles denote the location of active volcanoes. VI = Vancouver Island, OM = Olympic Mountains, CR = Oregon Coast Range. b) Topography of the Olympic Mountains, major river valleys (Elwha, Hoh, Quinault, Queets) and major Quaternary features are indicated. Limit of the Cordilleran Ice Sheet from Porter (1964), alpine moraines after geologic map of Tabor and Cady (1978). Locations of samples from this study (filled yellow circles) and previous studies (open white circles) are indicated. The white triangle denotes the location of Mt. Olympus. c) Geologic and structural map of the Olympic Mountains after Tabor and Cady (1978) and Brandon et al. (1998). The line pattern indicates the occurrence of sediments within the Coast Range Terrane. HRF = Hurricane Ridge Fault.

Plio-Pleistocene glaciation has strongly influenced the present-day appearance of the Olympic Mountains (Fig. 1b). During its maximum extent at ~14 ka, the Cordilleran Ice Sheet advanced from the Coast Mountains of British Columbia and covered Vancouver Island and large parts of todays' continental shelf (Booth et al., 2003; Clague and James, 2002). The Puget and Juan de Fuca lobes of the Cordilleran Ice Sheet surrounded the Olympic Mountains in the east/southeast and in the north, respectively (Fig. 1b). Alpine glaciers incised deep valleys in the landscape, particularly on the western side of the range (Adams and Ehlers, 2017;

Montgomery, 2002), where piedmont glaciers almost reached the Pacific Ocean (Thackray, 2001). Glacial erosion varied across the range, as the location of the Pleistocene equilibrium line altitude increases from 1000 m in the west to 1800 m in the east (Porter, 1964), due to a strong precipitation gradient (> 6000 mm/yr in the west, < 1000 mm/yr in the east). Determining the exact onset of glaciation in the Olympics has proven difficult, but the oldest deposits of the Cordilleran Ice Sheet in the Puget Lowland are as old as 2 Ma and deeply weathered alpine till on the west side of the Olympics is interpreted to be of the same age (Easterbrook, 1986).

2.2 Previous thermochronometry studies in the Olympic Mountains

Within the Olympic Mountains, an extensive dataset of thermochronometric cooling ages from bedrock samples (Figs. 1b and 2) exists for AHe (Batt et al., 2001; Michel et al., 2018), AFT (Brandon et al., 1998), ZHe (Michel et al., 2018) and ZFT (Brandon and Vance, 1992; Stewart and Brandon, 2004). These thermochronometer systems record cooling through a temperature range of ~60–240°C (e.g., Brandon et al., 1998; Farley, 2002; Gallagher et al., 1998; Reiners et al., 2004), as they have effective closure temperatures of 70°C, ~120°C, ~180°C and ~240°C, respectively, for a cooling rate of ~10°C/Myr (Ehlers, 2005). The interpretation of thermochronometric cooling ages from sedimentary rocks (such as in the Olympic Mountains) is often complicated when the cooling signal from the sediment source region(s) has not been reset due to reheating during subduction and metamorphism. If a sedimentary rock sample has not had sufficient exposure to temperatures above the closure temperature of a given thermochronometer, the sample might retain cooling ages that represent the source region's cooling history (referred to as unreset) or might be a mixture of provenance cooling histories and the reheating process (incompletely reset sample). Determining, whether a sample is completely, incompletely or un-reset can be difficult and usually depends on the statistics of cooling age populations, derived from the dated mineral grains (e.g., Brandon et al., 1998). The reproducibility of single grain (U-Th)/He ages from a sample provides an indication of whether a sample is reset or not. This is typically determined with n=4–7 grains. For the fission track method, a larger number of grains is typically dated (n=20–100) to reduce the uncertainty in the final cooling age calculation. For samples with a large population, statistical methods can be applied to decompose the chronometer date distribution into different populations, and to determine if some portion of the sample is reset (Brandon, 1992, 1996). In the case where a sample is incompletely reset, a significant young age peak is determined and interpreted as the sample cooling age (e.g., Brandon et al., 1998).

In the Olympics, the youngest published reset AHe ages (≤ 2.5 Ma) can be found in the western and central portions of the mountain range, and there are two unreset samples in the east (Fig. 2a). The pattern of AFT ages is more complicated (Fig. 2b), and most reset and incompletely reset samples are located in the central part of the mountain range, whereas unreset samples are restricted to areas outside the central (high topography) part of the range. The youngest reported AFT samples (2–4 Ma) are incompletely reset samples and fully reset samples have cooling ages between 7 Ma and 27 Ma. ZHe data show a well-developed trend of

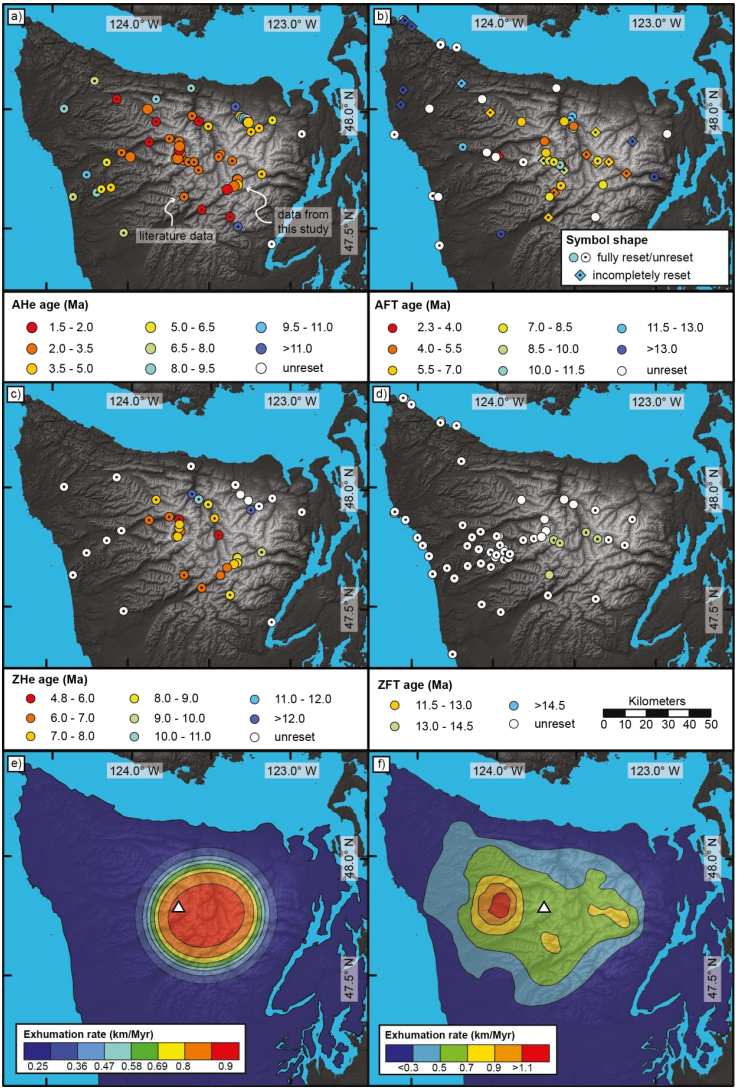

Figure 2: Map of new and previously published thermochronometric ages within the Olympic Mountains for a) AHe, b) AFT, c) ZHe and d) ZFT. Data from literature (Batt et al., 2001; Brandon et al., 1998; Brandon and Vance, 1992; Michel et al., 2018; Stewart and Brandon, 2004) are indicated by circles with black dot. Note that the colour coding of the symbols varies between panels. For AFT literature samples, the different reset states (fully reset, incompletely reset and unreset) are indicated by symbol shape. Maps of exhumation rates, as suggested by (e) Michel et al. (2018) and (f) Brandon et al. (1998). The white triangle denotes the location of Mt. Olympus.

unreset cooling ages at the coast and reset 5–6 Ma ages in the headwaters of Hoh and Elwha rivers (cf., Figs. 1b and 2c). Reset ZFT samples (~13–14 Ma) are confined to a small area east of Mt. Olympus (Fig. 2d).

Based on thermo-kinematic modelling, Michel et al. (2018) attributed the observed AHe and ZHe age pattern to an ellipse-shaped exhumation pattern (with highest exhumation rates in the central, high-topography part of the mountain range, Fig. 2e), as predicted for a mountain range situated in an orogenic syntaxis setting (Bendick and Ehlers, 2014). Here, a bend in the subducted slab creates a mechanical stiffening, which in turn leads to rapid and focused exhumation at the surface (Bendick and Ehlers, 2014). High uplift rates in the central, high topography part of the mountain range are also corroborated by topographic analyses (Adams and Ehlers, 2017) and denudation rates based on cosmogenic nuclides (Adams and Ehlers, 2018). Furthermore, modelling of particularly young AHe ages (<2.5 Ma) suggests that exhumation rates increased significantly by 50–150 % due to Plio-Pleistocene glacial erosion (Michel et al., 2018).

2.3 Offshore sediment record

Data constraining the sediment thickness on the Juan de Fuca Plate before incorporation of sediment into the accretionary wedge are summarized in Figure 3. Three boreholes were drilled into the blanketing sediments of the Juan de Fuca Plate during deep-sea drilling projects (ODP 888, ODP 1027 and DSDP 174; Fig. 3 and Table 1), and provide estimates of the sediment thickness and age constraints. The sediment thickness at the deformation front of the subduction zone has been estimated from three seismic studies (Adam et al., 2004; Booth-Rea et al., 2008; Han et al., 2016).

Most of the sediment is contained within two deep-sea sediment fans with different sediment sources. Today, sediment sources for the Nitinat Fan (offshore Vancouver Island and the Olympic Mountains) include detritus from Vancouver Island, the Olympic Mountains, and material delivered by the Fraser river system (Fig. 3), which drains large parts of the Canadian Cordillera including the British Columbian Coast Mountains (Carpentier et al., 2014; Kiyokawa and Yokoyama, 2009). The Astoria Fan offshore the Oregon coast is mostly fed by the Columbia River and is sourced by a large area in the interior of the USA (Fig. 3).

The total sediment thickness varies between 2600–3500 m at the deformation front and decreases rapidly to 600 or 900 m approximately 100 km away from the deformation front. At the locations of ODP 1027 and DSDP 174, up to 50–70 % of the total sediment thickness are Quaternary deposits, and sedimentation rates more than doubled during the Quaternary (from 80–110 m/Myr to 250–270 m/Myr, Table 1). At the location of ODP 888 the drilled 570 m of core were deposited over the past 600 kyr, suggesting very high sedimentation rates of 950 m/Myr compared to 400 m/Myr for the total sediment thickness of 2600 m at the location of the core (Table 1). As determined from detailed, stratigraphic analysis of core ODP 888, sedimentation rates are also highly variable during the Quaternary. Rates during glacial periods can be as high as 1900 m/Myr compared to 700 m/Myr during interglacials (Knudson and Hendy, 2009). At sites ODP 888 and 1027, the source region of the sediments has been the Canadian Cordillera for the past 3.5 Myr, which has not been affected by glacial-interglacial cycles (Carpentier et al., 2014; Kiyokawa and Yokoyama, 2009). The prove-

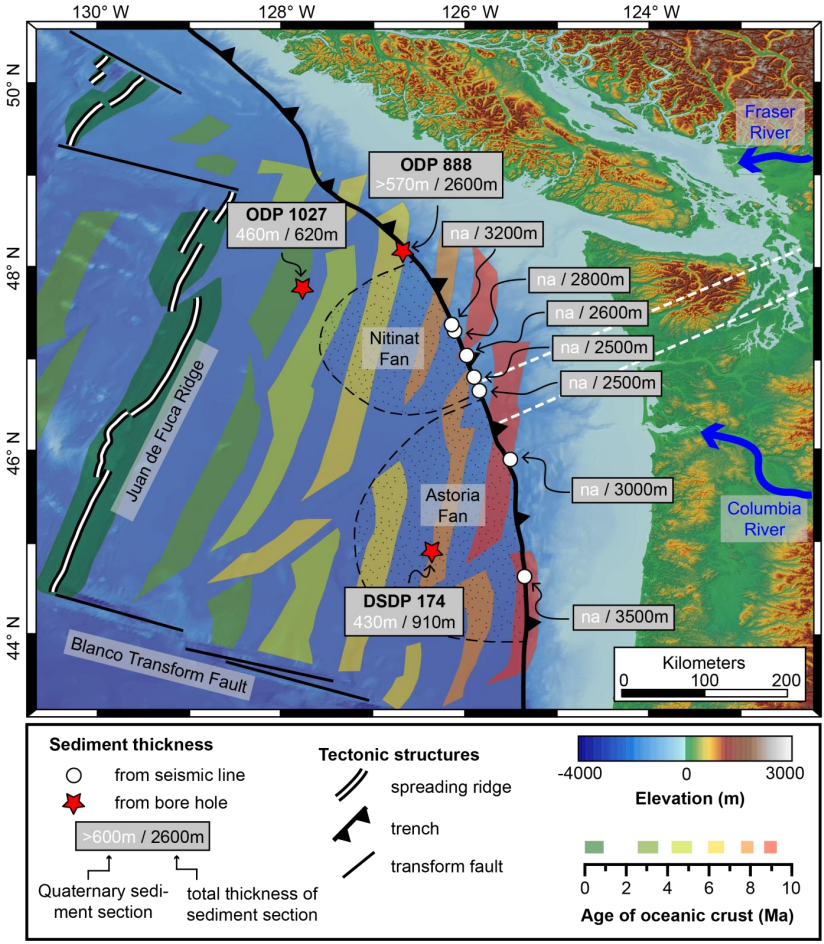

Figure 3: Map of the Cascadia Subduction Zone, showing the age of the oceanic crust (Wilson, 1993) and sediment thickness, estimated from sediment cores of the ocean drilling programs (holes ODP 888, OPD 1027 and DSDP 174) and seismic studies (Adam et al., 2004; Booth-Rea et al., 2008; Han et al., 2016). The amount of Quaternary sediment material estimated from cores is also included (Kulm et al., 1973; Su et al., 2000; Westbrook et al., 1994), more information about the drill cores is provided in Table 1. The locations of two major submarine fans (Nitinat Fan and Astoria Fan) are indicated by the dotted pattern. The Fraser and Columbia rivers are the main modern sediment sources for Nitinat and Astoria fans, respectively. White, dashed lines indicate the position of cross-sections presented in this study (cf., Fig. 7).

nance of the sediments at DSDP 174 is mostly the Proterozoic Belt Supergroup in the interior of the USA and differs significantly from present-day detritus of the Columbia River (Prytulak et al., 2006). Hence, Prytulak et al. (2006) suggest that deposition of the upper 630 m of sediment at this site and the build-up of the Astoria Fan were governed by glacial outburst floods.

3 Methods

We use a multi-method approach to assess flux steady-state in the Olympic Mountains. This includes thermochronometric dating, thermo-kinematic modelling of cooling ages to obtain exhumation rates, and independent estimates of accretionary influx and denudational outflux. We calculate the influx based on constraints of the incoming sediment thickness and plate convergence rate, and the outflux based on spatial constraints of exhumation rates within the Olympic Mountains. The procedure for each method is outlined below.

3.1 Thermochronometric methods

Our strategy with thermochronometric dating was (1) to obtain samples, which are multi-dated with up to four thermochronometer systems (because these are particularly sensitive to reveal variations in exhumation rate) and (2) to collect samples within vertical profiles in order to obtain estimates of the exhumation rate at the site of the respective profile. Therefore, we dated several literature samples with additional thermochronometer systems (Table 2) and we also present 19 new bedrock samples from vertical profiles (Fig. 4, Table 2) and two additional bedrock samples (OP1528 and OP1556; Fig. 2, Table 2) collected at an elevation of ~400 m, enlarging the existing ~400 m equal-elevation data of Michel et al. (2018). All new samples are sandstones of varying grain size. A sample transect at Mt. Olympus extends from the bottom of the Hoh Valley to the apex of the Olympic Peninsula (Mt. Olympus, 2428 m), covering ~2 km of relief (Figs. 4a and b). The Mt. Anderson transect starts in the upper reaches of the Quinault Valley and terminates on the flank of Mt. Anderson covering a total elevation difference of ~1600 m (Figs. 4a and c). The Blue Mountain transect is located in the northern part of the Olympic Peninsula close to Blue Mountain, covering an elevation difference of ~1300 m (Figs. 4a and d). All collected samples were dated with the AHe and ZHe techniques, three of these were dated by AFT, and two were dated by the ZFT technique. Additionally, we dated 13 samples from Michel et al. (2018) by AFT and five by ZFT thermochronometry. This process yielded seven samples with AHe, AFT, ZHe and ZFT cooling ages (Table 2).

Standard mineral separation techniques (sieving, magnetic and gravimetric separation) were used to obtain apatite and zircon separates from crushed rock samples. For AHe and ZHe dating mineral grains were hand-picked and dated in the thermochronometry lab of the University of Tübingen, following the dating protocol of Stübner et al. (2016). The Ft-correction for apatite (Farley, 2002) and zircon (Hourigan et al., 2005) is applied to the measured amount of helium. The (U-Th)/He age equation is solved using the approach of Meesters and Dunai (2005). From each sample, we dated 4–7 apatite grains or 3–6 zircon grains and the results of single-grain analyses can be found in Tables S1 and S2. Our approach for assessing whether a sample is reset or unreset and the procedure for exclusion of outliers is explained in the supplementary material (Section S1.1). For reset samples, we calculate the arithmetic mean age from the accepted single-grain ages, which is reported in Table 2 along with a one standard deviation (1SD) uncertainty.

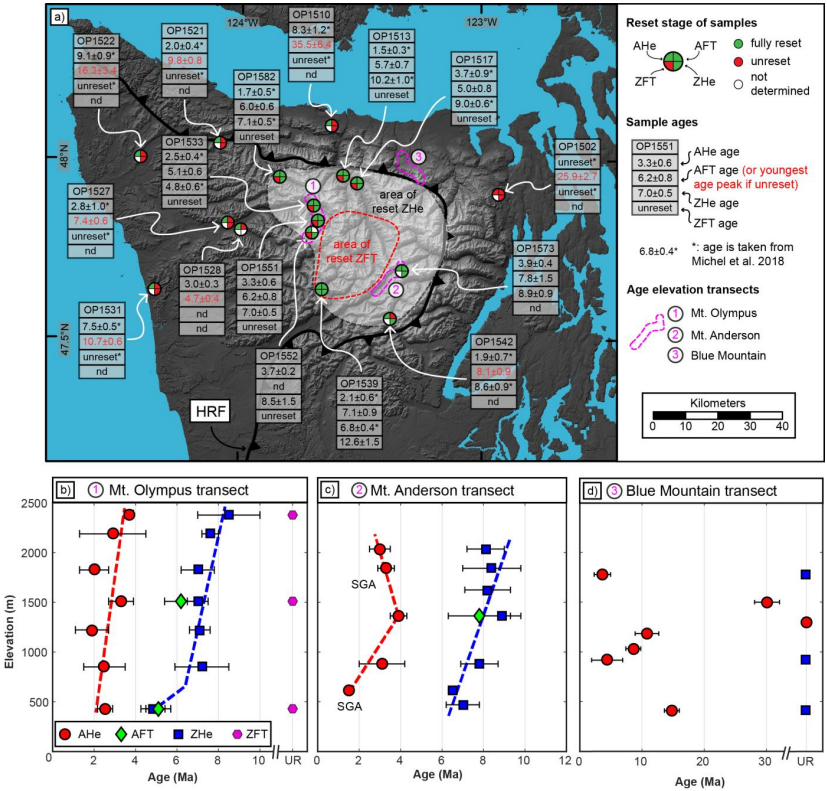

Figure 4: a) Map of samples, for which three to four different thermochronometer systems are available. The pie charts show the reset stage of a particular thermochronometer system for the sample. If AFT ages are unreset, the peak age of the youngest age population is given as sample age (see Table 3 for older populations). Ages denoted with an asterisk are taken from Michel et al. (2018). The Hurricane Ridge Fault (HRF) separates the rocks of the accretionary wedge from the surrounding Coast Range Terrane in the hanging wall. The locations of the three different elevation transects (Mt. Olympus, Mt. Anderson and Blue Mountain) are indicated on the map and the resulting age-elevation plots are shown in b) to d). In b) and c) the dashed coloured lines correspond to possible exhumation rates interpreted from the respective thermochronometer. All uncertainties are 1 standard deviation, SGA = single-grain age.

Fission-track dating of apatite and zircon was performed using the external detector and the ζ-calibration techniques (Hurford, 1990). Details about the treatment of the apatite and zircon mounts in the Tübingen thermochronometry laboratory can be found in Falkowski et al. (2014) and Falkowski and Enkelmann (2016). Table 3 contains the AFT and ZFT sample ages, and explains the procedure for assessing whether a sample is reset or unreset. Data for single-grain ages from fission-track dating of apatite and zircon are reported in Tables S3 and S4.

3.2 Thermo-kinematic modelling: model setup and boundary conditions

To interpret cooling histories recorded by our thermochronometers as exhumation histories, we used a modified version of the thermo-kinematic model Pecube (Braun, 2003), which contains a built-in Monte Carlo approach to resolve temporal variations in exhumation histories (Adams et al., 2015; Thiede and Ehlers, 2013). The model allows exploring possible exhumation histories for a particular sample by varying exhumation rates through time at defined time steps. The accuracy of a particular exhumation rate history is estimated by comparing modelled with observed cooling ages. More age constraints, and hence thermochronometer systems, lead to better resolved, modelled exhumation histories. Therefore, although we report 21 new thermochronometric ages, we only used the seven samples, which have age constraints from AHe, AFT, ZHe, and ZFT in our modelling efforts (OP1513, OP1517, OP1533, OP1539, OP1551, OP1573, OP1582; Table 2).

Thermo-physical parameters chosen for the modelling are typical values reported for the sandstones of the Olympic Mountains (Table 4). We performed a sensitivity analysis in order to find the most suitable time step for our simulations and the results of that analysis can be found in the supplementary material (Section S2). Based on the analysis, a time step interval of 1 Myr seems to be most appropriate to use, given the range of our thermochronometry ages and their respective uncertainties. During further modelling, we initiated the models at 20 Ma and used the time step interval of 1 Myr with a maximum testable exhumation rate of 6 km/Myr. For each sample, we ran 20,000 simulations (each corresponding to a different exhumation history) and assessed the goodness of fit between observed and modelled data for the respective exhumation history, using a reduced χ^2-test. Here, sample ages τ_o were compared with modelled ages τ_m, using the uncertainty of the sample age σ_o for the number (N) of thermochronometer systems available for the respective sample:

$$\chi^2 = \left(\left(\frac{(\tau_o-\tau_m)^2}{\sigma_o^2}\right)_{AHe} + \left(\frac{(\tau_o-\tau_m)^2}{\sigma_o^2}\right)_{AFT} + \left(\frac{(\tau_o-\tau_m)^2}{\sigma_o^2}\right)_{ZHe} + \left(\frac{(\tau_o-\tau_m)^2}{\sigma_o^2}\right)_{ZFT}\right) \cdot \frac{1}{N} \quad (1)$$

If $\chi^2 \leq 2$, a specific model run was accepted as good. The number of accepted exhumation histories is shown in Figure 5 for each sample. From the range of acceptable exhumation rates at each time step (shown as blue shaded areas in Fig. 5), we calculated the mean exhumation rate together with 1 standard deviation for each time step (red/dashed lines and grey areas in Fig. 5). Although the model provides output for the entire model duration of 20 Myr, a meaningful exhumation rate can only be obtained for the time interval between oldest thermochronometric age of a sample and today (shown in Fig. 5).

For our purpose, we focus on exploring temporal variations in exhumation rates and therefore use a 1D model, where each sample is modelled independently from each other. In a 1D model, heat transport and movement of particles is only considered in the vertical dimension within a column of rock, ignoring topography. This mode of modelling was selected because it allowed us to efficiently perform thousands of simulations quickly in order to cover a large range of possible exhumation rates. The high number of exhumation histories accurately predicts our observed cooling ages and allows for a robust statistical assessment of the best-fitting exhumation history. Previous publications addressing exhumation histories in other orogens have also highlighted that 1D models are often sufficient to explain most of the signal recorded in

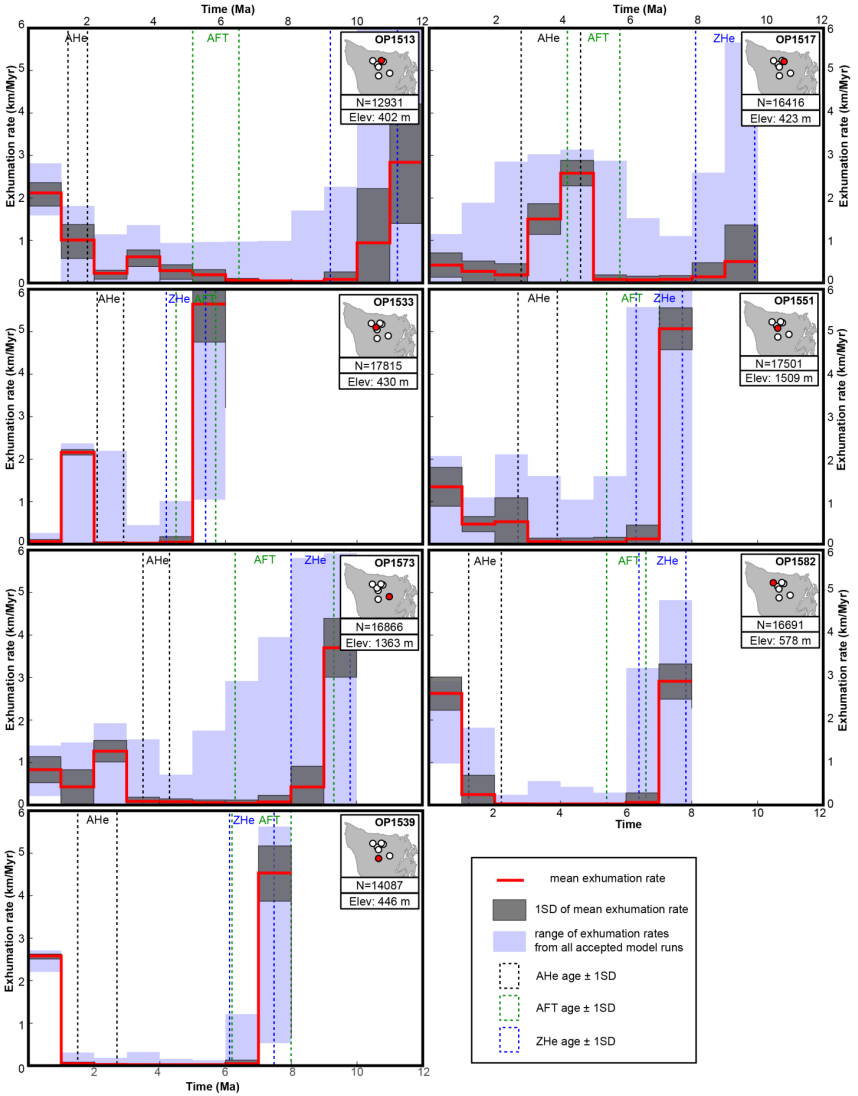

Figure 5: Results from the thermo-kinematic Monte Carlo modelling for the seven considered samples (OP1513, OP1517, OP1533, OP1539, OP1551, OP1573, OP1582). Location of each sample within the Olympic Peninsula is shown, together with the respective elevation (Elev). The entire range of exhumation rates from the number of accepted model runs (N) is outlined by the blue shaded area, from which the mean rate and one standard deviation (1SD) is calculated at each time step. Black, green, and blue stippled boxes outline measured AHe, AFT, and ZHe ages of the samples with 1SD.

thermochronometric systems (e.g., Adams et al., 2015; Thiede and Ehlers, 2013). In the Olympic Mountains, Michel et al. (2018) argued that exhumation histories for the thermochronometer systems considered here can be well explained by vertical velocity paths, too. Because the spatial resolution of our seven considered samples is poor and they are all from the interior part of the mountain range (Fig. 4), we cannot further resolve the exhumation rates outside this area, making a 3D model very difficult to validate. Therefore, we limit our interpretations to the better-resolved exhumation histories from the 1D model and focus on the primary temporal changes, rather than paleotopography, or specific differences in the exhumation rates between samples.

Five of the seven considered samples are from the same elevation range (400–580 m), but two samples are from higher elevations (1360 m and 1500 m, Fig. 5). Large differences in elevation between the samples can impact the direct comparison between them (e.g., it can affect how changes in exhumation rate are recorded from location to location). However, we are not able to correct for this circumstance (by using an age elevation relationship), and therefore try to consider this complication when interpreting our exhumation rate histories from the different samples.

3.3 Methods for estimating flux steady-state

To assess the flux steady-state hypothesis of the Olympic Mountains, we need independent estimates of the material influx and outflux over time. For this, we focus on the time period since 14 Ma, which corresponds to the proposed establishment of flux steady-state (Batt et al., 2001; Brandon et al., 1998). Flux steady-state requires that the material influx into the wedge equates the amount of accreted material, removed from the subducting slab. We assessed the amount of accreted sediment (material influx) with two approaches. First, we calculated the amount of sediment incorporated into the accretionary wedge at the deformation front (Fig. 6a) during the 14 Myr period. Second, we compared this amount of "expected" accreted sediment with the observed amount of sediment residing in the accretionary wedge along two cross sections. The material outflux from the mountain range is estimated using results from thermo-kinematic modelling, by equating modelled exhumation with denudation, which can then be integrated spatially and over the 14 Myr period.

The previous flux steady-state analyses in the Olympic Mountains were performed in two dimensions along a profile crossing the Olympic Peninsula. However, exhumation rates within the Olympic Mountains are known to vary spatially (Brandon et al. 1998; Michel et al., 2018). This suggests that the outflux is spatially variable, depending on the location within the mountain range. Hence, we performed our flux analysis in three dimensions and the resulting geometries are summarized in Figure 6. The influx is calculated along the length of the deformation front, and for the calculation of the outflux we considered almost the entire area of the Olympic Peninsula.

3.3.1 Calculating the accretionary influx

We used a similar approach as Batt et al. (2001) to calculate the accretionary influx, but used a three-dimensional geometry and additionally considered temporal variations of the used variables. Assuming all sediments resting on the subducting oceanic crust are incorporated into the accretionary wedge, the volume of accreted sediment (V_{sed}) can be approximated using the porosity of the sediment η, incoming sediment thickness d, length of the coast l, the duration of subduction t, and the subduction velocity perpendicular to the present-day deformation front u_{per}:

$$V_{sed} = (1 - \eta) \cdot d \cdot l \cdot t \cdot u_{per} \quad (2)$$

A limitation to this approach is the assumption that all sediment resting on the down-going plate is accreted. There is geochemical evidence that, at early stages of subduction at the Cascadia Subduction Zone, sediment has been incorporated into the mantle and been involved in the magmatism of the Cascades Arc (Leeman et al., 2005; Mullen et al., 2017). However, there are no estimates on the amount of sediment transported into the mantle at present, and most sediments seem to be accreted, either at the deformation front or underplated at depth (Calvert et al., 2011).

The variable with the greatest uncertainty in this calculation is the sediment thickness back in time that has now been subducted below the Olympic Mountains. As discussed above (Section 2.3), the present-day sediment thickness of 2.5 km is the product of increased offshore sedimentation during the Quaternary and the pre-Quaternary sediment thickness is difficult to determine. Following the approach described in the supplementary material (Section S3.1), we estimated a pre-Quaternary sediment thickness of 1.5 km. In total, we calculated three different sediment volumes based on different sediment thicknesses (Table 5). Assuming a thickness of 1.5 km and 2.5 km for the 14 Myr period yields a minimum and maximum value for the accreted sediment volume, respectively, representing a sediment volume unaffected by Quaternary sedimentation (1.5 km) and a volume for a likely too high sediment thickness, using the modern thickness (2.5 km). Alternatively, we considered an increase in sediment thickness from 1.5 km to 2.5 km at 2 Ma, which likely yields the geologically most meaningful volume.

The porosity of the sediment stack depends on the thickness and decreases with increasing overburden. According to Yuan et al. (1994), the porosity at depth z of the sediment stack can be approximated by

$$\eta = 0.6 \cdot e^{-z} \quad (3)$$

Using this equation, we calculated mean porosities of 31% and 22% for our sediment thicknesses of 1.5 km and 2.5 km, respectively.

Because the dip direction of the present-day deformation front is 72° (Φ_{def}) and we only considered accretion perpendicular to the deformation front, we corrected the convergence rate (u) by using the convergence angle (Φ) between the Juan de Fuca and the North American plates:

$$u_{per} = u \cdot \frac{\sin(\phi)}{\sin(\phi_{def})} \quad (4)$$

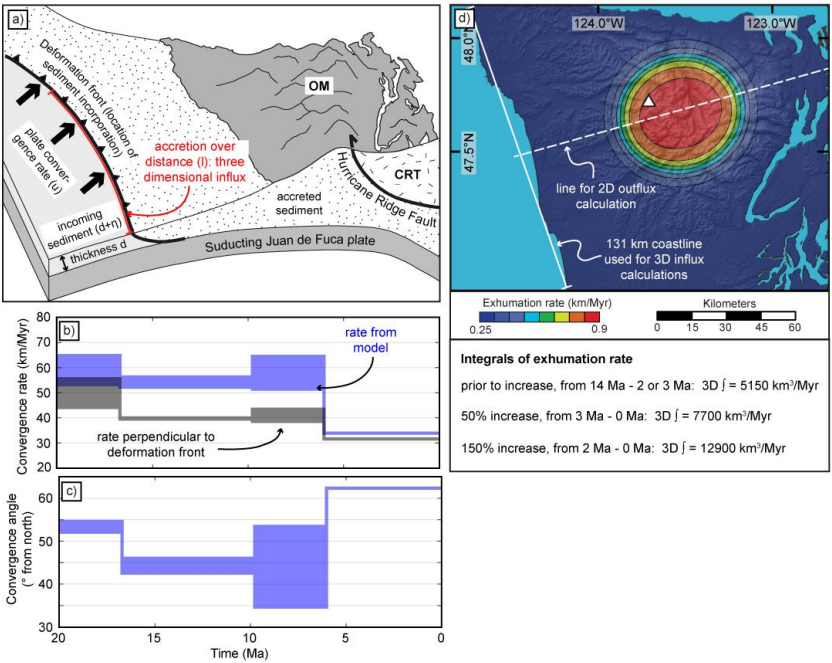

Figure 6: Constraints used for our quantitative accretionary influx and denudational outflux calculations. a) Cartoon illustrating our approach for calculating the accretionary influx. The influx corresponds to the sediment scraped off from the subducting Juan de Fuca Plate, and is governed by the plate convergence rate (u) and the incoming sediment properties (thickness d, porosity η). Because we use a three-dimensional geometry, accretion is considered along a length (l) within a vertical plane. This length corresponds to the length of the coastline indicated in panel (d). OM = Olympic Mountains, CRT = Coast Range Terrane. After Batt and Brandon (2002). b) Temporal evolution of the plate convergence rate used in the calculations, considering only the component perpendicular to the deformation front (black envelope), and the original output (blue envelope) from the plate reconstruction model of Doubrovine and Tarduno (2008). To provide an uncertainty for our calculations, we consider a range of convergence rates (comprising the width of the envelope) for each time step, based on two different rotation models in the model of Doubrovine and Tarduno (2008) (see text for details). c) Temporal evolution of the plate convergence angle (Doubrovine and Tarduno, 2008) used to correct the plate convergence rate in b). d) Exhumation rate pattern from Michel et al. (2018) used for our outflux calculations. The range of displayed rates (0.25–0.9 km/Ma) corresponds to the rates prior to the glacially induced increase in exhumation rates. The outflux is based on the spatial integration of the exhumation rate pattern. Values for the integrals are listed below the plot for the respective increase in exhumation and time. The white dashed line was used for integrating the exhumation rate using a two-dimensional geometry, which is further explained in the appendix.

Both convergence rate and angle are variable over time and, therefore, we capitalized on the plate reconstruction model of Doubrovine and Tarduno (2008) to estimate these parameters over the past 14 Myr. Values shown in Figures 6b and 6c were calculated using the East-West Antarctica plate circuit model from Doubrovine and Tarduno (2008) for two different rotation models (Farallon M1 and M2 in the original publication). This yields a range of possible convergence rates and angles, providing an uncertainty on the calculated sediment volume. The temporal resolution is given by the number of magnetic isochrons used for the plate circuit reconstruction by Doubrovine and Tarduno (2008). From the temporal evolution of the corrected convergence rate (Fig. 6b), we calculated the sediment volume V_{sed} accreted during the 14 Myr period using

Equation 2 and the parameters discussed above. For the length l in Equation 2 we assumed a value of 131 km, which corresponds to the length of the coastline in the area of the exhumation rate pattern (Fig. 6d). The calculated sediment volumes are reported in Table 5.

3.3.2 Sediment volumes along cross-sections

We estimated the actual volume of sediment currently residing in the accretionary wedge along two cross-sections, which are approximately 50 km apart (Profile 1 and 2 in Fig. 7). The lower boundary of the accretionary wedge is the top of the subducting oceanic plate, which is constrained from the Slab 1.0 model (Hayes et al., 2012; McCrory et al., 2012). The upper boundary is defined by the present-day topography/bathymetry (from 10 m- and 500 m-resolution digital elevation models, respectively) and the Hurricane Ridge Fault (HRF). At the surface, the location of the HRF is adopted from a geologic map (Tabor and Cady, 1978) and below the surface we use information provided by a seismic study at depths of 22 km and 34 km (Calvert et al., 2011). The uncertainty related to the position of the HRF (error bars at HRF nodes in Fig. 7) was propagated to estimate an uncertainty for the calculated sediment volumes. Further explanation of this approach is given in the supplementary material (Section S3.2). Because the location of the HRF is not resolved at greater depths, we truncate the area considered for volume calculation at 34-km depth. Finally, the calculated volume is corrected for the porosity of the sediment stack. Davis and Hyndman (1989) use porosities of 4–10% for sediments contained within the accretionary wedge offshore Vancouver Island. Hence, we use an average porosity of 6% in our correction.

3.3.3 Calculating the denudational outflux

In the absence of extensional faults, denudation acts as the prime mechanism for exhumation in the Olympic Mountains. Therefore, exhumation can be equated with denudation and the denudational outflux from the range can be obtained from the spatial and temporal integration of exhumation rates.

The exhumation histories presented in this paper (Fig. 5) are well-suited to resolve temporal variations in exhumation, and hence provide qualitative information about variations in the denudational outflux. The low spatial density of the seven considered samples prohibits a quantitative assessment of the denudational outflux. To overcome this problem, we reverted to the pattern and exhumation rates suggested by Michel et al. (2018), providing good spatial coverage of almost the entire Olympic Peninsula (Fig. 6d). The total amount of exhumation, which is used for calculating the outflux and corresponds to the temporal integration of the exhumation rates, is similar within uncertainty in both data sets. For example, the modelled exhumation rate is sufficient to explain the ZHe age of 10.2 Ma for sample OP1513 in both studies (Michel et al., 2018 and this study).

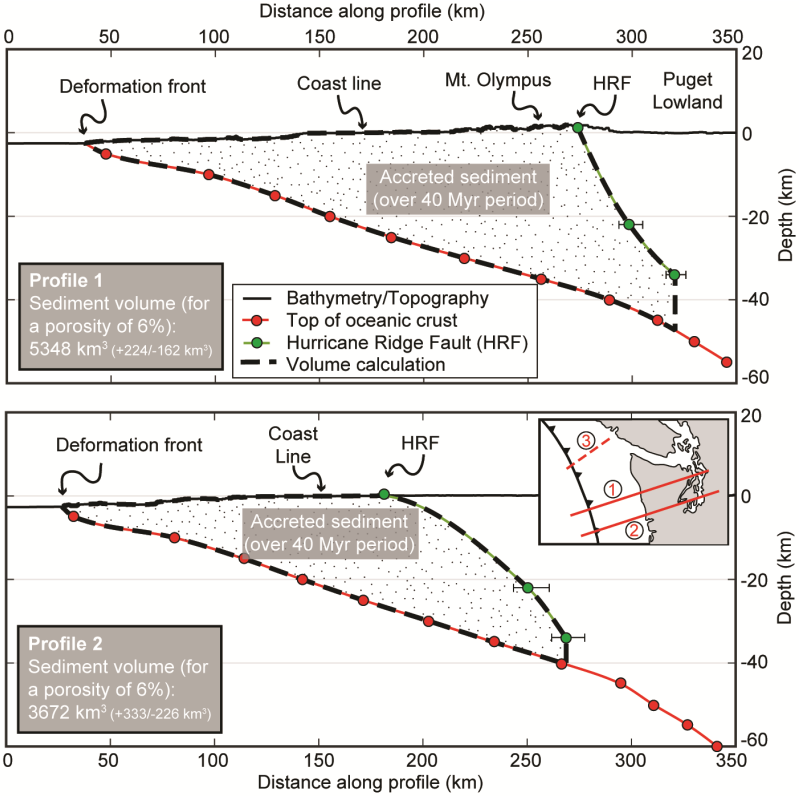

Figure 7: Sediment volumes calculated along two cross-sections spanning the Olympic Peninsula (Profile 1 and 2, vertical exaggeration=2, see inset for location). For explanation of the used procedure see text. The reported uncertainties for the volume are based on the uncertainties in the position of the Hurricane Ridge Fault (indicated with error bars at the respective symbol). Numbers in inset correspond to (1) = position of Profile 1, (2) = position of Profile 2, (3) = position of profile by Davis and Hyndman (1989), referred to in the text.

Our outflux calculations are based on the spatial integration of the entire exhumation rate pattern displayed in Figure 6d, which is then temporally integrated over the 14 Myr period. Additional to a constant exhumation scenario, we also considered an increase in exhumation rates, which is related to an increase in erosion due to Plio-Pleistocene glaciation of the Olympic Mountains (Michel et al., 2018). In Table 5, we report the denuded volumes for the case of constant exhumation rates, and for the two possible increase scenarios suggested by Michel et al. (2018), equating a 50% increase in rates occurring at 3 Ma or a 150% increase in rates occurring at 2 Ma. In order to account for the porosity of the denuded rocks, we corrected the denuded

volumes by a porosity of 6%, the same value we applied in the estimation of the volumes in the sedimentary cross sections

4 Results

4.1 Thermochronometry

Along the Mt. Olympus elevation transect (Fig. 4b), AHe ages (1.9–3.7 Ma) overlap with each other within sample error (except for the uppermost sample). ZHe ages (4.8–8.5 Ma) show a similar behaviour (with the exception of the lowermost sample; Fig. 4b). AFT ages for two samples are 5.1 Ma and 6.2 Ma, and the obtained ZFT ages of this transect are all unreset. Within the Mt. Anderson transect (Fig. 4c), AHe ages (1.5–3.9 Ma) increase with elevation up to an elevation of 1400 m and decrease between 1400 and 2100 m. ZHe ages vary between 6.5–8.9 Ma and one sample at ~1400 m has an AFT age of 7.8 Ma. For the Blue Mountain transect (Fig. 4d), AHe ages (3.6–30.1 Ma, and one unreset sample) do not show a clear correlation with elevation, but, interestingly, the uppermost sample yields the youngest age. ZHe ages of dated samples of this transect are all unreset.

Clear spatial patterns for the multi-dated thermochronometer samples are observable (cf., Fig. 2 and 4). AHe ages are reset (apart from one sample in the north-east of the mountain range) and decrease towards the centre of the mountain range, where very young ages (< 2.5 Ma) can be found. Seven fully reset AFT samples (5.0–7.8 Ma) are confined to the centre of the range (samples OP1513, OP1517, OP1533, OP1539, OP1551, OP1573, OP1582), overlapping with the area of reset ZHe samples. The remaining eight AFT samples are unreset (Table 3 and Fig. 4). Two samples at the north and east coast (OP1502 and OP1510) have the youngest age peaks at 26 Ma (comprising 29% of the dates) and 36 Ma (35%), respectively. Samples from the western part of the mountain range (OP1521, OP1522, OP1527, OP1528, OP1531) have younger age peaks of 5–16 Ma (comprising 20–76% of the dates). Furthermore, the youngest age peak of these samples decreases in age towards the area of fully reset AFT samples.

We also collected samples (OP1527 and OP1528) close to sample locations with the youngest AFT ages of Brandon et al. (1998), which were reported as incompletely reset samples (with youngest peak ages of 3.9 and 2.3 Ma). In the original publication, only a small number of grains were dated (n=31 and n=12). To improve the statistics of these two samples, we merge our single grain ages with those of Brandon et al. (1998) and obtain more robust age distributions (n=134 and n=80; Table 3). The youngest peak ages of the age populations for the two merged samples are 7.4 Ma and 4.7 Ma (2–4 Myr older than age populations reported by Brandon et al., 1998).

ZHe ages constrain an area of reset ages (4.8–10.2 Ma) in the central, high-topography portion of the mountain range (light grey-shaded area in Fig. 4a). Five of these samples have AFT (5.1–7.8 Ma) and ZHe (4.8–8.9 Ma) ages that overlap within sample errors, implying rapid cooling (and hence fast exhumation) through both systems' closure isotherms. AHe ages of these samples are younger (1.7–3.9 Ma) and do not

overlap with AFT ages, indicating that exhumation rates decreased after cooling below the AFT closure isotherm.

Of the seven samples dated with the ZFT method, only sample OP1539 has a fully reset age (12.6 Ma). Together with data from Brandon and Vance (1992) and Stewart and Brandon (2004) this confines reset ZFT samples to a very small area east/southeast of Mt. Olympus, encompassing the headwaters of Elwha and Quinault rivers (area outlined with a red dashed line in Fig. 4a).

4.2 Exhumation histories from thermo-kinematic modelling

Between 13,000–17,800 simulations provide a good fit to the data for each of the seven samples used in the thermo-kinematic modelling (Fig. 5). As expected, the four samples (OP1533, OP1539, OP1551, OP1582; Fig. 5) with overlapping AFT and ZHe ages require fast exhumation rates of >3 km/Myr between 5 Ma and 8 Ma, followed by a reduction to <0.2 km/Myr at 5 Ma or 7 Ma. The reduction of rates for sample OP1573 occurs at ~9 Ma. However, for this sample the AFT age has a larger uncertainty, hence we consider the 5–7 Ma decrease in exhumation rates as a more robust signal. Six of the seven samples (except for sample OP1517) also record an increase in exhumation rates at 2–3 Ma to rates >1 km/Myr.

4.3 Estimating the flux steady-state balance

The calculated volumes of the accretionary influx depend strongly on the incoming sediment thickness (Table 5). With our used three-dimensional geometry (Fig. 6a) volumes vary between ~70,000 km^3 (1.5 km), ~76,000 km^3 (increase from 1.5 km to 2.5 km at 2 Ma) and ~130,000 km^3 (2.5 km). The estimated amount of sediment within the accretionary wedge varies depending on the position within the wedge (Fig. 7). Offshore Vancouver Island, there is 950–1,000 km^3 of sediment within the wedge (Davis and Hyndman, 1989), while on the Olympic Peninsula there is up to ~5,300 km^3 and 3,600 km^3 of sediment within the central and southern parts of the mountain range, respectively. Our estimates of the denudational outflux vary for the different exhumation rate scenarios (Table 5) and volumes range from 68,000 km^3 for constant exhumation rates to 75,000–82,000 km^3 for the exhumation scenario with increasing rates.

5 Discussion

In the following, implications of the above described observations will be discussed in order to assess the flux steady-state balance between accretionary influx and denudational outflux within the Olympic Mountains. To do that, it is pivotal to have an understanding of both temporal and spatial variations in exhumation of the Olympic Mountains. First, we elaborate on results from thermochronometric dating, including the applicability of age-elevation relationships to reconstruct exhumation rates in the Olympic Mountains (Section 5.1). Second, we analyse the general pattern of exhumation based on the spatial distribution of cooling ages (Section 5.2). Third, we link thermochronometric cooling ages with thermo-kinematic modelling, which reveals the temporal evolution of exhumation rates (Section 5.3). Fourth, we discuss the

outcome of our qualitative and quantitative assessment of flux steady-state in the Olympic Mountains (Section 5.4). Finally, in Section 5.5, we elaborate on the limitations of the different approaches.

5.1 Age-elevation relationships

The cooling ages of samples collected from a quasi-vertical elevation profile (e.g., Fitzgerald et al., 1993; Reiners et al., 2003) can be analysed by looking at the age-elevation relationship. Often, the purpose is to determine an apparent exhumation rate by fitting a line through the data points when ages are positively correlated with elevation. However, the prerequisite for this approach is that, over the lateral extent of the sampled transect, no significant gradient in exhumation rates exists. This is not necessarily given in the Olympic Mountains (Michel et al., 2018; see also Fig. 2e) and the new data represent this complication (Figs. 4b–d).

At Mt. Olympus, the AHe and ZHe age-elevation relationships do show a positive correlation, suggesting fast exhumation rates of ~1 km/Myr between ~8 and 2 Ma (Fig. 4b). The Mt. Anderson age-elevation relationship for AHe shows a break in slope at ~1400 m and decreasing AHe ages at higher elevations, and the large uncertainties of the ZHe ages limit an interpretation (Fig. 4c). While such an 'inverse' age-elevation relationship could be caused by a change in relief (Braun, 2002), we interpret it to be a result of the strong spatial variation in exhumation rates along the horizontal distance of the transect (e.g., rates increase from 0.25 km/Myr to 0.9 km/Myr over a horizontal distance of 15–20 km; Fig. 2e). In the case of the Blue Mountain transect (Fig. 4d), we relate the non-correlation of AHe ages and elevation to an incomplete resetting of the AHe system in this area. Here, some samples experienced high enough temperatures to start, or even complete, resetting of the AHe thermochronometric system, causing the observed variability in AHe ages. All ZHe ages from this transect are unreset, corroborating that this part of the Olympic Mountains has not experienced high temperatures, compared to the other transects. Indeed, the Blue Mountain transect belongs to the Coast Range Terrane (CRT), which is at a structurally higher level compared to the accretionary wedge (Fig. 1c). In summary, the age-elevation plots support previous results of strong lateral variations in exhumation and incomplete resetting of thermochronometer systems in the outer part of the mountain range.

5.2 Pattern of exhumation

A well-constrained spatial pattern of exhumation is needed for calculating the denudational outflux. Looking at the spatial distribution of thermochronometric cooling ages provides qualitative information about the pattern of exhumation. In general, the distribution of thermochronometric ages indicates that in the Olympic Mountains the magnitude of exhumation increases from the coast to the centre. As discussed above, areas belonging to the Coast Range Terrane (close to the coast or the Blue Mountain area, where unreset AHe ages can be found, Fig. 2a) correspond to the structurally highest parts within the range (Fig. 1c) and were not sufficiently reheated to reset the AHe system. Assuming a geothermal gradient typical for the Cascadia Subduction Zone of ~20 °C/km (Booth-Rea et al., 2008; Hyndman and Wang, 1993) and an AHe closure

temperature of ~60–70°C, the cumulative exhumation magnitude since onset of exhumation at ~18 Ma cannot have been greater than 2–3 km.

The aerial exposure of the accretionary wedge (the Olympic Structural Complex, Fig. 1c) records exhumation from greater depths. Here, all samples yield reset AHe ages, requiring a minimum exhumation depth of 2–3 km. In the centre of the mountain range (encompassing the headwaters of Hoh, Queets, Quinault and Elwha rivers; Fig. 1b) the area of reset AFT ages approximately overlaps with the area of reset ZHe ages (Fig. 4a), requiring deeper exhumation, compared to the coastal part of the Olympic Structural Complex.

The area east/south-east of Mt. Olympus (corresponding to the area of reset ZFT samples, Fig. 4a) has been exhumed from the greatest depths within the Olympic Mountains. For an average ZFT closure temperature of ~240 °C (Ehlers, 2005) and the above geothermal gradient this corresponds to a maximum exhumation from depths of 10–12 km, confirming previous estimates (Brandon and Calderwood, 1990; Brandon and Vance, 1992).

In summary, the central, high topography part of the mountain range corresponds to the most deeply exhumed part. This corroborates the exhumation rate pattern (Fig. 2e) suggested by Michel et al. (2018), the pattern of denudation rates based on cosmogenic nuclide dating (Adams and Ehlers, 2018), and results from topographic analysis (Adams and Ehlers, 2017), which all suggest that most of the exhumation/denudation occurs at this location. Hence, we use this pattern for the calculation of the denudational outflux.

5.3 Temporal variations in exhumation

Our new thermo-kinematic modelling revealed temporal variations in exhumation rates in the Olympic Mountains (Fig. 5). The decrease of exhumation rates at 5–7 Ma can be readily explained by the reduction in plate convergence rate and the change in convergence direction (Fig. 8). A Pacific-wide reorganization of plate movement at 5.9 Ma has been suggested (Wilson, 2002), and rapid uplift of the Oregon Coast Range at 6–7.5 Ma with a subsequent cessation in uplift has also been attributed to variations in the plate subduction parameters (McNeill et al., 2000). Furthermore, the volcanic record of the Cascadia Subduction Zone shows temporal variations, where the strongest volcanic activity lasted from 25 Ma until 18 Ma (du Bray and John, 2011). A period of volcanic quiescence, lasting from 17 Ma until 8 Ma, was then followed by increased activity, starting at ~7 Ma. A change in the stress field of the Cascadia Subduction Zone occurred at 7 Ma, which likely also affected the composition of the magmatism (Priest, 1990). Therefore, we interpret our observed 5–7 Ma drop in exhumation rates in the Olympic Mountains as a response to changes in the plate tectonic conditions.

In contrast, the increase in exhumation rates at ~2 Ma indicates a response to climatic rather than tectonic changes. As previously suggested by Michel et al. (2018), increased denudation due to the heavy glaciation of the mountain range led to an increase in exhumation rates by 50–150%, starting at 2–3 Ma. Our study corroborates these findings and shows that the observed young AHe ages require a recent increase in exhumation rates from slower rates (<0.2 km/Myr) lasting from ~7 Ma until ~2 Ma. Glaciation of the North

American continent commenced at 2.7 Ma (Haug et al., 2005) and the oldest glacial deposits within the Olympics could be as old as 2 Ma (Easterbrook, 1986), overlapping with our modelled increase in rates at ~2 Ma. Due to the strong spatial variation of the Pleistocene equilibrium line altitude within the Olympic Mountains (Porter, 1964), glacial erosion likely also varied spatially, which could explain the different magnitude in increase of exhumation rates suggested for the different samples. Increased offshore sedimentation related to glacially eroded sediment affected the deformational style of the offshore wedge leading to formation of west-ward dipping thrust faults, which changed at ~1.5 Ma (Adam et al., 2004; Flueh et al., 1998; Gutscher et al., 2001).

Taken together, these observations indicate that temporal variations in exhumation rates within the Olympic Mountains are subject to both changes in the tectonic and climatic conditions (as summarized in Fig. 8). The implication of these variations should be considered for the flux steady-state assessment.

5.4 Flux steady-state in the Olympic Mountains

5.4.1 A qualitative perspective

Several variables that affect both the accretionary influx and the denudational outflux show temporal variations. Exhumation rates decrease at 5–7 Ma and increase at ~2 Ma (Fig. 8) and since exhumation is primarily controlled by denudation, we equate these variations in exhumation with variations in the denudational outflux. According to the model of Doubrovine and Tarduno (2008), the plate subduction velocity decreased at ~6 Ma (see Fig. 6b) after an earlier major decrease at ~25 Ma, causing a decrease in the accretionary influx. Conversely, the accretionary influx increased significantly during the Quaternary due to high offshore sedimentation rates and increased sediment thicknesses as a result of effective glacial erosion on the North American continent (i.e., 50–70 % of the present-day sediment thickness on the subducting Juan de Fuca Plate consists of Quaternary-aged sediments, Table 1 and Fig. 3).

It follows that, qualitatively, both influx and outflux vary through time and are heavily influenced by the Plio-Pleistocene glaciation, which increased denudation rates and offshore sedimentation rates. However, we cannot quantitatively constrain whether variations in the influx and outflux on these short timescales (2–3 Myr) balance each other (and the system would still be in a flux steady-state). Interestingly, measured denudation rates based on cosmogenic nuclide dating (temporally integrating over the Holocene) suggest that modern denudation rates have not been significantly influenced by Plio-Pleistocene glaciation, but are mostly driven by tectonic rock uplift (Adams and Ehlers, 2018). The Holocene accretionary influx, however, is still affected by the increased sediment thickness since the onset of glaciation. Hence, the current accretionary influx seems to exceed the denudational outflux in the Olympic Mountains.

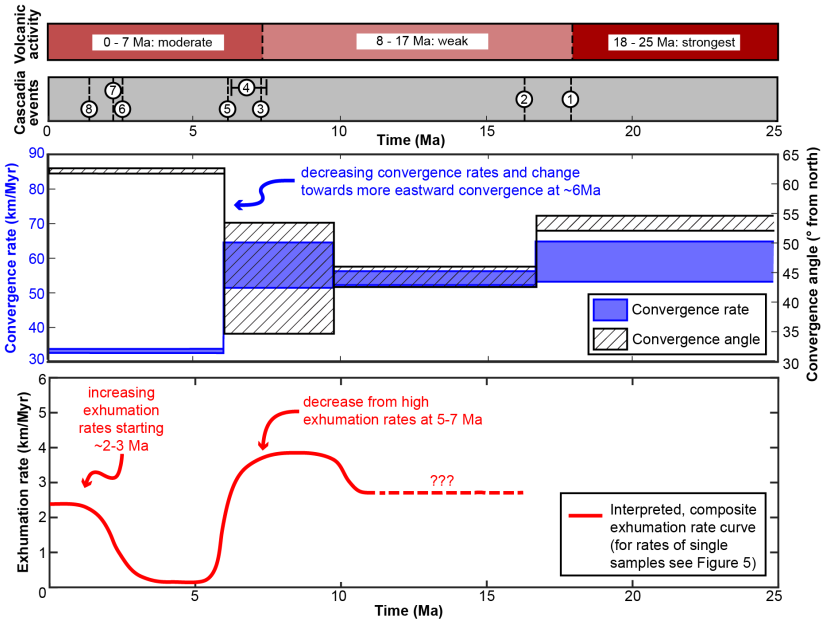

Figure 8: Summary of volcanic activity, tectonic and climatic events, and convergence rate and angle at the Cascadia Subduction Zone in comparison with our interpreted exhumation rates for the past 25 Myr. Exhumation rates are limited to the time interval covered by our thermochronometric ages (0–11 Ma). The curve depicts the interpreted evolution of exhumation rates, based on the modelling results shown in Figure 5 (see text for details). Volcanic activity after du Bray and John (2011). Tectonic and climatic events are (1) start of exhumation of the Olympic Mountains (Brandon et al., 1998), (2) onset of uplift of the Oregon Coast Range (McNeill et al., 2000), (3) rotation in stress field (Priest, 1990), (4) faster uplift in Oregon Coast Range (McNeill et al., 2000), (5) Pacific-wide plate reorganization (Wilson, 2002), (6) onset of North American glaciation (Haug et al., 2005), (7) onset of glaciation within the Olympic Mountains (Easterbrook, 1986), (8) change in the deformational style of the offshore accretionary wedge (Flueh et al., 1998). Convergence rate and angle from Doubrovine and Tarduno (2008).

5.4.2 A quantitative perspective

Here, we discuss the quantitative assessment of influx and outflux for the last 14 Myr (Table 5), the time since when the Olympic Mountains are supposed to be in flux steady-state (Batt et al., 2001; Brandon et al., 1998). In our used geometry (Figs. 6a and d), we calculate the accretionary influx over a distance along the deformation front and the spatial exhumation rate pattern is integrated to infer the denudational outflux (Fig. 6d). Assuming an increase in sediment thickness at 2 Ma yields an accretionary volume (~76,000 km^3) similar to the denudational outflux (75,000–82,000 km^3). Assuming a maximum sediment thickness of 2.5 km for the 14 Myr period yields an accretionary volume of ~130,000 km^3, which cannot be reconciled with our denudational outflux (Table 5). These results indicate that if temporal variations in the sediment thickness and denudation are considered, a reasonable balance between influx and outflux is attained. The previous flux steady-state analysis (Batt et al., 2001) was performed in two dimensions and used a constant sediment

thickness of 2.0 km. We also performed an influx and outflux calculation using a two-dimensional geometry to tie in with previous work (see appendix below). However, the results from the two-dimensional analysis suggest that for an area with spatially variable exhumation rates like the Olympic Mountains a three-dimensional geometry yields a more accurate prediction of influx and outflux.

Sediment volumes integrated along the cross-sections (Fig. 7) also provide an interesting perspective on the accretionary influx in the Olympic Mountains. These volumes are not directly comparable with the influx/outflux volumes discussed above (calculated from 14–0 Ma), because the sediment contained within the cross-sections (Fig. 7) records accretion since the ~40 Ma onset of subduction (Brandon et al., 1998; du Bray and John, 2011). Furthermore, these estimates are minimum volumes, because the amount of material that has been eroded during the 40 Myr period is not considered. Nevertheless, the amount of sediment currently residing in the accretionary wedge is variable along strike of the subduction zone (1000–5400 km^3) and is highest below the central part of the Olympic Mountains (Fig. 7). This requires that parameters affecting the accretionary influx (like plate subduction velocity or sediment thickness) are highly variable over short distances (Profile 1 and Profile 2 are only 50 km apart; Fig. 7). Another explanation might be that considering accretion only perpendicular to the deformation is an oversimplification and another velocity component also contributes to material transport (see Section 5.5). This is in accordance with the conclusion drawn above that considering flux steady-state in a two-dimensional scenario (as it is done with the cross-sections) leads to ambiguous results.

In summary, the assessment of flux steady-state in the Olympic Mountains is non-trivial and several scenarios are possible. From a qualitative viewpoint, flux steady-state is probably not achieved on short timescales (few Myr), because the thickness of incoming sediment, plate subduction velocity, and exhumation rates show strong temporal variations on timescales of 2–3 Myr. From a quantitative viewpoint, influx and outflux volumes equate each other over longer timescales (i.e., 14 Myr), if influx and outflux are considered in three dimensions.

5.5 Restrictions and limitations of our approaches

In the sections above, we discussed exhumation in the Olympic Mountains and the results from our flux calculations. In the following section, we want to elaborate on possible restrictions or limitations in our approaches.

With our 1D modelling, we revealed strong temporal variations in exhumation rates (Fig. 5) related both to variations in tectonic and climatic conditions (Fig. 8). However, two of our modelled samples (OP1513 and OP1517) do not display the decrease in exhumation rates at ~5–7 Ma. These are from the Elwha valley (Fig. 4), in contrast to the five samples displaying the decrease, which are located in the western part of the mountain range. This suggests that the response of the orogenic wedge to a variation in the tectonic conditions affects only parts of the wedge and might be controlled by discrete structures. Further sampling and thermochronometric dating would be required to localize possible faults. Furthermore, this places a limitation

on the application of a refined 3D model, because it requires to constrain parameters such as fault location or displacement on these faults. Besides the importance of single structures, the general pattern of deformation in the Olympic Mountains should still be viewed as controlled by the geometry of the subducted plate (Adams and Ehlers, 2017; Adams and Ehlers 2018; Brandon and Calderwood, 1990; Michel et al., 2018).

Regarding our flux analysis, we based our calculations on the volume of accreted sediment within a certain time (governed by the sediment thickness and the plate convergence rate) and the amount of denuded material (governed by the exhumation rates). As we mentioned in Section 3.3.1, a variable with great uncertainty is the sediment thickness over time, which has now been subducted below the Olympic Mountains. In the supplementary material (Section S3.1) we outlined our approach for assessing the pre-Quaternary sediment thickness, which is used in our calculations. Although the reported 1.5 km sediment thickness seems to be a plausible value, we note that this value is afflicted with uncertainties and might have been higher. Nonetheless, our proposed balance between influx and outflux is still tenable, if the pre-Quaternary sediment thickness deviated from the assumed 1.5 km. I.e., we suggested an influx volume of 75–78 x 10^3 km^3 and calculated outflux volumes between 75 x 10^3 km^3 and 82 x 10^3 km^3 (Table 5), so even an additional influx volume due to a thicker, unnoticed sediment thickness could be balanced with our calculated outflux volumes. Another simplification in our calculation is the assumption of a spatially uniform sediment thickness over the considered length. Figure 3 shows that the sediment thickness along the deformation front is variable and is highest in the Nitinat and Astoria fans. However, an attempt to reconstruct along-strike variations in sediment thickness over time is challenging and would introduce further uncertainties, and thus, we assume an average, constant thickness.

During our influx calculations, we did not distinguish between different modes of accretion, such as frontal accretion or underplating. Batt et al. (2001) concluded that most accretion occurs at the front of the wedge. However, a recent seismic study showed that sedimentary underplating is taking place below the Olympic Mountains (Calvert et al., 2011). For our approach, the mechanism of accretion does not matter, because we are only interested in whether mass is balanced over the entire wedge and not at a specific point. As indicated, this is a limitation of our approach and might lead to an overestimation of the actual influx volume, because we do not account for the amount of sediment transported towards the mantle.

Flux steady-state implies that the outflux from and influx into a mountain range balance each other. An inherent assumption is often that the material removed from a mountain range (the outflux) again enters the mountain range via the influx, which consists of the denuded material from the same source. So in case of an accretionary wedge, this implies that sediment is recycled and the system behaves as a closed system. As we described in Section 2.3 of the manuscript, the sediment currently entering the accretionary wedge of the Cascadia Subduction Zone is a mixture of sediment from different source regions (e.g., Olympic Mountains, Vancouver Island, Canadian Cordillera and in case of the Astoria fan the interior USA, Fig. 3). With the increased detrital input from the Cordilleran Ice Sheet from outside the Olympic Mountains, this effect became particularly pronounced since the onset of Plio-Pleistocene glaciation. Hence, our influx/outflux calculations for

the Olympic Mountains do not represent a closed system, where the influx into the Olympic Mountains is solely controlled by the outflux out of the system. However, our calculations indicate that on long timescales (i.e., over 14 Myr) flux steady-state is attained, which might seem surprising given that the sediment thickness is governed by contributions from different source regions. We suspect that processes during sediment deposition, like redistribution by turbidity currents and redeposition in more proximal parts of the Juan de Fuca Plate, play an important role in the final sediment budget. As a consequence, the amount of sediment denuded from the Olympic Peninsula in a given time period (the outflux) is dispersed as it enters the ocean, so that for the same time period only a fraction of the sediment thickness (governing the influx) is composed of material originating from the Olympic Peninsula.

Variations in the geometry or extent of the accretionary wedge were also not included in our flux analysis. Since onset of subduction at the Cascadia Subduction Zone with the present geometry at ~40 Ma, the wedge must have grown over time in order to attain its present shape. As soon as a balance between accretion and erosion is established, the shape of an orogenic wedge remains constant, controlled by its critical taper (e.g., Davis et al., 1983). However, Adam et al. (2004) showed that the Cascadia accretionary wedge responded to increased offshore sedimentation during the Quaternary by development of west-ward dipping thrust faults, shifting the deformation front further seawards thereby increasing the extent and volume of the wedge. An important parameter contributing to the shape of the accretionary wedge is the angle of subduction, which is flatter below the Olympic Mountains (compared to areas north or south) due to the bend in the subducted slab (Fig. 1a). A reason hypothesized for bending the subducting slab is extension in the Basin and Range Province, starting in the middle Miocene (Brandon and Calderwood, 1990). All these points indicate that parameters controlling the size and volume of the accretionary wedge are both spatially and temporally variable. However, we cannot account for all of these circumstances in our flux calculations, because they are difficult to constrain quantitatively from available observations. Furthermore, because we based our flux calculations only on volumes of accreted or eroded material over the 14 Myr period, a comparison between these two volumes itself should not depend on a change in the shape or extent of the accretionary wedge.

As we pointed out in Section 5.4.2, flux steady-state is obtained by using a three-dimensional geometry. However, we only considered the deformation front-perpendicular velocity component for our influx calculations. The different sediment volumes contained in the reported cross-sections (Fig. 7) could indicate that on long timescales additional velocity components must be considered. We can only speculate that margin-parallel transport, which is a contentious topic at the Cascadia Subduction Zone (e.g., Batt et al., 2001; McCrory, 1996; Wang, 1996), also contributes to the accretionary influx. Present-day GPS velocities corroborate this hypothesis, indicating northward movement of coastal areas south of the Olympic Mountains (e.g., McCaffrey et al., 2013; Wells and McCaffrey, 2013).

To summarize, several parameters like the location of faults within the orogenic wedge, the sediment source region, the temporal evolution of the wedge geometry or margin parallel transport are difficult to constrain from current observations. Although we emphasized that not all of these parameters affect our flux

analysis, further knowledge of these will refine the current understanding of steady-state in the Olympic Mountains.

6 Conclusion

Our new data set of multi-dated thermochronometer bedrock samples together with thermo-kinematic modelling suggests that several mechanisms contribute to the evolution of the Olympic Mountains. Modelling of the observed AHe, AFT, ZHe, and ZFT ages shows that variations in both tectonic and climatic conditions result in temporal variations of exhumation rates. We revealed a hitherto unnoticed response of exhumation to the tectonic signal (a reduction in plate convergence rate causing a drop in exhumation rates), which can also be observed in other parts of the Cascadia Subduction Zone. Plio-Pleistocene glaciation of the Olympic Mountains led to increased denudation, resulting in increased exhumation rates.

Our approach of assessing flux steady-state in the Olympic Mountains by estimating the material influx and outflux independently from each other is promising, but yields ambiguous results. The observed temporal variations in exhumation rate require a variation in the denudational outflux. Likewise, the accretionary influx is also temporally variable, because the plate subduction velocity and incoming sediment thickness are variable through time. Qualitatively, this suggests that flux steady-state is perturbed on short timescales by variations in the tectonic or climatic conditions. Our quantitative calculations of the influx and outflux show flux steady-state may be achievable over long timescales (i.e., 14 Myr). Contrary to a previous flux steady-state analysis in the Olympic Mountains, our calculated influx and outflux volumes only balance each other, if a three-dimensional geometry is considered.

This study demonstrates the timescale (10^5–10^6 vs. 10^7 Myr) and spatial dependence of a steady-state assessment in an orogenic wedge. Furthermore, the tremendous effect of the Plio-Pleistocene glaciation is demonstrated, which is capable of significantly perturbing the development of an orogenic wedge, where both the influx and outflux are affected. Because we obtain flux steady-state for a three-dimensional geometry (but only consider velocities parallel to the subduction direction), more work is needed to constrain the role of material transport parallel to the deformation front. Such studies will lead to a better understanding of the development of orogenic wedges situated in a complex tectonic setting like the Olympic Mountains.

Appendix: Two-dimensional flux steady-state analysis

In Section 3.3 we performed our flux analysis in three dimensions due to the spatially variable exhumation rates (Fig. 6d). In the following, we also calculate the influx and outflux using a two-dimensional geometry, so that our calculations can be compared to those from Batt et al. (2001). Here, the accretionary influx occurs at a single location at the deformation front, and the sediment volume (V_{sed2D}) is obtained by using a slightly modified version of Equation 2:

$$V_{sed2D} = (1 - \eta) \cdot d \cdot t \cdot u_{per} \quad (5)$$

Variables are porosity (η), incoming sediment thickness (d), time (t) and the deformation front perpendicular convergence rate (u_{per}). The further procedure is identical to the procedure outlined in Section 3.3.1. Although the volumes obtained with this equation have a unit of km^2, no great uncertainty is introduced if the analysis is expanded over a width of 1 km, which then yields values of km^3 and "true" volumes. Calculated volumes are 520–540 km^3 (for a 1.5 km thick sediment stack), 980–1020 km^3 (for a 2.5 km thick sediment stack), and 580–600 km^3 (for the increase in sediment thickness from 1.5 km to 2.5 km at 2 Ma).

The outflux calculations are not based on the integration of the entire exhumation pattern in Figure 6d, but rates are only integrated along the white line in Figure 6. These integrals yield values of 68 km^2/Myr (constant rate), 103 km^2/Myr (50% increase in rate) and 171 km^2/Myr (150% increase in rate). After also integrating temporally (and assuming a width of 1 km, in order to get units of km^3, see above), the respective volumes of two-dimensional outflux are 900 km^3, 1000 km^3, and 1090 km^3.

A comparison of two-dimensional influx and outflux shows that the accretionary influx (~1000 km^3) only balances the denudational outflux (1060–1160 km^3), if an incoming sediment thickness of 2.5 km is assumed for the 14 Myr period. Hence, flux steady-state can only be obtained using a two-dimensional geometry, if an unrealistically high sediment thickness is assumed. Contrary to that, the three-dimensional geometry yields flux steady-state using a more reasonable sediment thickness (an increase in sediment thickness from 1.5 km to 2.5 km at 2 Ma). This indicates that assuming a two-dimensional geometry during the flux steady-state analysis is an oversimplification.

Acknowledgements

This work was funded by a European Research Council (ERC) Consolidator Grant (615703) to Todd Ehlers. During field work, we had invaluable help and assistance by Holger Sprengel, William Baccus, Jerry Freilich, Roger Hofmann, and the Olympic National Park rangers. We acknowledge Matthias Nettesheim for sharing the code used for evaluation of the tectonic plate reconstruction model, and the help of Willi Kappler during Pecube modelling. We thank Associate Editor David Lundbek Egholm for editorial handling of the manuscript. The comments by Phillipe Steer and one anonymous referee helped to improve and clarify this manuscript.

References

Adam, J., Klaeschen, D., Kukowski, N. and Flueh, E.: Upward delamination of Cascadia Basin sediment infill with landward frontal accretion thrusting caused by rapid glacial age material flux, Tectonics, 23(3), doi:10.1029/2002TC001475, 2004.

Adams, B. A. and Ehlers, T. A.: Deciphering topographic signals of glaciation and rock uplift in an active orogen: a case study from the Olympic Mountains, USA: Signals of glaciation and rock uplift in the Olympic Mountains, Earth Surface Processes and Landforms, 42(11), 1680–1692, doi:10.1002/esp.4120, 2017.

Adams, B. A. and Ehlers, T. A.: Tectonic controls of Holocene erosion in a glaciated orogen, Earth Surf. Dynam., 6(3), 595–610, doi:10.5194/esurf-6-595-2018, 2018.

Adams, B. A., Hodges, K. V., Whipple, K. X., Ehlers, T. A., van Soest, M. C. and Wartho, J.: Constraints on the tectonic and landscape evolution of the Bhutan Himalaya from thermochronometry: Late Cenozoic Evolution of Bhutan, Tectonics, 34(6), 1329–1347, doi:10.1002/2015TC003853, 2015.

Batt, G. E., Brandon, M. T., Farley, K. A. and Roden-Tice, M.: Tectonic synthesis of the Olympic Mountains segment of the Cascadia wedge, using two-dimensional thermal and kinematic modeling of thermochronological ages, J. Geophys. Res., 106(B11), 26731–26746, doi:10.1029/2001JB000288, 2001.

Batt, G. E. and Brandon, M. T.: Lateral thinking: 2-D interpretation of thermochronology in convergent orogenic settings, Tectonophysics, 349(1), 185–201, doi:10.1016/S0040-1951(02)00053-7, 2002.

Bendick, R. and Ehlers, T. A.: Extreme localized exhumation at syntaxes initiated by subduction geometry, Geophys. Res. Lett., 41(16), 2014GL061026, doi:10/f6kfqz, 2014.

Bernard, T., Steer, P., Gallagher, K., Szulc, A., Whitham, A. and Johnson, C.: Evidence for Eocene–Oligocene glaciation in the landscape of the East Greenland margin, Geology, 44(11), 895–898, 2016

Berger, A. L., Gulick, S. P. S., Spotila, J. A., Upton, P., Jaeger, J. M., Chapman, J. B., Worthington, L. A., Pavlis, T. L., Ridgway, K. D., Willems, B. A. and McAleer, R. J.: Quaternary tectonic response to intensified glacial erosion in an orogenic wedge, Nature Geoscience, 1(11), 793–799, doi:10.1038/ngeo334, 2008.

Booth, D. B., Troost, K. G., Clague, J. J. and Waitt, R. B.: The Cordilleran Ice Sheet, in Developments in Quaternary Sciences, vol. 1, pp. 17–43, Elsevier, 2003.

Booth-Rea, G., Klaeschen, D., Grevemeyer, I. and Reston, T.: Heterogeneous deformation in the Cascadia convergent margin and its relation to thermal gradient (Washington, NW USA), Tectonics, 27(4), doi:10.1029/2007TC002209, 2008.

Brandon, M. T.: Decomposition of fission-track grain-age distributions, American Journal of Science, 292(8), 535–564, 1992.

Brandon, M. T.: Probability density plot for fission-track grain-age sample, Radiation Measurements, 26, 663–676, 1996.

Brandon, M. T. and Calderwood, A. R.: High-pressure metamorphism and uplift of the Olympic subduction complex, Geology, 18(12), 1252, doi:10.1130/0091-7613(1990)018<1252:HPMAUO>2.3.CO;2, 1990.

Brandon, M. T. and Vance, J. A.: Tectonic evolution of the Cenozoic Olympic subduction complex, Washington State, as deduced from fission track ages for detrital zircons, American Journal of Science, 292(8), 565–636, doi:10.2475/ajs.292.8.565, 1992.

Brandon, M. T., Roden-Tice, M. K. and Garver, J. I.: Late Cenozoic exhumation of the Cascadia accretionary wedge in the Olympic Mountains, northwest Washington State, Geological Society of America Bulletin, 110(8), 985–1009, doi:10.1130/0016-7606(1998)110<0985:LCEOTC>2.3.CO;2, 1998.

Braun, J.: Estimating exhumation rate and relief evolution by spectral analysis of age–elevation datasets, Terra Nova, 14(3), 210–214, 2002.

Braun, J.: Pecube: a new finite-element code to solve the 3D heat transport equation including the effects of a time-varying, finite amplitude surface topography, Computers & Geosciences, 29(6), 787–794, doi:10.1016/S0098-3004(03)00052-9, 2003.

du Bray, E. A. and John, D. A.: Petrologic, tectonic, and metallogenic evolution of the Ancestral Cascades magmatic arc, Washington, Oregon, and northern California, Geosphere, 7(5), 1102–1133, 2011.

Calvert, A. J., Preston, L. A. and Farahbod, A. M.: Sedimentary underplating at the Cascadia mantle-wedge corner revealed by seismic imaging, Nature Geosci., 4(8), 545–548, doi:10.1038/ngeo1195, 2011.

Carpentier, M., Weis, D. and Chauvel, C.: Fractionation of Sr and Hf isotopes by mineral sorting in Cascadia Basin terrigenous sediments, Chemical Geology, 382, 67–82, doi:10.1016/j.chemgeo.2014.05.028, 2014.

Clague, J. J. and James, T. S.: History and isostatic effects of the last ice sheet in southern British Columbia, Quaternary Science Reviews, 21(1), 71–87, 2002.

Clowes, R. M., Brandon, M. T., Green, A. G., Yorath, C. J., Brown, A. S., Kanasewich, E. R. and Spencer, C.: LITHOPROBE-southern Vancouver Island: Cenozoic subduction complex imaged by deep seismic reflections, Canadian Journal of Earth Sciences, 24(1), 31–51, 1987.

Davis, D., Suppe, J. and Dahlen, F. A.: Mechanics of fold-and-thrust belts and accretionary wedges, J. Geophys. Res., 88(B2), 1153–1172, 1983.

Davis, E. E. and Hyndman, R. D.: Accretion and recent deformation of sediments along the northern Cascadia subduction zone, Geological Society of America Bulletin, 101(11), 1465–1480, 1989.

Doubrovine, P. V. and Tarduno, J. A.: A revised kinematic model for the relative motion between Pacific oceanic plates and North America since the Late Cretaceous, Journal of Geophysical Research, 113(B12), doi:10.1029/2008JB005585, 2008.

Easterbrook, D. J.: Stratigraphy and chronology of quaternary deposits of the Puget Lowland and Olympic Mountains of Washington and the Cascade Mountains of Washington and Oregon, Quaternary Science Reviews, 5, 145–159, doi:10.1016/0277-3791(86)90180-0, 1986.

Eddy, M. P., Clark, K. P. and Polenz, M.: Age and volcanic stratigraphy of the Eocene Siletzia oceanic plateau in Washington and on Vancouver Island, Lithosphere, 9(4), 652–664, doi:10.1130/L650.1, 2017.

Ehlers, T. A.: Computational Tools for Low-Temperature Thermochronometer Interpretation, Reviews in Mineralogy and Geochemistry, 58(1), 589–622, doi:10.2138/rmg.2005.58.22, 2005.

Ehlers, T. A., Farley, K. A., Rusmore, M. E. and Woodsworth, G. J.: Apatite (U-Th)/He signal of large-magnitude accelerated glacial erosion, southwest British Columbia, Geology, 34(9), 765, doi:10.1130/G22507.1, 2006.

Falkowski, S. and Enkelmann, E.: Upper-crustal cooling of the Wrangellia composite terrane in the northern St. Elias Mountains, western Canada, Lithosphere, 8(4), 359–378, doi:10.1130/L508.1, 2016.

Falkowski, S., Enkelmann, E. and Ehlers, T. A.: Constraining the area of rapid and deep-seated exhumation at the St. Elias syntaxis, Southeast Alaska, with detrital zircon fission-track analysis, Tectonics, 33(5), 597–616, doi:10.1002/2013TC003408, 2014.

Farley, K. A.: (U-Th)/He Dating: Techniques, Calibrations, and Applications, Reviews in Mineralogy and Geochemistry, 47(1), 819–844, doi:10.2138/rmg.2002.47.18, 2002.

Fitzgerald, P. G., Stump, E. and Redfield, T. F.: Late Cenozoic uplift of Denali and its relation to relative plate motion and fault morphology, Science, 259, 497–497, 1993.

Flueh, E. R., Fisher, M. A., Bialas, J., Childs, J. R., Klaeschen, D., Kukowski, N., Parsons, T., Scholl, D. W., ten Brink, U. and Tréhu, A. M.: New seismic images of the Cascadia subduction zone from cruise SO108—ORWELL, Tectonophysics, 293(1), 69–84, 1998.

Galbraith, R. F.: Statistics for fission track analysis, CRC Press., 2005.

Gallagher, K., Brown, R. and Johnson, C.: FISSION TRACK ANALYSIS AND ITS APPLICATIONS TO GEOLOGICAL PROBLEMS, Annu. Rev. Earth Planet. Sci., 26(1), 519–572, doi:10/cj5xp8, 1998.

Glotzbach, C., van der Beek, P., Carcaillet, J. and Delunel, R.: Deciphering the driving forces of erosion rates on millennial to million-year timescales in glacially impacted landscapes: An example from the Western Alps, Journal of Geophysical Research: Earth Surface, 118(3), 1491–1515, doi:10.1002/jgrf.20107, 2013.

Gulick, S. P. S., Jaeger, J. M., Mix, A. C., Asahi, H., Bahlburg, H., Belanger, C. L., Berbel, G. B. B., Childress, L., Cowan, E., Drab, L., Forwick, M., Fukumura, A., Ge, S., Gupta, S., Kioka, A., Konno, S., LeVay, L. J., März, C., Matsuzaki, K. M., McClymont, E. L., Moy, C., Müller, J., Nakamura, A., Ojima, T., Ribeiro, F. R., Ridgway, K. D., Romero, O. E., Slagle, A. L., Stoner, J. S., St-Onge, G., Suto, I., Walczak, M. D., Worthington, L. L., Bailey, I., Enkelmann, E., Reece, R. and Swartz, J. M.: Mid-Pleistocene climate transition drives net mass loss from rapidly uplifting St. Elias Mountains, Alaska, Proceedings of the National Academy of Sciences, 112(49), 15042–15047, doi:10.1073/pnas.1512549112, 2015.

Gutscher, M.-A., Klaeschen, D., Flueh, E. and Malavieille, J.: Non-Coulomb wedges, wrong-way thrusting, and natural hazards in Cascadia, Geology, 29(5), 379–382, 2001.

Han, S., Carbotte, S. M., Canales, J. P., Nedimović, M. R., Carton, H., Gibson, J. C. and Horning, G. W.: Seismic reflection imaging of the Juan de Fuca plate from ridge to trench: New constraints on the distribution of faulting and evolution of the crust prior to subduction, Journal of Geophysical Research: Solid Earth, 121(3), 1849–1872, doi:10.1002/2015JB012416, 2016.

Haug, G. H., Ganopolski, A., Sigman, D. M., Rosell-Mele, A. and others: North Pacific seasonality and the glaciation of North America 2.7 million years ago, Nature, 433(7028), 821, 2005.

Hayes, G. P., Wald, D. J. and Johnson, R. L.: Slab1.0: A three-dimensional model of global subduction zone geometries:, Journal of Geophysical Research: Solid Earth, 117(B1), doi:10.1029/2011JB008524, 2012.

Herman, F. and Brandon, M.: Mid-latitude glacial erosion hotspot related to equatorial shifts in southern Westerlies, Geology, 43(11), 987–990, doi:10.1130/G37008.1, 2015.

Herman, F., Seward, D., Valla, P. G., Carter, A., Kohn, B., Willett, S. D. and Ehlers, T. A.: Worldwide acceleration of mountain erosion under a cooling climate, Nature, 504(7480), 423–426, doi:10.1038/nature12877, 2013.

Hourigan, J. K., Reiners, P. W. and Brandon, M. T.: U-Th zonation-dependent alpha-ejection in (U-Th)/He chronometry, Geochimica et Cosmochimica Acta, 69(13), 3349–3365, doi:10.1016/j.gca.2005.01.024, 2005.

Hurford, A. J.: Standardization of fission track dating calibration: Recommendation by the Fission Track Working Group of the I.U.G.S. Subcommission on Geochronology, Chemical Geology, 80, 171–178, 1990.

Hyndman, R. D. and Wang, K.: Thermal constraints on the zone of major thrust earthquake failure: The Cascadia Subduction Zone, Journal of Geophysical Research: Solid Earth, 98(B2), 2039–2060, doi:10.1029/92JB02279, 1993.

Hyndman, R. D., Yorath, C. J., Clowes, R. M. and Davis, E. E.: The northern Cascadia subduction zone at Vancouver Island: Seismic structure and tectonic history, Canadian Journal of Earth Sciences, 27(3), 313–329, 1990.

Kiyokawa, S. and Yokoyama, K.: Provenance of turbidite sands from IODP EXP 1301 in the northwestern Cascadia Basin, western North America, Marine Geology, 260(1–4), 19–29, doi:10.1016/j.margeo.2009.01.003, 2009.

Knudson, K. P. and Hendy, I. L.: Climatic influences on sediment deposition and turbidite frequency in the Nitinat Fan, British Columbia, Marine Geology, 262(1–4), 29–38, doi:10.1016/j.margeo.2009.03.002, 2009.

Kulm, L. V. D., von Huene, R., Duncan, J. R., Ingle, J. C., Kling, S. A., Musich, L. F., Piper, D. J. W., Pratt, R. M., Schrader, H.-J., Weser, O. E. and Wise, S. W.: Site 174, edited by L. V. D. Kulm, R. von Huene, J. R. Duncan, J. C. Ingle, S. A. Kling, D. J. W. Piper, R. M. Pratt, H.-J. Schrader, S. W. Wise, L. F. Musich, and O. E. Weser, Initial Reports of the Deep Sea Drilling Project, 18, 97, 1973.

Lease, R. O. and Ehlers, T. A.: Incision into the Eastern Andean Plateau During Pliocene Cooling, Science, 341(6147), 774–776, doi:10.1126/science.1239132, 2013.

Lease, R. O., Haeussler, P. J. and O'Sullivan, P.: Changing exhumation patterns during Cenozoic growth and glaciation of the Alaska Range: Insights from detrital thermochronology and geochronology, Tectonics, 35(4), 934–955, doi:10.1002/2015TC004067, 2016.

Leeman, W. P., Lewis, J. F., Evarts, R. C., Conrey, R. M. and Streck, M. J.: Petrologic constraints on the thermal structure of the Cascades arc, Journal of Volcanology and Geothermal Research, 140(1–3), 67–105, doi:10.1016/j.jvolgeores.2004.07.016, 2005.

Lewis, T. J. and Bentkowski, W. H.: Potassium, Uranium and Thorium Concentrations of Crustal Rocks: a Data File, Open File Report 1744, Geological Survey of Canada, Sidney, 1988.

Lewis, T. J., Bentkowski, W. H., Davis, E. E., Hyndman, R. D., Souther, J. G. and Wright, J. A.: Subduction of the Juan de Fuca Plate: Thermal consequences, Journal of Geophysical Research: Solid Earth, 93(B12), 15207–15225, doi:10.1029/JB093iB12p15207, 1988.

McCaffrey, R., King, R. W., Payne, S. J. and Lancaster, M.: Active tectonics of northwestern U.S. inferred from GPS-derived surface velocities, Journal of Geophysical Research: Solid Earth, 118(2), 709–723, doi:10.1029/2012JB009473, 2013.

McCrory, P. A.: Tectonic model explaining divergent contraction directions along the Cascadia subduction margin, Washington, Geology, 24(10), 929, doi:10.1130/0091-7613(1996)024<0929:TMEDCD>2.3.CO;2, 1996.

McCrory, P. A., Blair, J. L., Waldhauser, F. and Oppenheimer, D. H.: Juan de Fuca slab geometry and its relation to Wadati-Benioff zone seismicity, Journal of Geophysical Research: Solid Earth, 117(B9), doi:10.1029/2012JB009407, 2012.

McNeill, L. C., Goldfinger, C., Kulm, L. D. and Yeats, R. S.: Tectonics of the Neogene Cascadia forearc basin: Investigations of a deformed late Miocene unconformity, Geological Society of America Bulletin, 112(8), 1209–1224, 2000.

Meesters, A. G. C. A. and Dunai, T. J.: A noniterative solution of the (U-Th)/He age equation, Geochemistry, Geophysics, Geosystems, 6(4), doi:10.1029/2004GC000834, 2005.

Michel, L., Ehlers, T. A., Glotzbach, C., Adams, B. A. and Stübner, K.: Tectonic and glacial contributions to focused exhumation in the Olympic Mountains, Washington, USA, Geology, 46(6), 491–494, doi:10/gc8z9w, 2018.

Montgomery, D. R.: Valley formation by fluvial and glacial erosion, Geology, 30(11), 1047–1050, doi:10.1130/0091-7613(2002)030<1047:VFBFAG>2.0.CO;2, 2002.

Montgomery, D. R. and Greenberg, H. M.: Local relief and the height of Mount Olympus, Earth Surface Processes and Landforms, 25(4), 385–396, 2000.

Mullen, E. K., Weis, D., Marsh, N. B. and Martindale, M.: Primitive arc magma diversity: New geochemical insights in the Cascade Arc, Chemical Geology, 448, 43–70, doi:10.1016/j.chemgeo.2016.11.006, 2017.

Mutz, S. G., Ehlers, T. A., Werner, M., Lohmann, G., Stepanek, C. and Li, J.: Estimates of late Cenozoic climate change relevant to Earth surface processes in tectonically active orogens, Earth Surface Dynamics, 6(2), 271–301, doi:10/gc8sbw, 2018.

Pazzaglia, F. J. and Brandon, M. T.: A fluvial record of long-term steady-state uplift and erosion across the Cascadia forearc high, western Washington State, Am. J. Sci., 301(4–5), 385–431, 2001.

Phillips, B. A., Kerr, A. C., Mullen, E. K. and Weis, D.: Oceanic mafic magmatism in the Siletz terrane, NW North America: Fragments of an Eocene oceanic plateau?, Lithos, 274–275, 291–303, doi:10.1016/j.lithos.2017.01.005, 2017.

Porter, S. C.: Composite Pleistocene snow line of Olympic Mountains and Cascade Range, Washington, Geological Society of America Bulletin, 75(5), 477–482, 1964.

Priest, G. R.: Volcanic and tectonic evolution of the Cascade Volcanic Arc, central Oregon, Journal of Geophysical Research: Solid Earth, 95(B12), 19583–19599, doi:10.1029/JB095iB12p19583, 1990.

Prytulak, J., Vervoort, J. D., Plank, T. and Yu, C.: Astoria Fan sediments, DSDP site 174, Cascadia Basin: Hf–Nd–Pb constraints on provenance and outburst flooding, Chemical Geology, 233(3–4), 276–292, doi:10.1016/j.chemgeo.2006.03.009, 2006.

Reiners, P. W., Zhou, Z., Ehlers, T. A., Xu, C., Brandon, M. T., Donelick, R. A. and Nicolescu, S.: Post-orogenic evolution of the Dabie Shan, eastern China, from (U-Th)/He and fission-track thermochronology, American Journal of Science, 303(6), 489–518, 2003.

Reiners, P. W., Spell, T. L., Nicolescu, S. and Zanetti, K. A.: Zircon (U-Th)/He thermochronometry: He diffusion and comparisons with $^{40}Ar/^{39}Ar$ dating, Geochim. Cosmochim. Acta, 68(8), 1857–1887, doi:10.1016/j.gca.2003.10.021, 2004.

Stewart, R. J. and Brandon, M. T.: Detrital-zircon fission-track ages for the "Hoh Formation": implications for late Cenozoic evolution of the Cascadia subduction wedge, Geological Society of America Bulletin, 116(1–2), 60–75, 2004.

Stolar, D., Roe, G. and Willett, S.: Controls on the patterns of topography and erosion rate in a critical orogen, Journal of Geophysical Research, 112(F4), doi:10.1029/2006JF000713, 2007.

Stübner, K., Drost, K., Schoenberg, R., Böhme, M., Starke, J. and Ehlers, T. A.: Asynchronous timing of extension and basin formation in the South Rhodope core complex, SW Bulgaria, and northern Greece, Tectonics, 35(1), 136–159, doi:10.1002/2015TC004044, 2016.

Su, X., Baumann, K. H. and Thiede, J.: Calcareous nannofossils from Leg 168: biochronology and diagenesis, in Proceedings of the Ocean Drilling Program, Scientific Results, vol. 168, pp. 39–50., 2000.

Tabor, R. W. and Cady, W. M.: The structure of the Olympic Mountains, Washington: Analysis of a subduction zone, US Govt. Print. Off., 1978.

Thackray, G. D.: Extensive Early and Middle Wisconsin Glaciation on the Western Olympic Peninsula, Washington, and the Variability of Pacific Moisture Delivery to the Northwestern United States, Quaternary Research, 55(3), 257–270, doi:10.1006/qres.2001.2220, 2001.

Thiede, R. C. and Ehlers, T. A.: Large spatial and temporal variations in Himalayan denudation, Earth and Planetary Science Letters, 371–372, 278–293, doi:10.1016/j.epsl.2013.03.004, 2013.

Thomson, S. N., Brandon, M. T., Tomkin, J. H., Reiners, P. W., Vásquez, C. and Wilson, N. J.: Glaciation as a destructive and constructive control on mountain building, Nature, 467(7313), 313–317, doi:10.1038/nature09365, 2010.

Thomson, S. N., Reiners, P. W., Hemming, S. R. and Gehrels, G. E.: The contribution of glacial erosion to shaping the hidden landscape of East Antarctica, Nat. Geosci., 6(3), 203–207, doi:10.1038/ngeo1722, 2013

Tomkin, J. H. and Roe, G. H.: Climate and tectonic controls on glaciated critical-taper orogens, Earth and Planetary Science Letters, 262(3–4), 385–397, doi:10.1016/j.epsl.2007.07.040, 2007.

Valla, P. G., Shuster, D. L. and van der Beek, P. A.: Significant increase in relief of the European Alps during mid-Pleistocene glaciations, Nature Geosci, 4(10), 688–692, doi:10.1038/ngeo1242, 2011.

Wang, K.: Simplified analysis of horizontal stresses in a buttressed forearc sliver at an oblique subduction zone, Geophys. Res. Lett., 23(16), 2021–2024, doi:10/dz2xxt, 1996.

Wells, R. E. and McCaffrey, R.: Steady rotation of the Cascade arc, Geology, 41(9), 1027–1030, doi:10.1130/G34514.1, 2013.

Wells, R. E., Bukry, D., Friedman, R., Pyle, D., Duncan, R., Haeussler, P. and Wooden, J.: Geologic history of Siletzia, a large igneous province in the Oregon and Washington Coast Range: Correlation to the geomagnetic polarity time scale and implications for a long-lived Yellowstone hotspot, Geosphere, 10(4), 692–719, 2014.

Westbrook, G., Carson, B. and Musgrave, R.: Shipboard Scientific Party, 1994, Initial reports of the Ocean Drilling Program, 146(pt 1), 1994.

Whipple, K. X.: The influence of climate on the tectonic evolution of mountain belts, Nature Geosci., 2(2), 97–104, doi:10.1038/ngeo413, 2009.

Whipple, K. X. and Meade, B.: Orogen response to changes in climatic and tectonic forcing, Earth and Planetary Science Letters, 243(1–2), 218–228, doi:10.1016/j.epsl.2005.12.022, 2006.

Willett, S. D.: Orogeny and orography: The effects of erosion on the structure of mountain belts, J. Geophys. Res., 104(B12), 28957–28981, doi:10.1029/1999JB900248, 1999.

Willett, S. D. and Brandon, M. T.: On steady states in mountain belts, Geology, 30(2), 175–178, doi:10.1130/0091-7613(2002)030<0175:OSSIMB>2.0.CO;2, 2002.

Willett, S. D., McCoy, S. W., Perron, J. T., Goren, L. and Chen, C.-Y.: Dynamic Reorganization of River Basins, Science, 343(6175), 1248765–1248765, doi:10.1126/science.1248765, 2014.

Wilson, D. S.: Confidence intervals for motion and deformation of the Juan de Fuca Plate, Journal of Geophysical Research: Solid Earth, 98(B9), 16053–16071, doi:10.1029/93JB01227, 1993.

Wilson, D. S.: The Juan de Fuca plate and slab: Isochron structure and Cenozoic plate motions, in: The Cascadia Subduction Zone and related subduction systems: seismic structure, intraslab earthquakes and processes, and earthquake hazards, US Geological Survey, Reston, VA., 2002.

Yanites, B. J. and Ehlers, T. A.: Global climate and tectonic controls on the denudation of glaciated mountains, Earth and Planetary Science Letters, 325–326, 63–75, doi:10.1016/j.epsl.2012.01.030, 2012.

Yanites, B. J., Ehlers, T. A., Becker, J. K., Schnellmann, M. and Heuberger, S.: High magnitude and rapid incision from river capture: Rhine River, Switzerland, Journal of Geophysical Research: Earth Surface, 118(2), 1060–1084, doi:10.1002/jgrf.20056, 2013.

Yuan, T., Spence, G. D. and Hyndman, R. D.: Seismic velocities and inferred porosities in the accretionary wedge sediments at the Cascadia margin, Journal of Geophysical Research: Solid Earth, 99(B3), 4413–4427, doi:10/dfwxqf, 1994.

Tables

Table 1: Data for the ocean drill cores shown in Fig. 3.

Core	ODP 888	OPD 1027	DSDP 174
Drilled/total sediment thickness[a] (m)	570/2600	620/620	880/910
Cored Quaternary sediment (m)	570	460	430[b]
Maximum age of Quaternary sediments[c] (Ma)	0.6	1.7	1.7
Amount of Quaternary section of total core (%)	-	74	47
Age of oceanic crust[d] (Ma)	6.5	3.2	7.5
Quaternary sedimentation rate (m/Myr)	950[e]	270	250
Pre-Quaternary/total sedimentation rate[f] (m/Myr)	-/400	110/190	80/120

Notes: For core ODP 888, information is taken from Westbrook et al. (1994), for ODP 1027 from Su et al. (2000), and for DSDP 174 from Kulm et al. (1973). Sedimentation rates are calculated in this study using the reported thicknesses and age constraints.
[a]: If total thickness exceeds drilled thickness, then the total thickness was estimated from seismic data (e.g., ODP 888).
[b]: Due to poor core recovery, the Plio-Pleistocene boundary can only be confined to be between 418 and 446 m.
[c]: Ages based on biostratigraphy. For cores ODP 1027 and DSDP 174, the Plio-Pleistocene boundary was recovered and an age of 1.7 Ma is used here as reported by Su et al. (2000).
[d]: For cores ODP 888 and DSDP 174, the age refers to the age of the oceanic crust and is taken from Figure 3 at the respective location of the core. For ODP 1027, the age refers to the age of the oldest sediment in the core taken from Su et al. (2000).
[e]: This rate is calculated for the recovered core interval, which only encompasses 600 ka.
[f]: Total sedimentation rate = total thickness divided by age of oceanic crust.

Table 2: Coordinates, elevations, and thermochronometric cooling ages for samples considered in this study.

Sample	Latitude (°)	Longitude (°)	Elevation (m)	AHe ± 1SD (Ma)	AFT ± 1SD (Ma)	ZHe ± 1 SD (Ma)	ZFT ± 1SD (Ma)
Mount Olympus transect samples							
OP1533[a]	*47.87572*	*-123.69427*	*430*	*2.5 ± 0.4*	*5.1* ± 0.6	*4.8* ± 0.6	*unreset*
OP1550	47.81568	-123.69601	1825	2.0 ± 0.7	nd	7.0 ± 0.8	nd
OP1551	*47.82647*	*-123.68324*	*1509*	*3.3 ± 0.6*	*6.2 ± 0.8*	*7.0 ± 0.5*	*unreset*
OP1552	47.80155	-123.71102	2377	3.7 ± 0.2	nd	8.5 ± 1.5	unreset
OP1553	47.80377	-123.70244	2188	2.9 ± 1.6	nd	7.6 ± 0.4	nd
OP1554	47.83979	-123.69330	1222	1.9 ± 0.8	nd	7.1 ± 0.5	nd
OP1555	47.85457	-123.69194	851	2.5 ± 1.0	nd	7.2 ± 1.3	nd
Blue Mountain transect samples							
OP1548[a]	48.02186	-123.34295	410	14.8 ± 1.2	nd	unreset	nd
OP1557	47.98098	-123.31173	917	4.4 ± 2.5	nd	nd	nd
OP1558	47.97233	-123.30092	1032	8.6 ± 1.2	nd	unreset	nd
OP1559	47.97287	-123.28636	1184	10.8 ± 1.9	nd	nd	nd
OP1560	47.96709	-123.27110	1324	unreset	nd	nd	nd
OP1561	47.95783	-123.26785	1500	30.1 ± 2.0	nd	nd	nd
OP1562	47.95696	-123.26078	1778	3.6 ± 1.3	nd	unreset	nd
Mount Anderson transect samples							
OP1570	47.70483	-123.32813	1624	nd	nd	8.2 ± 1.1	nd
OP1571	47.71657	-123.32927	2035	3.0 ± 0.5	nd	8.1 ± 0.9	nd
OP1572[b]	47.71473	-123.32815	1842	3.3 ± 0.4	nd	8.4 ± 1.4	nd
OP1573	*47.69400*	*-123.32765*	*1363*	*3.9 ± 0.4*	*7.8 ± 1.5*	*8.9 ± 0.9*	*nd*
OP1574	47.68899	-123.35093	881	3.1 ± 1.1	nd	7.8 ± 0.9	nd
OP1576[b]	47.67451	-123.39235	614	1.5 ± 0.2	nd	6.5 ± 0.2	nd
OP1577	47.64185	-123.43398	470	nd	nd	7.0 ± 0.8	nd
Equal-elevation samples							
OP1502[a]	47.90796	-122.92804	325	unreset	unreset	unreset	nd
OP1510[a]	48.09852	-123.62231	273	8.3 ± 1.2	unreset	unreset	nd
OP1513[a]	*47.96015*	*-123.57273*	*402*	*1.5 ± 0.3*	*5.7 ± 0.7*	*10.2 ± 1.0*	*unreset*
OP1517[a]	*47.93891*	*-123.51376*	*423*	*3.7 ± 0.9*	*5.0 ± 0.8*	*9.0 ± 0.6*	*unreset*
OP1521[a]	48.04832	-124.08702	390	2.0 ± 0.4	unreset	unreset	nd
OP1522[a]	48.00530	-124.41620	367	9.1 ± 0.9	unreset	unreset	nd
OP1527[a]	47.82500	-124.05184	280	2.8 ± 1.0	unreset	unreset	nd
OP1528	47.80681	-123.99661	140	3.0 ± 0.3	unreset	nd	nd
OP1529[a]	47.78265	-124.14257	343	6.2 ± 1.1	unreset	unreset	nd
OP1531[a]	47.63659	-124.34966	50	7.5 ± 0.5	unreset	unreset	nd
OP1539[a]	*47.64151*	*-123.65870*	*446*	*2.1 ± 0.6*	*7.1 ± 0.9*	*6.8 ± 0.4*	*12.6 ± 1.5*
OP1542[a]	47.56001	-123.37533	450	1.9 ± 0.7	unreset	8.6 ± 0.9	nd
OP1556	48.00848	-123.89398	470	3.3 ± 0.9	nd	nd	nd
OP1582[a]	*47.95595*	*-123.83732*	*578*	*1.7 ± 0.5*	*6.0 ± 0.6*	*7.1 ± 0.5*	*unreset*

Notes: Samples in italics are used for 1D thermo-kinematic modelling. Results from single-grain analyses for AHe and ZHe are reported in Tables S1 and S2, respectively. Further details for AFT and ZFT dating can be found in Table 3, and single-grain analyses for apatite and zircon are reported in Tables S3 and S4, respectively. 1SD = one standard deviation, nd = not determined.

[a]: AHe and ZHe ages of the respective samples are from Michel et al. (2018).

[b]: Reported sample AHe ages are single-grain ages, because the yield of suitable apatite grains did not allow to date more grains.

Table 3: Results from fission-track dating.

Reset samples

Sample +Mineral	Grain ages (Ma)	χ^2(%)	N	reset state	Sample age ± 1SD (Ma)
OP1513 ap	0.9–17	47	24	R	5.7 ± 0.7
OP1517 ap	0–13	25	17	R	5.0 ± 0.8
OP1533 ap	2–15	11	20	R	5.1 ± 0.6
OP1539 ap	3–31	21	21	R	7.1 ± 0.9
OP1539 zr	8–18	19	21	R	12.6 ± 1.5
OP1551 ap	0–16	76	21	R	6.2 ± 0.8
OP1573 ap	5–17	11	6	R	7.8 ± 1.5
OP1582 ap	0–19	55	22	R	6.0 ± 0.6

Notes: For AFT and ZFT, 20 grains per sample were dated in a first step and it was checked whether the sample passes the χ^2-test and can be considered as reset (i.e., > 5%; an indication for belonging to the same age population, e.g., Galbraith, 2005). If so, the pooled ζ-age was considered as the sample age and reported here. If a sample failed the χ^2-test (i.e., < 5%), the sample is considered unreset and, in the case of AFT, 100 grains were dated if enough grains are available. The detrital age distribution was then decomposed into detrital age populations using BINOMFIT (Brandon, 1992, 1996) and the peak ages of those populations (with asymmetric error range for each age peak, corresponding to the 68% confidence interval, CI) are reported. For the ZFT method, the information whether the sample is reset or unreset is sufficient for this study and no further grains were dated. Fraction equals the amount of grains contained within the respective age peak. N=number of counted grains. Contrary to Brandon et al. (1998) we did not consider multiply or partially reset AFT samples but treated them as unreset, because our thermo-kinematic model can only be applied to fully reset samples.
[a]: Results for this sample are obtained by merging grains from our sample OP1527 (n=103) and sample AR39 (n=31) from Brandon et al. (1998).
[b]: Results for this sample are obtained by merging grains from our sample OP1528 (n=68) and sample AR40 (n=12) from Brandon et al. (1998).

Unreset samples

					Age peaks of the age populations											
Sample +Mineral	Grain ages (Ma)	χ^2(%)	N	reset state	Age (Ma)	68% CI (Ma)		Fraction (%)	Age (Ma)	68% CI (Ma)		Fraction (%)	Age (Ma)	68% CI (Ma)		Fraction (%)
OP1502 ap	10–630	0	94	UR	25.9	-2.5	+2.7	29.4	84.7	-8.1	+9.0	48.3	243	-54.6	+70.0	22.2
OP1510 ap	18–191	0	80	UR	35.5	-5.4	+6.4	34.5	52.6	-6.0	+6.8	52.9	100.3	-23.6	+30.7	12.6
OP1513 zr	17–82	0	23	UR	30.9	-3.5	+4.0	70.9	52.6	-7.5	+8.8	29.1	-	-	-	-
OP1517 zr	27–57	0	25	UR	33.7	-8.0	+10.5	15.5	41.4	-4.5	+5.1	84.5	-	-	-	-
OP1521 ap	0.5–499	0	103	UR	9.8	-0.8	+0.8	60.5	35.1	-4.0	+4.5	30.6	261.9	-50.4	+62.2	8.9
OP1522 ap	6–237	0	20	UR	16.3	-2.8	+3.4	20.2	41.8	-3.5	+3.8	59.7	130.1	-32.7	+43.5	20
OP1527[a] ap	1–992	0	134	UR	7.4	-0.5	+0.6	67.7	24.0	-2.0	+2.2	28.0	209.3	-65.4	+94.5	3.5
OP1528[b] ap	0.4–237	0	80	UR	4.7	-0.4	+0.4	75.7	14.6	-2.2	+2.5	24.1	-	-	-	-
OP1531 ap	6–684	0	100	UR	10.7	-0.5	+0.6	50.6	30.2	-1.8	+1.9	40.1	149.0	-21.7	+25.3	6.5
OP1533 zr	29–106	0	23	UR	35.6	-4.0	+4.5	43.5	53.5	-5.7	+6.4	47.7	95.8	-12.5	+14.3	8.7
OP1542 ap	3–43	0	19	UR	8.1	-0.8	+0.9	77.1	27.9	-3.6	+4.2	22.9	-	-	-	-
OP1551 zr	9–57	0	23	UR	15.1	-1.8	+2.0	62.7	25.5	-3.6	+4.1	21.0	49.9	-6.5	+7.4	16.3
OP1552 zr	10–38	0	24	UR	14.0	-1.5	+1.7	79.7	32.3	-3.7	+4.2	20.3	-	-	-	-
OP1582 zr	28–68	0	23	UR	31.1	-3.5	+3.9	35.0	52.1	-5.5	+6.2	65.0	-	-	-	-

Table 4: List of parameters used for the Pecube modelling.

Parameter	Value	Source
Thermal conductivity	1.83 W $m^{-1}K^{-1}$	average value for six drill cores in sediment material in the shelf offshore from Vancouver Island (Lewis et al., 1988)
Specific heat capacity	1200 J $kg^{-1}K^{-1}$	
Crustal density	2700 kg m^{-3}	
Mantle density	3200 kg m^{-3}	
Temperature at the base of the model	400 °C	extrapolation to greater depths from temperature estimates based on heat flow measurements on the shelf (Hyndman et al., 1990; Hyndman and Wang, 1993; Booth-Rea et al., 2008)
Temperature at sea level	8 °C	
Atmospheric lapse rate	6.69 °C km^{-1}	
Crustal heat production	0.77 µW m^{-3}	average value from drill cores on the shelf offshore Vancouver Island (Lewis and Bentkowski, 1988)
Model depth	20 km	minimum thickness of the accretionary wedge below the Olympic Mountains (e.g., Davis and Hyndman, 1989)

Table 5: Results from influx and outflux calculations using a three-dimensional geometry.

	Accretionary influx over 14 Myr period [a]			Denudational outflux over 14 Myr period		
	Minimum [a] (1.5 km)	Maximum [a] (2.5 km)	Increase at 2 Ma [a] (1.5 → 2.5 km)	Constant rates [b]	50% increase at 3 Ma [b]	150% increase at 2 Ma [b]
3D	68–71 x 10^3 km^3	128–133 x 10^3 km^3	75–78 x 10^3 km^3	68 x 10^3 km^3	75 x 10^3 km^3	82 x 10^3 km^3

Notes:
The entire procedure for calculating the influx and outflux is described in Section 3.3. The influx volumes are reported as ranges, because minimum and maximum convergence rates (Figure 6b) have been obtained from the plate reconstruction model of Doubrovine and Tarduno (2008).
[a]: Sensitivity to incoming sediment thickness: The accretionary influx volume is calculated for three different sediment thicknesses, yielding a minimum volume (1.5 km thickness), maximum volume (2.5 km thickness), and a more realistic volume (where the volume increases from 1.5 km to 2.5 km at 2 Ma).
[b]: Sensitivity to an increase in exhumation rates: The denudational outflux volume is calculated assuming constant exhumation rates, and considering the increase in exhumation rates due to glacial erosion, with an increase by 50% at 3 Ma or an increase by 150% at 2 Ma. Exhumation rates are based on Michel et al. (2018) and displayed in Figs. 6d and e.

3.2.3 Supplement for "How steady are steady-state mountain belts? – a re-examination of the Olympic Mountains (Washington State, USA)."

Electronic supplement to

How steady are steady-state mountain belts? – a re-examination of the Olympic Mountains by Michel et al.

S1 Details for thermochronometric dating

S1.1 Identifying outlier single-grain ages of (U-Th)/He dating

In the following we explain our procedure for deciding which apatite and zircon single grains are excluded from sample age calculation. The entire (U-Th-Sm)/He dataset of our analysed apatite and zircon single grains can be found in Tables S1 and S2, respectively. Calculating sample cooling ages for AHe and ZHe from single-grain ages was complicated in some samples for two main reasons: (1) Cooling ages for the sedimentary rocks from the Olympic Mountains can be unreset, (i.e., the single-grain ages can exhibit cooling ages representative of the sediment source terrains), and (2) The geologic uncertainty for (U-Th-Sm)/He dating is often larger than the analytic uncertainty, which can lead to over-dispersed single-grain ages (e.g., Fitzgerald et al., 2006; Flowers and Kelley, 2011).

In order to determine whether a sample contains outliers or is unrest, we used the following protocol. Samples where all single-grain ages are older than the depositional age of the sample or where single-grain ages show a large spread and do not overlap within analytical uncertainty (e.g., apatites of sample OP1560 or zircons of sample OP1557; Table S1 and S2), are considered as unreset samples. If samples pass this first test, we identify possible outliers by checking whether single-grain ages overlap within 2SD. Anomalously old single grains are considered outliers and excluded from sample cooling age calculations (e.g., single apatites of samples OP1552 and OP1553; Table S1). Furthermore, if single-grain ages of a sample are disputable, we consider information from the higher closure temperature system of the sample or other samples collected along the same elevation transect. For example, if the ZHe age of a certain sample is reset or if AHe ages of samples at higher or lower elevation have concordant ages, we consider the AHe system of that sample to be reset. This applies to AHe ages of samples OP1555, OP1572 and OP1576. For samples OP1572 and OP1576, we take the youngest apatite single-grain age as sample cooling age (due to the low high-quality apatite yield).

S1.2 Further information for FT dating

AFT and ZFT single-grain data are reported as additional files in Tables S3 and S4.

S2 Additional information for thermo-kinematic modeling

During thermo-kinematic modeling, we used a time step interval of 1 Myr (as reported in Figure 5). Using sample OP1513 as an example, we performed sensitivity tests for different time steps (Figure S1). We considered four additional intervals of 2 Myr, 3 Myr, 0.5 Myr, and an interval, where the duration is variable and depends on the time between the different thermochronometer ages of the sample.

For sample OP1513, the exhumation rate history using a 1 Myr time step (Fig. S1d) is as follows: High rates (~1 km/Myr) are observed between 10–12 Ma, slow rates (<0.5 km/Myr) between 4–10 Ma, and an increase

in rates to values >1 km/Myr staring at 2 Ma. Simulations using the four additional time steps (Fig. S1a-d) result in a similar history of "high-low-high" exhumation rates as the model with the 1 Myr time step. However, the timing of an increase or decrease in exhumation rates occurs at a multiple of 0.5 Myr, 2 Ma or 3 Ma, respectively. If the respective time step is long (e.g., for the 3 Myr simulation or for some time steps in S1c), then the corresponding exhumation rate has to be lower compared to the 1 Myr or 2 Myr simulations, in order to result in the same amount of exhumation during a given time span. Furthermore, for long time steps, the uncertainty for a given time step is reduced (grey area around the mean exhumation rate in Fig. S1).

The simulation with the 0.5 Myr time step (Fig. S1d) suggests a very fine temporal resolution and, in particular in the time interval between 3 Ma and 0 Ma, several spikes occur in the mean exhumation rate curve. It is important to consider that for most of our thermochronometer ages the respective uncertainties are between 0.5 Myr and 1.5 Myr. Hence, the suggested spikes in exhumation rates using a time step of 0.5 Myr are not well resolvable with our thermochronometry data. Although we did not test time steps shorter than 0.5 Myr, we suspect to observe a similar pattern of exhumation rate spikes. Due to the reason outlined above, we believe that models with a time step significantly shorter than 1 Myr pretend a temporal resolution that on the other hand is not resolved by our thermochronometry data, placing a minimum threshold on a reasonable time step.

In general, meaningful histories can only be derived for the time span covered between today and the oldest thermochronometer age of a sample. From all of our modeled samples, sample OP1513 has the oldest ZHe age (10.2 Ma). Therefore, it has the longest exhumation history resolved by our modeling and a time step of 3 Myr still results in a meaningful exhumation history (i.e., it has four time steps). Sample OP1533 (AFT/ZHe ages of ~6 Ma) has a much shorter time span resolved, hence a time step interval of 3 Myr would result in two time steps, and in case of a 2 Myr interval in three time steps. So, longer time steps place a limitation on the information obtained from exhumation histories for particularly young samples and model runs with longer time steps seem not to be feasible for some of the considered samples

A variation in exhumation rate can only occur at the beginning of a time step in our simulations. So, for the simulation where the duration of the time steps is controlled by the thermochronometer ages of the respective sample (Fig. S1c), the derived pattern of exhumation rates depends on the actual cooling ages. This impacts the direct comparison between the different samples, because a possible decrease or increase in exhumation rate occurs at different times, compared to simulations, where all samples use the same, fixed time step.

Based on the observations above, the general history of exhumation rates seems not to be sensitive to the time step. We believe that a time step interval of 1 Myr is the best trade-off between the investigated time steps and should yield reasonable exhumation rate patterns for all of our samples, which can have very different thermochronometer ages. Although the exhumation rate histories shown in Figure 5 have step-like patterns and suggest a high temporal sensitivity due to the 1 Myr time step, the interpretation of these histories should be based on a smoothed pattern, as we used in Figure 8. Furthermore, although we calculate the mean exhumation rate for each time step (red lines in Fig. 5 and Fig. S1), the respective uncertainty of this mean exhumation rate should also be considered (grey areas in Fig. 5 and Fig. S1).

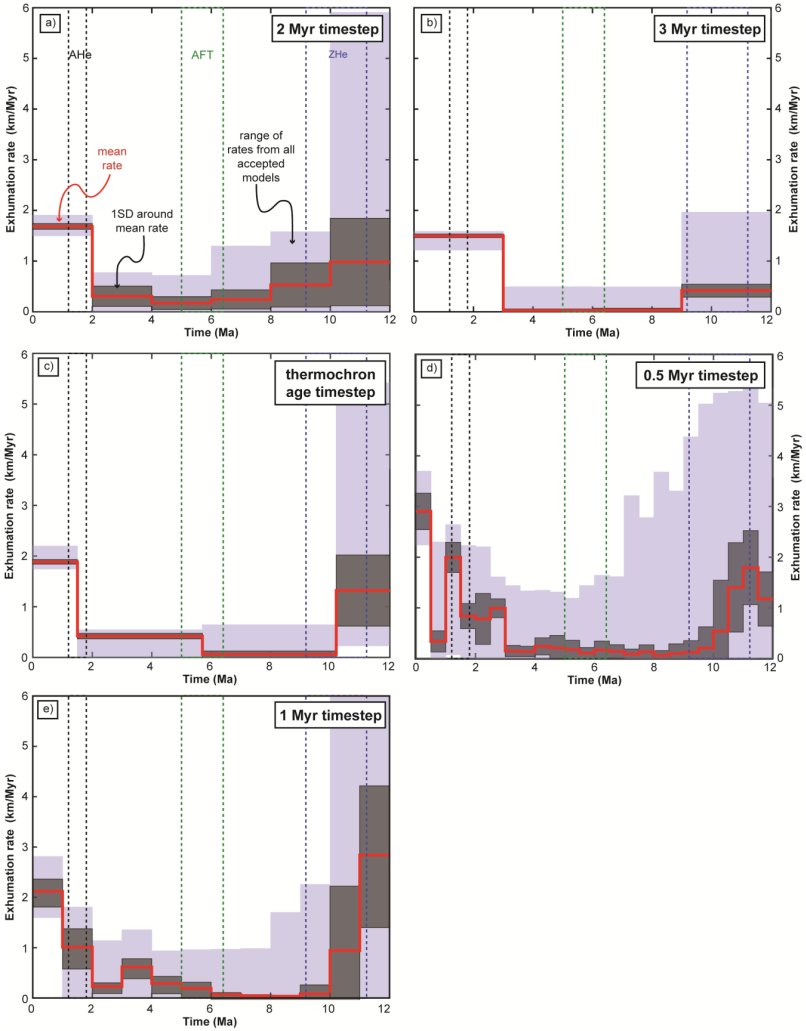

Figure S1: Outcomes from Pecube simulations investigating different time step durations for sample OP1513. Panels (a–d) display the exhumation rate histories for additional simulations using time steps of 2 Myr, 3 Myr, a duration defined by the thermochronometric ages of the sample, and 0.5 Myr, respectively. Panel (e) shows the exhumation rate history for a time step of 1 Myr, as already displayed in Figure 5 of the main manuscript. Dashed boxes indicate the cooling ages of AHe, AFT and ZHe with the respective uncertainty (1SD). For a detailed explanation of the modeling approach see Section 3.2 in the main manuscript.

S3 Additional information for flux steady-state analysis

S3.1 Sediment thickness during influx calculations

We calculated our influx volumes reported in Table 5 for three different sediment thicknesses, considering a pre-Quaternary thickness and present-day thickness as well as a possible increase in thickness occurring at 2 Ma. The sediment thickness of 2.5 km corresponds to the average present-day sediment thickness along the deformation front (Figure 3). The pre-Quaternary sediment thickness is difficult to determine for the entire 40 Myr duration of subduction and sediment accretion. However, we focused our analysis on the past 14 Myr, where we estimated the thickness by the following approach.

As displayed in Figure 3, the oceanic crust presently subducting is very young (~6–9 Ma). Together with the fast subduction rate of 34 km/Myr, which was even faster prior to 6 Ma (~60 km/Myr, Fig. 6), this prevents the accumulation of a thick succession of sediments on top of the oceanic crust. For instance, the pre-Quaternary sedimentation rates obtained from the ODP boreholes are around 80–110 m/Myr (Table 1). Assuming it takes the oceanic crust about 9 Myr to reach the deformation front (the oldest oceanic crust at the deformation front is currently 9 Ma old) would yield a sediment thickness of ~700–1000 m at the deformation front for the given sedimentation rate.

However, this is likely an underestimation of the actual thickness, because the inherent assumption for this calculation is that the spreading rate and convergence rate stay constant over time. Furthermore, the sedimentation rate likely increases with decreasing distance to the deformation front, because more detritus is delivered through submarine canyons and turbidity currents. Therefore, we suggest a minimum sediment thickness of 1500 m for the pre-Quaternary as a good estimate of this otherwise difficult to constrain parameter.

S3.2 Creation of the sediment cross-sections

For calculation of the sediment volumes in the two cross-sections (Fig. 7), the lower boundary of the area occupied by the sediments corresponds to the top of the subducted slab, which is derived from the Slab1.0 model (Hayes et al., 2012; McCrory et al., 2012). Unfortunately, no uncertainty estimates are provided for this model. McCrory et al. (2012) only note that their current estimate of the top of the subducted slab locally differs by 5 km in the vertical dimension from results from prior studies. As the current study is the most comprehensive and up-to-date one, we use their results for our calculations.

The upper boundary is defined by the topography/bathymetry or the Hurricane Ridge Fault (HRF), the roof thrust separating the accreted sediments from the overlying Coast Range Terrane (CRT). At the surface, the location of the HRF is taken from a geologic map (Tabor and Cady, 1978) and at depth we use information provided by a seismic study (Calvert et al., 2011). This study provides seismic velocities at depths of 22 km and 34 km for the Olympic Peninsula (Figures 3b and c in the original publication of Calvert et al., 2011), where a distinct area of low seismic velocities (LVZ = low velocity zone) can be observed beneath the Olympic Mountains. Calvert et al. (2011) interpret this LVZ to correspond to accreted/underplated sediments, which are enclosed by material of higher seismic velocities (possibly the subducted oceanic crust below or basaltic rocks

of the CRT on top of the sediments). Therefore, we assume that the eastern boundary of the LVZ represents the HRF and contour the boundary between low and high velocities at depths of 22 km and 34 km. According to Calvert et al. (2011), the seismic velocities of the accreted sediments vary with latitude and range from 5.8–6.5 km/s (between 47.25°N and 48.1°N) and 6.7–7.0 km/s (north of 48.1°N). Hence, we mapped and contoured the boundary between sediments and CRT, distinguished by different velocities. The solid black line in Figure S2 is constructed using a seismic velocity of ~6.6 km/s (boundary between yellow and orange pixels in Figures 3b and c of Calvert et al., 2011), and we consider the volumes calculated with this outline as the most representative estimates. The cross-sections and volumes shown in Figure 7 correspond to this geometry (yielding values of 5348 km2 and 3672 km2 for Profile 1 and 2, respectively).

In order to provide an uncertainty for our calculated volumes, we also estimate the geometry of the HRF using different velocities. A maximum extent uses a velocity of ~7.0 km/s as boundary between sediments and CRT (boundary between bright and dark orange pixels in Figure 3b and c of Calvert et al., 2011), and a minimum extent uses a velocity of ~6.4 km/s as boundary (boundary between light green and yellow pixels in Figure 3b and c of Calvert et al., 2011). These maximum and minimum estimates for the sediment extent are shown as thin, dashed lines in Figure S2 for the respective depths of 22 km and 34 km.

The uncertainties in the location for the HRF reported in Figure 7 are based on these maximum and minimum extents. Volumes calculated with these extents yield values of 5186 km2 and 5572 km2 (Profile 1), and 3446 km2 and 4005 km2 (Profile 2). The uncertainties of the calculated sediment in Figure 7 are derived from these minimum/maximum extents, and correspond to 5–10% of the reported volume. In general, the uncertainties of the location of the HRF at depth are largest in the southern part of the Olympic Peninsula (represented by the width of the dashed lines around the thick, solid line in Figure S2). Calvert et al. (2011) also note that the resolution of their reconstruction is reduced in the northern part of the peninsula, where velocities for the accreted sediments could be higher compared to areas in the south. Hence, we hesitate to construct a cross section for this part of the mountain range.

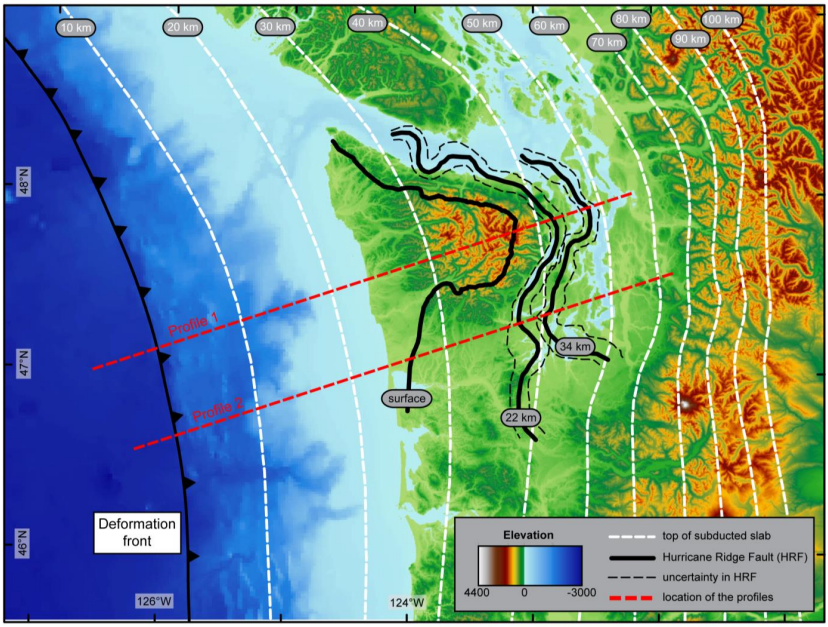

Figure S2: Map showing the data used for constructing Profile 1 and 2 (shown in Figure 7). Top of the subducted slab is taken from the Slab1.0 model (Hayes et al., 2012; McCrory et al., 2012). Trace of the Hurricane Ridge Fault (HRF) is taken from a geologic map at the surface (Tabor and Cady, 1978) and derived from the seismic study of Calvert et al., (2011) at depths of 22 and 34 km. The black dashed lines correspond to our estimates of uncertainty of the HRF at the respective depth. See Section S3.2 for details.

References

Calvert, A. J., Preston, L. A. and Farahbod, A. M.: Sedimentary underplating at the Cascadia mantle-wedge corner revealed by seismic imaging, Nat. Geosci., 4(8), 545–548, doi:10.1038/ngeo1195, 2011.

Fitzgerald, P. G., Baldwin, S. L., Webb, L. E. and O'Sullivan, P. .: Interpretation of (U–Th)/He single grain ages from slowly cooled crustal terranes: A case study from the Transantarctic Mountains of southern Victoria Land, Chem. Geol., 225(1–2), 91–120, doi:10.1016/j.chemgeo.2005.09.001, 2006.

Flowers, R. M. and Kelley, S. A.: Interpreting data dispersion and "inverted" dates in apatite (U–Th)/He and fission-track datasets: An example from the US midcontinent, Geochim. Cosmochim. Acta, 75(18), 5169–5186, doi:10.1016/j.gca.2011.06.016, 2011.

Hayes, G. P., Wald, D. J. and Johnson, R. L.: Slab1.0: A three-dimensional model of global subduction zone geometries, J. Geophys. Res. Solid Earth, 117(B1), doi:10.1029/2011JB008524, 2012.

McCrory, P. A., Blair, J. L., Waldhauser, F. and Oppenheimer, D. H.: Juan de Fuca slab geometry and its relation to Wadati-Benioff zone seismicity, J. Geophys. Res. Solid Earth, 117(B9), doi:10.1029/2012JB009407, 2012.

Tabor, R. W. and Cady, W. M.: The structure of the Olympic Mountains, Washington: Analysis of a subduction zone, US Govt. Print. Off., 1978.

3.3 Investigating deformation on various timescales

3.3.1 Declaration on contributions to joint work

The following section of the thesis is a manuscript that is currently in preparation and aims at comparing the deformation within the Olympic Mountains recorded on various timescales. The title of the manuscript will likely be "Frictional transition leaves a permanent mark in Cascadia". In section 3.3.2 the most recent version of the manuscript is provided, and section 3.3.3 contains the additional supplement. A data table containing the reported GPS velocities can be found at the end of the manuscript, and further data tables listing the published datasets used during the analysis are reported in the appendix (Section C).

Three authors contributed to the work presented in the manuscript: Lorenz Michel (LM), Todd Ehlers (TE) and Rebecca Bendick (RB). A summary of the respective contributions is provided in Table 3.3. The detailed contributions are as follows: LM developed the idea of comparing datasets integrating over various timescales, and RB contributed much of the understanding of the fault mechanic behavior. RB provided the GPS data and conducted the elastic component simulation, LM collected all other datasets from literature sources (thermochronometry, cosmogenic nuclides, episodic tremor and slip). LM, TE and RB were all involved in the data analysis, LM and TE had expertise on the long-term datasets, RB had expertise on the short-term datasets. LM drafted an initial version of the manuscript along with the swath profiles for comparison of the datasets. Later versions of the manuscript received significant contributions from TE and RB.

Table 3.3: Summary of contribution to joint work for the manuscript "Frictional transition leaves a permanent mark in Cascadia.", indicating the average fraction of work of the respective author in percent. The manuscript is currently in preparation.

Author	Position	Scientific ideas (in %)	Data generation (in %)	Analysis and Interpretation (in %)	Paper writing (in %)
LM	[1]	60	60	60	70
TE	[2]	10	0	20	15
RB	[3]	30	40	20	15

3.3.2 Manuscript: "Frictional transition leaves a permanent mark in Cascadia."

Frictional transition leaves a permanent mark in Cascadia

Lorenz Michel, Todd A. Ehlers, Rebecca Bendick

Abstract

Traditional mechanical models of the earthquake cycle assume that interseismic elastic deformation is completely recovered during earthquakes, closing the deformation budget of steady slip on the deep subduction interface and different types of episodic slip on the shallow subduction interface. However, at Cascadia, the presence of persistent, elevated topography in the Olympic Peninsula requires that some tectonic deformation is not recovered over the elastic cycle. Here, we compare estimates of deformation from various timescales with each other, in order to disentangle the contributions from elastic (recoverable) and permanent deformation within the Olympic Mountains. Elevated topography and high denudation rates from cosmogenic nuclides and thermochronometric data are located in the center of the Olympic Mountains. High values from these long-term observations are spatially coincident with geodetically observed residual tilting, overlapping with a published area of negative shear stress rates on the subduction interface. We attribute the observed tilting to time-dependent stresses and a spectrum of different slip types on the plate interface of the subduction zone. Visco-plastic deformation at the top of the episodic slip zone causes the dissipation of stress over time and initiates tilting in the overriding plate, which in turn creates topography and focuses denudation. Our findings indicate the importance of considering visco-plastic deformation additional to purely elastic deformation during the seismic cycle.

1 Introduction

The development or maintenance of mountain topography (corresponding to surface uplift) requires the accumulation of permanent tectonic deformation (through rock uplift) at a rate greater than, or equal to which denudation removes it, which leads to the exhumation of rocks over geologic timescales (e.g., Ellis et al., 1999). In the case when mountain topography is in steady state and no surface uplift occurs, rock uplift equals denudation and the respective measures can be compared with each other (England and Molnar, 1990). Rock uplift is commonly determined by geodetic methods whereas denudation and rock exhumation are often calculated with thermochronometry and cosmogenic radionuclide methods. Despite decades of research related to quantifying orogen deformation and exhumation processes, we still lack a clear understanding of the relationship between deformation at short time scales (e.g. $\sim 10^0$–10^2 year) and that at longer time scales (e.g. 10^6–10^7 year) and whether the observed respective deformation is elastic (so recoverable) or permanent.

Comparing observations from methods, which integrate over various timescales, contributes to fill this gap of knowledge.

At subduction zones, the observed deformation (on timescales of 10^0–10^2 years) is usually considered to correspond to purely elastic strain during the seismic cycle in between two major earthquakes. However, the mechanical models of time-dependent deformation related to subduction have evolved substantially from simple models of the elastic earthquake cycle on a planar fault interface that is either entirely locked or steadily slipping (e.g., Mansinha and Smylie, 1971; Okada, 1985; McCaffrey et al., 2007). In particular, recent work on fault mechanics and nonlinear friction conditions combined with direct observations of several different types of tectonic motion all demonstrate that subduction interfaces have locked domains, freely slipping domains, and transitional domains that host complicated sequences of stick and slip. In Cascadia and Japan, these domains appear to be arranged sequentially in the dip direction so that the shallowest part of the fault interface is locked, followed by a deeper enigmatic gap zone, then by a zone of conditional frictional stability hosting episodic tremor and slip (ETS), and finally a steadily slipping zone (Wang and Tréhu, 2016; Bruhat and Segall, 2016). However, whether and how the spatial extents of these zones in both the strike and dip directions change over long time scales or within the earthquake cycle is not well known, nor is the relationship of recoverable (elastic) strain to permanent strain that excites long-lived topography and landscape evolution.

This study investigates the generation of permanent deformation and topography over variable timescales and how deformation is related to the different domains of the subduction interface. We use the Olympic Mountains, overlying the Cascadia Subduction Zone, Western North America (Fig. 1), as a case study. This area is an ideal location to study the spatial and temporal variability of fault slip mechanisms because a syntaxial bend in the downgoing Juan de Fuca Plate (Mahadevan et al., 2010; Bendick and Ehlers, 2014) means that each domain of the fault interface is anomalously wide and also that the overriding plate above the transitional domains is subaerial, so both geodetic observations and geologic samples can be collected. Indeed, this region was the first place where ETS was observed (Rogers and Dragert, 2003), as well as one of the test locations for steady-state landscape models (Willett and Brandon, 2002).

For our purpose, we compare the position and magnitude of instantaneous residual vertical displacement from GPS time series with denudation rates derived from cosmogenic nuclide dating and thermochronometry within a transect spanning the Olympic Peninsula. We capitalize on the large dataset of published denudation rates from thermochronometric and cosmogenic nuclide methods (Brandon et al., 1998; Michel et al., 2018; Adams and Ehlers, 2018), that are available for the region. We further compare these observations with vertical displacement related to ETS and inversions for shear stress on the subduction interface from Bruhat and Segall (2016), as well as forward simulations of deformation due to elastic and viscous mechanics in subduction settings (Wang et al., 2003; Li et al., 2015).

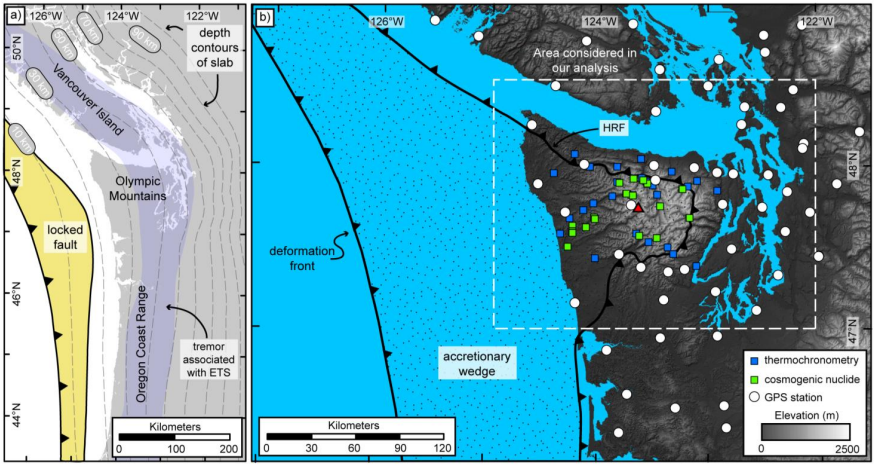

Figure 1: a) Overview of the Cascadia Subduction Zone of North America. Parts of the fore arc high, which are mentioned in the text (Vancouver Island, Olympic Mountains, Oregon Coast Range), are indicated. Dashed lines represent contour lines of the subducted slab at depth, according to McCrory et al. (2012). Note the bend in the slab at the latitude of the Olympic Mountains. The extent of locking of the thrust fault is indicated by the yellow area (after Hyndman and Wang, 1993). The extent of tremor is based on data from the Pacific Northwest Seismic Network (https://pnsn.org/tremor). b) Topography of the Olympic Mountains (red triangle denotes the location of Mount Olympus, 2430 masl), along with the location of GPS stations (data from this study), and the location of thermochronometry samples and cosmogenic nuclides (Michel et al. 2018; Adams and Ehlers 2018). The white box denotes the area considered for comparing the different datasets. The locations of GPS stations used by Bruhat and Segal (2016) for obtaining deformation related to slow slip events are mostly identical with our GPS stations. For full maps of thermochronometric cooling ages, denudation rates from cosmogenic nuclides, exhumation rates and GPS velocities, the reader is referred to the electronic supplement (Figures S1 and S2). Onshore location of the Hurricane Ridge Fault (HRF) is after Brandon et al. (1998).

2 Background

The Cascadia Subduction Zone (CSZ), where the Juan de Fuca Plate subducts below the North American continent, extends along the American west coast from northern California to the northern tip of Vancouver Island (Figure 1a). Currently the thrust fault is locked over much of its distance along the trench, although the locking depth is very poorly constrained by geodetic observations (e.g., Hyndman, 2013; Wang and Tréhu, 2016). At the latitude of the Olympic Mountains (which form the topographic apex of the subduction zone's forearc high), the locked zone of the fault is inferred to be wider than both further north and further south (Figure 1a) due to the lower angle of subduction below the mountain range, related to the upward bending of the subducted slab (McCrory et al., 2012; Mahadevan et al., 2010). The seismic cycle at the CSZ is long (about 300–500 years) and the last known rupture of the fault occurred in AD 1700 (Wang and Tréhu, 2016).

Early geodetic studies near the Cascadia Subduction Zone (CSZ) assume all observed displacement to be elastic (e.g., Szeliga et al., 2008; Burgette et al., 2009; McCaffrey, 2009). This assumption is based on the accumulation of elastic strain during interseismic periods of the earthquake cycle, which is then recovered coseismically during slip on the thrust fault (e.g., Hyndman and Wang, 1993). However, this assumption of elastic and fully recoverable deformation is contradictory to the presence of topography (i.e., the fore arc high), discrepancies between rock uplift rates integrating over different timescales (Kelsey et al., 1994; Penserini et al., 2017), and results from modeling studies (Wang et al., 2003; Simpson, 2015; Wang and Tréhu, 2016) which all suggest that permanent deformation accumulates in the CSZ, at least over longer timescales. In particular, Wang and Tréhu (2016) and Li et al. (2015) simulate cases where interseismic stressing of the lithosphere and mantle at the transition from the steadily slipping to the locked domains of the subduction interface produces viscoelastic as well as recovered elastic deformation. In Cascadia, the viscoelastic contribution to surface displacement has been aliased into apparent block motions (e.g., McCaffrey et al., 2007, 2013), or unrealistic or poorly constrained locking depths (e.g., Wang et al., 2012). Furthermore, such viscoelastic models predict that the spatial arrangement of interseismic uplift and subsidence of rocks should vary in time, with subsidence of the overriding plate surface expanding in the late stages of the interseismic interval (Li et al. 2015).

Even mechanical simulations that incorporate more realistic viscoelastic material properties usually simplify the transition from a freely slipping to a locked subduction interface. However, studies of ETS (e.g., Bartlow et al., 2011; Dragert and Wang, 2011; Wech and Creager, 2011; Wech and Bartlow, 2014), the Cascadia "gap" (e.g. Bruhat and Segall, 2016), and the strongly spatially heterogeneous distribution of coseismic slip in observed subduction megaquakes all point toward more complex zones over which tectonic stresses are relayed and partially stored. Specifically, recent models of the megathrust indicate fully locked conditions from the trench to depths of ~16 km (Krogstad et al., 2016) to 21 km (Bruhat and Seagall, 2016), then a "gap" zone inferred as velocity-strengthening where shear stress decreases over time (Bruhat and Segall, 2016), extending to the ETS zone from ~25-60 km (Bartlow et al., 2011; Hawthorne and Rubin, 2013; Wech and Bartlow, 2014). Below the ETS zone, the Cascadia subduction zone is inferred to be slipping steadily at the relative plate velocity. Because the area of the interface that slips during a major subduction earthquake determines the moment of the event, whether the gap zone and the ETS zone can store elastic potential energy and therefore slip coseismically are critical questions for seismic hazard assessment and basic fault mechanics.

The Olympic Mountains correspond to the aerially exposed part of the subduction zone's accretionary wedge (Brandon et al., 1998). They have been the location for studies applying various methods like thermochronometry, topographic analysis and cosmogenic nuclide dating in order to assess the landscape evolution of this orogen, hence the "permanent" deformation over many seismic cycles (e.g., Brandon et al., 1998; Adams and Ehlers, 2017, 2018; Michel et al., 2018). Based on thermochronometric cooling ages, cooling histories of rock samples collected at the earth's surface can be reconstructed, and by modeling the temporal

evolution of the geothermal gradient, exhumation histories can be reconstructed from the cooling histories. In the Olympic Mountains exhumation is localized and controlled by an ellipse-shaped pattern (Michel et al. 2018; see Figure S1a), which is a consequence of the bend in the subducted slab (e.g., Bendick and Ehlers, 2014). Results from the topographic analyses and denudation rates derived from cosmogenic nuclides also corroborate that the evolution of this mountain range is mostly controlled by the shape of the subducted slab (Adams and Ehlers, 2017; Adams and Ehlers, 2018).

3 Methods

We compare four different observational data sets and map view figures of the datasets are provided in Figures S1 and S2, respectively. For a direct comparison between the datasets, we project these along a transect crossing the Olympic Peninsula from west to east between -125°E and -122°E (Figure 2). However, the spatial extent of the datasets is different and the datasets based on geodetic methods (Figure S2) cover a larger area of the Cascadia Subduction Zone, compared to estimates of denudation, which are only constrained for the Olympic Peninsula (Figure S1). Because the subducted slab displays a bend, different slab depths can be observed for the same longitude along strike the subduction zone. If the hypothesized processes responsible for permanent deformation and the different zones of the subduction interface depend on the slab depth, then this longitudinal variation in slab depth should be considered. For these two reasons, we focus our analysis on the area between latitudes 47°N and 48.5°N (Figure 1b), in order to minimize the effects of the bent slab and the variable spatial coverage of the different datasets. Hence all large, colored symbols in the panels of Figures 2b-e are from locations between these latitudinal boundaries. Nonetheless, we also provide information from locations outside these boundaries for the geodetic methods, which correspond to the small, open symbols in Figures 2c-e.

Of our considered datasets, two are sensitive to denudation rate: Cosmogenic nuclide dating using ^{10}Be (Adams and Ehlers, 2018) and exhumation rates obtained from thermochronometry applying (U-Th)/He dating of apatite and zircon (Michel et al., 2018). These datasets have integration timescales of 10^3–10^4 or 10^5–10^6 years, respectively, and integrate over many seismic cycles to yield a proxy for denudation associated with long-term deformation. Rates obtained from cosmogenic nuclides provide basin-wide denudation rates (Figure S1b) and are plotted at the respective sample site within the transect (green symbols in Figure 2b). Michel et al. (2018) suggested an ellipse shaped pattern of denudation based on their thermochronometry data (Figure S1a), and in our transect, we plot the denudation rate at the respective thermochronometer sample location (blue squares in Figure 2b).

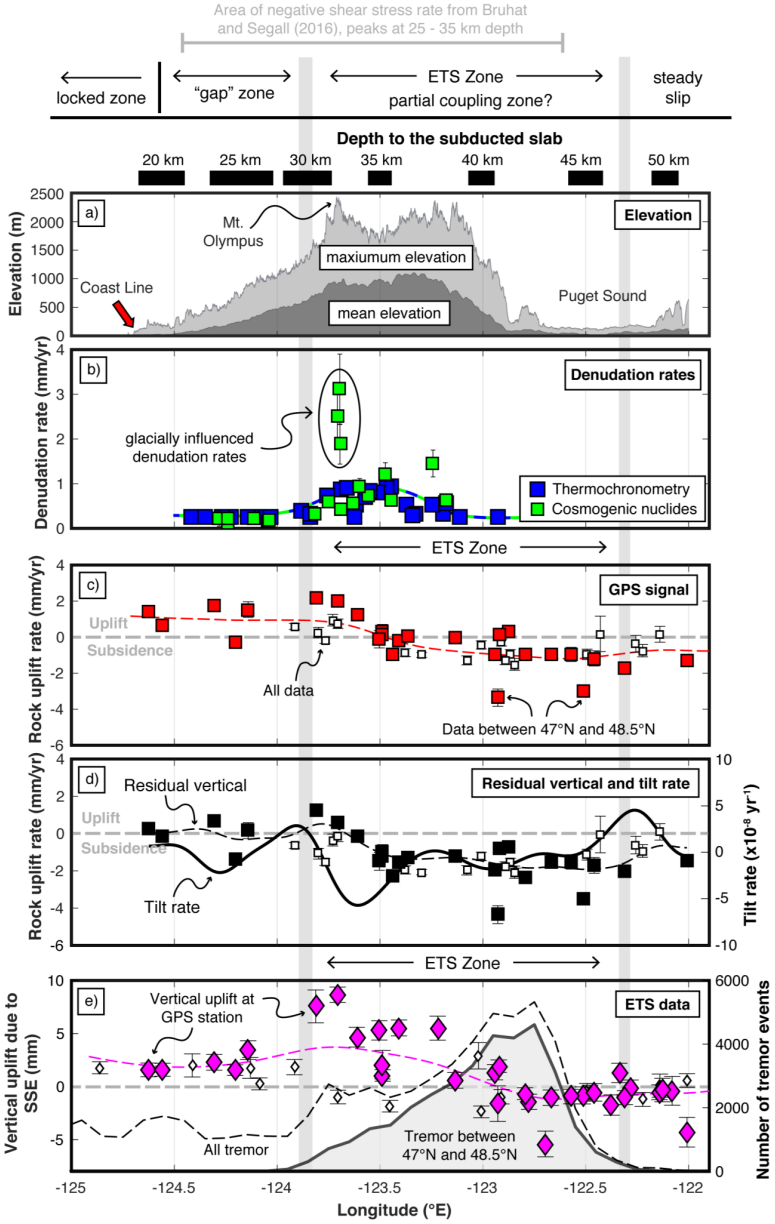
Area of negative shear stress rate from Bruhat and Segall (2016), peaks at 25 - 35 km depth
locked zone
"gap" zone
ETS Zone
partial coupling zone?
steady slip
Depth to the subducted slab
20 km
25 km
30 km
35 km
40 km
45 km
50 km
a)
Elevation
Elevation (m)
Mt. Olympus
maxiumum elevation
mean elevation
Coast Line
Puget Sound
b)
Denudation rates
Denudation rate (mm/yr)
glacially influenced denudation rates
Thermochronometry
Cosmogenic nuclides
ETS Zone
c)
GPS signal
Rock uplift rate (mm/yr)
Uplift
Subsidence
All data
Data between 47°N and 48.5°N
d)
Residual vertical and tilt rate
Residual vertical
Tilt rate
Tilt rate (x10⁻⁸ yr⁻¹)
ETS Zone
e)
ETS data
Vertical uplift at GPS station
Vertical uplift due to SSE (mm)
All tremor
Tremor between 47°N and 48.5°N
Number of tremor events
-125
-124.5
-124
-123.5
-123
-122.5
-122
Longitude (°E)

Figure 2: West to east transects across the Olympic Peninsula, showing the datasets considered in our analysis. We focus are analysis on the area between 47°N and 48.5°N, due to reasons outlined in the text. For completeness, we also provide data from outside these boundaries, which are shown with open, small symbols in panels c) to e). The thin dashed lines displayed in panels c) to e) were also fitted using all available data. a) Mean and maximum elevation of the Olympic Peninsula, on the central Olympic Peninsula between latitudes of 47.4°N and 48.1°N. The location of Mt. Olympus (2430 masl) is indicated). b) Estimates of denudation, based on cosmogenic nuclide dating (green squares; Adams and Ehlers, 2018) and thermochronometry (blue squares; Michel et al, 2018). Denudation rates influenced by glaciation are indicated and are excluded from our analysis. c) GPS velocities from this study, the signal was treated according to the procedure outlined in the methods section. d) Residual vertical velocities, which are obtained from the GPS velocities displayed in c) by subtracting a forward modeled elastic component, using the model of Wang et al. (2003). These residual verticals correspond to the permanent component of deformation contained in the GPS signal. The tilt rate corresponds to the derivative of the residual vertical in the x-direction and has units of 10^{-8} yr^{-1}. e) Data related to episodic tremor and slip (ETS), showing the vertical uplift due to ETS recorded by GPS stations as published by Bruhat and Segall (2016). Furthermore, the number of tremor events (in bins of 0.1° width) recorded during 2014–2018 are plotted along the transect. For our analysis we consider the tremor events between 47°N and 48.5°N. Because the occurrence of tremor follows the shape of the subducted slab (e.g., Figure 1a), the pattern of tremor outside the latitudinal boundaries is different from the pattern used in our analysis. Events are taken from the tremor database of the Pacific Northwest Seismic Network (https://pnsn.org/tremor). At the top of panel a), information regarding the depth of the subducted slab (from McCrory et al., 2012) and the different zones at the subduction interface is provided.

Two datasets are sensitive to rock uplift and are based on inversion of GPS timeseries, hence integrating over a timescale of about a decade: the observed vertical component associated with ETS (Figure 2e, Figure S2d) published in Bruhat and Segall, (2016), and the residual vertical displacement (Figure 2d, Figure S2c) which we obtained from GPS timeseries using the following approach.

The residual vertical displacement is calculated by first solving for the daily positions of 88 continuously logging GPS stations, 63 in the Cascadia region and 15 elsewhere. Daily positions were determined for every day and for fortnightly averages from 1 January 2005 to 31 December 2016 using a Kalman filter approach implemented in GAMIT/GLOBK and tied to the ITRF08 reference frame using the 15 IGS sites outside of the study area. Outlier positions were manually edited and Markov noise added to the time series using the station position variance and cross-correlations. Next, because vertical geodetic displacements are sensitive to many different loads, especially hydrologic and seasonal atmospheric masses, the daily vertical (UP) position time series with formal uncertainties were used to estimate independent annual sine and cosine harmonics, semiannual sine and cosine harmonics, and secular linear up velocities. The periodic terms together remove most of the seasonal hydrologic and atmospheric contributions, as well as draconitic and orbital residuals, as well as most of the ETS contribution. The steady linear rate is therefore the best geodetic estimate of steady decadal mean rock uplift in the late interseismic. A map view of this linear rate is provided in Figure S2a and in Figure 2c along the transect. Station names, locations, and vertical components are listed in Table 1.

Finally, station vertical velocity (**W**) can be considered a linear combination of an elastic part due to the seismic cycle on the locked part of the Cascadia subduction zone and a viscous part due to permanent deformation of the domain. In the standard interpretation of subduction zones, all stored elastic bending should be recovered in slip events, either earthquakes or phenomena like afterslip or longer term creep events; the

residual visco-plastic deformation should be the component of rock uplift, contributing to formation of topography and denudation. In order to place an upper bound on the unrecoverable vertical displacement, we subtract the modeled elastic bending due to the locked subduction zone from Wang et al. (2003) to give the reported residual vertical displacement (Figure S2c). Because the study area is well inland of the bottom of the preferred locked zone, the elastic correction is nearly constant across the study area (Figure S2b).

4 Results

Within the Olympic Mountains, the topography steadily increases in height from the coast towards the center of the mountain range (Figure 2a) where it reaches its highest elevation at Mt. Olympus (2430 masl, at -123.7°E in Figure 2a). Previous work (Michel et al. 2018) shows that million-year timescale denudation rates from thermochronometer data display an ellipse shaped pattern (Fig. S1a) and are highest in the core of the range, coincident with the location of the highest mean elevation of the range. The denudation rates decrease away from the core of the range in the profile (Figure 2b), and also in map view (Fig. S1a), such that rates vary between 0.25 mm/yr at the coast to 0.9 mm/yr in the area of high topography.

Previously reported (Adams and Ehlers, 2018) cosmogenic nuclide denudation rates that integrate over millennial timescales are lowest on the western side of the mountain range (~0.2 mm/yr) and increase to maximum values of 1.2–1.4 mm/yr in the core of the mountain range, coincident with the highest thermochronometer denudation rates and highest mean elevations (Figure 2a,b). Higher cosmogenic nuclide denudation rates (>1.8 mm/yr, indicated in Figure 2b) were previously interpreted as influenced by glaciation (Adams and Ehlers, 2018). Shielding of rocks from cosmic ray exposure by glacial ice results in lower cosmogenic nuclide concentrations and seemingly higher denudation rates. However, these high rates are unrelated to denudation caused by rock uplift and for this reason, we exclude the samples from catchments with significant recent glaciation from our analysis, because they are not comparable with denudation rates from thermochronometry or GPS-derived rock uplift rates.

Highest denudation rates both from thermochronometry and cosmogenic nuclides are observed between -123.8°E and -123.2°E along our transect (Figure 2b). The peak in residual vertical velocity from geodetic observations is located between -123.8°E and -123.6°E, close to the location of Mt. Olympus (Figure 2d). Only the western region of the peninsula between -124.4°E and -123.6°E has positive (upward) residual vertical velocities; the remainder of the residual velocities are zero or slightly negative. The peak vertical displacement in ETS events is also spatially coincident (between -123.8°E and -123.7°E, Figure 2e), and upward directed displacement can be observed between -124.6°E and -123°E, whereas east of -123°E most observed uplift is zero or negative (Bruhat and Seagall, 2016). The peak in tremor activity (events recorded from 2014–2018) associated with ETS is offset from the peak in vertical displacement and located at approximately -122.8°E.

From there, the occurrence of tremor gradually fades out towards the west and no tremor can be observed west of -124°E.

We also plot the horizontal spatial derivatives of the smoothed residual velocities (Figure 2d). Since **W** (the vertical velocity) is $\frac{\partial z}{\partial t}$, the x-derivative of **W** is $\frac{\partial z}{\partial x \partial t}$, which can be interpreted as a rate of topographic tilting. The derivatives of the residual vertical velocity show high rates of positive tilting (toward the west) on the west side of the Olympic range and negative tilting (toward the east) on the east side of the range. If we further consider the limiting case of a Newtonian viscous material, then the tilting rate is also a shear strain rate which should be proportional to the shear stress. This interpretation of the observed derivative is consistent with the inversion of Bruhat and Seagall (2016) indicating a negative shear stress rate at the transition from the gap zone to the ETS domain on the Cascadian subduction interface, hence the observed negative shear strain rate (Figure 2).

5 Discussion

The long-wavelength topography and denudation rates in the Olympic Peninsula all yield a convex pattern, with highest values located in the center of the Olympic Mountains between -124°E and -123°E (Figure 2a,b). This area also hosts the most rapid vertical velocities from geodetic observations, rapid tilting, and a change of sign of shear stress rate, assuming linear viscosity.

The location of these deformation anomalies lies above the inferred transition between an enigmatic "gap" zone and the zone that hosts episodic slip events, where the primary subduction interface is between 25 and 35 km depth (Figure 2). Based on a combination of observational constraints, emerging fault mechanics results, and basic continuum mechanics, this zone appears to be the part of the Cascadian subduction zone with the most complicated behavior, with consequences for both seismic hazard and landscape processes.

Below the ETS zone, the North American and Juan de Fuca plates move past one another at the steady relative plate velocity. This plate motion must be accommodated through the entire subduction zone to close the total tectonic velocity budget. In the ETS zone (which in our analysis corresponds to the area where tremor is recorded between -123.8°E and -122.3°E in Figure 2e) accumulation of stress from the steadily slipping domain below appears to interact with a nearly-constant frictional threshold, resulting in quasi-periodic slip events that then transfer the plate motion to the base of the "gap" zone. The mechanism of slip transfer through the gap is not well understood, but at least some of the tectonic stress must be loaded onto the base of the locked domain, eventually to be released coseismically. Bruhat and Seagall (2016) sought to characterize the "gap" zone by inverting for shear stress rate from surface displacement observations. They find a negative shear stress rate, especially in the lower gap zone, indicating that stresses applied to the gap zone by ETS

displacements are partially dissipated over time. This part of the fault is at depths of 25–35 km. Given that the continental lower crust is often inferred to be ductile at these depths and temperatures (Burov, 2011) and that accreted sediment is present at this depth (Calvert et al., 2011), one candidate for relaxation of applied stresses is viscous or plastic flow. These flows could be responsible for the observed tilt rate in the residual vertical velocity. Wang et al. (2012) and Li et al. (2015) have recently argued for interseismic viscous deformation excited by accumulation of tectonic stresses below the locked part of subduction zones that would not be recovered coseismically.

Such secular tilting arising from continuum deformation of overriding lower crust should produce persistent topography. In addition, tilting of the landscape surface should particularly enhance fluvial erosion transport by increasing local to regional relief and channel slopes. Therefore, we expect the spatial correlation between tilting rate, elevated topography and high rates of denudation at the surface. In the Olympic Mountains, we observe that the maximum denudation rates both from thermochronometry and cosmogenic nuclides are spatially correlated with the highest tilting rates (Figure 2a,b,d). Hence, viscous or plastic flow seems to be causing permanent deformation, which can be recorded on timescales ranging from 10^1 years to 10^3–10^4 years to 10^5–10^6 years. The plate geometry of the Cascadia Subduction Zone has been suggested to control the spatial pattern of deformation due to the locally flatter angle of subduction below the Olympic Mountains (Bendick and Ehlers, 2014; Michel et al., 2018). Seemingly the geometry also affects the efficacy of viscous or plastic flow, because compared to the areas north or south of the Olympic Peninsula, residual vertical velocities (Figure S2c), vertical uplift due to ETS (Figure S2d) and denudation rates are highest in the Olympic Mountains.

Interestingly, previous studies have highlighted that when methods integrating over different timescales are compared with each other, discrepancies between short term and long term observations exist (e.g., Friedrich et al., 2003; Stock et al., 2009; Penserini et al., 2017; Niemi and Clark, 2018). This could in part be due to methods integrating over short timescales (like geodetic methods) contain an elastic and inelastic component, whereas methods with long integration timescales only record the inelastic component. As we showed, an attempt to remove the elastic component by forward modeling is promising in order to derive the permanent (viscous) component of deformation contained in a GPS signal. In our case, the number of recorded events during the integration timescale is likely also a crucial point. For example, the seismic cycle at the Cascadia Subduction zone is 300–500 years such that available geodetic measurements do not integrate over several cycles, whereas our methods for estimating denudation integrate over 100s to 1000s of seismic cycles. A further important point to consider is the time dependence of stresses over a full seismic cycle. Elastic mechanical models (e.g. Wang et al., 2003) assume a temporally steady stress evolution. However, at present, the Cascadia Subduction Zone is in the late interseismic period (Wang and Trehu, 2016), and the outcome of elastic models might be more representative of the state of stress during an earlier phase of the interseismic

period. This could be responsible for some of the spatial misfit between residual vertical velocities, tilting rate and the long-term denudation rates, because our modeled elastic component could be an overestimation of the actual, present value.

Furthermore, there are uncertainties associated with the long-term denudation rates. The denudation rates suggested by Michel et al. (2018) could deviate from the proposed ellipsoid pattern, which would result in a slight (~10km) variation in the lateral extent of high denudation rates shown in Figure 2b (i.e., the blue symbols could move further to the west or east). As Michel et al. (2018) showed, denudation rates can also be temporally variable. Glacial erosion due to Pleistocene glaciation locally increased the denudation rates by 50–150 %, particularly affecting the western side of the mountain range (approximately between -123.9°E and -123.7°E in Figure 2). However, Adams and Ehlers (2018) also noted that their denudation rates (temporally integrating over the Holocene) show, that the effect of glacial erosion can no longer be recorded in most of the available cosmogenic nuclide samples.

6 Conclusion

In the Olympic Mountains, the patterns of denudation rates obtained from cosmogenic nuclides and thermochronometry as well as the long-wavelength topography are all similar, indicating that most long-term (permanent) deformation occurs in the center of the mountain range. The permanent deformation recorded by topography and dating techniques aligns with a peak in displacement observed using geodetic methods, as well as with high rates of surface tilting. High stresses on the Cascadian subduction zone may be exciting viscous deformation of the lower crust, dissipating some of the tectonic shear stress in the enigmatic “gap” zone, generating permanent topography, and enhancing erosion rates in a localized domain.

References

Adams, B.A., and Ehlers, T.A., 2017, Deciphering topographic signals of glaciation and rock uplift in an active orogen: a case study from the Olympic Mountains, USA: Earth Surface Processes and Landforms, doi:10.1002/esp.4120.

Adams, B.A., and Ehlers, T.A., 2018, Tectonic controls of Holocene erosion in a glaciated orogen: Earth Surface Dynamics, v. 6, p. 595–610, doi:10.5194/esurf-6-595-2018.

Bartlow, N.M., Miyazaki, S., Bradley, A.M., and Segall, P., 2011, Space-time correlation of slip and tremor during the 2009 Cascadia slow slip event: Geophysical Research Letters, v. 38, doi:10.1029/2011GL048714.

Bendick, R., and Ehlers, T.A., 2014, Extreme localized exhumation at syntaxes initiated by subduction geometry: Geophysical Research Letters, v. 41, p. 5861–5867, doi:10.1002/2014GL061026.

Brandon, M.T., Roden-Tice, M.K., and Garver, J.I., 1998, Late Cenozoic exhumation of the Cascadia accretionary wedge in the Olympic Mountains, northwest Washington State: Geological Society of America Bulletin, v. 110, p. 985–1009, doi:10.1130/0016-7606(1998)110<0985:LCEOTC>2.3.CO;2.

Bruhat, L., and Segall, P., 2016, Coupling on the northern Cascadia subduction zone from geodetic measurements and physics-based models: Journal of Geophysical Research: Solid Earth, v. 121, p. 8297–8314, doi:10.1002/2016JB013267.

Burgette, R.J., Weldon, R.J., and Schmidt, D.A., 2009, Interseismic uplift rates for western Oregon and along-strike variation in locking on the Cascadia subduction zone: Journal of Geophysical Research: Solid Earth, v. 114, doi:10/crqv5r.

Burov, E.B., 2011, Rheology and strength of the lithosphere: Marine and Petroleum Geology, v. 28, p. 1402–1443, doi:10.1016/j.marpetgeo.2011.05.008.

Calvert, A.J., Preston, L.A., and Farahbod, A.M., 2011, Sedimentary underplating at the Cascadia mantle-wedge corner revealed by seismic imaging: Nature Geoscience, v. 4, p. 545–548, doi:10.1038/ngeo1195.

Dragert, H., and Wang, K., 2011, Temporal evolution of an episodic tremor and slip event along the northern Cascadia margin: Journal of Geophysical Research, v. 116, doi:10.1029/2011JB008609.

Ellis, Densmore, and Anderson, 1999, Development of mountainous topography in the Basin Ranges, USA: Basin Research, v. 11, p. 21–41, doi:10/dqd54p.

England, P., and Molnar, P., 1990, Surface uplift, uplift of rocks, and exhumation of rocks: Geology, v. 18, p. 1173–1177, doi:10/brhdfj.

Friedrich, A.M., Wernicke, B.P., Niemi, N.A., Bennett, R.A., and Davis, J.L., 2003, Comparison of geodetic and geologic data from the Wasatch region, Utah, and implications for the spectral character of Earth deformation at periods of 10 to 10 million years: Journal of Geophysical Research: Solid Earth, v. 108, doi:10.1029/2001JB000682.

Hawthorne, J.C., and Rubin, A.M., 2013, Short-time scale correlation between slow slip and tremor in Cascadia: Journal of Geophysical Research: Solid Earth, v. 118, p. 1316–1329, doi:10.1002/jgrb.50103.

Hyndman, R.D., 2013, Downdip landward limit of Cascadia great earthquake rupture: Journal of Geophysical Research: Solid Earth, v. 118, p. 5530–5549, doi:10/gdg5dt.

Hyndman, R.D., and Wang, K., 1993, Thermal constraints on the zone of major thrust earthquake failure: The Cascadia Subduction Zone: Journal of Geophysical Research: Solid Earth, v. 98, p. 2039–2060, doi:10.1029/92JB02279.

Kelsey, H.M., Engebretson, D.C., Mitchell, C.E., and Ticknor, R.L., 1994, Topographic form of the Coast Ranges of the Cascadia Margin in relation to coastal uplift rates and plate subduction: Journal of Geophysical Research: Solid Earth, v. 99, p. 12245–12255, doi:10/b7xxpp.

Krogstad, R.D., Schmidt, D.A., Weldon, R.J., and Burgette, R.J., 2016, Constraints on accumulated strain near the ETS zone along Cascadia: Earth and Planetary Science Letters, v. 439, p. 109–116, doi:10.1016/j.epsl.2016.01.033.

Li, S., Moreno, M., Bedford, J., Rosenau, M., and Oncken, O., 2015, Revisiting viscoelastic effects on interseismic deformation and locking degree: A case study of the Peru-North Chile subduction zone: Journal of Geophysical Research: Solid Earth, v. 120, p. 4522–4538, doi:10.1002/2015JB011903.

Mahadevan, L., Bendick, R., and Liang, H., 2010, Why subduction zones are curved: Tectonics, v. 29, p. TC6002, doi:10.1029/2010TC002720.

Mansinha, L., and Smylie, D.E., 1971, The displacement fields of inclined faults: Bulletin of the Seismological Society of America, v. 61, p. 1433–1440.

McCaffrey, R., 2009, Time-dependent inversion of three-component continuous GPS for steady and transient sources in northern Cascadia: Geophysical Research Letters, v. 36, p. L07304, doi:10.1029/2008GL036784.

McCaffrey, R., King, R.W., Payne, S.J., and Lancaster, M., 2013, Active tectonics of northwestern U.S. inferred from GPS-derived surface velocities: Journal of Geophysical Research: Solid Earth, v. 118, p. 709–723, doi:10.1029/2012JB009473.

McCaffrey, R., Qamar, A.I., King, R.W., Wells, R., Khazaradze, G., Williams, C.A., Stevens, C.W., Vollick, J.J., and Zwick, P.C., 2007, Fault locking, block rotation and crustal deformation in the Pacific Northwest: Geophysical Journal International, v. 169, p. 1315–1340, doi:10.1111/j.1365-246X.2007.03371.x.

McCrory, P.A., Blair, J.L., Waldhauser, F., and Oppenheimer, D.H., 2012, Juan de Fuca slab geometry and its relation to Wadati-Benioff zone seismicity: Journal of Geophysical Research: Solid Earth, v. 117, p. B09306, doi:10.1029/2012JB009407.

Michel, L., Ehlers, T.A., Glotzbach, C., Adams, B.A., and Stübner, K., 2018, Tectonic and glacial contributions to focused exhumation in the Olympic Mountains, Washington, USA: Geology, v. 46, p. 491–494, doi:10/gc8z9w.

Niemi, N.A., and Clark, M.K., 2018, Long-term exhumation rates exceed paleoseismic slip rates in the central Santa Monica Mountains, Los Angeles County, California: Geology, v. 46, p. 63–66, doi:10/gcr9t5.

Okada, Y., 1985, Surface deformation due to shear and tensile faults in a half-space: Bulletin of the seismological society of America, v. 75, p. 1135–1154.

Penserini, B.D., Roering, J.J., and Streig, A., 2017, A morphologic proxy for debris flow erosion with application to the earthquake deformation cycle, Cascadia Subduction Zone, USA: Geomorphology, v. 282, p. 150–161, doi:10/f92b8h.

Rogers, G., and Dragert, H., 2003, Episodic Tremor and Slip on the Cascadia Subduction Zone: The Chatter of Silent Slip: Science, v. 300, p. 1942–1943, doi:10/bn8k7f.

Simpson, G., 2015, Accumulation of permanent deformation during earthquake cycles on reverse faults: Journal of Geophysical Research: Solid Earth, v. 120, p. 1958–1974, doi:10.1002/2014JB011442.

Stock, G.M., Frankel, K.L., Ehlers, T.A., Schaller, M., Briggs, S.M., and Finkel, R.C., 2009, Spatial and temporal variations in denudation of the Wasatch Mountains, Utah, USA: Lithosphere, v. 1, p. 34–40, doi:10.1130/L15.1.

Szeliga, W., Melbourne, T., Santillan, M., and Miller, M., 2008, GPS constraints on 34 slow slip events within the Cascadia subduction zone, 1997–2005: Journal of Geophysical Research, v. 113, doi:10/cg8z4f.

Wang, K., Hu, Y., and He, J., 2012, Deformation cycles of subduction earthquakes in a viscoelastic Earth: Nature, v. 484, p. 327–332, doi:10.1038/nature11032.

Wang, K., and Tréhu, A.M., 2016, Invited review paper: Some outstanding issues in the study of great megathrust earthquakes—The Cascadia example: Journal of Geodynamics, v. 98, p. 1–18, doi:10.1016/j.jog.2016.03.010.

Wang, K., Wells, R., Mazzotti, S., Hyndman, R.D., and Sagiya, T., 2003, A revised dislocation model of interseismic deformation of the Cascadia subduction zone: Journal of Geophysical Research: Solid Earth, v. 108, doi:10/fdqdh4.

Wech, A.G., and Bartlow, N.M., 2014, Slip rate and tremor genesis in Cascadia: Wech and Bartlow: Slip rate and tremor genesis: Geophysical Research Letters, v. 41, p. 392–398, doi:10.1002/2013GL058607.

Wech, A.G., and Creager, K.C., 2011, A continuum of stress, strength and slip in the Cascadia subduction zone: Nature Geoscience, v. 4, p. 624–628, doi:10.1038/ngeo1215.

Willett, S.D., and Brandon, M.T., 2002, On steady states in mountain belts: Geology, v. 30, p. 175–178, doi:10.1130/0091-7613(2002)030<0175:OSSIMB>2.0.CO;2.

Table 1: GPS data presented in this study.

	Coordinates		GPS signal[a]		Correction factor[b]	Residual vertical[c]	
Station name	Longitude (°)	Latitude (°)	Uplift rate (mm/yr)	1 SD (mm/yr)	Elastic component (mm/yr)	Uplift rate (mm/yr)	1SD (mm/yr)
ALBH	-123.4875	48.3898	0.35	0.35	1.29	-0.94	0.35
BLYN	-122.9275	48.0161	-3.36	0.48	1.00	-4.36	0.48
CPXX	-122.2565	46.8401	-0.38	0.47	0.24	-0.62	0.47
KTBW	-122.7954	47.5473	-0.96	0.19	1.37	-2.33	0.19
NEAH	-124.6249	48.2979	1.44	0.17	1.19	0.25	0.17
P064	-123.4877	47.9699	0.18	0.34	1.37	-1.19	0.34
P397	-123.7992	46.4216	0.25	0.29	1.33	-1.08	0.29
P398	-123.9162	46.9258	0.59	0.16	1.23	-0.64	0.16
P399	-123.6130	47.4339	1.21	0.23	1.37	-0.16	0.23
P400	-123.8125	47.5134	2.15	0.27	0.89	1.26	0.27
P401	-124.5570	47.9372	0.68	0.18	0.85	-0.17	0.18
P402	-124.3059	47.7662	1.74	0.24	1.07	0.67	0.24
P403	-124.1409	48.0623	1.53	0.43	1.37	0.16	0.43
P408	-123.3766	46.2005	-0.86	0.22	1.09	-1.95	0.22
P410	-123.0786	46.1111	-1.29	0.25	0.68	-1.97	0.25
P415	-123.7299	46.6560	0.94	0.32	1.29	-0.35	0.32
P417	-123.2979	46.5747	-0.99	0.14	1.08	-2.07	0.14
P418	-123.4078	47.2366	-0.19	0.2	1.31	-1.50	0.2
P419	-123.3665	47.4093	0.05	0.21	1.33	-1.28	0.21
P420	-122.8663	46.5886	-0.93	0.24	0.64	-1.57	0.24
P421	-122.4292	46.5319	0.18	0.98	0.23	-0.05	0.98
P423	-122.9412	47.2879	-0.92	0.16	1.05	-1.97	0.16
P424	-122.8747	47.8232	0.28	0.22	1.03	-0.75	0.22
P425	-122.8454	46.4527	-1.51	0.33	0.56	-2.07	0.33
P426	-122.5146	47.8027	-2.98	0.22	0.55	-3.53	0.22
P430	-123.4362	47.0038	-0.95	0.16	1.30	-2.25	0.16
P435	-123.5033	48.0596	-0.12	0.48	1.37	-1.49	0.48
P436	-123.1344	48.0453	-0.05	0.21	1.18	-1.23	0.21
P437	-122.4592	48.0018	-1.18	0.42	0.53	-1.71	0.42
P438	-122.6703	48.4192	-0.97	0.28	0.57	-1.54	0.28
P439	-122.9093	48.7082	-0.30	0.19	0.51	-0.81	0.19
P440	-122.4933	48.8562	-0.96	0.29	0.17	-1.13	0.29
P441	-122.1396	48.9160	0.16	0.44	0.07	0.09	0.44
P446	-122.8928	46.1157	-1.29	0.24	0.47	-1.76	0.24
PABH	-124.2046	47.2128	-0.25	0.17	1.12	-1.37	0.17
PCOL	-122.5708	47.1721	-0.96	0.39	0.56	-1.52	0.39
PUPU	-122.0081	47.4996	-1.26	0.26	0.18	-1.44	0.26
SC02	-123.0076	48.5462	-0.43	0.23	0.80	-1.23	0.23
SC03	-123.7057	47.8166	2.00	0.22	1.38	0.62	0.22
SC04	-123.7041	48.9232	0.74	0.26	0.92	-0.18	0.26
SEAT	-122.3095	47.6540	-1.70	0.2	0.36	-2.06	0.2
SEDR	-122.2239	48.5216	-0.75	0.34	0.18	-0.93	0.34
TPW2	-123.7684	46.2074	-0.17	0.18	1.36	-1.53	0.18
TWHL	-122.9229	47.0159	0.16	0.23	0.94	-0.78	0.23

Notes:

[a]: In order to remove effects of hydrology and seasonal atmospheric loading, the GPS signal has been treated according to the procedure in the text

[b]: The correction factor corresponds to the elastic component of the GPS signal, as calculated with the elastic model of Wang et al. (2003).

[c]: The residual verticals corresponds to the GPS signal corrected by the elastic component. It should yield an estimate of the permanent deformation as recorded by GPS.

3.3.3 Supplement for "Frictional transition leaves a permanent mark in Cascadia."

Electronic supplement for

Frictional transition leaves a permanent mark in Cascadia

Lorenz Michel, Todd A. Ehlers, Rebecca Bendick

1 Details for denudation rates

Figure S1a displays the pattern of denudation rates from Michel et al. (2018) obtained from thermo-kinematic modeling of thermochronologic cooling ages. The modeled denudation rates are based on the bedrock cooling ages reported in Michel et al. (2018), as well as earlier thermochronology data (Brandon and Vance, 1992; Brandon et al., 1998; Batt et al., 2001). Further details about the modeling procedure are reported in Michel et al. (2018). In the profiles of Figure 2 in the main manuscript, the denudation rates are plotted at the respective sample location (white squares in Fig. S1a).

Denudation rates from cosmogenic nuclide dating are based on denudation rates derived from ^{10}Be dating of detrital river sand samples (Adams and Ehlers, 2018). Figure S1b displays the values of the reported denudation rates at the respective sample location. Note however, that these rates correspond to catchment-wide denudation rates, so strictly speaking they also provide information about the denudation rates in the respective catchment upstream of the sample location

2 Details for GPS datasets

The procedure of how our GPS data are treated is described in the main text and a data table containing the respective GPS stations locations along with the respective velocities can be found in supplementary Table 1. A map view of the GPS velocities is provided in Figure S2a. As we mention in the text, we forward model the elastic component of deformation using the model of Wang et al. (2003). The corresponding calculated values are shown in map view in Figure S2b. After subtraction of the calculated elastic component from the GPS signal, the obtained residual vertical velocities should correspond to the permanent deformation component of the GPS signal (Figure S2c).

We also consider the vertical displacement caused by slow slip events (SSE), which have been reported in Bruhat and Segall (2016). The corresponding values are depicted in Figure S2d.

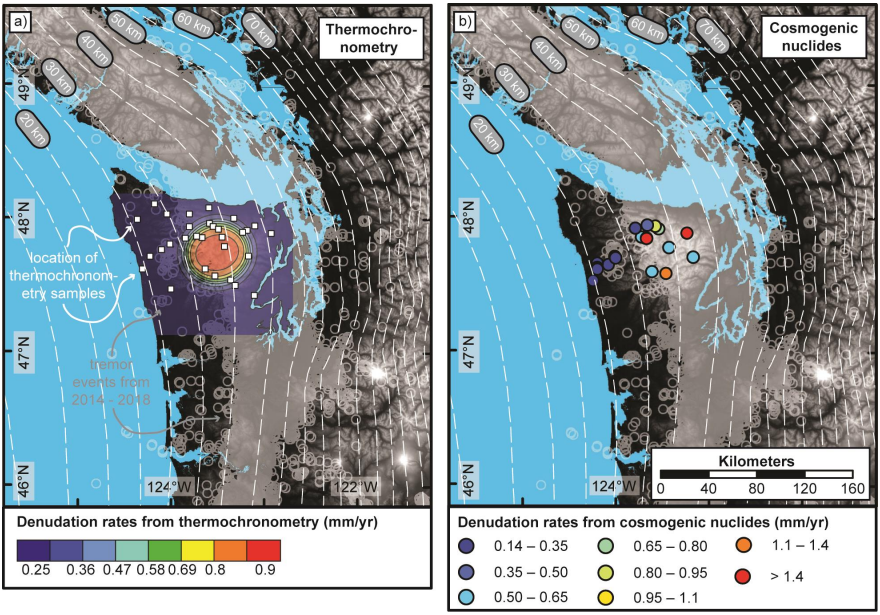

Figure S1: a) Ellipse-shaped map of denudation rates obtained from thermo-kinematic modeling of thermochronologic cooling ages (Michel et al., 2018). b) Catchment-wide denudation rates based on cosmogenic nuclide dating from Adams and Ehlers (2018). Data presented in all subpanels include the depth to the top of the subducted slab (white dashed lines; from McCrory et al., 2012) and the spatial occurrence of tremor events from 2014 – 2018 (grey circles or grey area), which is based on data from the Pacific Northwest Seismic Network (https://pnsn.org/tremor).

3 Seismicity within the Olympic Mountains

Figure S3 displays the seismicity along a transect across the center of the Olympic Peninsula. Plotted are all earthquakes from the USGS catalog with a magnitude >2.5 for the time period from 1980 until today, within a 80 km wide box. Contrary to that, the topography, top of oceanic crust and the location of the Hurricane Ridge Fault (HRF) are plotted along a line. The depth to the top of the subducted slab is taken from the Slab1.0 model (McCrory et al., 2012). The location of the HRF, which separates the accreted sediment from the overlying basaltic rocks of the Coast Range Terrane, is taken from a geologic map (Tabor and Cady, 1978) at the surface and from a seismic study (Calvert et al., 2011) at depth.

The profile shows, that the accretionary wedge below the Olympic Mountains is basically devoid of seismicity. All recorded earthquakes occur either close to or in the hanging wall of the HRF, or can be found close to the top of the subducting slab.

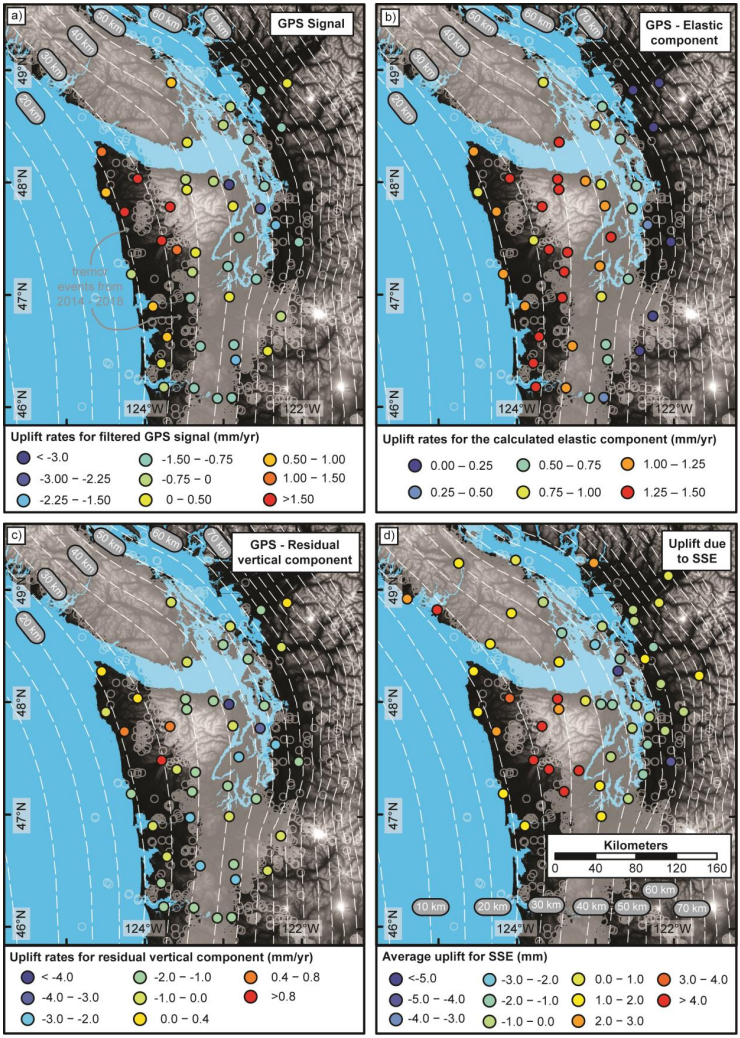

Figure S2: Maps of the location of GPS stations considered in this study and the respective velocities. a) Rock uplift rates for GPS stations reported in this study. The rates are not corrected for the elastic component. b) Values for the elastic component calculated at the respective location of the GPS station using the model of Wang et al. (2003). c) Residual vertical GPS velocities, which are corrected for the elastic component. d) Rock uplift due to slow slip events (SSE) as reported by Bruhat and Segall (2016). The observed displacement corresponds to the average displacement from eight events recorded between 2000 – 2015. Data presented in all subpanels include the depth to the top of the subducted slab (white dashed lines; from McCrory et al., 2012) and the spatial occurrence of tremor events from 2014 – 2018 (grey circles or grey area), which is based on data from the Pacific Northwest Seismic Network (https://pnsn.org/tremor).

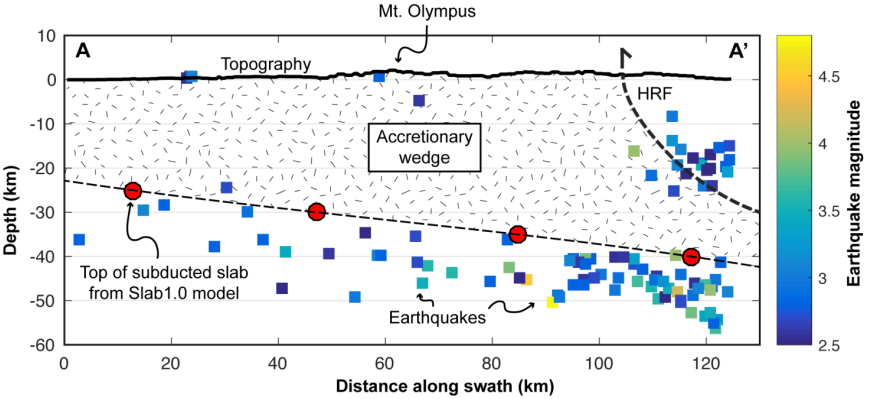

Figure S3: Cross section through the Olympic Peninsula in the middle of swath profile A/A'. The accretionary wedge is bounded by the top of the subducted slab (McCrory et al. 2012) and the Hurricane Ridge Fault (HRF), which is taken from Tabor ad Cady (1978) at the surface and from Calvert et al. (2011) at depth. Earthquakes are from the USGS earthquake catalog (https://earthquake.usgs.gov/earthquakes/search/) and color-coded by magnitude.

4 References

Adams, B.A., and Ehlers, T.A., 2018, Tectonic controls of Holocene erosion in a glaciated orogen: Earth Surf. Dynam., v. 6, p. 595–610, doi:10/gdzw94.

Batt, G.E., Brandon, M.T., Farley, K.A., and Roden-Tice, M., 2001, Tectonic synthesis of the Olympic Mountains segment of the Cascadia wedge, using two-dimensional thermal and kinematic modeling of thermochronological ages: Journal of Geophysical Research: Solid Earth, v. 106, p. 26731–26746, doi:10.1029/2001JB000288.

Brandon, M.T., Roden-Tice, M.K., and Garver, J.I., 1998, Late Cenozoic exhumation of the Cascadia accretionary wedge in the Olympic Mountains, northwest Washington State: Geological Society of America Bulletin, v. 110, p. 985–1009, doi:10.1130/0016-7606(1998)110<0985:LCEOTC>2.3.CO;2.

Brandon, M.T., and Vance, J.A., 1992, Tectonic evolution of the Cenozoic Olympic subduction complex, Washington State, as deduced from fission track ages for detrital zircons: American Journal of Science, v. 292, p. 565–636, doi:10.2475/ajs.292.8.565.

Bruhat, L., and Segall, P., 2016, Coupling on the northern Cascadia subduction zone from geodetic measurements and physics-based models: Journal of Geophysical Research: Solid Earth, v. 121, p. 8297–8314, doi:10.1002/2016JB013267.

Calvert, A.J., Preston, L.A., and Farahbod, A.M., 2011, Sedimentary underplating at the Cascadia mantle-wedge corner revealed by seismic imaging: Nature Geoscience, v. 4, p. 545–548, doi:10.1038/ngeo1195.

McCrory, P.A., Blair, J.L., Waldhauser, F., and Oppenheimer, D.H., 2012, Juan de Fuca slab geometry and its relation to Wadati-Benioff zone seismicity: Journal of Geophysical Research: Solid Earth, v. 117, p. B09306, doi:10.1029/2012JB009407.

Michel, L., Ehlers, T.A., Glotzbach, C., Adams, B.A., and Stübner, K., 2018, Tectonic and glacial contributions to focused exhumation in the Olympic Mountains, Washington, USA: Geology, v. 46, p. 491–494, doi:10/gc8z9w.

Tabor, R.W., and Cady, W.M., 1978, The structure of the Olympic Mountains, Washington: Analysis of a subduction zone: US Govt. Print. Off., v. 1033.

Wang, K., Wells, R., Mazzotti, S., Hyndman, R.D., and Sagiya, T., 2003, A revised dislocation model of interseismic deformation of the Cascadia subduction zone: Journal of Geophysical Research: Solid Earth, v. 108, doi:10/fdqdh4.

3.4 Effects of glacial erosion on topography

3.4.1 Declaration on contributions to joint work

The following section contains an early version of a manuscript entitled "Reduction of topography by glacial erosion in the Olympic Mountains (USA)". It aims at evaluating the role played by glacial erosion in modifying the topography of the Olympic Mountains. At the time of submission of the thesis, this manuscript represents an initial draft version and it has not been through several rounds of commenting by the co-authors.

Two authors are responsible for developing this manuscript: Lorenz Michel (LM) and Todd Ehlers (TE). TE and LM developed the idea of investigating the role of glacial erosion on topography in more detail, by using a new modelling approach, compared to the modelling of sections 3.1.2. LM compiled all available thermochronometer ages and conducted the simulations using Pecube. Analysis of the model outcomes was done by LM with suggestions by TE. LM created this draft version of the manuscript along with the figures and TE provided minor comments on it.

Table 3.4: Summary of the contribution to joint work for the manuscript "Reduction of topography by glacial erosion in the Olympic Mountains (USA)", indicating the average fraction of work by the respective author in percent. The manuscript is currently in preparation.

Author	Position	Scientific ideas (in %)	Data generation (in %)	Analysis and Interpretation (in %)	Paper writing (in %)
LM	[1]	80	100	90	90
TE	[2]	20	0	10	10

3.4.2 Draft version of manuscript: "Reduction of topography by glacial erosion in the Olympic Mountains (USA)"

Reduction of topography by glacial erosion in the Olympic Mountains (USA)

Lorenz Michel, Todd Ehlers

Introduction

The opposingly directed processes of tectonically-driven rock uplift and climate-controlled denudation create the topography of active mountain ranges. A balance between the two processes, implying topographic steady-state whereby topography is invariant through time, is an assumption that is inherent for many studies investigating the evolution of mountain ranges (e.g., Willett, 1999; Willett and Brandon, 2002). However, the assumption that the present-day topography (as for instance derived from digital elevation models) is equivalent to the topography over the entire, million-year lifespan of an orogen is not ambiguous: The dynamic behavior of climate leads to temporal variations in denudation, which could potentially lead to changes in topography. Hence, reconstructing the temporal evolution of topography or putting temporal constraints on changes in topography contributes to a better understanding of the evolution of mountain belts and of the effects that tectonics or climate have on the development of orogens (Champagnac et al., 2012).

In particular, the effect of Cenozoic climate change, which led to intense glaciation of many mid- to high-latitude orogens during the Plio-Pleistocene, could have affected the topography of mountain ranges (Molnar and England, 1990). Alpine glaciers as well as icesheets are powerful agents of erosion, efficiently remove mass, and thereby significantly overprint an existing, pre-glacial landscape. This includes the formation of U-shaped valleys, an increase in relief, development of bimodal landscapes with low relief plateaus and deeply incised fjords, and an overall limitation of mountain elevation (Montgomery, 2002; Shuster et al., 2005; Mitchell and Montgomery, 2006; Egholm et al., 2009, 2017; Valla et al., 2011; Steer et al., 2012; Sternai et al., 2012; Andersen et al., 2018). The erosive capability of glaciers depends on the conditions at the base of the glacier (e.g., Herman et al., 2011; Yanites and Ehlers, 2016), and is generally highest close to the equilibrium line altitude (ELA) of a glacier (Egholm et al., 2009; Sternai et al., 2011; Herman et al., 2011). In turn, the distribution of the ELA can be a consequence of the orographic precipitation pattern between windward and leeward sides of mountain ranges (Porter, 1964). Hence, particularly orogens with well-developed precipitation gradients are potentially affected by glacial erosion, but on the other hand, also offer the opportunity to constrain the effects of glaciation on topography.

An estimate of the volume of material removed by glacial erosion can be obtained from offshore sediment records in front of mountain ranges, which allows to approximate the pre-glacial paleo-topography (e.g., Steer et al., 2012). However, where the sediment record is sparse, not continuous or the sediment is derived from various source regions, the approach is hindered. On the other hand, the thermal structure of the Earth's crust is sensitive to the long- and short-wavelength topography (Stüwe et al., 1994; Mancktelow and Grasemann, 1997), affecting the cooling histories of rock samples during exhumation. Hence, constraints on the temporal evolution of topography can be obtained from rock samples dated with low-temperature thermochronometry methods (House et al., 1998; Braun, 2003), and attempts to use low-temperature thermochronometry together with thermo-kinematic modelling were successful to constrain the effect of glacial erosion on topography (Ehlers et al., 2006; Olen et al., 2012).

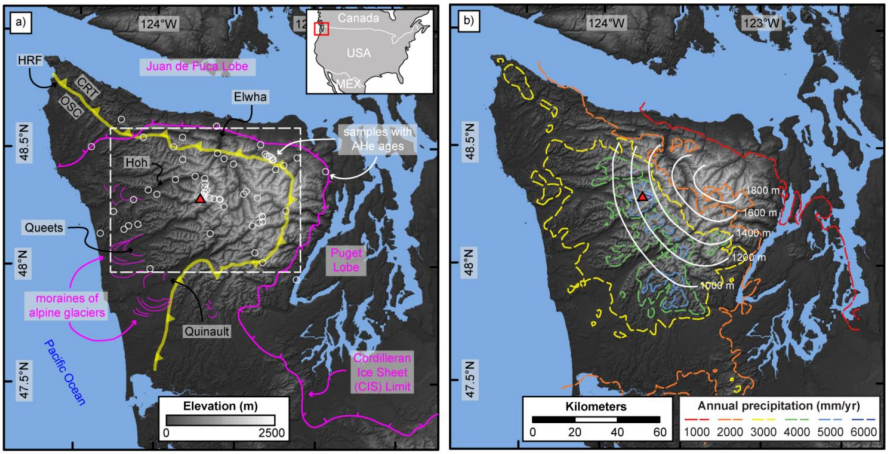

Figure 1: Topography of the Olympic Peninsula, along with **(a)** quaternary features and the location of the Hurricane Ridge Fault (HRF), which separates the Olympic Structural Complex (OSC) from the surrounding Coast Range Terrane (CRT). Major river valleys (Hoh, Queets, Quinault, Elwha) are indicated. The white circles are locations of low-temperature thermochronometry samples, for which AHe ages are available. The dashed, white box outlines the area considered for the modelling of this study, which is shown in a close-up view in Figure 2. **(b)** Precipitation pattern in the Olympic Mountains together with the distribution of the Pleistocene equilibrium line altitude (ELA, white lines). In both panels, the red triangle corresponds to the location of Mt. Olympus (2430 masl). Location of the HRF is based on Brandon et al. (1998). The quaternary features are from Porter (1964) and Tabor and Cady (1978). Precipitation pattern is taken from the prism dataset (http://prism.oregonstate.edu/) and the ELA is from Porter (1964).

Here, we try to constrain the effects of glacial erosion on the topographic evolution of the Olympic Mountains (USA, Figure 1a). The Olympic Mountains were introduced as a textbook steady-state mountain range (Brandon et al., 1998; Batt et al., 2001; Willett and Brandon, 2002), but the topography also displays clear evidence of Plio-Pleistocene glaciation (Montgomery, 2002; Adams and Ehlers, 2017). A strong precipitation gradient between the west and east side of the orogen can be observed, which also results in a strong west-east variation of the location of the Pleistocene ELA (Figure 1b). The role of glacial erosion on the orogen-wide denudation and exhumation rates is viewed contentious, suggesting either a pronounced increase in denudation rates with the onset of glaciation (Herman et al., 2013; Michel et al., 2018a, 2018b) or a negligible effect (Schildgen et al., 2018). Michel et al. (2018a) suggested an increase in denudation rates by 50–150 % occurring at 2–3 Ma and indicated that the western flank of the Olympic Mountains likely experienced a reduction in topography. Based on topographic analysis, a potential reduction in topography related to glacial erosion was also suggested for the area around Mt. Olympus, the highest peak of the range (Montgomery and Greenberg, 2000). However, a detailed analysis of the effects of glacial erosion on the topography and a quantification of the variation in topography has not been obtained so far.

We capitalize on the large, low-temperature thermochronometry dataset that is available for the Olympic Mountains (Batt et al., 2001; Michel et al., 2018a,2018b). We use these thermochronometric ages in order to deploy the thermo-kinematic model Pecube, building upon the exhumation histories suggested by Michel et al. (2018a). Based on the

misfit between observed and modelled thermochronometric cooling ages, we try to assess, in which part of the Olympic Mountains the suggested exhumation histories can successfully predict apatite (U-Th)/He (AHe) ages. We observe that even an increase in exhumation rates by 70–200% at 2–3 Ma is not enough to explain the young AHe ages on the western side of the mountain range. However, the same relative amount of increase results in modeled AHe ages that are too young compared to observed ages in the central part of the orogen. This suggests that the increase in exhumation rates is spatially extremely variable and strongest on the western side, which also corresponds to the area of lowest, Plio-Pleistocene ELA. We interpret that the increase in exhumation rate must result in a reduction in topography, because it is not accompanied by a commensurate increase in rock uplift, as is evidenced by published cosmogenic nuclide data. Based on the absolute increase in exhumation rate, a reduction in topography by up to 1000 m could have occurred locally during the past 2 Myr.

Regional Background

The Olympic Mountains are part of the Cascadia Subduction zone and are located at the west coast of the North American continent (Figure 1a). The orogen corresponds to the aerially exposed accretionary wedge of the subduction zone (Tabor and Cady, 1978; Brandon et al., 1998), consisting of Oligocene to Miocene-aged turbidite deposits in the center of the range, which are enclosed by basaltic and minor sedimentary rocks of the Coast Range Terrane (Figure 1a). Exhumation of the mountain range commenced at around 18 Ma, and since 14 Ma the orogen is suggested to be in steady-state (Brandon et al., 1998; Batt et al., 2001). In general, the exhumation and topography of the range is controlled by the subducting Juan de Fuca plate, which due to its bent shape leads to a localization of deformation and exhumation at the location of the Olympic Mountains (Bendick and Ehlers, 2014; Adams and Ehlers, 2017; Michel et al., 2018a; Adams and Ehlers, 2018). Hence, the general pattern of exhumation is ellipse-shaped, with highest exhumation rates in the center of the mountain range (Figure 3b), but exhumation is also temporally variable, either due to tectonic (Michel et al., 2018b) or climatic variations (Herman et al., 2013; Michel et al., 2018a). A large thermochronometry datasets exists for the Olympic Mountains, encompassing apatite and zircon (U-Th)/He (AHe and ZHe, respectively) and apatite and zircon fission-track (AFT and ZFT) ages (Brandon et al., 1998; Batt et al., 2001; Michel et al., 2018a, 2018b). In general, ages are youngest in the center of the mountain range and increase in age towards the coast. Here unreset ages can be observed, implying that the sandstones of this area have not been exposed to temperatures high enough to overprint the thermochronometric signal from the source region of the sandstones.

Because the Olympic Peninsula is surrounded by sea in the west, north and east, elevation increases within a short distance (~30–40 km) from the low-elevation, low-relief coastal areas towards the central, high topography part of the mountain range. Here, the maximum elevations are between 2000–2400 masl, cresting in Mt. Olympus (2430 masl). The Plio-Pleistocene glaciation shaped the present-day topography. Alpine glaciers incised into the landscape (Montgomery, 2002; Adams and Ehlers, 2017), forming the deeply incised valleys of the major rivers within the Olympic Mountains (Hoh, Quinault, Queets, Elwha, Dosewallips), which originate in the central high topography part and trend radially towards the coast (Figure 1a, 2). Alpine glaciers originating in the center of the range formed large piedmont-glaciers, almost reaching the Pacific Ocean on the western side of the range (Thackray, 2001). The Juan de Fuca and the Puget

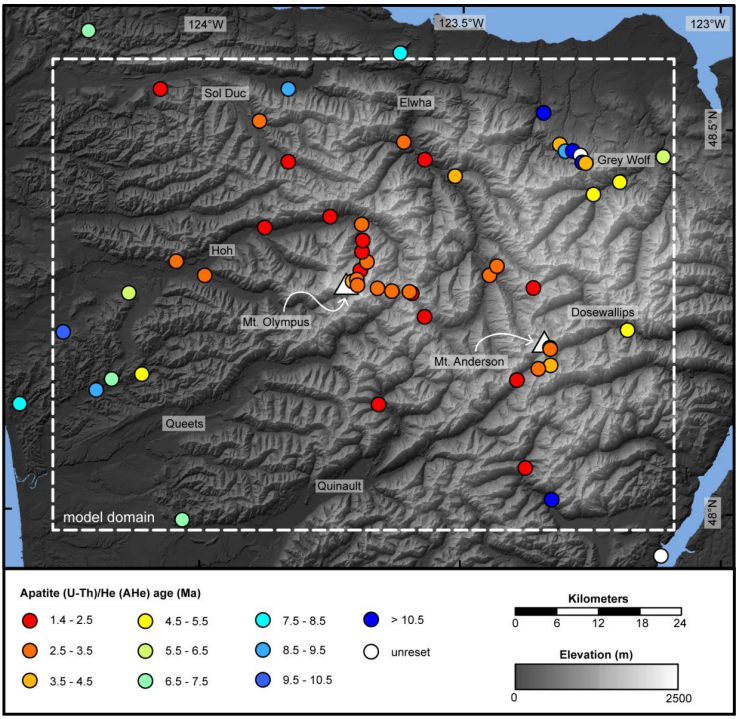

Figure 2: Close up view of the Olympic Mountains. Colored symbols correspond to AHe ages, taken from Batt et al. (2001) and Michel et al. (2018a, 2018b). The area inside the white box is the model domain, considered for the topographic inversion in this study. The names of the major river valleys are given as well, and the white triangles denote the location of major mountains referred to in the text (Mt. Olympus and Mt. Anderson).

Lobe of the Cordilleran Ice Sheet surrounded the mountain range on the northern and eastern side (Booth et al., 2003), respectively, covering large parts of today's low-elevation, low-relief landscape (Figure 1b).

Due to the proximity to the Pacific Ocean and the barrier effect of the mountain range, the Olympic Mountains receive high amounts of precipitation and display a strong orographic precipitation pattern (Figure 1b). The western parts generally receive more than 3000 mm/yr of precipitation, culminating in 5000–6000 mm/yr close to Mt. Olympus. On the contrary, the area to the east of the Elwha valley is much drier and receives less than 2000 mm/yr. This strong precipitation gradient also affected the distribution of the Pleistocene equilibrium line altitude (ELA). To the east of the Elwha valley, the ELA is located at locations above 1600 m, to the west of the Elwha valley the ELA is located between 1000–1400 m (Porter, 1964).

Methods

In the case a mountain range is in topographic steady-state, so that topography is temporally invariant and no surface uplift occurs, rock uplift equals exhumation (England and Molnar, 1990). In the absence of extensional faults, removal of rock by denudation at the Earth's surface is the prime mechanism controlling exhumation. If a change in exhumation occurs, i.e., an increase in denudation due to a variation in climate, which is not counterbalanced by an equal amount of change in rock uplift, a variation in the topography must occur. Therefore, knowing the exhumation history of an area allows to obtain estimates of possible variations in topography.

Quantitative constraints on exhumation can be obtained by dating rock samples with low-temperature thermochronometry like AHe or ZHe, which allows to reconstruct the cooling histories of rock samples during their path from depth to the surface of the Earth. The technique is based on the principle, that the obtained radiometric age corresponds to the time, when the rock sample cooled below a certain temperature, the closure temperature of the respective thermochronometric system. For instance, the closure temperature of AHe is about 60–70 °C (Farley, 2002), which allows to constrain cooling through the upper 2–3 km of the Earth's crust, assuming a geothermal gradient of 20–30 °C/km. This near surface temperature field is particularly sensitive to the effects of long- and short-wavelength topography (Figure 3a), so that low-temperature isotherms often reflect the shape of the topography (Stüwe et al., 1994).

However, the assumption of a temporally constant geothermal gradient is a limitation, because the temporal evolution of the geothermal gradient depends on contributions from heat advection, heat conduction, heat production and the effects of topography, and can therefore be transient over time. Hence, the usage of thermo-kinematic models is required in order to obtain quantitative constraints on exhumation or variations in topography from thermochronometric data. Various studies have documented the potential of using AHe ages together with thermo-kinematic models in order to reconstruct the effects of fluvial or glacial erosion on topography (House et al., 1998; Braun, 2003; Ehlers et al., 2006; Olen et al., 2012). Pecube is a finite-element, thermo-kinematic model (Braun, 2003), which allows to predict thermochronometric cooling ages by prescribing an exhumation history, topography and physical parameters like heat conduction or heat production. Depending on the misfit between modelled and observed thermochronometric cooling ages, the viability of a certain exhumation history can be assessed.

In this work, we use Pecube for our modeling purposes and we base our modelling approach on the work of Michel et al. (2018a). They suggested that an ellipse-shaped exhumation pattern with exhumation rates of 0.9 km/Myr in the center of the ellipse and exhumation rates of 0.25 km/Myr outside the ellipse (Figure 3b) is required to explain the observed thermochronometric age pattern of the higher closure temperature systems (AFT, ZHe, ZFT). Furthermore, they suggested that an increase in exhumation rates by 50–150% at 2–3 Ma is required to explain the young AHe ages (i.e., 1.5–2.5 Ma, Figure 2). They also noted that the increase in exhumation is likely higher on the western side of the mountain range (i.e., in the Hoh valley west of Mt. Olympus, Figure 2). For this work, we build upon these findings, but also include the additional AHe ages published in Michel et al. (2018b), significantly increasing the resolution of the model in the areas surrounding Mt. Olympus and Mt. Anderson (Figure 2). Michel et al. (2018a) assessed the viability of their models by using a cumulative misfit criterion, where the misfit of the single samples is totaled. We apply a redefined

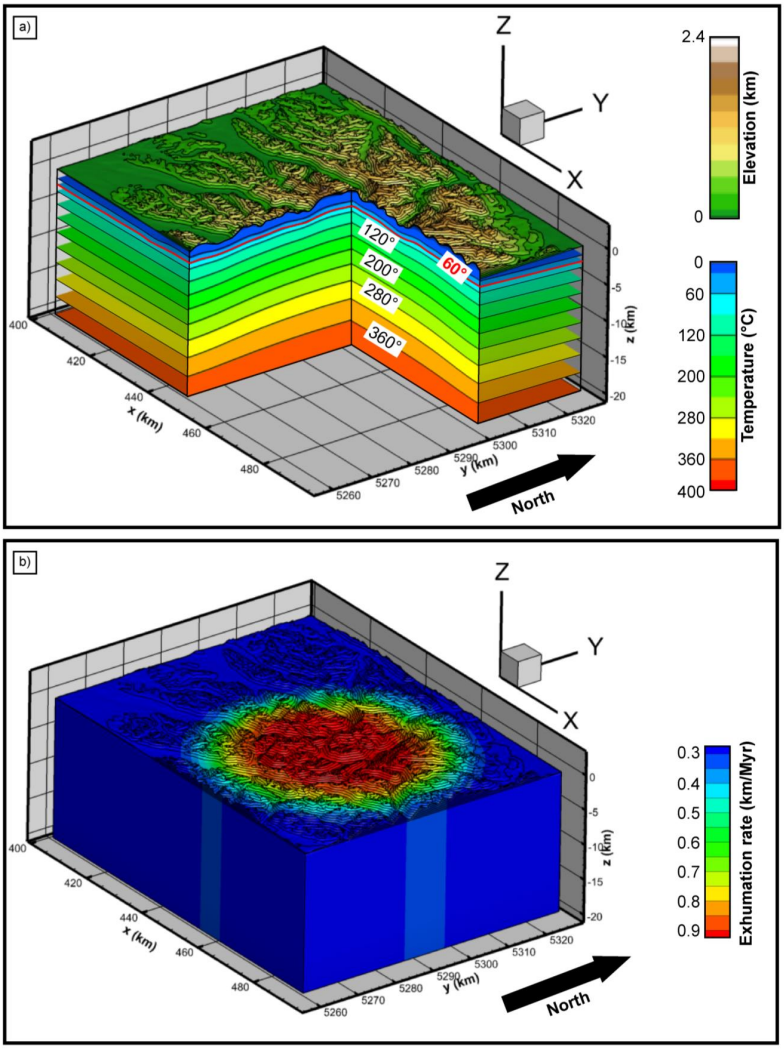

Figure 3: **(a)** Three-dimensional view showing the thermal structure in the center of the model domain. Isotherms (lines of equal temperature) are bent because of heat advection by exhumation (long wavelength bend) and the low temperature isotherms are deflected due to the effects of topography. The 60°C isotherm corresponds to the approximate closure temperature of AHe. **(b)** Ellipse-shaped exhumation rate pattern suggested by Michel et al. (2018a) and used in our modeling. Rates are as high as 0.9 km/Myr in the center of the ellipse and decrease to values of 0.25 km/Myr at the edges of the model domain. Both panels are vertically exaggerated by a value of x1.4.

misfit criterion in order to assess the goodness of fit of our simulations, where the misfit for each sample is considered separately. Here, the misfit (Δ) is defined as

$$\Delta = \frac{age_{mod} - age_{obs}}{\sigma_{obs}} \quad (1)$$

and depends on the modelled age (age_{mod}), the observed age (age_{obs}) and the reported uncertainty of the observed age (σ_{obs}). We explicitly do not square our misfit as e.g., is commonly done for a χ^2-misfit criterion and has been done in Michel et al. (2018a), hence the observed misfit can be positive or negative. An explanation of the meaning of the positive or negative nature and the actual value of the misfit is given in the discussion section.

Our detailed model setup is as follows. The model domain encompasses an area approximately 90x60 km wide in the central, high topography part of the Olympic Mountains, including most of the AHe ages available in the orogen (Figure 2). The physical parameters used for our simulations are given in Table 2. Furthermore, we use the present-day topography as input in our simulations and keep the topography constant during the entire duration of the model. Following Brandon et al. (1998), exhumation of the Olympic Mountains starts at 18 Ma and reaches steady exhumation at 14 Ma. We deploy the ellipse-shaped exhumation rate pattern (Figure 3b) suggested by Michel et al. (2018a) and either consider the case of steady exhumation rates during the entire 14 Myr period or the increase scenarios suggested by Michel et al. (2018a), where exhumation rates increase at 2 Ma, 3 Ma or 5 Ma by the respective amount. The resulting eight increase scenarios are summarized in Table 1. Based on these simulations, we calculate the misfit between observed and modeled ages according to Equation 1, which is displayed at the location of each sample for the respective model scenario (Figure 4). However, there are some samples, which have unreset AHe ages (white circles in Figure 2). None of our simulations is able to predict unreset AHe ages, hence we exclude samples with unreset AHe ages from our further analysis (the respective locations are not shown on Figure 4). In total, we use the AHe ages from 52 samples during our further analysis and Table 3 summarizes the data of all these samples.

Results

The calculated misfit between modeled and observed AHe ages at the location of the respective sample site is displayed in Figure 4. In the case of steady exhumation and no temporal variation in exhumation rate over 14 Myr the observed misfit varies between values of -11.1 and 21.6, but most samples have misfit values between 0 and 5 (Table 3). Looking at the spatial distribution of misfit reveals that the misfit for the samples from the central part of the orogen is low (i.e., many white or light reddish/blueish symbols in Figure 4i). This particularly pertains to the samples from higher elevations at Mt. Olympus or Mt. Anderson. However, samples from the western part of the orogen or samples taken at lower elevation close to the bottom of river valleys (e.g. Hoh, Elwha or Sol Duc valleys) display a misfit larger than 3 (i.e., deep red symbols in Figure 4i).

Considering an increase in exhumation rate at 2 Ma, 3 Ma or 5 Ma by 50–200% changes the observed misfit compared to the constant rate simulation (Table 3) and results in a spatial dichotomy of the observed misfit pattern. In the center of the orogen encompassing the area of the Elwha valley, Mt. Olympus and Mt. Anderson, all eight increase scenarios (Figure 4a-h) yield misfit values smaller than -3 (i.e., deep blue symbols). However, an increase by 50% or 70%

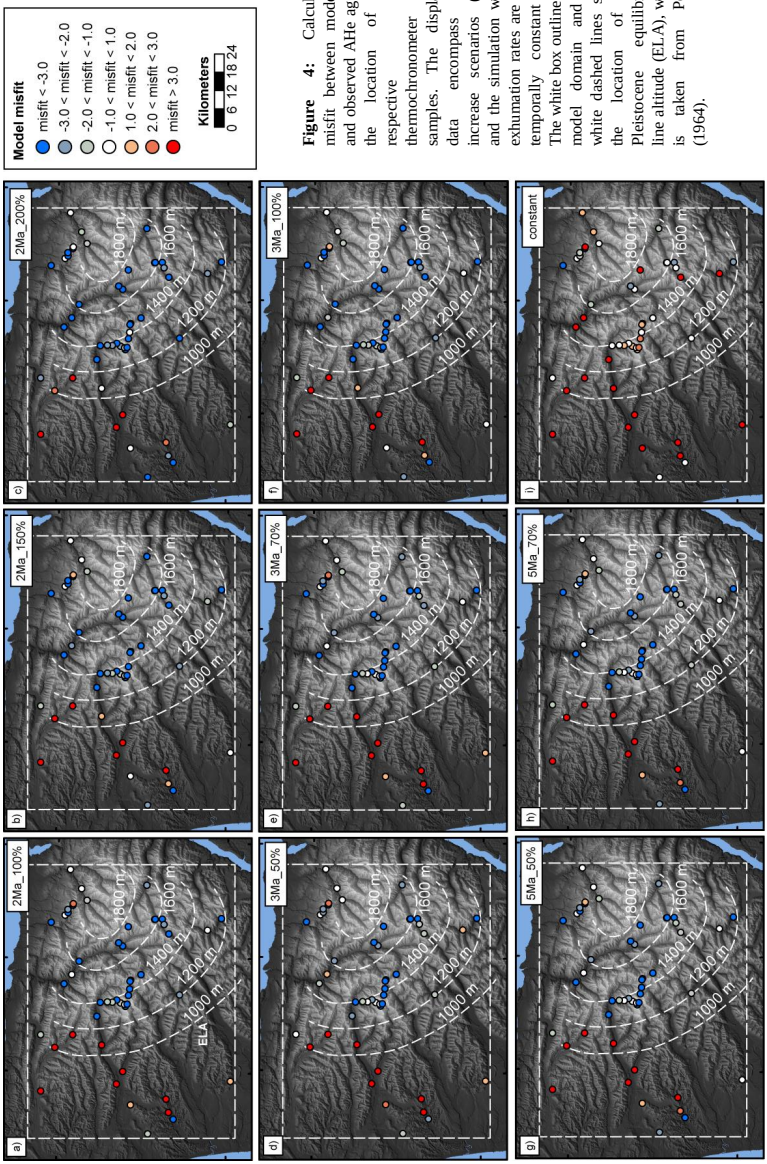

Figure 4: Calculated misfit between modelled and observed AHe ages at the location of the respective thermochronometer samples. The displayed data encompass the increase scenarios (a-h) and the simulation where exhumation rates are kept temporally constant (i). The white box outlines the model domain and the white dashed lines show the location of the Pleistocene equilibrium line altitude (ELA), which is taken from Porter (1964).

at 3 Ma or 5 Ma produces an acceptable misfit between -3 and 1 for some of the samples close to Mt. Olympus. On the contrary, most samples from the western part of the mountain range (Hoh and Sol Duc valleys) still display highly positive misfit values larger than 3.

Discussion

The aim of this study is to investigate, how glacial erosion has affected the topography of the Olympic Mountains. Therefore, it is important to know the exhumation history of this orogen and to constrain possible effects of glacial erosion on the exhumation. With our modeling, we tried to investigate, how a possible increase of the exhumation rate due to the onset of Plio-Pleistocene glaciation affected thermochronometric cooling ages. The calculated misfit allows to judge, whether a particular exhumation history suffices to explain the observed AHe ages.

In Figure 5, all the misfit values for the variable exhumation scenarios are summarized along a west-east transect crossing the Olympic Peninsula. A positive misfit implies that the modeled age is too old and hence that the assumed exhumation was too slow, whereas a negative misfit implies that the modeled age is too young such that the assumed exhumation was too fast (Figure 5b). The actual value yields information about how well a particular model can reproduce the observed AHe age. In our case we consider a misfit between 2 and -2 as a good fit (Figure 5b), meaning that the respective simulation can reproduce the observed age within two times the reported uncertainty. Hence, a reduction in misfit is obtained during a simulation with an increase in exhumation rate (compared to the simulation with temporally constant exhumation rates,), if the respective misfit approaches values of 2 to -2. A deterioration in misfit occurs, if the misfit approaches values significantly outside the bounds of 2 to -2. Bearing that in mind, the observed misfit (e.g. Figure 4 and 5b) can be interpreted as follows.

A constant exhumation history over 14 Myr with no increase in exhumation rates results in an acceptable misfit for many of the observed samples (i.e., their misfit is between -2 and 2) in the central, high topography part of the orogen (between longitudes 123.8°W and 123.2°W in Figure 5). The misfit for most of these samples tends to more negative values (therefore the misfit is increased) if the exhumation rates are increased, because the modeled AHe ages are then too young compared to the observed ages. With the exception for some samples close to Mt. Olymus, this effect is also irrespective of the considered timing (2 Ma, 3 Ma or 5 Ma) and amount of increase (50–200 %). These observations suggest that at least in the central part of the orogen the relative amount of increase in exhumation rates as suggested by Michel et al. (2018a) is too high, and is less in that part of the mountain range. We hypothesize that an increase in exhumation rate by 10–25% at 2–3 Ma is likely a more realistic value. On the contrary, samples from the western, low elevation part of the orogen (i.e., between longitudes of 124.2°W and 123.8°W) can not successfully be modeled using a temporally constant exhumation rate and the modeled ages are too old. Here, increasing the exhumation rate decreases the observed misfit, but for many of the samples the misfit is still not in the accepted range of 2 to -2, such that the modeled ages are still too old. These observations suggest that an increase in exhumation rate by 100–200 % at 2 or 3 Ma is not enough to explain the young AHe ages in the western part of the orogen.

The dichotomy between central and western part of the orogen indicates, that the increase in exhumation rates is spatially extremely variable within the Olympic Mountains, because the central part likely experienced an increase by less

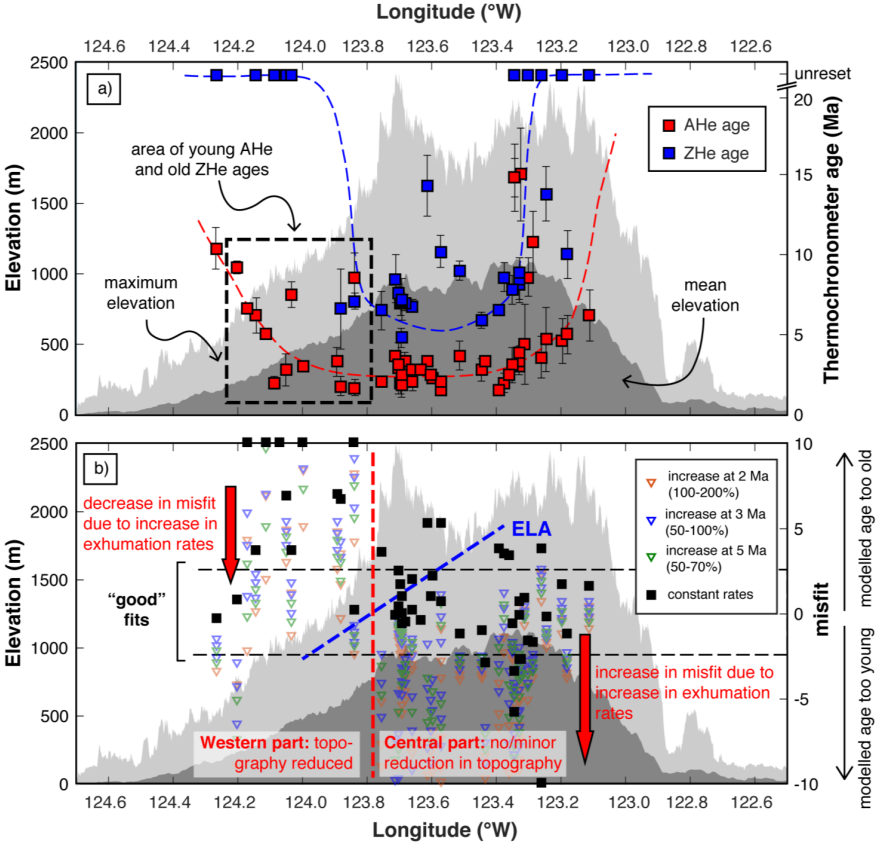

Figure 5: West to east transects across the Olympic Peninsula, showing **(a)** maximum and mean elevation as well as apatite and zircon (U-Th)/He ages (AHe and ZHe, respectively). The area west of 123.8°W has anomalously young AHe ages, but unreset ZHe ages, indicating a recent increase in exhumation. Thermochronometer ages are from Michel et al, (2018a, 2018b) and Batt et al. (2001). Note the break in the y-axis for the thermochronometer ages and that several ZHe ages are unreset. **(b)** Mean and maximum elevation and the location of the equilibrium line altitude (ELA, blue line). The symbols give information about the misfit between modelled and observed AHe ages from our simulations. The black squares are from the simulation with temporally constant exhumation rates and the triangles correspond to our considered increase scenarios and are color coded by the increase times of 2 Ma, 3 Ma or 5 Ma. The black, dashed line indicates the range of misfit (2 to -2), which we consider as a good fit between modelled and observed ages. Based on the observed misfit, a western and central part of the mountain range can be discerned (separated at ~123.8°W). In the western part, using temporally constant exhumation rates results in modelled AHe ages that are too old, and the observed misfit is decreased by an increase in exhumation rates, suggesting that here a decrease in topography occurred. In the western part, most AHe ages can successfully be modelled with temporally constant exhumation rates, and an increase in exhumation increases the observed misfit, suggesting that here the decrease in topography is small. Note that the range of the displayed misfit is limited to values between 10 and -10, and results from simulations outside these bounds are not included (samples with constant rate misfit >10 are indicated). The location of the ELA is based on Porter (1964).

than 25%, whereas an increase in excess of 200% in the western part could be possible. However, it is important to consider, that the exhumation rate pattern prescribed in our simulations is already spatially variable, even for the case of a temporally constant exhumation rate (Figure 3b) and that the considered increase in percent affects the entire exhumation pattern. In the center of the orogen, exhumation rates have values of 0.8–0.9 km/Myr, whereas the western part displays values of 0.25–0.3 km/Myr (Figure 3b), hence an increase in exhumation rates by 200% would correspond to values of 2.4–2.7 km/Myr and 0.75–0.9 km/Myr, respectively. This clearly shows, that by just considering the relative increase in exhumation rates some bias is introduced in the direct comparison between the two areas. On the other hand, the suggested, relative increase by 25% and 200% in the two considered areas corresponds to exhumation rates of ~1.0 km/Myr and 0.75 km/Myr, respectively. Hence, the absolute increase in exhumation rate is 0.2 km/Myr and 0.5 km/Myr in the central and western parts of the orogen, respectively. So, although the increase in exhumation rate is still spatially variable, the absolute difference between the two areas is not as strong as might be pretended by the relative increase.

Our proposed increase in exhumation rate is also strongly dependent on the accuracy of the underlying exhumation rate pattern used in the modeling (Figure 3b). If the area of high exhumation rates would extend from the central part of the orogen further to the west, younger AHe ages would be predicted by the model without the necessity of a temporal increase in exhumation rate. However, the spatial distribution of higher closure temperature thermochronometers like AFT, ZHe and ZFT clearly restricts the area of fast (pre-increase) exhumation rates to the central part of the orogen. For instance, in Figure 5a reset and young ZHe ages can only be found between longitudes 123.8°W and 123.4°W, whereas the ZHe ages west of ~123.8°W are all unreset. However, just west of 123.8°W is an area of particularly young AHe ages (<2.5 Ma), requiring faster exhumation rates than used in the constant rate simulation (Figure 5b). If these young AHe ages would be the result of a different exhumation pattern, then also the ZHe ages would be reset and younger than observed. Therefore, the increase in exhumation must be a young feature, which was not capable of exhuming young ages for the high temperature thermochronometer systems.

As outlined in the beginning of the methods section, an increase in exhumation due to an increase in denudation corresponds to a reduction in topography, if no commensurate increase in rock uplift balances the increase in denudation (England and Molnar, 1990). Michel et al. (2018) interpreted their pre-increase, ellipse-shaped exhumation rate pattern (Figure 3b) to correspond to rock uplift rates, which are controlled by the bend in the subducted slab below the Olympic Mountains. These exhumation rates are based on thermochronometry, providing a long-term perspective on rock uplift rates. Adams and Ehlers (2018) published denudation rates based on cosmogenic nuclide dating, temporally integrating over the Holocene. They interpret their rates as being representative of the rock uplift rates in the Olympic Mountains and report values of 0.1 – 0.2 km/Myr on the western side and ~1.0 km/Myr in the central part, very similar to the pattern and rates suggested by Michel et al. (2018). Hence, the pattern of rock uplift is temporally stable and controlled by the tectonic setting (Bendick and Ehlers, 2014; Adams and Ehlers, 2017; Michel et al., 2018a; Adams and Ehlers, 2018).

Therefore, any increase in exhumation rate as evidenced by our modeling and as required to explain the young AHe ages must be related to a reduction in topography. Glacial erosion due to the onset of Plio-Pleistocene glaciation is a prime candidate for increasing exhumation and reducing topography, given that the Olympic Mountains show clear evidence of glaciation (Figure 1a; Adams and Ehlers, 2017; Montgomery 2002; Montgomery and Greenberg, 2000). Glaciation is thought to have commenced at around 2 Ma in the Olympic Mountains (Easterbrook, 1986), which is

temporally overlapping with our modelled increase in exhumation at 2 Ma or 3 Ma. The spatial variability of the location of the Pleistocene equilibrium line altitude (ELA) could explain the spatial variability in the magnitude of increase in exhumation between the central and western parts of the orogen, because a glacier has its strongest erosive potential at the location of the ELA (Egholm et al., 2009; Sternai et al., 2011; Herman et al., 2011). Due to the precipitation gradient, the Pleistocene ELA was 800 m lower on the western side of the orogen compared to the eastern side (Figure 1b), which implies that glaciers extended to much lower elevations and more parts of the topography were subjected to glacial erosion. Indeed, all our modelled samples that require a particularly strong increase in exhumation are from areas, where the ELA was lower than 1200 m (Figure 4). We observe that the ELA most closely approximates the mean elevation of the orogen in the western part (Figure 5b), which is a consequence of glacial over-deepening of the landscape (Brocklehurst and Whipple, 2004; Adams and Ehlers, 2017). All these observations indicate that on the western side, topography was more affected by glacial erosion compared to the central and eastern part of the range and that on the western side the reduction in topography was strongest.

Putting a quantitative constraint on the amount of reduction in topography is difficult with our modelling approach, because due to the model setup the topography is kept constant during our simulations and all observed increase is exhumation is interpreted to be the result of changes in topography. For the western part of the range, our hypothesized increase in exhumation rate by 0.5 km/Myr (on top of the background rock uplift rate of 0.25 km/Myr) would correspond to a reduction in topography by 1 km for a duration of 2 Myr. However, such calculations should be viewed with caution, because any transient effect that changes in topography have on the cooling history of the samples are not considered in our simulations and hence the actual reduction in topography could be less. Furthermore, the mean elevation of the orogen was likely reduced by less than 1 km, because all the samples requiring the particularly strong increase in exhumation are from river valleys (e.g., Figure 4i). On the other hand, this indicates that the deeply incised valleys like the Hoh, Sol Duc, Queets or Quinault on the western side of the Olympic Mountains are a young feature, and the pre-glacial valley bottoms were probably at higher elevations. Topographic analysis also corroborates that the present-day river profiles of the Olympic Mountains are out of steady state due to the glacial overprint (Adams and Ehlers, 2017). Studies investigating the incision rate of alpine glaciers into landscapes also highlighted that valley incision is a rapid process, and can locally exceed rates of 1 km/Myr (Shuster et al., 2005; Haeuselmann et al., 2007; Valla et al., 2011).

Conclusions

Using our thermo-kinematic modelling approach and a large dataset of AHe ages reveals several important aspects of glacial erosion in the Olympic Mountains. An increase in denudation due to the onset of Plio-Pleistocene glaciation requires a spatially variable increase in exhumation, which is higher on the western side of the orogen compared to the center of the range. However, the magnitude in increase is larger in the west and smaller in the center than hitherto thought. Because no commensurate increase in rock uplift rates balances the additional amount of denudation, the increase in exhumation corresponds to a reduction in topography. Based on the required exhumation, the topography could have been locally reduced by up to 1 km during the past 2 Myr and in particular the major river valleys on the western side of the orogen are a young feature. Because we did not include the transient effects of a reduction in

topography in our simulation, the next step would be to use an iterative inversion for paleotopography like the approach of Olen et al. (2012), which is capable of considering the transient effects of a reduction in topography.

References

Adams, B.A., and Ehlers, T.A., 2017, Deciphering topographic signals of glaciation and rock uplift in an active orogen: a case study from the Olympic Mountains, USA: Signals of glaciation and rock uplift in the Olympic Mountains: Earth Surface Processes and Landforms, v. 42, p. 1680–1692, doi:10.1002/esp.4120.

Adams, B.A., and Ehlers, T.A., 2018, Tectonic controls of Holocene erosion in a glaciated orogen: Earth Surface Dynamics, v. 6, p. 595–610, doi:10.5194/esurf-6-595-2018.

Andersen, J.L. et al., 2018, Widespread erosion on high plateaus during recent glaciations in Scandinavia: Nature Communications, v. 9, doi:10.1038/s41467-018-03280-2.

Batt, G.E., Brandon, M.T., Farley, K.A., and Roden-Tice, M., 2001, Tectonic synthesis of the Olympic Mountains segment of the Cascadia wedge, using two-dimensional thermal and kinematic modeling of thermochronological ages: Journal of Geophysical Research: Solid Earth, v. 106, p. 26731–26746, doi:10.1029/2001JB000288.

Bendick, R., and Ehlers, T.A., 2014, Extreme localized exhumation at syntaxes initiated by subduction geometry: Geophysical Research Letters, v. 41, p. 5861–5867, doi:10.1002/2014GL061026.

Booth, D.B., Troost, K.G., Clague, J.J., and Waitt, R.B., 2003, The Cordilleran Ice Sheet, *in* Developments in Quaternary Sciences, Elsevier, v. 1, p. 17–43.

Booth-Rea, G., Klaeschen, D., Grevemeyer, I., and Reston, T., 2008, Heterogeneous deformation in the Cascadia convergent margin and its relation to thermal gradient (Washington, NW USA): Tectonics, v. 27, doi:10.1029/2007TC002209.

Brandon, M.T., Roden-Tice, M.K., and Garver, J.I., 1998, Late Cenozoic exhumation of the Cascadia accretionary wedge in the Olympic Mountains, northwest Washington State: Geological Society of America Bulletin, v. 110, p. 985–1009, doi:10.1130/0016-7606(1998)110<0985:LCEOTC>2.3.CO;2.

Braun, J., 2003, Pecube: a new finite-element code to solve the 3D heat transport equation including the effects of a time-varying, finite amplitude surface topography: Computers & Geosciences, v. 29, p. 787–794, doi:10.1016/S0098-3004(03)00052-9.

Brocklehurst, S.H., and Whipple, K.X., 2004, Hypsometry of glaciated landscapes: Earth Surface Processes and Landforms, v. 29, p. 907–926, doi:10.1002/esp.1083.

Champagnac, J.-D., Molnar, P., Sue, C., and Herman, F., 2012, Tectonics, climate, and mountain topography: Journal of Geophysical Research: Solid Earth, v. 117, doi:10.1029/2011JB008348.

Davis, E.E., and Hyndman, R.D., 1989, Accretion and recent deformation of sediments along the northern Cascadia subduction zone: Geological Society of America Bulletin, v. 101, p. 1465–1480.

Easterbrook, D.J., 1986, Stratigraphy and chronology of quaternary deposits of the Puget Lowland and Olympic Mountains of Washington and the Cascade Mountains of Washington and Oregon: Quaternary Science Reviews, v. 5, p. 145–159, doi:10.1016/0277-3791(86)90180-0.

Egholm, D.L., Jansen, J.D., Brædstrup, C.F., Pedersen, V.K., Andersen, J.L., Ugelvig, S.V., Larsen, N.K., and Knudsen, M.F., 2017, Formation of plateau landscapes on glaciated continental margins: Nature Geoscience, v. 10, p. 592–597, doi:10.1038/ngeo2980.

Egholm, D.L., Nielsen, S.B., Pedersen, V.K., and Lesemann, J.-E., 2009, Glacial effects limiting mountain height: Nature, v. 460, p. 884–887, doi:10.1038/nature08263.

Ehlers, T.A., Farley, K.A., Rusmore, M.E., and Woodsworth, G.J., 2006, Apatite (U-Th)/He signal of large-magnitude accelerated glacial erosion, southwest British Columbia: Geology, v. 34, p. 765–768.

England, P., and Molnar, P., 1990, Surface uplift, uplift of rocks, and exhumation of rocks: Geology, v. 18, p. 1173–1177, doi:10/brhdfj.

Farley, K.A., 2002, (U-Th)/He Dating: Techniques, Calibrations, and Applications: Reviews in Mineralogy and Geochemistry, v. 47, p. 819–844, doi:10.2138/rmg.2002.47.18.

Haeuselmann, P., Granger, D.E., Jeannin, P.-Y., and Lauritzen, S.-E., 2007, Abrupt glacial valley incision at 0.8 Ma dated from cave deposits in Switzerland: Geology, v. 35, p. 143, doi:10/dvpk56.

Herman, F., Beaud, F., Champagnac, J.-D., Lemieux, J.-M., and Sternai, P., 2011, Glacial hydrology and erosion patterns: A mechanism for carving glacial valleys: Earth and Planetary Science Letters, v. 310, p. 498–508, doi:10.1016/j.epsl.2011.08.022.

Herman, F., Seward, D., Valla, P.G., Carter, A., Kohn, B., Willett, S.D., and Ehlers, T.A., 2013, Worldwide acceleration of mountain erosion under a cooling climate: Nature, v. 504, p. 423–426, doi:10.1038/nature12877.

House, M.A., Wernicke, B.P., and Farley, K.A., 1998, Dating topography of the Sierra Nevada, California, using apatite (U-Th)/He ages: Nature, v. 396, p. 66–69, doi:10.1038/23926.

Hyndman, R.D., and Wang, K., 1993, Thermal constraints on the zone of major thrust earthquake failure: The Cascadia Subduction Zone: Journal of Geophysical Research: Solid Earth, v. 98, p. 2039–2060, doi:10.1029/92JB02279.

Hyndman, R.D., Yorath, C.J., Clowes, R.M., and Davis, E.E., 1990, The northern Cascadia subduction zone at Vancouver Island: Seismic structure and tectonic history: Canadian Journal of Earth Sciences, v. 27, p. 313–329.

Lewis, T.J., and Bentkowski, W.H., 1988, Potassium, Uranium and Thorium Concentrations of Crustal Rocks: a Data File: Geological Survey of Canada Open File Report 1744, 165 p.

Lewis, T.J., Bentkowski, W.H., Davis, E.E., Hyndman, R.D., Souther, J.G., and Wright, J.A., 1988, Subduction of the Juan de Fuca Plate: Thermal consequences: Journal of Geophysical Research: Solid Earth, v. 93, p. 15207–15225, doi:10.1029/JB093iB12p15207.

Mancktelow, N.S., and Grasemann, B., 1997, Time-dependent effects of heat advection and topography on cooling histories during erosion: Tectonophysics, v. 270, p. 167–195.

Michel, L., Ehlers, T.A., Glotzbach, C., Adams, B.A., and Stübner, K., 2018a, Tectonic and glacial contributions to focused exhumation in the Olympic Mountains, Washington, USA: Geology, v. 46, p. 491–494, doi:10/gc8z9w.

Michel, L., Glotzbach, C., Falkowski, S., Adams, B.A., and Ehlers, T.A., 2018b, How steady are steady-state mountain belts? – a re-examination of the Olympic Mountains (Washington State, USA): Earth Surface Dynamics Discussions, p. 1–36, doi:10.5194/esurf-2018-65.

Mitchell, S.G., and Montgomery, D.R., 2006, Influence of a glacial buzzsaw on the height and morphology of the Cascade Range in central Washington State, USA: Quaternary Research, v. 65, p. 96–107, doi:10.1016/j.yqres.2005.08.018.

Molnar, P., and England, P., 1990, Late Cenozoic uplift of mountain ranges and global climate change: chicken or egg? Nature, v. 346, p. 29–34, doi:10.1038/346029a0.

Montgomery, D.R., 2002, Valley formation by fluvial and glacial erosion: Geology, v. 30, p. 1047–1050, doi:10.1130/0091-7613(2002)030<1047:VFBFAG>2.0.CO;2.

Montgomery, D.R., and Greenberg, H.M., 2000, Local relief and the height of Mount Olympus: Earth Surface Processes and Landforms, v. 25, p. 385–396.

Olen, S.M., Ehlers, T.A., and Densmore, M.S., 2012, Limits to reconstructing paleotopography from thermochronometer: Journal of Geophysical Research: Earth Surface, v. 117, doi:10.1029/2011JF001985.

Porter, S.C., 1964, Composite Pleistocene snow line of Olympic Mountains and Cascade Range, Washington: Geological Society of America Bulletin, v. 75, p. 477–482.

Schildgen, T.F., van der Beek, P.A., Sinclair, H.D., and Thiede, R.C., 2018, Spatial correlation bias in late-Cenozoic erosion histories derived from thermochronology: Nature, v. 559, p. 89–93, doi:10/gdshbq.

Shuster, D.L., Ehlers, T.A., Rusmoren, M.E., and Farley, K.A., 2005, Rapid Glacial Erosion at 1.8 Ma Revealed by 4He/3He Thermochronometry: Science, v. 310, p. 1668–1670, doi:10.1126/science.1118519.

Steer, P., Huismans, R.S., Valla, P.G., Gac, S., and Herman, F., 2012, Bimodal Plio–Quaternary glacial erosion of fjords and low-relief surfaces in Scandinavia: Nature Geoscience, v. 5, p. 635–639, doi:10.1038/ngeo1549.

Sternai, P., Herman, F., Champagnac, J.-D., Fox, M., Salcher, B., and Willett, S.D., 2012, Pre-glacial topography of the European Alps: Geology, v. 40, p. 1067–1070, doi:10/gdkzjj.

Sternai, P., Herman, F., Fox, M.R., and Castelltort, S., 2011, Hypsometric analysis to identify spatially variable glacial erosion: Journal of Geophysical Research, v. 116, doi:10.1029/2010JF001823.

Stüwe, K., White, L., and Brown, R., 1994, The influence of eroding topography on steady-state isotherms. Application to fission track analysis: Earth and Planetary Science Letters, v. 124, p. 63–74, doi:10.1016/0012-821X(94)00068-9.

Tabor, R.W., and Cady, W.M., 1978, The structure of the Olympic Mountains, Washington: Analysis of a subduction zone: US Govt. Print. Off., v. 1033.

Thackray, G.D., 2001, Extensive Early and Middle Wisconsin Glaciation on the Western Olympic Peninsula, Washington, and the Variability of Pacific Moisture Delivery to the Northwestern United States: Quaternary Research, v. 55, p. 257–270, doi:10.1006/qres.2001.2220.

Valla, P.G., Shuster, D.L., and van der Beek, P.A., 2011, Significant increase in relief of the European Alps during mid-Pleistocene glaciations: Nature Geosci, v. 4, p. 688–692, doi:10.1038/ngeo1242.

Willett, S.D., 1999, Orogeny and orography: The effects of erosion on the structure of mountain belts: Journal of Geophysical Research: Solid Earth, v. 104, p. 28957–28981, doi:10.1029/1999JB900248.

Willett, S.D., and Brandon, M.T., 2002, On steady states in mountain belts: Geology, v. 30, p. 175–178, doi:10.1130/0091-7613(2002)030<0175:OSSIMB>2.0.CO;2.

Yanites, B.J., and Ehlers, T.A., 2016, Intermittent glacial sliding velocities explain variations in long-timescale denudation: Earth and Planetary Science Letters, v. 450, p. 52–61, doi:10.1016/j.epsl.2016.06.022.

Tables

Table 1: Possible scenarios for an increase in exhumation rate at the respective time and by the respective amount. The exhumation rates prior to the increase are 0.25/0.9 km/Myr.

Increase time	**2 Ma**			**3 Ma**			**5 Ma**	
Increase (relative)	100 %	150 %	200%	50 %	70 %	100 %	50 %	70 %
Increase (absolute, km/Myr)	0.25/0.9	0.38/1.45	0.5/1.8	0.13/0.45	0.19/0.63	0.25/0.9	0.13/0.45	0.19/0.63

Table 2: List of parameters used for the Pecube modeling, based on values listed in Michel et al. (2018b).

Parameter	**Value**	**Source**
Thermal conductivity	1.83 W $m^{-1}K^{-1}$	average value for six drill cores in sediment material in the shelf offshore from Vancouver Island (Lewis et al., 1988)
Specific heat capacity	1200 J $kg^{-1}K^{-1}$	
Crustal density	2700 kg m^{-3}	
Mantle density	3200 kg m^{-3}	
Temperature at the base of the model	400 °C	extrapolation to greater depths from temperature estimates based on heat flow measurements on the shelf (Hyndman et al., 1990; Hyndman and Wang, 1993; Booth-Rea et al., 2008)
Temperature at sea level	8 °C	
Atmospheric lapse rate	6.69 °C km^{-1}	
Crustal heat production	0.77 µW m^{-3}	average value from drill cores on the shelf offshore Vancouver Island (Lewis and Bentkowski, 1988)
Model depth	20 km	minimum thickness of the accretionary wedge below the Olympic Mountains (Davis and Hyndman, 1989)
Model resolution	0.5 km	

Table 3: Information on samples used in our simulations, including the location and the respective AHe ages. The modelled ages and the calculated misfit for the various simulations are reported as well. Models were performed using a temporally constant exhumation rate, or an increase in exhumation rate at the respective time and amount. AHe sample ages are from Michel et al. (2018a, 2018b) and Batt et al. (2001).

Sample information				Model data: ages (Ma)									Model data: Misfit (modelled age-observed age)/uncertainty								
Longitude (°W)	Latitude (°N)	AHe age (Ma)	Age 1 SD (Ma)	2 Ma 100%	2 Ma 150 %	2 Ma 200%	3 Ma 50%	3 Ma 70%	3 Ma 100%	5 Ma 50 %	5 Ma 70%	constant	2 Ma 100%	2 Ma 150 %	2 Ma 200%	3 Ma 50%	3 Ma 70%	3 Ma 100%	5 Ma 50 %	5 Ma 70%	constant
123.19509	47.93235	4.6	1.4	5.1	4.2	3.0	5.6	5.1	4.2	4.8	3.9	7.1	0.4	-0.3	-1.1	0.7	0.3	-0.3	0.1	-0.5	1.8
123.11056	47.96521	6.2	1.6	6.9	5.9	4.9	7.4	6.8	5.9	6.4	5.6	8.8	0.4	-0.2	-0.8	0.7	0.4	-0.2	0.2	-0.4	1.7
123.61359	47.98306	3.3	0.2	2.4	1.4	0.8	3.0	2.4	1.7	2.5	2.0	4.4	-4.4	-9.5	-12.7	-1.7	-4.4	-7.8	-3.8	-6.3	5.3
123.57273	47.96015	1.5	0.3	1.2	0.7	0.4	1.8	1.5	1.0	1.7	1.3	3.1	-0.9	-2.7	-3.7	1.1	-0.1	-1.6	0.6	-0.6	5.3
123.44630	47.81028	2.8	0.7	0.6	0.3	0.1	1.1	0.8	0.5	1.0	0.7	2.1	-3.1	-3.5	-3.8	-2.4	-2.8	-3.2	-2.6	-2.9	-1.0
123.51377	47.93893	3.7	0.9	0.9	0.5	0.3	1.5	1.2	0.8	1.4	1.1	2.6	-3.1	-3.5	-3.8	-2.4	-2.8	-3.2	-2.6	-2.9	-1.2
123.83886	48.05065	8.6	1.5	7.0	6.1	5.1	7.6	7.0	6.1	6.7	5.8	9.0	-1.0	-1.7	-2.3	-0.7	-1.1	-1.7	-1.3	-1.9	0.3
124.08703	48.04830	2.0	0.4	8.1	7.2	6.2	8.6	8.1	7.2	7.7	6.8	10.1	15.3	12.9	10.5	16.6	15.2	13.0	14.3	12.0	20.4
124.05184	47.82504	2.8	1.0	7.8	6.8	5.8	8.3	7.7	6.8	7.4	6.4	9.8	5.0	4.0	3.0	5.5	4.9	4.0	4.6	3.6	7.0
123.99660	47.80682	3.0	0.3	6.5	5.5	4.5	7.0	6.4	5.6	6.1	5.2	8.5	11.6	8.4	5.2	13.3	11.4	8.5	10.4	7.4	18.2
124.14258	47.78269	6.2	1.1	8.3	7.3	6.3	8.8	8.2	7.3	7.8	6.9	10.3	1.9	1.0	0.1	2.3	1.8	1.0	1.5	0.7	3.7
124.26813	47.73081	10.4	1.3	8.0	7.1	6.1	8.5	8.0	7.1	7.6	6.7	10.0	-1.8	-2.6	-3.3	-1.4	-1.9	-2.6	-2.1	-2.8	-0.3
123.88135	47.87020	1.8	0.6	3.9	2.9	1.7	4.4	3.8	3.0	3.6	3.0	5.8	3.5	1.8	-0.2	4.3	3.4	1.9	3.1	2.0	6.7
123.69426	47.87572	2.5	0.4	0.7	0.4	0.2	1.2	0.9	0.6	1.1	0.8	2.3	-4.4	-5.4	-5.8	-3.1	-3.9	-4.7	-3.4	-4.1	-0.5
123.75552	47.88532	2.1	0.2	1.1	0.6	0.3	1.6	1.3	0.9	1.5	1.2	2.8	-5.2	-7.7	-8.9	-2.3	-4.1	-6.0	-3.0	-4.7	3.7
124.03370	47.48913	7.5	0.8	8.5	7.5	6.5	9.0	8.4	7.5	8.1	7.1	10.5	1.2	0.0	-1.2	1.9	1.1	0.0	0.7	-0.5	3.7
123.65869	47.64154	2.1	0.6	0.7	0.4	0.2	1.2	0.9	0.6	1.1	0.8	2.2	-2.3	-2.9	-3.2	-1.5	-2.0	-2.5	-1.6	-2.1	0.2
123.37533	47.56004	2.0	0.6	2.2	1.2	0.6	2.7	2.2	1.6	2.4	1.9	4.1	0.3	-1.4	-2.3	1.2	0.3	-0.7	0.6	-0.2	3.6
123.32442	47.51916	15.0	2.9	5.4	4.4	3.4	5.9	5.3	4.5	5.1	4.2	7.4	-3.3	-3.6	-4.0	-3.1	-3.3	-3.6	-3.4	-3.7	-2.6
123.34295	48.02189	14.8	1.2	5.9	4.9	3.9	6.4	5.8	4.9	5.5	4.6	7.8	-7.4	-8.3	-9.1	-7.0	-7.5	-8.2	-7.8	-8.5	-5.8
123.34295	48.02189	14.8	2.1	5.9	4.9	3.9	6.4	5.8	4.9	5.5	4.6	7.8	-4.2	-4.7	-5.2	-4.0	-4.3	-4.7	-4.4	-4.8	-3.3
123.69600	47.81569	2.0	0.7	1.2	0.6	0.3	1.9	1.5	1.0	1.7	1.3	3.2	-1.2	-2.0	-2.4	-0.2	-0.8	-1.5	-0.4	-1.0	1.8
123.68324	47.82648	3.3	0.6	1.1	0.5	0.3	1.7	1.3	0.9	1.5	1.2	3.0	-3.7	-4.6	-5.0	-2.7	-3.3	-4.0	-2.9	-3.5	-0.5
123.71102	47.80157	3.7	0.2	1.6	0.8	0.5	2.2	1.8	1.2	2.0	1.6	3.7	-10.6	-14.4	-16.2	-7.3	-9.7	-12.4	-8.5	-10.7	-0.1
123.70244	47.80378	2.9	1.6	1.4	0.7	0.4	2.1	1.6	1.1	1.9	1.5	3.5	-0.9	-1.3	-1.6	-0.5	-0.8	-1.1	-0.6	-0.9	0.4
123.69330	47.83982	1.9	0.8	0.9	0.5	0.3	1.5	1.2	0.8	1.4	1.1	2.7	-1.2	-1.8	-2.1	-0.5	-0.9	-1.4	-0.6	-1.0	1.1
123.69195	47.85459	2.5	1.0	0.8	0.4	0.2	1.4	1.1	0.7	1.3	1.0	2.6	-1.7	-2.1	-2.3	-1.1	-1.4	-1.8	-1.2	-1.5	0.1
123.89397	48.00848	3.3	0.9	7.7	6.7	5.7	8.2	7.6	6.7	7.2	6.3	9.7	4.8	3.8	2.7	5.4	4.8	3.8	4.4	3.4	7.1
123.31173	47.98095	4.4	2.5	4.9	3.9	2.8	5.4	4.8	4.0	4.6	3.7	6.9	0.2	-0.2	-0.6	0.4	0.2	-0.2	0.1	-0.3	1.0
123.30092	47.97234	8.6	1.2	4.8	3.8	2.6	5.3	4.7	3.8	4.4	3.6	6.7	-3.2	-4.0	-5.0	-2.8	-3.3	-4.0	-3.5	-4.2	-1.6

Table 3 continued

Sample information				Model data: ages (Ma)									Model data: Misfit (modelled age-observed age)/uncertainty								
Longitude (°W)	Latitude (°N)	AHe age (Ma)	Age 1 SD (Ma)	2 Ma 100%	2 Ma 150 %	2 Ma 200%	3 Ma 50%	3 Ma 70%	3 Ma 100%	5 Ma 50 %	5 Ma 70%	constant	2 Ma 100%	2 Ma 150 %	2 Ma 200%	3 Ma 50%	3 Ma 70%	3 Ma 100%	5 Ma 50 %	5 Ma 70%	constant
123.28635	47.97283	10.8	1.9	5.8	4.8	3.7	6.3	5.7	4.8	5.4	4.4	7.8	-2.6	-3.2	-3.7	-2.4	-2.7	-3.2	-2.9	-3.4	-1.6
123.26785	47.95785	30.1	2.0	5.9	4.9	3.9	6.4	5.8	4.9	5.5	4.5	7.9	-12.1	-12.6	-13.1	-11.8	-12.1	-12.6	-12.3	-12.8	-11.1
123.26078	47.95696	3.6	1.3	6.6	5.6	4.6	7.1	6.5	5.6	6.2	5.2	8.6	2.3	1.6	0.8	2.7	2.2	1.6	2.0	1.2	3.8
123.24616	47.91642	4.7	2.0	2.5	1.4	0.7	3.0	2.5	1.7	2.6	2.1	4.5	-1.1	-1.6	-2.0	-0.8	-1.1	-1.5	-1.1	-1.3	-0.1
123.32927	47.71656	3.0	0.5	1.3	0.7	0.4	2.0	1.6	1.1	1.8	1.4	3.4	-3.3	-4.6	-5.2	-2.0	-2.8	-3.8	-2.4	-3.2	0.8
123.32815	47.71476	3.3	0.4	1.3	0.7	0.4	1.9	1.5	1.0	1.8	1.4	3.3	-5.1	-6.6	-7.3	-3.4	-4.5	-5.7	-3.9	-4.9	0.0
123.32764	47.69398	3.9	0.4	1.0	0.5	0.3	1.6	1.2	0.8	1.4	1.1	2.8	-7.3	-8.5	-9.1	-5.8	-6.7	-7.7	-6.1	-7.0	-2.7
123.35093	47.68896	3.1	1.1	0.8	0.4	0.2	1.3	1.0	0.6	1.2	0.9	2.5	-2.1	-2.5	-2.7	-1.6	-1.9	-2.2	-1.7	-2.0	-0.6
123.39235	47.67452	1.5	0.2	0.7	0.3	0.2	1.2	0.9	0.6	1.1	0.8	2.3	-4.1	-5.8	-6.7	-1.5	-2.9	-4.6	-2.0	-3.4	3.9
123.17929	47.73974	5.0	1.2	1.7	0.9	0.5	2.3	1.8	1.3	2.0	1.6	3.7	-2.7	-3.4	-3.8	-2.3	-2.7	-3.1	-2.5	-2.9	-1.1
123.83733	47.95592	1.7	0.5	5.8	4.8	3.8	6.3	5.7	4.8	5.5	4.5	7.8	8.2	6.2	4.2	9.2	8.0	6.3	7.5	5.7	12.1
123.43234	47.82230	3.3	0.3	0.8	0.4	0.2	1.3	1.0	0.7	1.2	0.9	2.4	-8.4	-9.7	-10.3	-6.7	-7.6	-8.8	-7.0	-7.9	-2.9
123.59566	47.78630	2.3	0.2	0.9	0.5	0.2	1.5	1.2	0.8	1.4	1.0	2.8	-6.9	-9.2	-10.3	-3.9	-5.7	-7.6	-4.6	-6.3	2.3
123.70134	47.79649	3.1	0.2	1.5	0.8	0.4	2.2	1.7	1.2	1.9	1.5	3.6	-8.0	-11.6	-13.3	-4.6	-7.0	-9.7	-5.8	-8.0	2.5
123.57117	47.75601	2.1	0.2	0.6	0.3	0.1	1.2	0.9	0.6	1.1	0.8	2.2	-7.3	-9.0	-9.8	-4.7	-6.2	-7.7	-5.2	-6.6	0.7
123.66250	47.79250	2.8	0.2	1.2	0.6	0.3	1.8	1.4	1.0	1.7	1.3	3.2	-8.1	-10.9	-12.4	-4.9	-6.8	-9.2	-5.7	-7.6	2.0
123.63483	47.78896	2.8	0.1	0.9	0.5	0.2	1.5	1.2	0.8	1.4	1.0	2.8	-18.8	-23.4	-25.6	-12.9	-16.3	-20.4	-14.2	-17.5	-0.3
123.36134	47.79429	2.5	0.2	1.2	0.6	0.3	1.8	1.4	1.0	1.7	1.3	3.2	-6.6	-9.4	-10.8	-3.3	-5.3	-7.6	-4.2	-6.0	3.5
124.20267	47.65602	9.2	0.4	7.6	6.6	5.6	8.1	7.5	6.6	7.2	6.3	9.5	-4.1	-6.5	-8.9	-2.8	-4.3	-6.4	-5.1	-7.3	0.8
124.17317	47.67054	6.6	0.3	7.9	6.9	6.0	8.4	7.8	6.9	7.5	6.6	9.9	4.4	1.0	-2.2	6.0	4.0	1.1	2.9	-0.1	11.0
124.11517	47.67769	5.1	0.2	7.4	6.5	5.5	8.0	7.4	6.5	7.0	6.1	9.4	11.7	7.0	2.0	14.3	11.3	7.1	9.7	5.2	21.6
123.60067	47.78816	2.5	0.2	0.9	0.4	0.2	1.5	1.1	0.7	1.4	1.0	2.7	-8.0	-10.3	-11.3	-5.1	-6.8	-8.8	-5.7	-7.4	1.0

Chapter 4

Conclusions

The Olympic Mountains have been the location for various studies, investigating the evolution of the mountain range (Brandon et al., 1998; Batt et al., 2001; Pazzaglia & Brandon, 2001). By applying thermochronometric dating and thermo-kinematic modeling, outcomes from this thesis along with results from recent studies in the Olympic Mountains (Adams & Ehlers, 2017, 2018) contribute to a more refined understanding of the evolution of this orogen in particular, but also of processes involved in mountain building in general. Five hypothesis have been investigated:

① **If the plate geometry plays an important role in focusing deformation in mountain ranges, then a focused pattern of exhumation rates should be observed within orogenic syntaxes.**

② **If changes in the tectonic conditions or climate affect the evolution of orogens, then an increase in exhumation rates should be caused by an increase in plate convergence rate or the onset of Plio-Pleistocene glaciation.**

③ **If the denudational outflux out of an orogen is increased by glacial erosion, then the flux steady-state balance of an orogen should be disturbed unless the accretionary influx increases by the same amount.**

④ **If the effects of viscoelastic deformation during the seismic cycle permanently deform landscapes, then these effects should be detectable with methods measuring deformation over different timescales.**

⑤ **If glacial erosion is capable of significantly lowering the elevation of mountain ranges, then a concomitant increase in exhumation rate must occur.**

In the following section, the outcomes from chapter 3 are summarized and the hypotheses are re-evaluated. The last section provides an outlook and indicates, in which direction future work in the Olympic Mountains or the Cascadia Subduction Zone might be directed.

4.1 A Summary – The hypotheses revisited

The Olympic Mountains are a good example for an orogen, where the plate geometry plays a pivotal role in affecting deformation and exhumation. As demonstrated in section 3.1, the observed thermochronometric age pattern can be best explained with an ellipse-shaped exhumation pattern. The young thermochronometer ages in the central, high topography part of the orogen require higher exhumation rates (0.9 km/Myr), compared to rates (0.25 km/Myr) in the low-elevation areas close to the coast. These exhumation rates are interpreted to correspond to rock uplift rates, which are a consequence of the bend in the subducted slab below the Olympic Mountains. This is what the rigid indenter model proposes to occur in an orogenic syntaxis (Bendick & Ehlers, 2014). However, compared to the Himalayan syntaxes or the St. Elias syntaxis (Figure 1.1), where the maximum exhumation rates can exceed 5 km/Myr (Enkelmann et al., 2011, 2015; Lang et al., 2016), the maximum exhumation rates in the Olympic Mountains are distinctly slower. **Taken together, the observations prove hypothesis ①, indicating that the plate geometry plays an important role in controlling exhumation**. Hence, the Olympic Mountains are a good example of an orogen impacted by a rigid indenter, suggesting that in addition to the tectonic aneurysm model (Zeitler et al., 2001; Enkelmann et al., 2009; Koons et al., 2013) the rigid indenter model is a model that can explain focused and rapid exhumation. However, there is also a dispute about the contribution of oroclinal bending to focused exhumation within the Olympic Mountains (Finley et al., 2019), which might instigate future work.

Both tectonics and climate contribute to the formation and evolution of the Olympic Mountains. Due to the shape of the subducted slab, the tectonic setting controls the general pattern of rock uplift, which is evidenced in the ellipse-shaped exhumation pattern, cosmogenic denudation rates (Adams & Ehlers, 2018) and topography (Adams & Ehlers, 2017). In addition to the general control of tectonics on exhumation, temporal variations in the tectonic framework also result in temporal variations of exhumation. As shown in section 3.2.2, a reduction in convergence rate between the Juan de Fuca Plate and the North American Plate at around 6 Ma is coincident with a reduction in exhumation rate in the Olympic Mountains. At that time, rock uplift is reduced due to the decrease in plate convergence rate. Furthermore, as demonstrated in sections 3.1 and section 3.2, a change in climate with onset of Plio-Pleistocene glaciation and increased glacial erosion significantly affected exhumation rates, leading to an increase in exhumation rates by up to 150–200 % at 2 to 3 Ma. **These observed temporal variations in exhumation rate either due to changes in the convergence rate or the onset of glaciation prove hypotheses ②.** However, the direction of change in convergence rate and the subsequent change in exhuma-

tion rate is opposite to the one suggested in hypothesis (2), i.e., a decrease in exhumation rates is observed due to a decrease in plate convergence rate.

Because the glacially-induced increase in exhumation is not accompanied with a commensurate increase in rock uplift (i.e., the plate convergence rate is not increasing), a lowering of topography must occur. Topographic analysis corroborates that the present-day topography of the Olympic Mountains is the result of Plio-Pleistocene glaciation (Montgomery, 2002; Montgomery & Greenberg, 2000; Adams & Ehlers, 2017). Based on the thermo-kinematic model work presented in section 3.1 and section 3.4, the western side of the Olympic Mountains seems to be particularly affected, because here the young AHe ages require an exceptionally strong increase in exhumation rate (locally exceeding an increase in 200% relative to pre-increase exhumation rates). On the western side, the location of the equilibrium line altitude (ELA) is lowest within the orogen, indicating that the topography-lowering effect of glacial erosion is strongest in that area. As shown in section 3.4 the increase in exhumation rates is less in the central part of the orogen, coinciding with a much higher ELA. **Hence, the effect of glacial erosion to lower the mean elevation of orogens and thereby increase exhumation is detectable and hypothesis (5) could be proven during the thesis**. However, the effects of glacial erosion on topography could only be demonstrated qualitatively and a full quantification of the actual reduction in topography needs to be done with future model work, for instance by using the iterative topographic inversion scheme of Olen et al. (2012).

The Olympic Mountains have been introduced as a textbook steady-state mountain range (Pazzaglia & Brandon, 2001; Batt et al., 2001; Willett & Brandon, 2002). The results presented in this thesis provide a new view of this tenet. Topography has changed during the past 2–3 Ma due to the Plio-Pleistocene glaciation, violating the assumption of topographic steady-state. A reassessment of the flux steady-state hypothesis of the Olympic Mountains as presented in section 3.2 reveals several interesting aspects. From a qualitative viewpoint, exhumation rates and hence denudation rates display strong temporal variations, so that the denudational outflux from the Olympics is temporally variable. The accretional influx is also temporally variable, due to increased off-shore sedimentation rates related to an increased sediment delivery to the ocean in the Plio-Pleistocene and due to a decrease in plate convergence rate. However, it was not possible to assess quantitatively whether the changes in influx and outflux balance each other, so that the mountain range is in flux steady-state on short timescales (i.e., 2–3 Ma). A quantitative assessment over a 14 Myr period reveals that the Olympic Mountains are in flux steady-state, but only if a three-dimensional geometry is assumed for the flux analysis, contrary to previous results suggesting flux steady-state assuming a two-dimensional geometry. **Hence, hypothesis (3) is refuted,**

because flux steady-state is still possible, although temporal variations in the influx and outflux occur. Nonetheless, these outcomes emphasize that many parameters need to be constrained for a reasonable flux steady-state assessment and that in particular Plio-Pleistocene glaciation is capable of disturbing an orogenic system, affecting both the outflux and influx.

Comparing datasets with different integration timescales in section 3.3 reveals interesting aspects of deformation in the Olympic Mountains. On intermediate to long timescales, the denudation rates derived from cosmogenic nuclides (Adams & Ehlers, 2018) and from thermochronometry (this work) as well as the long-wavelength pattern of topography suggest that most permanent deformation occurs in the central part of the Olympic Mountains. This focusing of permanent deformation is the consequence of the bend in the subducted slab below the Olympic Mountains.

On short timescales, rock uplift rates derived from present-day GPS observations display a disparate pattern, because the GPS signal is dominated by the elastic deformation of the seismic cycle: Because the shallow parts of the Cascadia Subduction Zone plate interface are locked, high rates of rock uplift close to the western coast of the Olympic Peninsula can be observed, contrary to what is suggested from the long-term methods. After forward modelling the elastic component and subtracting it from the GPS signal, the pattern of residual vertical velocities (which should now only contain the permanent component of rock uplift) partially overlaps with the long-term pattern of permanent deformation. Furthermore, the area of high residual vertical velocities (where also a change in surface tilt rate occurs) overlaps spatially with the area, where Bruhat & Segall (2016) suggested negative shear stress rates on the plate interface. From a fault mechanical viewpoint, negative shear stress rates (so a reduction in shear stress over time) can be caused by visco-plastic flow. This viscous flow would initiate permanent deformation in the overriding crust and could explain the focusing of surface tilting, denudation and high elevation within the Olympic Mountains. Hence, additional to the elastic component, the GPS signal records a viscous (permanent) component of deformation. **Based on these observations hypothesis ④ is proven and the effects of viscoelastic deformation can be detected with both short- and long-term methods.** However, it is important to consider the elastic and permanent components of the short-term signal independently from each other. The results also highlight the potential of characterizing the behavior of the plate interface by combining observations from short- and long-term methods and corroborate the view of Li et al. (2015) that viscoelastic deformation plays an important role during the seismic cycle of subduction zones.

Taken together, all these observations both on short and long timescales reveal a more complicate history of the Olympic Mountains than previously suggested by Brandon et al. (1998) and Batt et al. (2001). Clearly, the formation and evolution of the Olympic Mountains is controlled both by tectonics and climate, indicating the importance of considering possible feedbacks between these parameters during the evolution of orogens (Figure 2.2). Exhumation of the Olympic Mountains is spatially and temporally variable, corroborating the notion that exhumation during the lifespan of an orogen is temporally not steady (e.g., Carrapa et al., 2003; Glotzbach et al., 2011; Adams et al., 2015; Enkelmann et al., 2017; Georgieva et al., 2019). Furthermore, deviations from steady-state seem to be likely, at least on short time scales. As a summary, the Olympic Mountains were used as a case study in order to investigate mountain building processes and several intriguing aspects of the evolution of this mountain range could be revealed. However, as indicated in section 1.2 the outcomes from a case study should be viewed to be representative of mountain building processes in general. For instance, the idea that the plate geometry is important in controlling the deformation of orogens is a hypothesis that could also be evaluated in other orogens, where this effect has hitherto not been considered.

4.2 Outlook and future work

New insights into the evolution of the Olympic Mountains were provided by this thesis. However, many open and unresolved questions remain. Reconstructing the topographic evolution of the Olympic Mountains in light of the Plio-Pleistocene glaciation still requires to conduct more sophisticated thermokinematic modeling with Pecube using the topographic inversion scheme of Olen et al. (2012). Similar studies in different orogens were able to capitalize on a spatially dense thermochronometry dataset and could reconstruct paleotopography within a very fine spatial resolution (e.g., Ehlers et al., 2006; Olen et al., 2012). Although the additional thermochronometer samples from this study enlarge the existing thermochronometry dataset of the Olympic Mountains, especially AHe ages are absent or less densely spaced in parts of the mountain range, which experienced strong glaciation (i.e., the Queets valley and upper reaches of the Quinault valley, Figure 1.3a). Collecting additional thermochronometry samples in these parts of the orogen might improve the outcomes from the modeling. Otherwise, the most robust estimates of paleotopography will be limited to the area where most AHe ages exist, i.e., the Hoh valley and Mt. Olympus area.

The importance of the plate geometry in controlling the exhumation of the Olympic Mountains could be demonstrated. The effect seems to be localized in the Olympic Mountains, due to the bend in the subducted slab. However, other

parts of the Cascadia Subduction Zone to the south and north of the Olympic Peninsula were not further investigated in this study. No thermochronometric ages are available for the Oregon Coast Range and old AFT ages (50 – 60 Ma, England et al., 1997) on central Vancouver Island require slow exhumation, indicating that indeed the area seems not to be affected by the rigid indenter, but a dense thermochronometric dataset including (U-Th)/He systems is absent. Hence, one part of future work might be to obtain more thermochronometry ages both from Vancouver Island and from the Coast Range south of the Olympic Mountains to further constrain the area of focused exhumation. Although the isolated, high topography of the Olympic Mountains also suggests that deformation is focused in this part of the Cascadia Subduction Zone, a better spatial knowledge of the subduction-wide exhumation pattern will clearly show, how localized the effect of the rigid indenter is.

All thermo-kinematic modeling in this work considers only vertical velocities. However, modern GPS velocities indicate that the southern and central part of the Cascadia Subduction Zone are rotating clock-wise (Wells & McCaffrey, 2013), resulting in margin-parallel displacement. The flux steady-state analysis as well as the sediment cross-sections from this study revealed that the influx should be considered in three-dimensions and is spatially variable along the Cascadia Subduction Zone. Hence, a refined, three-dimensional kinematic field could help to reveal the contributions from non-vertical velocities and margin-parallel velocities to exhumation in the Olympic Mountains. Future work could build upon the approach from Batt et al. (2001) for deriving the horizontal velocity component, but should also consider possible temporal variations in plate convergence rates or rotation rates.

As shown in this study, the comparison between the short-term and long-term observations of deformation helps to understand the mechanics of the Cascadia Subduction Zone. This could have important implications for the hazard assessment of the subduction zone, because the magnitude of a future earthquake is controlled by the size of the locked zone (e.g., Wang & Tréhu, 2016). So, a spatially refined, subduction-wide pattern of exhumation on Vancouver Island and in Oregon would give invaluable insights into the long-term deformation of the Cascadua Subduction Zone. Furthermore, a more detailed analysis of how episodic tremor and slip is related to permanent deformation could aid in understanding the mechanisms involved in mountain building.

References of Chapters 1, 2 and 4

Adam, J., Klaeschen, D., Kukowski, N., & Flueh, E. (2004). Upward delamination of Cascadia Basin sediment infill with landward frontal accretion thrusting caused by rapid glacial age material flux. *Tectonics*, 23(3). DOI: 10.1029/2002TC001475.

Adams, B. A. & Ehlers, T. A. (2017). Deciphering topographic signals of glaciation and rock uplift in an active orogen: a case study from the Olympic Mountains, USA: Signals of glaciation and rock uplift in the Olympic Mountains. *Earth Surface Processes and Landforms*, 42(11), 1680–1692. DOI: 10.1002/esp.4120.

Adams, B. A. & Ehlers, T. A. (2018). Tectonic controls of Holocene erosion in a glaciated orogen. *Earth Surface Dynamics*, 6(3), 595–610. DOI: 10.5194/esurf-6-595-2018.

Adams, B. A., Hodges, K. V., Whipple, K. X., Ehlers, T. A., van Soest, M. C., & Wartho, J. (2015). Constraints on the tectonic and landscape evolution of the Bhutan Himalaya from thermochronometry: Late Cenozoic Evolution of Bhutan. *Tectonics*, 34(6), 1329–1347. DOI: 10.1002/2015TC003853.

Avdievitch, N., Ehlers, T. A., & Glotzbach, C. (2018). Slow long-term exhumation of the West Central Andean Plate Boundary, Chile. *Tectonics*, 37(7), 2243–2267. DOI: 10.1029/2017TC004944.

Avouac, J. P. & Burov, E. B. (1996). Erosion as a driving mechanism of intracontinental mountain growth. *Journal of Geophysical Research-Solid Earth*, 101(B8), 17747–17769. DOI: 10.1029/96JB01344.

Banta, R. M. (1990). The role of mountain flows in making clouds. In W. Blumen (Ed.), *Atmospheric Processes over Complex Terrain* (pp. 229–283). Boston, MA: American Meteorological Society. DOI: 10.1007/978-1-935704-25-6_9.

Barnett, E. A., Sherrod, B. L., Hughes, J. F., Kelsey, H. M., Czajkowski, J. L., Walsh, T. J., Contreras, T. A., Schermer, E. R., & Carson, R. J. (2015). Paleoseismic evidence for Late Holocene Tectonic Deformation along the Saddle Mountain Fault Zone, Southeastern Olympic Peninsula, Washington. *Bulletin of the Seismological Society of America*, 105(1), 38–71. DOI: 10.1785/0120140086.

Batt, G. E., Brandon, M. T., Farley, K. A., & Roden-Tice, M. (2001). Tectonic synthesis of the Olympic Mountains segment of the Cascadia wedge, using

two-dimensional thermal and kinematic modeling of thermochronological ages. *Journal of Geophysical Research: Solid Earth*, 106(B11), 26731–26746. DOI: 10.1029/2001JB000288.

Beaumont, C., Fullsack, P., & Hamilton, J. (1992). Erosional control of active compressional orogens. In K. R. McClay (Ed.), *Thrust Tectonics* (pp. 1–18). Dordrecht: Springer Netherlands. DOI: 10.1007/978-94-011-3066-0_1.

Belmont, P., Pazzaglia, F., & Gosse, J. (2007). Cosmogenic ^{10}Be as a tracer for hillslope and channel sediment dynamics in the Clearwater River, western Washington State. *Earth and Planetary Science Letters*, 264, 123–135. DOI: 10.1016/j.epsl.2007.09.013.

Bendick, R. & Ehlers, T. A. (2014). Extreme localized exhumation at syntaxes initiated by subduction geometry. *Geophysical Research Letters*, 41(16), 5861–5867. DOI: 10.1002/2014GL061026.

Berner, R. A., Lasaga, A. C., & Garrels, R. M. (1983). The carbonate-silicate geochemical cycle and its effect on atmospheric carbon dioxide over the past 100 million years. *American Journal of Science*, 283(7), 641–683. 10.2475/ajs.283.7.641.

Bookhagen, B. & Burbank, D. W. (2010). Toward a complete Himalayan hydrological budget: Spatiotemporal distribution of snowmelt and rainfall and their impact on river discharge. *Journal of Geophysical Research*, 115(F3). DOI: 10.1029/2009JF001426.

Booth, D. B., Troost, K. G., Clague, J. J., & Waitt, R. B. (2003). The Cordilleran Ice Sheet. In A. Gillespie, S. Porter, & B. Atwater (Eds.), *Developments in Quaternary Sciences*, volume 1 (pp. 17–43). Elsevier. DOI: 10.1016/S1571-0866(03)01002-9.

Booth-Rea, G., Klaeschen, D., Grevemeyer, I., & Reston, T. (2008). Heterogeneous deformation in the Cascadia convergent margin and its relation to thermal gradient (Washington, NW USA). *Tectonics*, 27(4). DOI: 10.1029/2007TC002209.

Brandon, M. T. (1992). Decomposition of fission-track grain-age distributions. *American Journal of Science*, 292(8), 535–564. DOI: 10.2475/ajs.292.8.535.

Brandon, M. T. & Calderwood, A. R. (1990). High-pressure metamorphism and uplift of the Olympic subduction complex. *Geology*, 18(12), 1252–1255. DOI: 10.1130/0091-7613(1990)018<1252:HPMAUO>2.3.CO;2.

Brandon, M. T., Roden-Tice, M. K., & Garver, J. I. (1998). Late Cenozoic exhumation of the Cascadia accretionary wedge in the Olympic Mountains, northwest Washington State. *Geological Society of America Bulletin*, 110(8), 985–1009. DOI: 10.1130/0016-7606(1998)110<0985:LCEOTC>2.3.CO;2.

Brandon, M. T. & Vance, J. A. (1992). Tectonic evolution of the Cenozoic Olympic subduction complex, Washington State, as deduced from fission track ages for detrital zircons. *American Journal of Science*, 292(8), 565–636. DOI: 10.2475/ajs.292.8.565.

Braun, J. (2002). Estimating exhumation rate and relief evolution by spectral analysis of age–elevation datasets. *Terra Nova*, 14(3), 210–214. 10.1046/j.1365-3121.2002.00409.x.

Braun, J. (2003). Pecube: a new finite-element code to solve the 3D heat transport equation including the effects of a time-varying, finite amplitude surface topography. *Computers & Geosciences*, 29(6), 787–794. DOI: 10.1016/S0098-3004(03)00052-9.

Braun, J. (2005). Quantitative Constraints on the Rate of Landform Evolution Derived from Low-Temperature Thermochronology. *Reviews in Mineralogy and Geochemistry*, 58(1), 351–374. DOI: 10.2138/rmg.2005.58.13.

Braun, J., van der Beek, P., & Batt, G. (2006). *Quantitative thermochronology: numerical methods for the interpretation of thermochronological data*. Cambridge: Cambridge Univ. Press, 1st edition.

Braun, J., van der Beek, P., Valla, P., Robert, X., Herman, F., Glotzbach, C., Pedersen, V., Perry, C., Simon-Labric, T., & Prigent, C. (2012). Quantifying rates of landscape evolution and tectonic processes by thermochronology and numerical modeling of crustal heat transport using PECUBE. *Tectonophysics*, 524-525, 1–28. 10.1016/j.tecto.2011.12.035.

Brozović, N., Burbank, D. W., & Meigs, A. J. (1997). Climatic Limits on Landscape Development in the Northwestern Himalaya. *Science*, 276(5312), 571–574. DOI: 10.1126/science.276.5312.571.

Bruhat, L. & Segall, P. (2016). Coupling on the northern Cascadia subduction zone from geodetic measurements and physics-based models. *Journal of Geophysical Research: Solid Earth*, 121(11), 8297–8314. DOI: 10.1002/2016JB013267.

Burgette, R. J., Weldon, R. J., & Schmidt, D. A. (2009). Interseismic uplift rates for western Oregon and along-strike variation in locking on the Cascadia subduction zone. *Journal of Geophysical Research: Solid Earth*, 114(B1). DOI: 10.1029/2008JB005679.

Bätzing, W. (2002). *Die aktuellen Veränderungen von Umwelt, Wirtschaft, Gesellschaft und Bevölkerung in den Alpen*. Technical report, Bundesministerium für Umwelt, Naturschutz und Reaktorsicherheit. `https://www.umweltbundesamt.de/sites/default/files/medien/publikation/long/2150.pdf`.

Bürgmann, R. (2018). The geophysics, geology and mechanics of slow fault slip. *Earth and Planetary Science Letters*, 495, 112–134. DOI: 10.1016/j.epsl.2018.04.062.

Carrapa, B., Wijbrans, J., & Bertotti, G. (2003). Episodic exhumation in the Western Alps. *Geology*, 31(7), 601–604. DOI: 10.1130/0091-7613(2003)031<0601:EEITWA>2.0.CO;2.

Champagnac, J.-D., Molnar, P., Sue, C., & Herman, F. (2012). Tectonics, climate, and mountain topography. *Journal of Geophysical Research: Solid Earth*, 117(B2). 10.1029/2011JB008348.

Clague, J. J. & James, T. S. (2002). History and isostatic effects of the last ice sheet in southern British Columbia. *Quaternary Science Reviews*, 21(1), 71–87.

Colombaroli, D., Beckmann, M., van der Knaap, W. O., Curdy, P., & Tinner, W. (2013). Changes in biodiversity and vegetation composition in the central Swiss Alps during the transition from pristine forest to first farming. *Diversity and Distributions*, 19(2), 157–170. DOI: 10.1111/j.1472-4642.2012.00930.x.

Craw, D., Upton, P., Burridge, C. P., Wallis, G. P., & Waters, J. M. (2015). Rapid biological speciation driven by tectonic evolution in New Zealand. *Nature Geoscience*, 9(2), 140–144. DOI: 10.1038/ngeo2618.

Crosson, R. S. & Owens, T. J. (1987). Slab geometry of the Cascadia Subduction Zone beneath Washington from earthquake hypocenters and teleseismic converted waves. *Geophysical Research Letters*, 14(8), 824–827. DOI: 10.1029/GL014i008p00824.

Delano, J. E., Amos, C., Loveless, J., M. Rittenour, T., L. Sherrod, B., & M. Lynch, E. (2017). Influence of the megathrust earthquake cycle on upper-plate deformation in the Cascadia forearc of Washington State, USA. *Geology*, 45(11), 1051–1054. DOI: 10.1130/G39070.1.

Dodson, M. H. (1973). Closure temperature in cooling geochronological and petrological systems. *Contributions to Mineralogy and Petrology*, 40(3), 259–274.

Doubrovine, P. V. & Tarduno, J. A. (2008). A revised kinematic model for the relative motion between Pacific oceanic plates and North America since the Late Cretaceous. *Journal of Geophysical Research*, 113(B12). DOI: 10.1029/2008JB005585.

Dragert, H. & Wang, K. (2011). Temporal evolution of an episodic tremor and slip event along the northern Cascadia margin. *Journal of Geophysical Research*, 116(B12). DOI: 10.1029/2011JB008609.

Dragert, H., Wang, K., & James, T. S. (2001). A Silent Slip Event on the Deeper Cascadia Subduction Interface. *Science*, 292(5521), 1525–1528. DOI: 10.1126/science.1060152.

du Bray, E. A. & John, D. A. (2011). Petrologic, tectonic, and metallogenic evolution of the Ancestral Cascades magmatic arc, Washington, Oregon, and northern California. *Geosphere*, 7(5), 1102–1133.

Easterbrook, D. J. (1986). Stratigraphy and chronology of quaternary deposits of the Puget Lowland and Olympic Mountains of Washington and the Cascade Mountains of Washington and Oregon. *Quaternary Science Reviews*, 5, 145–159. DOI: 10.1016/0277-3791(86)90180-0.

Eddy, M. P., Clark, K. P., & Polenz, M. (2017). Age and volcanic stratigraphy of the Eocene Siletzia oceanic plateau in Washington and on Vancouver Island. *Lithosphere*, 9(4), 652–664. DOI: 10.1130/L650.1.

Egholm, D. L., Nielsen, S. B., Pedersen, V. K., & Lesemann, J.-E. (2009). Glacial effects limiting mountain height. *Nature*, 460(7257), 884–887. DOI: 10.1038/nature08263.

Ehlers, T. A. (2005). Computational Tools for Low-Temperature Thermochronometer Interpretation. *Reviews in Mineralogy and Geochemistry*, 58(1), 589–622. DOI: 10.2138/rmg.2005.58.22.

Ehlers, T. A., Farley, K. A., Rusmore, M. E., & Woodsworth, G. J. (2006). Apatite (U-Th)/He signal of large-magnitude accelerated glacial erosion, southwest British Columbia. *Geology*, 34(9), 765–768. DOI: 10.1130/G22507.1.

England, P. & Molnar, P. (1990). Surface uplift, uplift of rocks, and exhumation of rocks. *Geology*, 18(12), 1173–1177. DOI: 10.1130/0091-7613(1990)018<1173:SUUORA>2.3.CO;2.

England, T. D. J., Currie, L. D., Massey, N. W. D., Roden-Tice, M. K., & Miller, D. S. (1997). Apatite fission-track dating of the Cowichan fold and thrust system, southern Vancouver Island, British Columbia. *Canadian Journal of Earth Sciences*, 34(5), 635–645.

Enkelmann, E., Ehlers, T., Zeitler, P., & Hallet, B. (2011). Denudation of the Namche Barwa antiform, eastern Himalaya. *Earth and Planetary Science Letters*, 307(3-4), 323–333. DOI: 10.1016/j.epsl.2011.05.004.

Enkelmann, E., Koons, P. O., Pavlis, T. L., Hallet, B., Barker, A., Elliott, J., Garver, J. I., Gulick, S. P. S., Headley, R. M., Pavlis, G. L., Ridgway, K. D., Ruppert, N., & Van Avendonk, H. J. A. (2015). Cooperation among tectonic and surface processes in the St. Elias Range, Earth's highest coastal mountains. *Geophysical Research Letters*, 42(14), 5838–5846. DOI: 10.1002/2015GL064727.

Enkelmann, E., Piestrzeniewicz, A., Falkowski, S., Stübner, K., & Ehlers, T. A. (2017). Thermochronology in southeast Alaska and southwest Yukon: Implications for North American Plate response to terrane accretion. *Earth and Planetary Science Letters*, 457, 348–358. DOI: 10.1016/j.epsl.2016.10.032.

Enkelmann, E., Zeitler, P. K., Pavlis, T. L., Garver, J. I., & Ridgway, K. D. (2009). Intense localized rock uplift and erosion in the St. Elias orogen of Alaska. *Nature Geoscience*, 2(5), 360–363. DOI: 10.1038/ngeo502.

Farley, K. A. (2000). Helium diffusion from apatite: General behavior as illustrated by Durango fluorapatite. *Journal of Geophysical Research: Solid Earth*, 105(B2), 2903–2914. DOI: 10.1029/1999JB900348.

Farley, K. A. (2002). (U-Th)/He Dating: Techniques, Calibrations, and Applications. *Reviews in Mineralogy and Geochemistry*, 47(1), 819–844. DOI: 10.2138/rmg.2002.47.18.

Farley, K. A., Wolf, R. A., & Silver, L. T. (1996). The effects of long alpha-stopping distances on (U-Th)/He ages. *Geochimica et Cosmochimica Acta*, 60(21), 4223–4229. DOI: 10.1016/S0016-7037(96)00193-7.

Finley, T., Morell, K., Leonard, L., Regalla, C., Johnston, S. T., & Zhang, W. (2019). Ongoing oroclinal bending in the Cascadia forearc and its relation to concave-outboard plate margin geometry. *Geology*, 47(2), 155–158. DOI: 10.1130/G45473.1.

Finnegan, N. J., Hallet, B., Montgomery, D. R., Zeitler, P. K., Stone, J. O., Anders, A. M., & Yuping, L. (2008). Coupling of rock uplift and river incision in the Namche Barwa-Gyala Peri massif, Tibet. *Geological Society of America Bulletin*, 120(1-2), 142–155. DOI: 10.1130/B26224.1.

Finnegan, N. J., Schumer, R., & Finnegan, S. (2014). A signature of transience in bedrock river incision rates over timescales of 10^4–10^7 years. *Nature*, 505, 391–394. DOI: doi.org/10.1038/nature12913.

Flowers, R. M., Ketcham, R. A., Shuster, D. L., & Farley, K. A. (2009). Apatite (U–Th)/He thermochronometry using a radiation damage accumulation and annealing model. *Geochimica et Cosmochimica Acta*, 73(8), 2347–2365. DOI: 10.1016/j.gca.2009.01.015.

Fowler, C. M. R. (2005). *The solid earth: an introduction to global geophysics*. Cambridge: Cambridge University Press, 2nd edition.

Fox, M., Herman, F., Willett, S. D., & May, D. A. (2014). A linear inversion method to infer exhumation rates in space and time from thermochronometric data. *Earth Surface Dynamics*, 2(1), 47–65. DOI: 10.5194/esurf-2-47-2014.

Friedrich, A. M., Wernicke, B. P., Niemi, N. A., Bennett, R. A., & Davis, J. L. (2003). Comparison of geodetic and geologic data from the Wasatch region, Utah, and implications for the spectral character of Earth deformation at periods of 10 to 10 million years. *Journal of Geophysical Research: Solid Earth*, 108(B4). DOI: 10.1029/2001JB000682.

Galbraith, R. F. (2005). *Statistics for fission track analysis*. New York: CRC Press, 1st edition. DOI: 10.1201/9781420034929.

Garreaud, R. D., Vuille, M., Compagnucci, R., & Marengo, J. (2009). Present-day South American climate. *Palaeogeography, Palaeoclimatology, Palaeoecology*, 281(3-4), 180–195. DOI: 10.1016/j.palaeo.2007.10.032.

Garver, J. I. & Brandon, M. T. (1994). Erosional denudation of the British Columbia Coast Ranges as determined from fission-track ages of detrital zircon from the Tofino basin, Olympic Peninsula, Washington. *GSA Bulletin*, 106(11), 1398. DOI: 10.1130/0016-7606(1994)106<1398:EDOTBC>2.3.CO;2.

Georgieva, V., Gallagher, K., Sobczyk, A., Sobel, E., Schildgen, T., Ehlers, T., & Strecker, M. (2019). Effects of slab-window, alkaline volcanism, and glaciation on thermochronometer cooling histories, Patagonian Andes. *Earth and Planetary Science Letters*, 511, 164–176. DOI: 10.1016/j.epsl.2019.01.030.

Glotzbach, C. (2015). Deriving rock uplift histories from data-driven inversion of river profiles. *Geology*, 43(6), 467–470. DOI: 10.1130/G36702.1.

Glotzbach, C., van der Beek, P., Carcaillet, J., & Delunel, R. (2013). Deciphering the driving forces of erosion rates on millennial to million-year

timescales in glacially impacted landscapes: An example from the Western Alps. *Journal of Geophysical Research: Earth Surface*, 118(3), 1491–1515. DOI: 10.1002/jgrf.20107.

Glotzbach, C., van der Beek, P., & Spiegel, C. (2011). Episodic exhumation and relief growth in the Mont Blanc massif, Western Alps from numerical modelling of thermochronology data. *Earth and Planetary Science Letters*, 304(3-4), 417–430. DOI: 10.1016/j.epsl.2011.02.020.

Godard, V., Bourles, D. L., Spinabella, F., Burbank, D. W., Bookhagen, B., Fisher, G. B., Moulin, A., & Leanni, L. (2014). Dominance of tectonics over climate in Himalayan denudation. *Geology*, 42(3), 243–246. DOI: 10.1130/G35342.1.

Granger, D. E. & Schaller, M. (2014). Cosmogenic Nuclides and Erosion at the Watershed Scale. *Elements*, 10, 369–373. DOI: 10.2113/gselements.10.5.369.

Green, P., Duddy, I., Gleadow, A., Tingate, P., & Laslett, G. (1985). Fission-track annealing in apatite: Track length measurements and the form of the Arrhenius plot. *Nuclear Tracks and Radiation Measurements*, 10(3), 323–328. DOI: 10.1016/0735-245X(85)90121-8.

Griffiths, G. & McSaveney, M. (1983). Distribution of mean annual precipitation across some steepland regions of New Zealand (Southern Alps). *New Zealand Journal of Science*, 26, 197–209.

Grujic, D., Coutand, I., Bookhagen, B., Bonnet, S., Blythe, A., & Duncan, C. (2006). Climatic forcing of erosion, landscape, and tectonics in the Bhutan Himalayas. *Geology*, 34(10), 801–804. DOI: 10.1130/G22648.1.

Guenthner, W. R., Reiners, P. W., Ketcham, R. A., Nasdala, L., & Giester, G. (2013). Helium diffusion in natural zircon: Radiation damage, anisotropy, and the interpretation of zircon (U-Th)/He thermochronology. *American Journal of Science*, 313(3), 145–198. DOI: 10.2475/03.2013.01.

Han, S., Carbotte, S. M., Canales, J. P., Nedimović, M. R., Carton, H., Gibson, J. C., & Horning, G. W. (2016). Seismic reflection imaging of the Juan de Fuca plate from ridge to trench: New constraints on the distribution of faulting and evolution of the crust prior to subduction. *Journal of Geophysical Research: Solid Earth*, 121(3), 1849–1872. DOI: 10.1002/2015JB012416.

Herman, F., Beaud, F., Champagnac, J.-D., Lemieux, J.-M., & Sternai, P. (2011). Glacial hydrology and erosion patterns: A mechanism for carving glacial valleys. *Earth and Planetary Science Letters*, 310(3-4), 498–508. DOI: 10.1016/j.epsl.2011.08.022.

Herman, F. & Champagnac, J.-D. (2016). Plio-Pleistocene increase of erosion rates in mountain belts in response to climate change. *Terra Nova*, 28(1), 2–10. DOI: 10.1111/ter.12186.

Herman, F., Seward, D., Valla, P. G., Carter, A., Kohn, B., Willett, S. D., & Ehlers, T. A. (2013). Worldwide acceleration of mountain erosion under a cooling climate. *Nature*, 504(7480), 423–426. DOI: 10.1038/nature12877.

Hirsch, D. M. & Babcock, R. S. (2009). Spatially heterogeneous burial and high-P/T metamorphism in the Crescent Formation, Olympic Peninsula, Washington. *American Mineralogist*, 94(8-9), 1103–1110. DOI: 10.2138/am.2009.3187.

Hoorn, C., Guerrero, J., Sarmiento, G. A., & Lorente, M. A. (1995). Andean tectonics as a cause for changing drainage patterns in Miocene northern South America. *Geology*, 23(3), 237–240. DOI: 10.1130/0091-7613(1995)023<0237:ATAACF>2.3.CO;2.

Hoorn, C., Mosbrugger, V., Mulch, A., & Antonelli, A. (2013). Biodiversity from mountain building. *Nature Geosci*, 6(3), 154–154. DOI: 10.1038/ngeo1742.

Hoorn, C., Wesselingh, F. P., ter Steege, H., Bermudez, M. A., Mora, A., Sevink, J., Sanmartín, I., Sanchez-Meseguer, A., Anderson, C. L., Figueiredo, J. P., Jaramillo, C., Riff, D., Negri, F. R., Hooghiemstra, H., Lundberg, J., Stadler, T., Särkinen, T., & Antonelli, A. (2010). Amazonia Through Time: Andean Uplift, Climate Change, Landscape Evolution, and Biodiversity. *Science*, 330(6006), 927–931. DOI: 10.1126/science.1194585.

House, M. A., Wernicke, B. P., & Farley, K. A. (1998). Dating topography of the Sierra Nevada, California, using apatite (U-Th)/He ages. *Nature*, 396(6706), 66–69. DOI: 10.1038/23926.

House, M. A., Wernicke, B. P., & Farley, K. A. (2001). Paleo-geomorphology of the Sierra Nevada, California, from (U-Th)/He ages in apatite. *American Journal of Science*, 301(2), 77–102. DOI: 10.2475/ajs.301.2.77.

Houston, H., Delbridge, B. G., Wech, A. G., & Creager, K. C. (2011). Rapid tremor reversals in Cascadia generated by a weakened plate interface. *Nature Geoscience*, 4(6), 404–409. DOI: 10.1038/ngeo1157.

Hyndman, R. D. (2013). Downdip landward limit of Cascadia great earthquake rupture. *Journal of Geophysical Research: Solid Earth*, 118(10), 5530–5549. DOI: 10.1002/jgrb.50390.

Hyndman, R. D. & Wang, K. (1993). Thermal constraints on the zone of major thrust earthquake failure: The Cascadia Subduction Zone. *Journal of Geophysical Research: Solid Earth*, 98(B2), 2039–2060. DOI: 10.1029/92JB02279.

Häckel, H. (2016). *Meteorologie*. Stuttgart: UTB GmbH, 8th edition.

Jiao, R., Herman, F., & Seward, D. (2017). Late Cenozoic exhumation model of New Zealand: Impacts from tectonics and climate. *Earth-Science Reviews*, 166, 286–298. DOI: 10.1016/j.earscirev.2017.01.003.

Kasahara, A., Sasamori, T., & Washington, W. M. (1973). Simulation experiments with a 12-layer stratospheric global circulation model. i. dynamical effect of the earth's orography and thermal influence of continentality. *Journal of the Atmospheric Sciences*, 30(7), 1229–1251. DOI: 10.1175/1520-0469(1973)030<1229:SEWALS>2.0.CO;2.

Kearey, P., Klepeis, K. A., & Vine, F. J. (2009). *Global tectonics*. Oxford: Wiley-Blackwell, 3rd edition.

Ketcham, R. A., Donelick, R. A., & Carlson, W. D. (1999). Variability of apatite fission-track annealing kinetics: III. Extrapolation to geological time scales. *American Mineralogist*, 84(9), 1235–1255. DOI: 10.2138/am-1999-0903.

Koons, P., Zeitler, P., & Hallet, B. (2013). Tectonic Aneurysms and Mountain Building. In *Treatise on Geomorphology* (pp. 318–349). Elsevier. DOI: 10.1016/B978-0-12-374739-6.00094-4.

Krogstad, R. D., Schmidt, D. A., Weldon, R. J., & Burgette, R. J. (2016). Constraints on accumulated strain near the ETS zone along Cascadia. *Earth and Planetary Science Letters*, 439, 109–116. DOI: 10.1016/j.epsl.2016.01.033.

Kuhlemann, J. & Rahn, M. (2013). Plio-Pleistocene landscape evolution in Northern Switzerland. *Swiss Journal of Geosciences*, 106(3), 451–467. DOI: 10.1007/s00015-013-0152-6.

Kulm, L. V. D., von Huene, R., Duncan, J. R., Ingle, J. C., Kling, S. A., Musich, L. F., Piper, D. J. W., Pratt, R. M., Schrader, H.-J., Weser, O. E., & Wise, S. W. (1973). Site 174. *Initial Reports of the Deep Sea Drilling Project*, 18, 97. DOI: 10.2973/dsdp.proc.18.105.1973.

Lang, K. A., Huntington, K. W., Burmester, R., & Housen, B. (2016). Rapid exhumation of the eastern Himalayan syntaxis since the late Miocene. *Geological Society of America Bulletin*, 128(9-10), 1403–1422. DOI: 10.1130/B31419.1.

Lease, R. O. & Ehlers, T. A. (2013). Incision into the Eastern Andean plateau during Pliocene cooling. *Science*, 341(6147), 774–776. DOI: 10.1126/science.1239132.

Lease, R. O., Haeussler, P. J., & O'Sullivan, P. (2016). Changing exhumation patterns during Cenozoic growth and glaciation of the Alaska Range: Insights from detrital thermochronology and geochronology. *Tectonics*, 35(4), 934–955. DOI: 10.1002/2015TC004067.

Li, S., Moreno, M., Bedford, J., Rosenau, M., & Oncken, O. (2015). Revisiting viscoelastic effects on interseismic deformation and locking degree: A case study of the Peru-North Chile subduction zone. *Journal of Geophysical Research: Solid Earth*, 120(6), 4522–4538. DOI: 10.1002/2015JB011903.

Madella, A., Delunel, R., Akçar, N., Schlunegger, F., & Christl, M. (2018). ^{10}Be-inferred paleo-denudation rates imply that the mid-Miocene western central Andes eroded as slowly as today. *Scientific Reports*, 8(1), 2299. DOI: 10.1038/s41598-018-20681-x.

Mahadevan, L., Bendick, R., & Liang, H. (2010). Why subduction zones are curved. *Tectonics*, 29(6), TC6002. DOI: 10.1029/2010TC002720.

Mancktelow, N. S. & Grasemann, B. (1997). Time-dependent effects of heat advection and topography on cooling histories during erosion. *Tectonophysics*, 270(3-4), 167–195. DOI: 10.1016/S0040-1951(96)00279-X.

McCaffrey, R. (2009). Time-dependent inversion of three-component continuous GPS for steady and transient sources in northern Cascadia. *Geophysical Research Letters*, 36(7). DOI: 10.1029/2008GL036784.

McCrory, P. A., Blair, J. L., Waldhauser, F., & Oppenheimer, D. H. (2012). Juan de Fuca slab geometry and its relation to Wadati-Benioff zone seismicity. *Journal of Geophysical Research: Solid Earth*, 117(B9). DOI: 10.1029/2012JB009407.

McDannell, K. T., Zeitler, P. K., & Idleman, B. D. (2018). Relict Topography Within the Hangay Mountains in Central Mongolia: Quantifying Long-Term Exhumation and Relief Change in an Old Landscape. *Tectonics*, 37(8), 2531–2558. DOI: 10.1029/2017TC004682.

Mitchell, S. G. & Montgomery, D. R. (2006). Influence of a glacial buzzsaw on the height and morphology of the Cascade Range in central Washington State, USA. *Quaternary Research*, 65(01), 96–107. DOI: 10.1016/j.yqres.2005.08.018.

Molnar, P., Boos, W. R., & Battisti, D. S. (2010). Orographic Controls on Climate and Paleoclimate of Asia: Thermal and Mechanical Roles for the Tibetan Plateau. *Annual Review of Earth and Planetary Sciences*, 38(1), 77–102. DOI: 10.1146/annurev-earth-040809-152456.

Molnar, P. & England, P. (1990). Late Cenozoic uplift of mountain ranges and global climate change: chicken or egg? *Nature*, 346(6279), 29–34. DOI: 10.1038/346029a0.

Montgomery, D. R. (2002). Valley formation by fluvial and glacial erosion. *Geology*, 30(11), 1047–1050. DOI: 10.1130/0091-7613(2002)030<1047:VFBFAG>2.0.CO;2.

Montgomery, D. R. & Greenberg, H. M. (2000). Local relief and the height of Mount Olympus. *Earth Surface Processes and Landforms*, 25(4), 385–396. DOI: 10.1002/(SICI)1096-9837(200004)25:4<385::AID-ESP61>3.0.CO;2-H.

Nasdala, L., Wenzel, M., Vavra, G., Irmer, G., Wenzel, T., & Kober, B. (2001). Metamictisation of natural zircon: accumulation versus thermal annealing of radioactivity-induced damage. *Contributions to Mineralogy and Petrology*, 141(2), 125–144. DOI: 10.1007/s004100000235.

Nelson, A. R., Bradley, L.-A., Reitman, N., Personius, S. F., Wells, R. E., Schermer, E. R., & Buck, J. (2017). Holocene Earthquakes of Magnitude 7 during Westward Escape of the Olympic Mountains, Washington. *Bulletin of the Seismological Society of America*, 107(5), 2394–2415. DOI: 10.1785/0120160323.

Nettesheim, M., Ehlers, T. A., Whipp, D. M., & Koptev, A. (2018). The influence of upper-plate advance and erosion on overriding plate deformation in orogen syntaxes. *Solid Earth*, 9(6), 1207–1224. DOI: 10.5194/se-9-1207-2018.

Niemi, N. A. & Clark, M. K. (2018). Long-term exhumation rates exceed paleoseismic slip rates in the central Santa Monica Mountains, Los Angeles County, California. *Geology*, 46(1), 63–66. DOI: 10.1130/G39388.1.

Olariu, C., Krezsek, C., & Jipa, D. C. (2018). The Danube River inception: Evidence for a 4 Ma continental-scale river born from segmented ParaTethys basins. *Terra Nova*, 30(1), 63–71. DOI: 10.1111/ter.12308.

Olen, S. M., Ehlers, T. A., & Densmore, M. S. (2012). Limits to reconstructing paleotopography from thermochronometer data. *Journal of Geophysical Research: Earth Surface*, 117(F1). DOI: 10.1029/2011JF001985.

Pazzaglia, F. J. & Brandon, M. T. (2001). A fluvial record of long-term steady-state uplift and erosion across the Cascadia forearc high, western Washington State. *American Journal of Science*, 301(4-5), 385–431. DOI: 10.2475/ajs.301.4-5.385.

Phillips, B. A., Kerr, A. C., Mullen, E. K., & Weis, D. (2017). Oceanic mafic magmatism in the Siletz terrane, NW North America: Fragments of an Eocene oceanic plateau? *Lithos*, 274-275, 291–303. DOI: 10.1016/j.lithos.2017.01.005.

Porter, S. C. (1964). Composite Pleistocene snow line of Olympic Mountains and Cascade Range, Washington. *Geological Society of America Bulletin*, 75(5), 477–482. DOI: 10.1130/0016-7606(1964)75[477:CPSLOO]2.0.CO;2.

Pritchard, D., Roberts, G. G., White, N. J., & Richardson, C. N. (2009). Uplift histories from river profiles. *Geophysical Research Letters*, 36(24). DOI: 10.1029/2009GL040928.

Rahn, M. K., Brandon, M. T., Batt, G. E., & Garver, J. I. (2004). A zero-damage model for fission-track annealing in zircon. *American Mineralogist*, 89(4), 473–484. DOI: 10.2138/am-2004-0401.

Ramírez-Herrera, M. T., Gaidzik, K., Forman, S., Kostoglodov, V., Bürgmann, R., & Johnson, C. (2018). Relating the long-term and short-term vertical deformation across a transect of the forearc in the central Mexican subduction zone. *Geosphere*, 14(2), 419–439. DOI: 10.1130/GES01446.1.

Raymo, M. E. & Ruddiman, W. F. (1992). Tectonic forcing of late Cenozoic climate. *Nature*, 359(6391), 117–122. DOI: 10.1038/359117a0.

Reiners, P. W., Ehlers, T. A., Mitchell, S. G., & Montgomery, D. R. (2003). Coupled spatial variations in precipitation and long-term erosion rates across the Washington Cascades. *Nature*, 426(6967), 645–647. DOI: 10.1038/nature02111.

Reiners, P. W., Spell, T. L., Nicolescu, S., & Zanetti, K. A. (2004). Zircon (U-Th)/He thermochronometry: He diffusion and comparisons with $^{40}Ar/^{39}Ar$ dating. *Geochimica et Cosmochimica Acta*, 68(8), 1857–1887. DOI: 10.1016/j.gca.2003.10.021.

Riedel, J., Wilson, S., Baccus, W., Larrabee, M., Fudge, T., & Fountain, A. (2015). Glacier status and contribution to streamflow in the Olympic Mountains, Washington, USA. *Journal of Glaciology*, 61(225), 8–16. DOI: 10.3189/2015JoG14J138.

Ring, U., Brandon, M. T., Willett, S. D., & Lister, G. S. (1999). Exhumation processes. *Geological Society, London, Special Publications*, 154(1), 1–27. DOI: 10.1144/GSL.SP.1999.154.01.01.

Robert, X., van der Beek, P., Braun, J., Perry, C., & Mugnier, J.-L. (2011). Control of detachment geometry on lateral variations in exhumation rates in the Himalaya: Insights from low-temperature thermochronology and numerical modeling. *Journal of Geophysical Research*, 116(B5). DOI: 10.1029/2010JB007893.

Roe, G. H. (2005). Orographic Precipitation. *Annual Review of Earth and Planetary Sciences*, 33(1), 645–671. DOI: 10.1146/annurev.earth.33.092203.122541.

Rogers, G. & Dragert, H. (2003). Episodic Tremor and Slip on the Cascadia Subduction Zone: The Chatter of Silent Slip. *Science*, 300(5627), 1942–1943. DOI: 10.1126/science.1084783.

Rutherford, E. (1905). Present problems in radioactivity. *Popular Science Monthly*, 67, 5–34.

Rutherford, E. & Soddy, F. (1903a). Radioactive Change. *Philosophical Magazine*, 5(29), 576–591. DOI: 10.1080/14786440309462960.

Rutherford, E. & Soddy, F. (1903b). The radioactivity of uranium. *Philosophical Magazine*, 5(28), 441–445. DOI: 10.1080/14786440309462942.

Satake, K., Wang, K., & Atwater, B. F. (2003). Fault slip and seismic moment of the 1700 Cascadia earthquake inferred from Japanese tsunami descriptions. *Journal of Geophysical Research: Solid Earth*, 108(B11). DOI: 10.1029/2003JB002521.

Schildgen, T. F., van der Beek, P. A., Sinclair, H. D., & Thiede, R. C. (2018). Spatial correlation bias in late-Cenozoic erosion histories derived from thermochronology. *Nature*, 559(7712), 89–93. DOI: 10.1038/s41586-018-0260-6.

Schmidl, A., Kofler, W., Oeggl-Wahlmüller, N., & Oeggl, K. (2005). Land use in the eastern Alps during the Bronze Age—An archaeobotanical case study of a hilltop settlement in the Montafon (Western Austria). *Archaeometry*, 47(2), 455–470.

Schmidt, D. A. & Gao, H. (2010). Source parameters and time-dependent slip distributions of slow slip events on the Cascadia subduction zone from 1998 to 2008. *Journal of Geophysical Research*, 115. DOI: 10.1029/2008JB006045.

Seager, R., Battisti, D. S., Yin, J., Gordon, N., Naik, N., Clement, A. C., & Cane, M. A. (2002). Is the gulf stream responsible for europe's mild winters? *Quarterly Journal of the Royal Meteorological Society*, 128(586), 2563–2586. DOI: 10.1256/qj.01.128.

Seward, D. & Burg, J.-P. (2008). Growth of the Namche Barwa Syntaxis and associated evolution of the Tsangpo Gorge: Constraints from structural and thermochronological data. *Tectonophysics*, 451(1-4), 282–289. DOI: 10.1016/j.tecto.2007.11.057.

Shephard, G. E., Müller, R. D., Liu, L., & Gurnis, M. (2010). Miocene drainage reversal of the Amazon River driven by plate–mantle interaction. *Nature Geoscience*, 3, 870–871. DOI: 10.1038/ngeo1017.

Shuster, D. L., Ehlers, T. A., Rusmoren, M. E., & Farley, K. A. (2005). Rapid Glacial Erosion at 1.8 Ma Revealed by $^{4}He/^{3}He$ Thermochronometry. *Science*, 310(5754), 1668–1670. DOI: 10.1126/science.1118519.

Starke, J., Ehlers, T. A., & Schaller, M. (2017). Tectonic and Climatic Controls on the Spatial Distribution of Denudation Rates in Northern Chile (18°S to 23°S) Determined From Cosmogenic Nuclides. *Journal of Geophysical Research: Earth Surface*, 122(10), 1949–1971. DOI: 10.1002/2016JF004153.

Steer, P., Huismans, R. S., Valla, P. G., Gac, S., & Herman, F. (2012). Bimodal Plio–Quaternary glacial erosion of fjords and low-relief surfaces in Scandinavia. *Nature Geoscience*, 5(9), 635–639. DOI: 10.1038/ngeo1549.

Sternai, P., Herman, F., Fox, M. R., & Castelltort, S. (2011). Hypsometric analysis to identify spatially variable glacial erosion. *Journal of Geophysical Research*, 116(F3). DOI: 10.1029/2010JF001823.

Stewart, R. J. & Brandon, M. T. (2004). Detrital-zircon fission-track ages for the "Hoh Formation": implications for late Cenozoic evolution of the Cascadia subduction wedge. *Geological Society of America Bulletin*, 116(1-2), 60–75. DOI: 10.1130/B22101.1.

Stüwe, K., White, L., & Brown, R. (1994). The influence of eroding topography on steady-state isotherms. Application to fission track analysis. *Earth and Planetary Science Letters*, 124(1-4), 63–74. DOI: 10.1016/0012-821X(94)00068-9.

Su, X., Baumann, K. H., & Thiede, J. (2000). Calcareous nannofossils from Leg 168: biochronology and diagenesis. In *Proceedings of the Ocean Drilling Program, Scientific Results*, volume 168 (pp. 39–50).

Tabor, R. W. & Cady, W. M. (1978). *The structure of the Olympic Mountains, Washington: Analysis of a subduction zone*, volume 1033. US Govt. Print. Off.

Tagami, T. & O'Sullivan, P. B. (2005). Fundamentals of Fission-Track Thermochronology. *Reviews in Mineralogy and Geochemistry*, 58(1), 19–47. DOI: 10.2138/rmg.2005.58.2.

Thackray, G. D. (2001). Extensive Early and Middle Wisconsin Glaciation on the Western Olympic Peninsula, Washington, and the Variability of Pacific Moisture Delivery to the Northwestern United States. *Quaternary Research*, 55(3), 257–270. DOI: 10.1006/qres.2001.2220.

Thiede, R. C. & Ehlers, T. A. (2013). Large spatial and temporal variations in Himalayan denudation. *Earth and Planetary Science Letters*, 371-372, 278–293. DOI: 10.1016/j.epsl.2013.03.004.

Thomson, S. N., Brandon, M. T., Tomkin, J. H., Reiners, P. W., Vásquez, C., & Wilson, N. J. (2010). Glaciation as a destructive and constructive control on mountain building. *Nature*, 467(7313), 313–317. DOI: 10.1038/nature09365.

Valla, P. G., Shuster, D. L., & van der Beek, P. (2011). Significant increase in relief of the European Alps during Mid-Pleistocene glaciations. *Nature Geoscience*, 4, 688–692. DOI: 10.1038/ngeo1242.

van der Beek, P., Litty, C., Baudin, M., Mercier, J., Robert, X., & Hardwick, E. (2016). Contrasting tectonically driven exhumation and incision patterns, western versus central Nepal Himalaya. *Geology*, 44(4), 327–330. DOI: 10.1130/G37579.1.

van der Beek, P., Van Melle, J., Guillot, S., Pêcher, A., Reiners, P. W., Nicolescu, S., & Latif, M. (2009). Eocene Tibetan plateau remnants preserved in the northwest Himalaya. *Nature Geoscience*, 2(5), 364–368. DOI: 10.1038/ngeo503.

Vidale, J. E. & Houston, H. (2012). Slow slip: A new kind of earthquake. *Physics Today*, 65(1), 38–43. DOI: 10.1063/PT.3.1399.

von Blanckenburg, F. (2005). The control mechanisms of erosion and weathering at basin scale from cosmogenic nuclides in river sediment. *Earth and Planetary Science Letters*, 237(3-4), 462–479. DOI: 10.1016/j.epsl.2005.06.030.

von Blanckenburg, F. & Willenbring, J. (2014). Cosmogenic Nuclides: Dates and Rates of Earth-Surface Change. *Elements*, 10, 341–346. DOI: 10.2113/gselements.10.5.341.

Wang, K. & Tréhu, A. M. (2016). Invited review paper: Some outstanding issues in the study of great megathrust earthquakes—The Cascadia example. *Journal of Geodynamics*, 98, 1–18. DOI: 10.1016/j.jog.2016.03.010.

Wang, P., Scherler, D., Liu-Zeng, J., Mey, J., Avouac, J.-P., Zhang, Y., & Shi, D. (2014). Tectonic control of Yarlung Tsangpo Gorge revealed by a buried canyon in Southern Tibet. *Science*, 346(6212), 978–981. DOI: 10.1126/science.1259041.

Wang, P.-L., Engelhart, S. E., Wang, K., Hawkes, A. D., Horton, B. P., Nelson, A. R., & Witter, R. C. (2013). Heterogeneous rupture in the great Cascadia earthquake of 1700 inferred from coastal subsidence estimates. *Journal of Geophysical Research: Solid Earth*, 118(5), 2460–2473. DOI: 10.1002/jgrb.50101.

Wech, A. G. & Bartlow, N. M. (2014). Slip rate and tremor genesis in Cascadia. *Geophysical Research Letters*, 41(2), 392–398. DOI: 10.1002/2013GL058607.

Wech, A. G. & Creager, K. C. (2011). A continuum of stress, strength and slip in the Cascadia subduction zone. *Nature Geoscience*, 4(9), 624–628. DOI: 10.1038/ngeo1215.

Wells, R. E., Blakely, R. J., Wech, A. G., McCrory, P. A., & Michael, A. (2017). Cascadia subduction tremor muted by crustal faults. *Geology*, 45(6), 515–518. DOI: 10.1130/G38835.1.

Wells, R. E., Bukry, D., Friedman, R., Pyle, D., Duncan, R., Haeussler, P., & Wooden, J. (2014). Geologic history of Siletzia, a large igneous province in the Oregon and Washington Coast Range: Correlation to the geomagnetic polarity time scale and implications for a long-lived Yellowstone hotspot. *Geosphere*, 10(4), 692–719. DOI: 10.1130/GES01018.1.

Wells, R. E. & McCaffrey, R. (2013). Steady rotation of the Cascade arc. *Geology*, 41(9), 1027–1030. DOI: 10.1130/G34514.1.

Westbrook, G., Carson, B., & Musgrave, R. (1994). Shipboard Scientific Party, 1994. In *Initial reports of the Ocean Drilling Program*, volume 146.

Whipple, K. X. (2009). The influence of climate on the tectonic evolution of mountain belts. *Nature Geoscience*, 2(2), 97–104. DOI: 10.1038/ngeo413.

Whipple, K. X. & Meade, B. (2006). Orogen response to changes in climatic and tectonic forcing. *Earth and Planetary Science Letters*, 243(1-2), 218–228. DOI: 10.1016/j.epsl.2005.12.022.

Willenbring, J. K. & Jerolmack, D. J. (2016). The null hypothesis: globally steady rates of erosion, weathering fluxes and shelf sediment accumulation during Late Cenozoic mountain uplift and glaciation. *Terra Nova*, 28(1), 11–18. DOI: 10.1111/ter.12185.

Willenbring, J. K. & von Blanckenburg, F. (2010). Long-term stability of global erosion rates and weathering during late-Cenozoic cooling. *Nature*, 465(7295), 211–214. DOI: 10.1038/nature09044.

Willett, S. D. (1999). Orogeny and orography: The effects of erosion on the structure of mountain belts. *Journal of Geophysical Research: Solid Earth*, 104(B12), 28957–28981. DOI: 10.1029/1999JB900248.

Willett, S. D. & Brandon, M. T. (2002). On steady states in mountain belts. *Geology*, 30(2), 175. DOI: 10.1130/0091-7613(2002)030<0175:OSSIMB>2.0.CO;2.

Willett, S. D. & Brandon, M. T. (2013). Some analytical methods for converting thermochronometric age to erosion rate. *Geochemistry, Geophysics, Geosystems*, 14(1), 209–222. DOI: 10.1029/2012GC004279.

Willett, S. D., McCoy, S. W., Perron, J. T., Goren, L., & Chen, C.-Y. (2014). Dynamic Reorganization of River Basins. *Science*, 343(6175). DOI: 10.1126/science.1248765.

Wilson, D. S. (1993). Confidence intervals for motion and deformation of the Juan de Fuca Plate. *Journal of Geophysical Research: Solid Earth*, 98(B9), 16053–16071. DOI: 10.1029/93JB01227.

Wilson, J. R., Bartholomew, M. J., & Carson, R. J. (1979). Late Quaternary faults and their relationship to tectonism in the Olympic Peninsula, Washington. *Geology*, 7(5), 235–239. DOI: 10.1130/0091-7613(1979)7<235:LQFATR>2.0.CO;2.

Yanites, B. J. & Ehlers, T. A. (2012). Global climate and tectonic controls on the denudation of glaciated mountains. *Earth and Planetary Science Letters*, 325-326, 63–75. DOI: 10.1016/j.epsl.2012.01.030.

Yanites, B. J. & Ehlers, T. A. (2016). Intermittent glacial sliding velocities explain variations in long-timescale denudation. *Earth and Planetary Science Letters*, 450, 52–61. DOI: 10.1016/j.epsl.2016.06.022.

Yanites, B. J., Ehlers, T. A., Becker, J. K., Schnellmann, M., & Heuberger, S. (2013). High magnitude and rapid incision from river capture: Rhine River, Switzerland. *Journal of Geophysical Research: Earth Surface*, 118(2), 1060–1084. DOI: 10.1002/jgrf.20056.

Zeitler, P. K., Meltzer, A. S., Koons, P. O., Craw, D., Hallet, B., Chamberlain, C. P., Kidd, W. S., Park, S. K., Seeber, L., Bishop, M., & others (2001). Erosion, Himalayan geodynamics, and the geomorphology of metamorphism. *GSA Today*, 11(1), 4–9.

Zhang, P., Molnar, P., & Downs, W. R. (2001). Increased sedimentation rates and grain sizes 2—4 Myr ago due to the influence of climate change on erosion rates. *Nature*, 410(6831), 891–897. 10.1038/35073504.

Ziegler, P. A. & Fraefel, M. (2009). Response of drainage systems to Neogene evolution of the Jura fold-thrust belt and Upper Rhine Graben. *Swiss Journal of Geosciences*, 102(1), 57–75. DOI: 10.1007/s00015-009-1306-4.

Appendices

Appendix A

Additional data tables of section 3.1

The following pages contain supplementary data tables for the paper "Tectonic and glacial contribution to focused exhumation in the Olympic Mountains, Washington, USA." presented in section 3.1.2.

These data include single grain analyses from apatite (U-Th)/He dating (Table DR2, section A.1) and single grain analyses from zircon (U-Th)/He dating (Table DR3, section A.2). These tables are also available online as excel spreadsheets in the GSA data repository (`https://www.geosociety.org/datarepository/2018/`) under the data item 2018161.

A.1 Apatite (U-Th)/He single grain analyses

Table DR 2: Apatite (U-Th-Sm)/He single grain data

Note: Aliquots which are strike-through are not considered for the sample age calculation. ppm values of U, Th and Sm are calculated from iCAP results by deviding the mass of the respective element by the grain mass (which is derived from measurements of ^{43}Ca). eU is calculated by adding U-content and 0.235*Th-content. Mean sample ages are reported in table DR1.

Sample/ Aliquot	U (ppm)	U ± 2SD (pg)	Th (ppm)	Th ± 2SD (pg)	Sm (ppm)	Sm ± 2SD (pg)	He ± 1SD (mol)	grain mass (µg)	eU (ppm)	Th/U	Uncorrected grain age (Ma)	FT correction	Corrected grain age ± 1SD (Ma)
Ap_OP1502-1	2	7.5 ± 0.5	5	23.1 ± 0.7	144	636.2 ± 9.0	1.09E-15 ± 1.58E-17	4.4	3	3.18	15.6	0.73	21.2 ± 1.4
Ap_OP1502-3	7	7.7 ± 0.4	10	11.1 ± 0.5	393	420.4 ± 5.8	9.12E-16 ± 1.64E-17	1.1	10	1.49	16.4	0.59	27.5 ± 1.9
Ap_OP1502-4	6	8.8 ± 0.7	6	10.2 ± 0.4	323	510.7 ± 5.6	1.06E-15 ± 1.60E-17	1.6	7	1.19	17.5	0.68	25.8 ± 2.1
Ap_OP1502-5	12	15.1 ± 0.6	19	22.8 ± 0.7	466	565.6 ± 8.4	2.64E-15 ± 3.36E-17	1.2	17	1.55	23.8	0.60	40.0 ± 2.4
Ap_OP1504-1	21	42.3 ± 8.2	19	37.5 ± 1.4	280	568.4 ± 11.5	5.98E-16 ± 1.59E-17	2.0	25	0.91	2.2	0.67	3.3 ± 0.6
~~Ap_OP1504-2~~	~~81~~	~~35.8 ± 8.2~~	~~30~~	~~13.1 ± 1.1~~	~~333~~	~~147.0 ± 9.0~~	~~1.24E-16 ± 6.90E-18~~	~~0.4~~	~~88~~	~~0.38~~	~~0.6~~	~~0.62~~	~~1.0 ± 0.3~~
Ap_OP1504-3	161	150.5 ± 30.5	186	174.1 ± 7.6	215	201.2 ± 19.5	4.58E-15 ± 6.52E-17	0.9	205	1.19	4.6	0.62	7.3 ± 1.3
Ap_OP1504-4	94	110.2 ± 17.3	22	26.0 ± 1.2	212	247.3 ± 24.5	1.93E-15 ± 3.19E-17	1.2	100	0.24	3.2	0.69	4.5 ± 0.7
Ap_OP1505-1	39	48.2 ± 14.1	27	33.8 ± 1.7	127	156.9 ± 14.6	8.19E-16 ± 1.73E-17	1.2	46	0.72	2.9	0.64	4.5 ± 1.6
~~Ap_OP1505-2~~	~~65~~	~~129.7 ± 18.6~~	~~20~~	~~39.2 ± 1.6~~	~~240~~	~~475.3 ± 12.8~~	~~6.67E-15 ± 9.93E-17~~	~~2.0~~	~~70~~	~~0.31~~	~~9.1~~	~~0.68~~	~~13.4 ± 1.9~~
Ap_OP1505-3	53	65.3 ± 14.7	39	47.6 ± 1.9	88	108.3 ± 10.6	1.82E-15 ± 3.14E-17	1.2	62	0.75	4.6	0.62	7.4 ± 1.6
Ap_OP1505-4	38	64.2 ± 11.0	10	17.3 ± 1.1	300	505.4 ± 11.7	1.86E-15 ± 3.09E-17	1.7	41	0.28	5.2	0.66	7.9 ± 1.4
Ap_OP1507-1	10	57.3 ± 2.0	64	355.8 ± 13.2	321	1776.6 ± 15.1	2.05E-15 ± 3.02E-17	5.5	25	6.37	2.7	0.76	3.5 ± 0.2
Ap_OP1507-2	11	18.3 ± 0.7	61	105.3 ± 2.1	290	498.6 ± 6.5	5.28E-16 ± 1.17E-17	1.7	25	5.89	2.3	0.64	3.5 ± 0.2
Ap_OP1507-3	16	21.7 ± 0.9	41	55.6 ± 1.8	281	381.7 ± 5.9	3.72E-16 ± 9.68E-18	1.4	26	2.62	2.0	0.62	3.2 ± 0.2
Ap_OP1510-1	13	23.4 ± 0.8	39	68.9 ± 1.8	202	354.2 ± 5.1	1.24E-15 ± 1.93E-17	1.8	23	3.02	5.8	0.70	8.2 ± 0.5
Ap_OP1510-2	9	12.2 ± 0.6	14	19.2 ± 0.7	62	84.9 ± 4.4	6.30E-16 ± 1.33E-17	1.4	12	1.62	7.0	0.68	10.2 ± 0.7
Ap_OP1510-3	18	22.5 ± 0.7	40	51.5 ± 1.3	197	252.3 ± 3.0	8.75E-16 ± 1.55E-17	1.3	27	2.34	4.7	0.66	7.1 ± 0.4
Ap_OP1513-5	61	66.1 ± 13.3	300	322.8 ± 11.2	203	218.0 ± 13.7	8.12E-16 ± 1.43E-17	1.1	132	5.01	1.1	0.61	1.7 ± 0.2
Ap_OP1513-6	57	45.7 ± 11.9	71	57.4 ± 2.8	222	178.7 ± 10.1	2.11E-16 ± 6.85E-18	0.8	74	1.29	0.7	0.59	1.2 ± 0.3
Ap_OP1513-7	39	39.6 ± 12.5	95	96.1 ± 4.6	102	102.9 ± 9.1	2.91E-16 ± 9.63E-18	1.0	62	2.49	0.9	0.62	1.5 ± 0.3
Ap_OP1513-8	54	43.5 ± 9.3	55	44.0 ± 1.5	275	221.9 ± 8.7	2.43E-16 ± 7.57E-18	0.8	67	1.04	0.9	0.57	1.5 ± 0.3
Ap_OP1515-1	26	31.3 ± 1.0	14	17.2 ± 0.6	58	71.0 ± 3.3	3.59E-16 ± 8.44E-18	1.2	29	0.56	1.9	0.61	3.1 ± 0.2
Ap_OP1515-2	8	16.1 ± 0.6	18	36.3 ± 1.4	201	398.7 ± 5.4	2.99E-16 ± 9.24E-18	2.0	12	2.31	2.2	0.65	3.4 ± 0.2
Ap_OP1515-3	3	3.4 ± 0.3	31	36.5 ± 1.2	292	349.2 ± 5.0	7.43E-17 ± 5.73E-18	1.2	10	11.13	1.1	0.61	1.9 ± 0.2
Ap_OP1517-1	40	54.3 ± 1.4	83	112.8 ± 2.0	141	191.4 ± 3.9	1.32E-15 ± 2.25E-17	1.4	60	2.13	3.0	0.66	4.6 ± 0.3
Ap_OP1517-4	44	181.7 ± 27.1	57	236.9 ± 9.6	114	475.2 ± 43.2	2.56E-15 ± 3.71E-17	4.2	57	1.34	2.0	0.72	2.8 ± 0.3
Ap_OP1518-1	41	91.4 ± 16.7	45	99.6 ± 4.4	54	119.7 ± 8.2	2.95E-15 ± 4.58E-17	2.2	51	1.12	4.9	0.69	7.1 ± 1.2
Ap_OP1518-2	129	227.9 ± 19.4	139	244.8 ± 5.8	155	273.1 ± 7.6	1.05E-14 ± 1.38E-16	1.8	162	1.10	6.8	0.68	9.9 ± 0.8
Ap_OP1521-1	173	77.5 ± 23.1	272	121.6 ± 7.4	400	179.0 ± 28.4	5.95E-16 ± 1.21E-17	0.4	237	1.61	1.1	0.61	1.8 ± 0.5
Ap_OP1521-2	8	56.2 ± 14.8	5	34.3 ± 2.2	61	407.1 ± 18.6	4.05E-16 ± 1.14E-17	6.7	10	0.63	1.2	0.75	1.6 ± 0.5
Ap_OP1521-3	52	205.6 ± 22.7	63	249.8 ± 10.8	216	851.8 ± 43.7	2.00E-15 ± 2.91E-17	3.9	67	1.25	1.4	0.71	2.0 ± 0.2
Ap_OP1521-4	30	69.4 ± 14.5	144	331.9 ± 12.5	337	779.5 ± 45.1	1.40E-15 ± 1.93E-17	2.3	64	4.91	1.8	0.65	2.7 ± 0.3

Ap_OP1521-5	16	79.6	±	19.9	19	97.0	±	5.5	66	331.8	±	51.8	6.71E-16	±	1.44E-17	5.0	20	1.25	1.3	0.74	1.7	±	0.4
Ap_OP1522-1	20	38.8	±	1.3	35	69.1	±	1.7	124	243.7	±	3.5	1.78E-15	±	2.34E-17	2.0	28	1.83	6.0	0.67	8.9	±	0.5
Ap_OP1522-2	2	2.1	±	0.3	1	1.4	±	0.1	144	169.8	±	3.8	8.19E-17	±	5.75E-18	1.2	2	0.69	6.2	0.62	10.0	±	1.5
~~Ap_OP1522-3~~	~~2~~	~~7.4~~	~~±~~	~~0.4~~	~~2~~	~~7.7~~	~~±~~	~~0.5~~	~~154~~	~~634.2~~	~~±~~	~~9.6~~	~~8.13E-16~~	~~±~~	~~1.59E-17~~	~~4.1~~	~~2~~	~~1.06~~	~~16.4~~	~~0.74~~	~~22.3~~	~~±~~	~~1.5~~
Ap_OP1522-4	36	118.5	±	17.6	5	15.8	±	1.1	46	149.2	±	18.1	4.98E-15	±	7.04E-17	3.3	38	0.14	7.7	0.73	10.6	±	1.7
Ap_OP1523-2	30	109.4	±	20.1	49	177.6	±	8.0	64	230.9	±	18.9	4.25E-15	±	6.31E-17	3.6	42	1.66	5.3	0.72	7.2	±	1.0
Ap_OP1523-3	65	69.6	±	17.1	94	101.0	±	5.4	66	70.6	±	11.6	1.98E-15	±	3.56E-17	1.1	87	1.49	4.1	0.63	6.4	±	1.3
Ap_OP1527-1	84	96.7	±	2.9	11	12.6	±	0.6	158	181.7	±	3.8	1.34E-15	±	2.02E-17	1.2	87	0.13	2.5	0.62	4.1	±	0.2
Ap_OP1527-2	86	90.2	±	13.0	54	57.3	±	2.5	159	168.0	±	9.8	6.25E-16	±	1.42E-17	1.1	98	0.65	1.1	0.60	1.9	±	0.3
Ap_OP1527-3	21	32.5	±	1.0	20	30.3	±	0.9	325	497.1	±	7.4	3.96E-16	±	8.41E-18	1.5	26	0.96	1.9	0.65	2.8	±	0.2
Ap_OP1527-4	9	16.7	±	0.6	12	23.0	±	0.7	197	376.9	±	8.4	1.20E-16	±	7.00E-18	1.9	12	1.41	1.0	0.66	1.5	±	0.1
Ap_OP1527-5	57	131.5	±	3.2	50	114.5	±	2.5	115	264.9	±	6.1	2.09E-15	±	3.11E-17	2.3	69	0.89	2.4	0.68	3.6	±	0.2
Ap_OP1529-2	82	196.2	±	4.2	24	56.5	±	1.3	166	397.9	±	3.5	5.89E-15	±	7.67E-17	2.4	87	0.30	5.2	0.67	7.8	±	0.4
Ap_OP1529-3	50	91.5	±	2.6	9	17.0	±	0.7	54	99.0	±	3.5	2.01E-15	±	2.95E-17	1.8	52	0.19	3.9	0.66	5.9	±	0.3
Ap_OP1529-4	45	135.0	±	3.3	13	39.6	±	1.1	140	421.5	±	5.8	2.70E-15	±	3.57E-17	3.0	48	0.30	3.5	0.70	4.9	±	0.3
~~Ap_OP1529-5~~	~~103~~	~~103.9~~	~~±~~	~~17.9~~	~~79~~	~~79.4~~	~~±~~	~~3.1~~	~~192~~	~~193.6~~	~~±~~	~~14.0~~	~~1.30E-15~~	~~±~~	~~1.30E-15~~	~~1.0~~	~~122~~	~~0.78~~	~~2.0~~	~~0.62~~	~~3.3~~	~~±~~	~~0.5~~
Ap_OP1530-1	12	16.7	±	0.7	14	20.5	±	0.6	34	48.4	±	2.4	7.80E-16	±	7.80E-16	1.4	15	1.26	6.7	0.64	10.4	±	0.6
Ap_OP1530-2	33	186.4	±	4.3	38	216.6	±	5.0	102	578.7	±	6.1	1.18E-14	±	1.18E-14	5.7	42	1.19	9.2	0.75	12.3	±	0.7
Ap_OP1530-3	14	30.7	±	0.9	14	31.4	±	1.2	50	113.7	±	3.6	1.27E-15	±	1.27E-15	2.3	17	1.05	6.1	0.67	9.2	±	0.5
Ap_OP1531-1	3	16.3	±	0.6	6	40.3	±	0.9	65	403.8	±	4.7	8.39E-16	±	1.43E-17	6.2	4	2.53	6.0	0.78	7.7	±	0.4
Ap_OP1531-4	8	25.4	±	1.0	9	26.0	±	0.7	27	82.5	±	3.4	8.54E-16	±	1.40E-17	3.0	10	1.05	5.1	0.70	7.2	±	0.5
Ap_OP1531-5	7	17.4	±	0.9	3	8.2	±	0.5	64	151.9	±	4.7	5.61E-16	±	1.04E-17	2.4	8	0.48	5.4	0.68	8.0	±	0.5
Ap_OP1532-1	15	37.0	±	1.0	42	101.6	±	2.7	129	312.3	±	4.8	5.04E-16	±	9.68E-18	2.4	25	2.82	1.5	0.69	2.2	±	0.1
Ap_OP1532-2	58	76.1	±	12.7	46	60.7	±	4.5	111	145.9	±	29.6	2.69E-16	±	7.20E-18	1.3	69	0.82	0.6	0.62	0.9	±	0.1
Ap_OP1532-3	142	107.5	±	18.2	95	71.8	±	3.8	86	65.2	±	17.0	6.61E-16	±	1.65E-17	0.8	164	0.69	1.0	0.60	1.7	±	0.3
Ap_OP1532-4	64	138.6	±	3.5	112	243.6	±	4.4	102	221.5	±	4.4	1.98E-15	±	3.22E-17	2.2	90	1.80	1.9	0.70	2.7	±	0.1
Ap_OP1532-5	10	14.9	±	0.8	25	38.6	±	1.0	170	258.5	±	6.4	1.28E-16	±	5.60E-18	1.5	16	2.66	1.0	0.65	1.5	±	0.1
Ap_OP1533-1	9	20.8	±	0.7	19	43.7	±	1.3	25	59.8	±	2.1	2.65E-16	±	8.91E-18	2.3	13	2.16	1.6	0.66	2.4	±	0.2
Ap_OP1533-2	32	37.3	±	1.1	36	42.5	±	1.4	67	78.5	±	3.2	3.54E-16	±	1.03E-17	1.2	40	1.17	1.4	0.61	2.3	±	0.1
Ap_OP1533-3	26	31.8	±	1.4	14	17.2	±	0.7	20	24.9	±	2.5	3.75E-16	±	1.03E-17	1.2	29	0.56	1.9	0.62	3.1	±	0.2
Ap_OP1534-2	56	84.1	±	14.8	52	77.1	±	3.0	66	98.4	±	4.9	6.81E-16	±	1.29E-17	1.5	69	0.94	1.3	0.67	1.9	±	0.3
Ap_OP1534-3	114	278.6	±	22.3	69	168.8	±	4.8	121	295.8	±	7.1	2.75E-15	±	4.10E-17	2.4	131	0.62	1.6	0.70	2.3	±	0.2
Ap_OP1534-4	88	108.6	±	12.7	103	127.0	±	5.6	184	227.1	±	5.8	9.37E-16	±	1.76E-17	1.2	112	1.20	1.3	0.64	2.0	±	0.2
Ap_OP1536-1	25	49.7	±	1.5	32	62.8	±	1.3	155	308.2	±	4.3	1.74E-15	±	2.67E-17	2.0	32	1.30	5.0	0.68	7.4	±	0.4
Ap_OP1536-2	41	98.6	±	2.6	88	210.2	±	4.4	138	330.2	±	5.4	3.91E-15	±	5.49E-17	2.4	62	2.19	4.9	0.73	6.7	±	0.4
Ap_OP1536-3	61	138.5	±	2.9	103	231.5	±	4.0	137	307.8	±	6.5	6.55E-15	±	8.05E-17	2.3	86	1.71	6.3	0.72	8.8	±	0.5
Ap_OP1539-1	69	131.6	±	2.4	210	398.8	±	11.1	132	250.5	±	4.0	1.87E-15	±	2.34E-17	1.9	119	3.11	1.5	0.69	2.2	±	0.1
Ap_OP1539-2	106	126.1	±	2.8	33	39.1	±	1.0	218	259.7	±	4.1	1.29E-15	±	1.77E-17	1.2	113	0.32	1.8	0.62	2.9	±	0.2
Ap_OP1539-3	20	44.1	±	12.4	69	154.8	±	6.4	247	553.3	±	27.8	3.33E-16	±	9.79E-18	2.2	36	3.60	0.8	0.68	1.2	±	0.2
Ap_OP1539-4	111	135.9	±	18.6	107	131.4	±	5.0	248	303.3	±	28.0	1.11E-15	±	1.83E-17	1.2	136	0.99	1.2	0.62	2.0	±	0.2
Ap_OP1539-5	11	21.0	±	1.1	41	76.3	±	2.6	39	73.2	±	3.1	3.00E-16	±	7.14E-18	1.9	21	3.73	1.4	0.64	2.2	±	0.1
Ap_OP1540-1	21	104.5	±	14.5	25	124.0	±	4.7	144	715.9	±	16.0	8.98E-16	±	2.20E-17	5.0	27	1.22	1.3	0.75	1.7	±	0.2

Ap_OP1540-2	34	59.6	±	11.0	8	13.3	±	0.9	118	207.6	±	11.4	1.34E-16	±	8.23E-18	1.8	36	0.23	0.4	0.66	0.6	±	0.1
Ap_OP1540-3	145	129.6	±	14.9	92	82.0	±	3.3	296	263.8	±	16.6	8.95E-16	±	1.94E-17	0.9	167	0.65	1.1	0.63	1.8	±	0.2
Ap_OP1540-4	63	194.9	±	26.5	16	50.0	±	2.2	75	229.9	±	13.9	1.62E-15	±	2.71E-17	3.1	67	0.26	1.5	0.70	2.1	±	0.3
Ap_OP1542-5	39	50.1	±	14.1	39	51.2	±	2.0	135	175.7	±	11.2	4.36E-16	±	1.07E-17	1.3	48	1.05	1.4	0.69	2.0	±	0.5
Ap_OP1542-6	37	47.0	±	9.4	48	60.9	±	2.4	146	183.2	±	8.3	3.16E-16	±	8.77E-18	1.3	49	1.33	1.0	0.64	1.5	±	0.3
Ap_OP1542-7	40	47.0	±	10.0	29	33.8	±	1.1	138	161.0	±	8.4	2.92E-16	±	8.06E-18	1.2	47	0.74	1.0	0.69	1.5	±	0.3
Ap_OP1542-8	6	100.5	±	20.2	30	494.7	±	15.3	83	1390.0	±	12.6	2.88E-15	±	4.04E-17	16.7	13	5.05	2.5	0.81	3.0	±	0.3
Ap_OP1545-1	52	46.1	±	8.6	41	36.4	±	1.2	494	441.5	±	11.7	2.49E-15	±	3.73E-17	0.9	61	0.81	8.6	0.62	14.0	±	2.4
Ap_OP1545-2	52	54.1	±	16.8	52	54.5	±	2.0	474	497.5	±	17.0	3.90E-15	±	5.49E-17	1.0	64	1.03	11.6	0.63	18.3	±	5.6
Ap_OP1545-3	51	61.0	±	12.0	37	43.9	±	1.6	386	462.4	±	17.4	4.26E-15	±	5.53E-17	1.2	59	0.74	11.4	0.68	16.8	±	3.2
~~Ap_OP1545-4~~	~~60~~	~~48.1~~	~~±~~	~~9.6~~	~~55~~	~~43.5~~	~~±~~	~~1.4~~	~~485~~	~~386.4~~	~~±~~	~~9.9~~	~~4.48E-15~~	~~±~~	~~6.66E-17~~	~~0.8~~	~~73~~	~~0.93~~	~~14.6~~	~~0.66~~	~~21.9~~	~~±~~	~~3.9~~
Ap_OP1547-1	3	59.6	±	13.7	6	106.1	±	4.1	122	2173.2	±	44.2	5.28E-15	±	6.66E-17	17.8	5	1.83	11.8	0.83	14.2	±	2.6
Ap_OP1547-2	2	13.6	±	0.6	3	26.9	±	1.0	139	1234.5	±	12.1	2.55E-15	±	3.65E-17	8.9	2	2.02	23.6	0.77	30.8	±	2.0
Ap_OP1547-3	2	11.8	±	0.6	7	46.1	±	0.9	144	935.6	±	8.8	2.01E-15	±	2.69E-17	6.5	3	4.00	16.4	0.76	21.6	±	1.2
Ap_OP1547-4	2	14.7	±	0.6	8	53.3	±	1.0	164	1095.8	±	8.5	2.79E-15	±	3.56E-17	6.7	4	3.72	18.9	0.76	25.0	±	1.4
Ap_OP1547-5	2	13.7	±	0.5	8	51.3	±	1.3	136	853.4	±	10.7	3.66E-15	±	5.13E-17	6.3	4	3.85	26.1	0.75	35.0	±	1.9
Ap_OP1548-1	105	136.8	±	3.2	88	114.5	±	2.8	216	280.4	±	4.8	7.20E-15	±	1.06E-16	1.3	126	0.86	8.1	0.63	12.9	±	0.7
Ap_OP1548-2	16	19.4	±	0.9	39	46.0	±	1.4	66	77.9	±	3.1	1.40E-15	±	2.38E-17	1.2	26	2.43	8.6	0.61	14.0	±	0.9
Ap_OP1548-3	5	8.3	±	0.4	16	27.8	±	0.8	355	599.8	±	7.4	9.87E-16	±	1.64E-17	1.7	9	3.42	12.2	0.68	18.0	±	1.1
~~Ap_OP1548-4~~	~~2~~	~~4.7~~	~~±~~	~~0.3~~	~~5~~	~~11.0~~	~~±~~	~~0.6~~	~~23~~	~~50.7~~	~~±~~	~~2.3~~	~~7.66E-16~~	~~±~~	~~1.24E-17~~	~~2.2~~	~~3~~	~~2.39~~	~~19.5~~	~~0.68~~	~~28.7~~	~~±~~	~~2.1~~
Ap_OP1565-1	40	223.2	±	19.4	12	68.7	±	3.1	83	458.7	±	24.9	5.96E-15	±	9.28E-17	5.5	43	0.32	4.6	0.76	6.1	±	0.6
Ap_OP1565-2	36	77.7	±	14.3	23	49.6	±	2.3	174	379.0	±	12.5	1.72E-15	±	3.12E-17	2.2	41	0.65	3.6	0.68	5.4	±	1.0
Ap_OP1565-3	33	41.2	±	10.4	11	13.8	±	0.9	106	132.2	±	9.8	2.52E-16	±	8.44E-18	1.2	36	0.34	1.1	0.64	1.7	±	0.7
Ap_OP1565-4	38	152.9	±	21.0	27	107.4	±	3.9	90	366.5	±	10.7	4.61E-15	±	5.48E-17	4.1	44	0.72	4.9	0.78	6.2	±	0.8
Ap_OP1580-1	9	56.7	±	14.3	42	275.4	±	10.5	154	1000.3	±	12.1	2.80E-15	±	4.87E-17	6.5	19	4.98	4.3	0.73	5.9	±	0.8
Ap_OP1580-2	21	276.6	±	31.3	24	325.6	±	9.7	82	1090.9	±	16.8	9.73E-15	±	1.22E-16	13.4	26	1.21	5.1	0.81	6.3	±	0.7
Ap_OP1580-3	19	93.7	±	10.9	11	51.3	±	2.6	137	669.2	±	10.0	1.46E-15	±	2.60E-17	4.9	22	0.56	2.6	0.78	3.3	±	0.4
Ap_OP1580-4	31	169.6	±	24.5	36	199.1	±	5.8	118	652.0	±	12.9	4.36E-15	±	5.46E-17	5.5	39	1.20	3.8	0.75	5.0	±	0.6
Ap_OP1582-1	13	68.9	±	12.4	8	40.7	±	1.9	39	200.7	±	13.6	6.45E-16	±	1.32E-17	5.2	15	0.61	1.6	0.75	2.1	±	0.4
Ap_OP1582-2	12	48.2	±	11.6	14	53.1	±	2.3	155	601.9	±	11.4	3.10E-16	±	7.56E-18	3.9	16	1.13	1.0	0.73	1.3	±	0.3
Ap_OP1582-3	40	110.7	±	19.9	56	154.0	±	5.2	149	409.1	±	11.8	1.28E-15	±	2.22E-17	2.8	53	1.43	1.6	0.69	2.4	±	0.3
Ap_OP1582-4	12	50.6	±	10.7	8	31.2	±	1.3	21	87.4	±	4.0	2.71E-16	±	8.94E-18	4.1	14	0.63	0.9	0.72	1.2	±	0.3

A.2 Zircon (U-Th)/He single grain analyses

Table DR3: Zircon (U-Th)/He single grain data

Note: Aliquots which are strike-through are not considered for the sample age calculation. ppm values of U and Th are calculated from iCAP results by deviding the mass of the respective element by the grain mass (which is derived from measurements of ^{91}Zr). eU is calculated by adding U-content and 0.235*Th-content. Mean sample ages are reported in Table DR1.

Sample/ Aliquot	U (ppm)	U ± 2SD (pg)	Th (ppm)	Th ± 2SD (pg)	He ± 1SD (mol)	grain mass (µg)	eU (ppm)	Th/U	Uncorrected grain age (Ma)	FT correction	Corrected grain age ± 1SD (Ma)
Zr_OP1502-1	110	1023.2 ± 59.4	52	485.3 ± 46.3	1.95E-13 ± 2.31E-15	9.3	122	0.49	31.9	0.81	39.4 ± 2.8
Zr_OP1502-2	56	572.8 ± 36.3	36	363.4 ± 28.0	1.20E-13 ± 1.54E-15	10.2	65	0.65	33.7	0.81	41.3 ± 3.2
Zr_OP1504-1	320	2224.8 ± 210.5	61	422.1 ± 26.6	1.65E-13 ± 2.30E-15	6.9	335	0.19	13.2	0.79	16.8 ± 1.7
Zr_OP1504-2	395	3861.8 ± 61.0	170	1660.3 ± 42.1	4.06E-13 ± 5.23E-15	9.8	435	0.44	17.7	0.82	21.5 ± 1.1
Zr_OP1504-3	751	4376.2 ± 55.6	98	571.8 ± 11.0	9.62E-13 ± 1.19E-14	5.8	774	0.13	39.4	0.78	50.1 ± 2.6
Zr_OP1505-1	746	2495.4 ± 211.2	289	967.8 ± 63.1	4.57E-13 ± 4.99E-15	3.3	814	0.40	31.3	0.74	42.0 ± 3.9
Zr_OP1505-2	198	907.7 ± 37.7	131	601.2 ± 22.0	2.54E-13 ± 2.83E-15	4.6	228	0.68	44.9	0.76	58.7 ± 3.6
Zr_OP1505-3	174	1674.6 ± 72.5	75	717.6 ± 34.4	7.88E-13 ± 8.68E-15	9.6	192	0.44	79.0	0.76	104.0 ± 6.5
Zr_OP1507-1	382	2325.8 ± 29.8	104	630.3 ± 12.1	1.21E-13 ± 1.56E-15	6.1	407	0.28	9.1	0.77	11.8 ± 0.6
Zr_OP1507-2	610	4290.8 ± 65.5	158	1113.1 ± 13.2	3.12E-13 ± 4.01E-15	7.0	648	0.27	12.7	0.79	16.1 ± 0.9
Zr_OP1507-3	206	1735.5 ± 36.2	130	1100.5 ± 25.0	1.32E-13 ± 1.70E-15	8.4	236	0.65	12.3	0.80	15.3 ± 0.8
Zr_OP1510-1	130	494.3 ± 13.2	49	185.6 ± 7.8	2.56E-13 ± 2.97E-15	3.8	141	0.39	87.4	0.77	113.0 ± 6.3
Zr_OP1510-2	334	1685.3 ± 32.3	181	914.1 ± 18.0	8.82E-13 ± 9.36E-15	5.1	376	0.56	85.5	0.77	110.4 ± 5.8
Zr_OP1510-3	179	618.0 ± 20.1	78	268.3 ± 6.1	3.16E-13 ± 3.65E-15	3.4	197	0.45	85.3	0.76	112.4 ± 6.7
Zr_OP1513-1	755	1070.1 ± 42.6	240	340.4 ± 9.5	5.00E-14 ± 6.02E-16	1.4	811	0.33	8.1	0.71	11.3 ± 0.7
Zr_OP1513-2	610	712.0 ± 28.0	270	315.2 ± 8.3	2.73E-14 ± 3.13E-16	1.2	674	0.45	6.5	0.70	9.2 ± 0.6
~~Zr_OP1513-3~~	~~478~~	~~494.6 ± 13.9~~	~~456~~	~~471.4 ± 12.9~~	~~4.41E-14~~ ± 5.25E-16	1.0	~~585~~	~~0.98~~	~~13.5~~	~~0.67~~	~~20.1 ± 1.1~~
Zr_OP1515-3	102	982.4 ± 121.1	29	276.6 ± 29.7	2.78E-14 ± 3.33E-16	9.6	109	0.29	5.0	0.82	6.0 ± 0.8
Zr_OP1515-4	626	3893.5 ± 147.4	126	786.8 ± 23.0	1.01E-13 ± 1.38E-15	6.2	656	0.21	4.6	0.79	5.8 ± 0.4
~~Zr_OP1516-1~~	~~136~~	~~827.3 ± 48.4~~	~~63~~	~~382.7 ± 17.7~~	~~4.22E-14~~ ± 5.31E-16	6.1	~~151~~	~~0.47~~	~~8.6~~	~~0.78~~	~~10.9 ± 0.8~~
Zr_OP1516-2	254	1340.6 ± 31.8	76	400.2 ± 27.6	5.17E-14 ± 6.51E-16	5.3	272	0.31	6.7	0.76	8.8 ± 0.5
Zr_OP1516-3	571	6283.9 ± 182.1	142	1563.6 ± 61.2	1.96E-13 ± 2.32E-15	11.0	605	0.26	5.5	0.83	6.6 ± 0.4
Zr_OP1517-1	158	597.2 ± 47.5	108	408.4 ± 20.6	2.42E-14 ± 3.09E-16	3.8	183	0.70	6.5	0.72	9.0 ± 0.8
Zr_OP1517-2	60	335.3 ± 10.6	59	330.8 ± 10.5	1.53E-14 ± 1.81E-16	5.6	74	1.01	6.9	0.76	9.0 ± 0.5
~~Zr_OP1517-3~~	~~528~~	~~1972.3 ± 25.3~~	~~228~~	~~850.6 ± 18.6~~	~~1.15E-13~~ ± 1.37E-15	3.7	~~581~~	~~0.44~~	~~9.8~~	~~0.74~~	~~13.2 ± 0.7~~
Zr_OP1521-1	123	958.1 ± 14.2	50	384.9 ± 8.1	2.34E-12 ± 2.16E-14	7.8	135	0.41	398.3	0.81	490.4 ± 25.0
Zr_OP1521-2	1099	6339.4 ± 111.5	142	816.4 ± 12.4	7.20E-13 ± 9.28E-15	5.8	1132	0.13	20.4	0.78	26.0 ± 1.4
Zr_OP1521-3	473	3099.1 ± 43.9	97	633.7 ± 10.7	3.39E-13 ± 4.51E-15	6.5	496	0.21	19.4	0.76	25.3 ± 1.3
Zr_OP1522-1	319	1616.8 ± 45.4	134	678.3 ± 34.3	4.23E-13 ± 4.84E-15	5.1	350	0.43	44.2	0.79	55.5 ± 3.0

Zr_OP1522-2	180	1780.5	±	47.8	59	586.3	±	13.7	4.60E-13	±	5.28E-15	9.9	194	0.34	44.3	0.81	54.8	±	3.2
Zr_OP1527-1	170	1990.6	±	77.8	34	397.2	±	19.4	1.51E-13	±	1.84E-15	11.7	178	0.20	13.5	0.80	16.8	±	1.1
Zr_OP1527-2	494	3828.6	±	107.9	173	1338.8	±	29.0	5.40E-13	±	6.25E-15	7.8	534	0.36	24.2	0.78	31.1	±	1.8
Zr_OP1527-3	68	442.1	±	16.2	20	126.9	±	5.6	3.67E-14	±	4.64E-16	6.5	73	0.29	14.5	0.78	18.6	±	1.1
Zr_OP1529-1	143	1344.1	±	31.9	45	424.5	±	13.7	3.42E-13	±	4.36E-15	9.4	154	0.32	43.7	0.82	53.5	±	3.0
Zr_OP1529-2	313	2745.1	±	69.7	138	1205.1	±	40.0	6.73E-13	±	7.47E-15	8.8	346	0.45	41.1	0.79	51.8	±	3.0
Zr_OP1529-3	712	12046.6	±	395.3	107	1818.1	±	47.4	2.12E-12	±	1.97E-14	16.9	737	0.15	31.4	0.82	38.2	±	2.2
Zr_OP1530-1	234	1520.6	±	79.5	126	818.4	±	30.1	3.61E-13	±	4.91E-15	6.5	263	0.55	39.0	0.79	49.5	±	3.3
Zr_OP1530-2	413	2879.0	±	121.8	143	997.3	±	43.8	7.56E-13	±	9.03E-15	7.0	447	0.36	44.9	0.77	58.3	±	3.7
Zr_OP1530-3	160	1309.0	±	61.7	26	215.5	±	7.7	2.43E-13	±	3.32E-15	8.2	166	0.17	33.2	0.80	41.4	±	2.8
Zr_OP1531-1	266	3647.6	±	291.9	109	1495.4	±	71.6	1.25E-12	±	1.26E-14	13.7	292	0.42	58.1	0.82	70.9	±	6.4
Zr_OP1531-2	113	905.9	±	63.3	34	268.3	±	11.6	6.84E-14	±	9.48E-16	8.0	121	0.30	13.1	0.79	16.6	±	1.4
Zr_OP1531-3	113	1104.3	±	99.2	31	299.9	±	29.6	1.20E-13	±	1.67E-15	9.8	120	0.28	19.0	0.81	23.5	±	2.3
~~Zr_OP1532-1~~	~~189~~	~~1795.2~~	~~±~~	~~77.6~~	~~50~~	~~473.5~~	~~±~~	~~15.5~~	~~1.31E-13~~	~~±~~	1.61E-15	9.5	~~201~~	~~0.27~~	~~12.7~~	~~0.79~~	~~16.0~~	~~±~~	~~1.0~~
Zr_OP1532-3	210	1756.0	±	85.9	47	392.2	±	20.1	7.26E-14	±	8.71E-16	8.4	221	0.23	7.3	0.80	9.1	±	0.6
Zr_OP1532-4	139	984.9	±	47.4	24	166.8	±	12.7	1.83E-14	±	2.46E-16	7.1	145	0.17	3.3	0.79	4.2	±	0.3
Zr_OP1533-1	239	2648.6	±	208.6	121	1342.7	±	91.0	5.45E-14	±	7.02E-16	11.1	268	0.52	3.4	0.79	4.3	±	0.4
~~Zr_OP1533-2~~	~~203~~	~~1482.3~~	~~±~~	~~112.2~~	~~69~~	~~504.2~~	~~±~~	~~34.8~~	~~1.08E-13~~	~~±~~	1.43E-15	7.3	~~220~~	~~0.35~~	~~12.5~~	~~0.81~~	~~15.5~~	~~±~~	~~1.3~~
Zr_OP1533-3	549	2271.8	±	162.1	200	826.2	±	43.2	5.78E-14	±	7.53E-16	4.1	596	0.37	4.4	0.79	5.5	±	0.4
Zr_OP1534-1	713	9063.9	±	146.5	78	997.0	±	15.5	3.17E-13	±	3.72E-15	12.7	731	0.11	6.3	0.81	7.8	±	0.4
Zr_OP1534-2	773	11279.9	±	326.1	73	1073.0	±	27.7	2.73E-13	±	3.32E-15	14.6	790	0.10	4.4	0.82	5.4	±	0.3
~~Zr_OP1534-3~~	~~1491~~	~~11832.0~~	~~±~~	~~237.2~~	~~150~~	~~1186.7~~	~~±~~	~~17.3~~	~~3.23E-14~~	~~±~~	3.87E-16	7.9	~~1526~~	~~0.10~~	~~0.5~~	~~0.80~~	~~0.6~~	~~±~~	~~0.0~~
Zr_OP1536-1	312	2063.1	±	51.6	112	738.5	±	21.0	3.61E-13	±	4.29E-15	6.6	338	0.37	29.9	0.79	37.7	±	2.0
Zr_OP1536-2	128	881.3	±	26.3	58	402.1	±	14.5	7.61E-14	±	9.03E-16	6.9	142	0.47	14.5	0.80	18.1	±	1.0
Zr_OP1536-3	473	2200.3	±	51.4	284	1321.1	±	38.1	1.66E-13	±	1.95E-15	4.6	540	0.62	12.2	0.76	16.2	±	0.9
Zr_OP1539-1	231	2402.0	±	54.1	108	1126.6	±	23.1	8.27E-14	±	1.04E-15	10.4	256	0.48	5.7	0.80	7.2	±	0.4
Zr_OP1539-2	263	2427.0	±	38.0	224	2067.7	±	32.5	7.99E-14	±	9.38E-16	9.2	316	0.87	5.1	0.79	6.5	±	0.3
Zr_OP1539-3	283	2988.4	±	66.7	131	1386.9	±	27.6	9.50E-14	±	1.09E-15	10.6	313	0.48	5.3	0.79	6.7	±	0.4
Zr_OP1540-1	603	5763.2	±	273.9	58	551.2	±	22.3	1.47E-13	±	1.64E-15	9.6	616	0.10	4.6	0.79	5.9	±	0.4
Zr_OP1540-2	601	4006.9	±	248.4	165	1101.5	±	75.6	1.02E-13	±	1.22E-15	6.7	640	0.28	4.4	0.79	5.6	±	0.4
Zr_OP1540-3	105	720.8	±	21.8	52	358.3	±	11.5	2.43E-14	±	2.93E-16	6.9	117	0.51	5.6	0.79	7.1	±	0.4
Zr_OP1542-1	249	1767.4	±	136.7	63	446.7	±	22.7	7.58E-14	±	8.84E-16	7.1	264	0.26	7.6	0.77	9.8	±	0.9
Zr_OP1542-2	822	7785.2	±	356.9	148	1397.0	±	60.1	3.24E-13	±	3.86E-15	9.5	857	0.18	7.4	0.82	9.1	±	0.6
Zr_OP1542-3	920	8788.2	±	198.4	132	1256.9	±	25.9	2.94E-13	±	3.40E-15	9.6	951	0.15	6.0	0.79	7.6	±	0.4
Zr_OP1547-1	31	289.7	±	13.0	20	183.9	±	6.9	6.43E-14	±	7.62E-16	9.3	36	0.65	35.8	0.80	44.6	±	2.8
Zr_OP1547-2	52	420.6	±	13.3	26	209.4	±	6.4	9.16E-14	±	1.07E-15	8.1	58	0.51	36.0	0.79	45.8	±	2.5
Zr_OP1548-1	108	1260.5	±	23.0	38	447.6	±	11.6	5.00E-13	±	6.31E-15	11.7	117	0.36	67.5	0.82	82.0	±	4.3
Zr_OP1548-2	592	7765.4	±	206.9	91	1197.7	±	20.6	2.69E-12	±	2.47E-14	13.1	614	0.16	61.9	0.82	75.1	±	4.3

Zr_OP1565-1	162	1412.8	±	31.4	52	450.0	±	15.2	8.35E-14	±	1.15E-15	8.7	174	0.33	10.2	0.80	12.7	±	0.7
Zr_OP1565-2	121	1022.0	±	12.3	57	477.7	±	11.3	7.74E-14	±	1.08E-15	8.4	135	0.48	12.6	0.77	16.3	±	0.9
Zr_OP1565-3	293	2141.1	±	38.3	65	474.6	±	10.5	1.22E-13	±	1.51E-15	7.3	308	0.23	10.0	0.80	12.6	±	0.7
Zr_OP1580-1	89	584.1	±	11.3	39	254.0	±	7.8	2.85E-14	±	3.52E-16	6.5	99	0.45	8.2	0.79	10.4	±	0.5
Zr_OP1580-2	422	2138.6	±	51.0	99	503.7	±	14.9	8.08E-14	±	9.78E-16	5.1	445	0.24	6.6	0.82	8.2	±	0.4
Zr_OP1580-3	232	2292.1	±	65.5	69	684.9	±	16.0	1.23E-13	±	1.58E-15	9.9	249	0.31	9.3	0.79	11.8	±	0.7
Zr_OP1582-1	324	2592.4	±	70.2	32	254.5	±	8.9	8.44E-14	±	1.02E-15	8.0	331	0.10	5.9	0.81	7.3	±	0.4
~~Zr_OP1582-2~~	~~210~~	~~1488.5~~	~~±~~	~~40.7~~	~~93~~	~~658.2~~	~~±~~	~~16.5~~	~~1.59E-13~~	~~±~~	2.02E-15	7.1	~~232~~	~~0.45~~	~~17.9~~	~~0.79~~	~~22.6~~	~~±~~	~~1.3~~
Zr_OP1582-3	81	306.8	±	6.3	45	170.2	±	5.1	1.01E-14	±	1.38E-16	3.8	92	0.57	5.4	0.79	6.8	±	0.4

Appendix B

Additional data tables of section 3.2

The following pages contain supplementary data tables for the manuscript "How steady are steady-state mountain belts? – a re-examination of the Olympic Mountains (Washington State, USA)." presented in section 3.2.2.

These data include single grain analyses from apatite (U-Th)/He dating (Table DR1, section B.1), single grain analyses from zircon (U-Th)/He dating (Table DR2, section B.2), single grain analyses from apatite fission-track dating (Table DR3, section B.3) and single grain analyses from zircon fission-track dating (Table DR4, section B.4). These tables are also available online as excel spreadsheets or PDF files on the Earth Surface Dynamics homepage (`https://www.earth-surf-dynam-discuss.net/esurf-2018-65/#discussion`).

B.1 Apatite (U-Th)/He single grain analyses

Table DR 1: Apatite (U-Th-Sm)/He data

Notes: Aliquots which are strike-through are not considered for the sample age calculation.For two samples (OP1572 and OP1576) a single grain age (aliquot is red) is taken as sample age. ppm values of U, Th and Sm are calculated from iCAP results by deviding the mass of the respective element by the grain mass (which is derived from measurements of ^{43}Ca). eU is calculated by adding U-content and 0.235*Th-content.

Sample/ Aliquot	U (ppm)	U ± 2SD (pg)	Th (ppm)	Th ± 2SD (pg)	Sm (ppm)	Sm ± 2SD (pg)	He ± 1SD (mol)	grain mass (µg)	eU (ppm)	Th/U	Uncorrected grain age (Ma)	FT correction	Corrected grain age ± 1SD (Ma)
Ap_OP1550-1	27	130.8 ± 18.5	24	115.8 ± 3.2	147	711.7 ± 10.7	1.66E-15 ± 3.14E-17	4.8	33	0.91	2.0	0.80	2.5 ± 0.3
Ap_OP1550-2	14	56.6 ± 10.9	10	40.1 ± 1.3	166	677.7 ± 10.8	4.92E-16 ± 1.15E-17	4.1	16	0.73	1.4	0.79	1.8 ± 0.3
Ap_OP1550-3	18	38.8 ± 9.9	11	25.1 ± 1.0	36	77.6 ± 8.2	1.80E-16 ± 7.31E-18	2.2	20	0.66	0.8	0.70	1.1 ± 0.3
Ap_OP1550-4	70	118.0 ± 16.0	50	85.1 ± 2.5	100	170.2 ± 8.6	1.36E-15 ± 2.19E-17	1.7	81	0.74	1.8	0.62	3.0 ± 0.4
Ap_OP1551-1	159	728.3 ± 20.7	125	571.7 ± 8.8	74	339.4 ± 7.3	1.20E-14 ± 1.65E-16	4.6	188	0.81	2.6	0.76	3.4 ± 0.2
Ap_OP1551-2	56	130.7 ± 3.1	112	262.8 ± 6.4	114	266.6 ± 7.0	2.86E-15 ± 4.08E-17	2.3	82	2.06	2.7	0.70	3.9 ± 0.2
Ap_OP1551-3	14	10.0 ± 0.7	37	27.4 ± 1.1	68	50.6 ± 3.5	1.41E-16 ± 6.15E-18	0.7	22	2.80	1.6	0.66	2.4 ± 0.2
Ap_OP1551-4	46	71.2 ± 2.5	68	106.1 ± 3.4	193	300.1 ± 8.5	1.19E-15 ± 1.72E-17	1.6	62	1.53	2.3	0.65	3.5 ± 0.2
Ap_OP1552-1	3	19.8 ± 1.1	4	32.4 ± 1.1	114	845.5 ± 13.2	4.48E-16 ± 1.10E-17	7.4	4	1.68	3.0	0.81	3.7 ± 0.3
~~Ap_OP1552-2~~	~~57~~	~~127.8 ± 4.8~~	~~64~~	~~145.0 ± 3.9~~	~~508~~	~~1145.2 ± 13.7~~	~~2.46E-14 ± 2.90E-16~~	~~2.3~~	~~72~~	~~1.16~~	~~28.1~~	~~0.69~~	~~40.6 ± 2.3~~
Ap_OP1552-3	3	10.6 ± 0.4	5	21.2 ± 1.0	100	409.5 ± 6.0	2.24E-16 ± 7.61E-18	4.1	4	2.05	2.7	0.74	3.6 ± 0.3
Ap_OP1552-4	79	201.9 ± 5.9	54	136.5 ± 3.4	227	578.9 ± 8.0	3.31E-15 ± 3.98E-17	2.5	92	0.69	2.6	0.71	3.7 ± 0.2
Ap_OP1553-1	14	46.2 ± 6.0	13	43.6 ± 1.2	86	291.3 ± 9.9	2.13E-16 ± 8.73E-18	3.4	17	0.97	0.7	0.70	1.0 ± 0.1
Ap_OP1553-2	80	225.8 ± 19.8	45	127.6 ± 2.6	144	403.9 ± 9.0	3.59E-15 ± 4.28E-17	2.8	91	0.58	2.6	0.73	3.6 ± 0.3
Ap_OP1553-3	5	70.9 ± 13.0	6	83.2 ± 2.1	85	1149.8 ± 12.9	8.08E-16 ± 1.13E-17	13.5	7	1.20	1.7	0.83	2.0 ± 0.3
~~Ap_OP1553-4~~	~~6~~	~~43.7 ± 8.6~~	~~7~~	~~46.2 ± 1.5~~	~~184~~	~~1290.4 ± 13.7~~	~~9.20E-14 ± 1.03E-15~~	~~7.0~~	~~8~~	~~1.08~~	~~312.2~~	~~0.78~~	~~399.0 ± 67.7~~
Ap_OP1553-5	6	25.2 ± 1.1	8	36.4 ± 1.0	129	585.0 ± 7.9	6.77E-16 ± 1.57E-17	4.5	7	1.48	3.7	0.73	5.1 ± 0.3
Ap_OP1554-1	22	79.9 ± 11.6	15	52.0 ± 1.2	77	276.2 ± 8.3	8.21E-16 ± 1.47E-17	3.6	26	0.67	1.7	0.78	2.1 ± 0.3
Ap_OP1554-2	35	72.0 ± 9.1	35	72.0 ± 1.5	98	199.2 ± 6.8	5.64E-16 ± 1.17E-17	2.0	44	1.03	1.2	0.65	1.8 ± 0.2
Ap_OP1554-3	36	43.3 ± 8.4	9	11.4 ± 0.6	87	105.8 ± 7.7	1.20E-16 ± 7.09E-18	1.2	38	0.27	0.5	0.63	0.8 ± 0.2
Ap_OP1554-4	53	106.4 ± 12.2	19	38.1 ± 1.1	105	211.4 ± 9.1	1.18E-15 ± 2.31E-17	2.0	57	0.37	1.9	0.64	3.0 ± 0.4
~~Ap_OP1555-1~~	~~10~~	~~40.0 ± 7.8~~	~~5~~	~~18.1 ± 0.7~~	~~196~~	~~757.2 ± 9.8~~	~~2.48E-14 ± 2.63E-16~~	~~3.9~~	~~11~~	~~0.47~~	~~106.5~~	~~0.74~~	~~143.5 ± 25.6~~
Ap_OP1555-2	19	37.9 ± 5.1	20	39.0 ± 1.4	119	238.3 ± 8.5	2.23E-16 ± 5.87E-18	2.0	24	1.05	0.9	0.68	1.3 ± 0.2
Ap_OP1555-3	80	263.6 ± 21.9	8	26.2 ± 0.7	155	509.2 ± 11.2	2.93E-15 ± 3.69E-17	3.3	82	0.10	2.0	0.76	2.7 ± 0.2
~~Ap_OP1555-4~~	~~57~~	~~135.4 ± 15.9~~	~~66~~	~~157.4 ± 3.9~~	~~186~~	~~444.6 ± 9.6~~	~~3.27E-14 ± 3.48E-16~~	~~2.4~~	~~72~~	~~1.19~~	~~35.2~~	~~0.68~~	~~51.6 ± 5.5~~
~~Ap_OP1555-5~~	~~32~~	~~126.8 ± 4.0~~	~~53~~	~~211.7 ± 5.7~~	~~135~~	~~538.1 ± 11.6~~	~~3.67E-14 ± 4.01E-16~~	~~4.0~~	~~44~~	~~1.71~~	~~38.4~~	~~0.72~~	~~53.5 ± 2.9~~
Ap_OP1555-6	30	96.8 ± 3.8	17	54.9 ± 1.7	132	434.0 ± 7.7	1.55E-15 ± 2.27E-17	3.3	33	0.58	2.6	0.72	3.7 ± 0.2

Ap_OP1557-1	30	54.6	±	9.2	6	11.2	±	0.5	64	116.9	±	5.2	5.56E-16	±	1.11E-17	1.8	31	0.21	1.9	0.63	2.9	±	0.5
~~Ap_OP1557-2~~	~~48~~	~~398.0~~	~~±~~	~~23.9~~	~~9~~	~~73.9~~	~~±~~	~~1.5~~	~~253~~	~~2081.3~~	~~±~~	~~20.4~~	~~5.43E-14~~	~~±~~	~~6.34E-16~~	~~8.2~~	~~50~~	~~0.19~~	~~24.3~~	~~0.79~~	~~30.9~~	~~±~~	~~2.4~~
~~Ap_OP1557-3~~	~~48~~	~~83.1~~	~~±~~	~~10.2~~	~~34~~	~~58.6~~	~~±~~	~~1.2~~	~~308~~	~~531.9~~	~~±~~	~~10.7~~	~~7.45E-15~~	~~±~~	~~9.51E-17~~	~~1.7~~	~~56~~	~~0.72~~	~~14.4~~	~~0.67~~	~~21.6~~	~~±~~	~~2.6~~
~~Ap_OP1557-4~~	~~61~~	~~287.3~~	~~±~~	~~17.9~~	~~28~~	~~133.3~~	~~±~~	~~2.8~~	~~380~~	~~1794.7~~	~~±~~	~~22.4~~	~~5.08E-14~~	~~±~~	~~6.06E-16~~	~~4.7~~	~~68~~	~~0.48~~	~~29.6~~	~~0.77~~	~~38.4~~	~~±~~	~~2.8~~
Ap_OP1557-5	11	19.0	±	0.9	38	62.7	±	1.5	61	102.2	±	4.8	2.86E-16	±	8.59E-18	1.7	20	3.39	1.6	0.66	2.4	±	0.2
Ap_OP1557-6	27	72.3	±	3.2	43	117.0	±	3.9	109	294.2	±	6.4	3.07E-15	±	4.54E-17	2.7	37	1.66	5.7	0.71	8.1	±	0.5
~~Ap_OP1557-7~~	~~60~~	~~155.6~~	~~±~~	~~3.1~~	~~39~~	~~100.6~~	~~±~~	~~2.7~~	~~480~~	~~1243.4~~	~~±~~	~~16.0~~	~~3.54E-14~~	~~±~~	~~4.89E-16~~	~~2.6~~	~~69~~	~~0.66~~	~~36.5~~	~~0.75~~	~~48.4~~	~~±~~	~~2.6~~
Ap_OP1558-1	7	9.6	±	0.7	10	14.3	±	0.7	183	255.7	±	6.3	5.14E-16	±	1.10E-17	1.4	9	1.53	7.4	0.63	11.8	±	0.9
Ap_OP1558-2	11	9.9	±	0.8	10	8.7	±	0.7	93	79.7	±	3.6	2.89E-16	±	7.36E-18	0.9	14	0.91	4.5	0.60	7.4	±	0.6
~~Ap_OP1558-3~~	~~16~~	~~31.9~~	~~±~~	~~1.3~~	~~70~~	~~142.6~~	~~±~~	~~3.0~~	~~276~~	~~564.4~~	~~±~~	~~7.0~~	~~5.89E-15~~	~~±~~	~~6.58E-17~~	~~2.0~~	~~32~~	~~4.58~~	~~16.6~~	~~0.66~~	~~25.0~~	~~±~~	~~1.4~~
Ap_OP1558-4	31	56.1	±	2.2	8	14.7	±	0.6	102	187.3	±	4.7	1.52E-15	±	2.12E-17	1.8	33	0.27	4.7	0.68	7.0	±	0.4
Ap_OP1559-1	22	15.9	±	1.1	6	4.4	±	0.4	224	160.6	±	5.5	8.25E-16	±	1.49E-17	0.7	24	0.29	9.1	0.66	13.7	±	1.1
Ap_OP1559-2	50	45.0	±	1.8	90	80.7	±	1.9	223	200.8	±	5.9	2.05E-15	±	2.85E-17	0.9	71	1.84	5.9	0.66	9.0	±	0.5
Ap_OP1559-3	71	43.5	±	1.9	153	94.3	±	2.5	167	103.0	±	3.5	2.29E-15	±	3.26E-17	0.6	107	2.22	6.4	0.54	12.0	±	0.7
Ap_OP1559-4	46	56.3	±	2.6	37	45.6	±	1.4	213	262.7	±	8.9	2.14E-15	±	3.63E-17	1.2	54	0.83	5.9	0.64	9.3	±	0.6
Ap_OP1560-1	21	58.8	±	10.4	18	49.7	±	1.2	57	157.0	±	5.5	1.37E-15	±	2.20E-17	2.8	25	0.87	3.7	0.68	5.4	±	0.8
Ap_OP1560-2	58	160.3	±	18.1	49	134.6	±	2.5	138	380.9	±	6.4	2.87E-14	±	3.36E-16	2.8	69	0.86	27.9	0.69	40.5	±	4.2
Ap_OP1560-3	21	34.3	±	6.5	2	3.5	±	0.2	169	278.9	±	9.7	1.54E-15	±	2.55E-17	1.7	21	0.10	8.4	0.67	12.7	±	2.7
Ap_OP1560-4	30	35.8	±	6.0	2	2.5	±	0.2	70	82.4	±	6.4	7.90E-17	±	6.33E-18	1.2	31	0.07	0.4	0.62	0.7	±	0.1
Ap_OP1561-1	12	65.0	±	2.3	15	80.6	±	2.6	202	1111.7	±	14.0	9.98E-15	±	1.25E-16	5.5	15	1.27	21.9	0.78	28.1	±	1.7
Ap_OP1561-2	17	24.7	±	1.3	15	20.7	±	0.8	192	273.9	±	6.6	3.13E-15	±	4.98E-17	1.4	21	0.86	19.7	0.68	28.9	±	2.0
Ap_OP1561-3	13	17.0	±	0.9	9	11.7	±	0.6	204	268.9	±	6.4	2.45E-15	±	3.85E-17	1.3	15	0.71	23.1	0.68	34.2	±	2.2
Ap_OP1561-4	70	16.4	±	0.6	221	52.0	±	1.9	1199	282.1	±	7.9	2.50E-15	±	3.36E-17	0.2	122	3.26	16.1	0.52	31.1	±	1.8
Ap_OP1562-1	35	61.4	±	9.3	15	27.3	±	1.0	47	82.6	±	5.4	1.20E-15	±	2.17E-17	1.8	38	0.46	3.3	0.68	4.9	±	0.7
Ap_OP1562-2	62	63.9	±	8.2	7	7.4	±	0.3	144	147.4	±	5.8	9.89E-16	±	2.26E-17	1.0	64	0.12	2.8	0.55	5.2	±	0.8
Ap_OP1562-3	36	45.7	±	11.8	9	11.1	±	0.5	21	26.8	±	5.2	4.31E-16	±	9.95E-18	1.3	38	0.25	1.7	0.59	3.0	±	0.8
Ap_OP1562-4	17	38.8	±	8.6	4	9.0	±	0.5	61	138.3	±	6.6	3.31E-16	±	9.71E-18	2.3	18	0.24	1.6	0.72	2.2	±	0.5
Ap_OP1571-1	31	122.9	±	13.5	37	143.7	±	3.3	104	407.7	±	11.4	1.95E-15	±	3.21E-17	3.9	40	1.20	2.3	0.76	3.0	±	0.3
~~Ap_OP1571-2~~	~~14~~	~~42.5~~	~~±~~	~~7.1~~	~~9~~	~~26.8~~	~~±~~	~~1.0~~	~~321~~	~~943.5~~	~~±~~	~~10.3~~	~~9.98E-15~~	~~±~~	~~1.31E-16~~	~~2.9~~	~~17~~	~~0.65~~	~~38.6~~	~~0.73~~	~~53.1~~	~~±~~	~~8.0~~
Ap_OP1571-3	19	62.2	±	9.7	20	67.2	±	1.8	82	271.3	±	10.6	7.34E-16	±	1.45E-17	3.3	24	1.11	1.8	0.71	2.5	±	0.3
Ap_OP1571-4	44	181.5	±	18.8	19	76.1	±	1.2	161	655.9	±	12.5	2.92E-15	±	4.26E-17	4.1	49	0.43	2.7	0.73	3.7	±	0.4
Ap_OP1572-1	55	247.9	±	19.5	46	208.0	±	4.0	178	796.6	±	11.2	2.47E-14	±	2.76E-16	4.5	66	0.86	15.5	0.77	20.2	±	1.7
Ap_OP1572-2	55	89.7	±	14.3	26	42.7	±	1.5	121	197.5	±	8.7	1.04E-14	±	1.24E-16	1.6	61	0.49	19.5	0.61	31.9	±	5.1
Ap_OP1572-3	56	127.1	±	12.4	34	77.2	±	1.6	122	277.7	±	9.6	9.64E-15	±	1.23E-16	2.3	64	0.62	12.4	0.68	18.2	±	1.8

Ap_OP1572-4	30	70.5	± 10.0	19	44.3	± 1.5	111	262.8	± 10.8	1.01E-15	± 1.63E-17	2.4	34	0.64	2.3	0.72	3.3 ± 0.4
Ap_OP1572-5	59	186.7	± 6.7	55	175.0	± 4.7	209	659.4	± 9.1	1.86E-14	± 2.29E-16	3.2	72	0.96	15.1	0.74	20.5 ± 1.2
Ap_OP1572-6	72	117.5	± 4.3	56	92.7	± 2.5	185	304.2	± 4.9	1.18E-14	± 1.47E-16	1.6	85	0.81	15.7	0.73	21.4 ± 1.2
Ap_OP1573-1	83	19.1	± 1.1	55	12.8	± 0.3	290	66.9	± 3.9	3.14E-16	± 9.55E-18	0.2	96	0.69	2.6	0.70	3.7 ± 0.3
Ap_OP1573-2	32	75.1	± 3.0	75	174.2	± 4.6	141	328.4	± 7.1	2.44E-14	± 3.08E-16	2.3	50	2.38	38.9	0.68	56.9 ± 3.2
~~Ap_OP1573-3~~	~~53~~	~~107.3~~	~~± 2.6~~	~~11~~	~~21.6~~	~~± 1.0~~	~~148~~	~~298.8~~	~~± 5.0~~	~~1.72E-15~~	~~± 2.57E-17~~	~~2.0~~	~~56~~	~~0.21~~	~~2.8~~	~~0.69~~	~~4.1 ± 0.2~~
Ap_OP1573-4	89	123.1	± 5.0	147	202.7	± 4.5	191	263.9	± 6.9	2.29E-15	± 3.26E-17	1.4	124	1.69	2.5	0.64	3.9 ± 0.2
Ap_OP1574-1	36	82.0	± 15.0	1	1.8	± 0.2	293	662.8	± 7.2	1.49E-15	± 2.25E-17	2.3	36	0.02	3.5	0.71	4.9 ± 1.0
~~Ap_OP1574-2~~	~~87~~	~~208.2~~	~~± 21.1~~	~~63~~	~~151.3~~	~~± 3.3~~	~~223~~	~~536.5~~	~~± 13.1~~	~~1.61E-14~~	~~± 2.29E-16~~	~~2.4~~	~~101~~	~~0.75~~	~~12.3~~	~~0.69~~	~~17.9 ± 1.8~~
Ap_OP1574-3	57	93.1	± 12.1	10	16.6	± 1.0	96	156.0	± 8.6	5.69E-16	± 1.18E-17	1.6	59	0.18	1.1	0.63	1.8 ± 0.2
Ap_OP1574-4	32	44.5	± 10.8	18	25.2	± 0.9	46	65.4	± 4.2	2.71E-16	± 7.90E-18	1.4	36	0.58	1.0	0.65	1.6 ± 0.4
Ap_OP1574-5	32	46.4	± 1.4	34	49.9	± 2.0	100	145.9	± 4.8	7.24E-16	± 1.72E-17	1.5	40	1.10	2.3	0.66	3.5 ± 0.2
Ap_OP1574-6	13	40.3	± 1.7	12	36.8	± 1.4	160	492.7	± 9.9	7.32E-16	± 1.58E-17	3.1	16	0.94	2.8	0.71	3.9 ± 0.2
Ap_OP1574-7	19	25.6	± 1.3	7	10.0	± 0.5	187	251.3	± 6.1	3.86E-16	± 1.04E-17	1.3	21	0.40	2.6	0.64	4.0 ± 0.3
Ap_OP1576-1	9	40.9	± 7.6	6	26.8	± 0.9	192	905.3	± 13.4	2.87E-14	± 3.46E-16	4.7	10	0.67	114.0	0.77	147.3 ± 25.6
Ap_OP1576-3	35	89.5	± 11.6	29	72.8	± 1.4	150	380.3	± 6.6	5.88E-16	± 1.37E-17	2.5	42	0.83	1.0	0.67	1.5 ± 0.2
Ap_OP1576-4	15	36.5	± 6.8	4	8.7	± 0.5	156	373.6	± 7.8	4.36E-14	± 5.71E-16	2.4	16	0.24	211.9	0.72	291.8 ± 56.4
Ap_OP1528-1	39	110.1	± 3.6	72	205.3	± 5.1	73	208.3	± 5.8	1.55E-15	± 2.23E-17	2.9	55	1.91	1.8	0.70	2.6 ± 0.2
Ap_OP1528-2	12	14.2	± 0.7	18	22.2	± 1.2	90	109.6	± 4.8	2.17E-16	± 8.41E-18	1.2	16	1.61	2.1	0.63	3.3 ± 0.2
Ap_OP1528-3	13	39.3	± 1.3	30	90.2	± 2.0	75	226.4	± 4.9	6.44E-16	± 1.64E-17	3.0	20	2.35	2.0	0.69	2.8 ± 0.2
Ap_OP1528-4	33	49.4	± 2.5	61	92.0	± 2.5	136	203.8	± 5.6	8.30E-16	± 1.27E-17	1.5	47	1.91	2.2	0.65	3.3 ± 0.2
Ap_OP1556-1	17	12.7	± 0.9	10	7.7	± 0.5	75	56.3	± 3.8	1.04E-16	± 5.49E-18	0.7	19	0.62	1.3	0.63	2.1 ± 0.2
Ap_OP1556-2	29	57.7	± 1.8	12	23.3	± 0.8	149	295.0	± 6.2	9.73E-16	± 1.60E-17	2.0	32	0.41	2.9	0.68	4.2 ± 0.2
Ap_OP1556-3	6	13.4	± 0.8	15	35.0	± 1.2	135	319.6	± 6.9	2.84E-16	± 7.76E-18	2.4	9	2.68	2.4	0.69	3.5 ± 0.2

B.2 Zircon (U-Th)/He single grain analyses

Table DR2: Zircon (U-Th)/He data

Note: Aliquots which are strike-through are not considered for the sample age calculation. ppm values of U and Th are calculated from iCAP results by deviding the mass of the respective element by the grain mass (which is derived from measurements of ^{91}Zr). eU is calculated by adding U-content and 0.235*Th-content.

Sample/ Aliquot	U (ppm)	U ± 2SD (pg)	Th (ppm)	Th ± 2SD (pg)	He ± 1SD (mol)	grain mass (µg)	eU (ppm)	Th/U	Uncorrected grain age (Ma)	FT correction	Corrected grain age ± 1SD (Ma)
Zr_OP1550-1	283	1955.9 ± 49.3	53	364.0 ± 9.4	7.37E-14 ± 9.07E-16	6.9	295	0.19	6.7	0.82	8.2 ± 0.4
Zr_OP1550-2	421	1982.2 ± 33.7	98	459.5 ± 12.8	5.27E-14 ± 6.43E-16	4.7	444	0.24	4.7	0.76	6.2 ± 0.3
~~Zr_OP1550-3~~	~~865~~	~~1449.5 ± 32.9~~	~~86~~	~~144.5 ± 4.2~~	~~7.16E-14 ± 8.34E-16~~	~~1.7~~	~~885~~	~~0.10~~	~~9.0~~	~~0.74~~	~~12.2 ± 0.7~~
Zr_OP1550-4	628	3753.8 ± 55.0	148	886.8 ± 17.5	1.15E-13 ± 1.37E-15	6.0	662	0.24	5.4	0.80	6.7 ± 0.3
~~Zr_OP1551-2~~	~~628~~	~~3891.7 ± 75.4~~	~~76~~	~~469.0 ± 12.5~~	~~3.73E-13 ± 2.39E-15~~	~~6.2~~	~~646~~	~~0.12~~	~~17.3~~	~~0.83~~	~~20.9 ± 1.1~~
~~Zr_OP1551-3~~	~~341~~	~~2429.3 ± 47.9~~	~~106~~	~~756.4 ± 18.9~~	~~1.16E-13 ± 1.45E-15~~	~~7.1~~	~~366~~	~~0.32~~	~~8.2~~	~~0.83~~	~~10.0 ± 0.5~~
Zr_OP1551-4	730	5134.3 ± 123.4	289	2034.2 ± 53.6	1.66E-13 ± 2.18E-15	7.0	798	0.41	5.5	0.80	6.8 ± 0.4
Zr_OP1551-5	164	774.0 ± 18.0	51	238.8 ± 7.4	2.34E-14 ± 3.03E-16	4.7	176	0.32	5.2	0.77	6.8 ± 0.4
Zr_OP1551-6	259	2145.2 ± 37.4	144	1195.0 ± 30.0	7.42E-14 ± 9.30E-16	8.3	293	0.57	5.7	0.80	7.1 ± 0.4
Zr_OP1551-7	176	537.8 ± 12.7	67	205.6 ± 9.0	1.75E-14 ± 2.10E-16	3.1	191	0.39	5.5	0.75	7.4 ± 0.4
Zr_OP1552-1	347	728.7 ± 20.7	122	256.8 ± 8.7	3.14E-14 ± 3.42E-16	2.1	376	0.36	7.4	0.68	10.8 ± 0.6
Zr_OP1552-2	413	2298.7 ± 42.4	77	430.6 ± 11.9	9.18E-14 ± 1.05E-15	5.6	431	0.19	7.1	0.79	9.0 ± 0.5
Zr_OP1552-3	117	323.0 ± 6.5	39	107.6 ± 4.8	9.18E-15 ± 1.16E-16	2.8	126	0.34	4.9	0.74	6.6 ± 0.4
Zr_OP1552-4	517	855.2 ± 25.6	153	252.5 ± 9.0	2.68E-14 ± 3.18E-16	1.7	552	0.30	5.4	0.70	7.8 ± 0.4
Zr_OP1553-1	248	1927.2 ± 38.4	43	338.2 ± 9.6	6.95E-14 ± 8.91E-16	7.8	258	0.18	6.4	0.80	8.0 ± 0.5
Zr_OP1553-2	553	6195.5 ± 130.2	136	1523.9 ± 34.3	2.27E-13 ± 2.87E-15	11.2	585	0.25	6.4	0.84	7.7 ± 0.4
Zr_OP1553-3	173	2082.4 ± 30.0	71	851.0 ± 22.5	7.63E-14 ± 9.95E-16	12.1	189	0.42	6.2	0.85	7.3 ± 0.4
Zr_OP1554-1	113	355.6 ± 7.4	26	82.9 ± 3.2	1.17E-14 ± 1.70E-16	3.2	119	0.24	5.8	0.75	7.7 ± 0.4

Zr_OP1554-2	433	1348.3	±	34.4	147	458.7	±	26.3	3.90E-14	±	4.74E-16	3.1	468	0.35	5.0	0.75	6.6	±	0.4
Zr_OP1554-3	363	754.1	±	10.6	63	130.4	±	5.0	1.93E-14	±	2.42E-16	2.1	377	0.18	4.6	0.70	6.5	±	0.4
Zr_OP1554-4	640	789.2	±	19.1	256	315.8	±	12.5	2.33E-14	±	3.07E-16	1.2	700	0.41	5.0	0.66	7.6	±	0.4
Zr_OP1555-1	197	1440.1	±	34.7	92	673.0	±	18.5	5.68E-14	±	7.17E-16	7.3	218	0.48	6.6	0.81	8.1	±	0.4
Zr_OP1555-2	252	1977.7	±	44.7	103	809.1	±	21.2	7.71E-14	±	9.58E-16	7.9	276	0.42	6.6	0.81	8.2	±	0.4
Zr_OP1555-3	309	1575.4	±	38.5	79	403.5	±	11.7	3.78E-14	±	4.57E-16	5.1	328	0.26	4.2	0.82	5.1	±	0.3
Zr_OP1555-4	190	877.2	±	25.9	101	464.8	±	9.0	3.10E-14	±	4.02E-16	4.6	214	0.54	5.8	0.79	7.3	±	0.4
Zr_OP1557-1	334	2568.3	±	64.5	103	792.2	±	15.1	5.97E-13	±	7.29E-15	7.7	358	0.32	40.1	0.75	53.1	±	3.0
Zr_OP1557-2	653	4708.8	±	74.3	176	1266.6	±	34.4	1.02E-12	±	1.16E-14	7.2	694	0.28	37.8	0.80	47.1	±	2.5
Zr_OP1557-3	236	1901.9	±	42.3	95	763.3	±	20.8	2.08E-13	±	2.53E-15	8.1	258	0.41	18.5	0.74	25.1	±	1.4
Zr_OP1557-4	189	1225.3	±	30.5	76	493.3	±	13.6	1.13E-13	±	1.40E-15	6.5	207	0.41	15.6	0.78	20.1	±	1.1
Zr_OP1562-1	356	1205.1	±	30.6	141	479.2	±	11.9	1.46E-13	±	1.75E-15	3.4	389	0.41	20.5	0.80	25.5	±	1.4
Zr_OP1562-2	369	1959.8	±	42.4	39	208.6	±	7.9	2.82E-13	±	3.45E-15	5.3	379	0.11	26.0	0.81	32.3	±	1.8
Zr_OP1562-3	237	869.4	±	24.4	57	209.9	±	7.5	1.02E-13	±	1.28E-15	3.7	250	0.25	20.6	0.81	25.4	±	1.4
Zr_OP1562-4	190	962.4	±	24.7	142	720.7	±	16.2	1.58E-13	±	1.96E-15	5.1	223	0.77	25.9	0.77	33.6	±	1.8
Zr_OP1570-1	345	2886.9	±	89.4	103	857.4	±	16.4	1.15E-13	±	1.48E-15	8.4	369	0.30	6.9	0.82	8.4	±	0.5
Zr_OP1570-2	574	3152.9	±	44.1	192	1056.8	±	27.6	1.42E-13	±	1.89E-15	5.5	619	0.34	7.7	0.78	9.8	±	0.5
Zr_OP1570-3	466	2264.1	±	50.3	33	158.4	±	4.8	7.36E-14	±	9.25E-16	4.9	474	0.07	5.9	0.76	7.7	±	0.4
Zr_OP1570-4	160	1158.4	±	32.9	29	209.2	±	7.1	3.70E-14	±	4.79E-16	7.2	167	0.19	5.7	0.82	6.9	±	0.4
Zr_OP1571-1	548	2883.0	±	70.9	47	247.9	±	7.2	8.68E-14	±	1.06E-15	5.3	559	0.09	5.5	0.77	7.1	±	0.4
Zr_OP1571-2	139	2304.5	±	47.1	33	550.4	±	15.8	1.09E-13	±	1.33E-15	16.5	147	0.24	8.3	0.86	9.7	±	0.5
Zr_OP1571-3	519	1215.3	±	28.7	161	377.0	±	13.7	4.19E-14	±	5.34E-16	2.3	557	0.32	6.0	0.72	8.3	±	0.5
Zr_OP1571-4	420	3548.8	±	62.5	97	822.7	±	16.0	1.26E-13	±	1.69E-15	8.4	443	0.24	6.3	0.82	7.6	±	0.4

Zr_OP1572-1	435	674.6	±	17.8	114	177.1	±	7.8	2.31E-14	±	2.66E-16	1.6	462	0.27	6.0	0.67	8.9	±	0.5
Zr_OP1572-2	1002	4173.2	±	61.1	255	1062.4	±	26.1	1.12E-13	±	1.34E-15	4.2	1062	0.26	4.7	0.77	6.1	±	0.3
Zr_OP1572-3	258	1378.8	±	34.3	35	187.6	±	7.0	4.66E-14	±	5.32E-16	5.3	266	0.14	6.1	0.78	7.7	±	0.4
Zr_OP1572-4	682	2496.6	±	42.5	187	684.2	±	16.3	1.12E-13	±	1.17E-15	3.7	726	0.28	7.8	0.76	10.3	±	0.5
Zr_OP1572-5	217	1863.6	±	29.7	92	793.4	±	14.1	8.09E-14	±	8.64E-16	8.6	239	0.44	7.3	0.81	9.1	±	0.5
Zr_OP1573-1	286	745.7	±	18.0	129	337.0	±	10.6	2.46E-14	±	2.74E-16	2.6	317	0.46	5.5	0.73	7.6	±	0.4
Zr_OP1573-2	89	308.0	±	9.1	29	99.0	±	4.0	1.25E-14	±	1.35E-16	3.5	96	0.33	7.0	0.75	9.3	±	0.5
Zr_OP1573-3	409	1664.9	±	35.1	122	496.7	±	10.3	7.05E-14	±	8.25E-16	4.1	438	0.31	7.3	0.75	9.7	±	0.5
Zr_OP1573-4	276	2324.7	±	54.0	50	424.9	±	6.3	9.48E-14	±	1.07E-15	8.4	288	0.19	7.3	0.80	9.1	±	0.5
Zr_OP1574-1	232	669.4	±	10.6	44	126.9	±	5.4	2.15E-14	±	2.85E-16	2.9	242	0.19	5.7	0.74	7.7	±	0.4
Zr_OP1574-2	69	622.9	±	18.2	34	308.7	±	8.0	2.84E-14	±	3.81E-16	9.0	78	0.51	7.6	0.82	9.2	±	0.5
Zr_OP1574-3	1124	6696.8	±	117.3	66	393.8	±	7.4	1.88E-13	±	2.60E-15	6.0	1140	0.06	5.1	0.77	6.6	±	0.4
Zr_OP1574-4	698	3205.0	±	55.5	215	987.7	±	23.1	1.10E-13	±	1.45E-15	4.6	749	0.32	6.0	0.76	7.9	±	0.4
Zr_OP1576-1	161	396.4	±	6.9	43	105.3	±	2.6	1.13E-14	±	1.53E-16	2.5	171	0.27	5.0	0.73	6.8	±	0.4
~~Zr_OP1576-2~~	~~194~~	~~398.7~~	~~±~~	~~9.9~~	~~87~~	~~179.7~~	~~±~~	~~7.1~~	~~1.59E-14~~	~~±~~	~~1.93E-16~~	~~2.1~~	~~214~~	~~0.46~~	~~6.7~~	~~0.69~~	~~9.7~~	~~±~~	~~0.5~~
Zr_OP1576-3	129	212.4	±	8.7	26	42.8	±	2.7	5.27E-15	±	7.11E-17	1.7	135	0.21	4.4	0.72	6.1	±	0.4
Zr_OP1576-4	213	586.5	±	14.5	56	154.4	±	5.9	1.63E-14	±	2.18E-16	2.8	226	0.27	4.9	0.73	6.6	±	0.4
Zr_OP1576-5	369	1186.5	±	31.0	89	287.7	±	9.5	3.30E-14	±	4.26E-16	3.2	390	0.25	4.9	0.76	6.4	±	0.4
Zr_OP1577-1	341	3594.9	±	64.8	145	1523.0	±	36.9	1.32E-13	±	1.66E-15	10.5	375	0.43	6.2	0.83	7.4	±	0.4
Zr_OP1577-2	777	3966.1	±	78.2	131	667.5	±	16.9	1.21E-13	±	1.51E-15	5.1	808	0.17	5.5	0.75	7.2	±	0.4
Zr_OP1577-3	1265	4039.0	±	82.2	394	1257.0	±	36.0	1.35E-13	±	1.58E-15	3.2	1357	0.32	5.8	0.75	7.7	±	0.4
Zr_OP1577-4	132	351.2	±	10.6	35	92.3	±	3.9	8.35E-15	±	1.06E-16	2.7	140	0.27	4.2	0.74	5.6	±	0.3

B.3 Apatite fission track single grain analyses

Table DR3: Apatite fission track single grain ages listed for each sample.

==========ZetaAge Program v. 4.8 (Brandon 8/13/02)==========
OP1502 (Olympics) sedimentary bedrock, (Counted by Sarah Falkowski Nov. 2016)
EFFECTIVE TRACK DENSITY FOR FLUENCE MONITOR (tracks/cm^2): 8.270E+05
RELATIVE ERROR (%): 1.48
EFFECTIVE URANIUM CONTENT OF MONITOR (ppm): 15.00
ZETA FACTOR AND STANDARD ERROR (yr cm^2): 252.90 5.00
SIZE OF COUNTER SQUARE (cm^2): 1.000E-06

Grain no.	RhoS (cm^-2)	(Ns)	RhoI (cm^-2)	(Ni)	Squares	U+/-2s		Grain Age (Ma)	Age	--95% CI--
1	8.33E+05	(5)	1.67E+05	(1)	6	3	5	454.2	58.2	10161.2
2	3.33E+05	(2)	1.67E+05	(1)	6	3	5	193.6	10.9	6895.4
3	8.70E+04	(4)	4.35E+05	(20)	46	8	3	21.5	5.2	62.2
4	2.50E+05	(4)	2.50E+05	(4)	16	5	4	103.7	19.4	538.5
5	1.67E+05	(1)	3.33E+05	(2)	6	6	8	55.4	0.9	933.6
6	6.25E+05	(5)	1.00E+06	(8)	8	18	12	65.8	16.8	222.8
7	3.13E+05	(5)	8.75E+05	(14)	16	16	8	38.0	10.5	108.9
8	2.12E+05	(11)	2.50E+05	(13)	52	5	2	88.1	35.8	210.7
9	5.00E+05	(6)	1.67E+05	(2)	12	3	4	292.1	55.8	2584.3
10	1.56E+04	(1)	4.69E+04	(3)	64	1	1	37.9	0.7	420.3
11	1.07E+06	(15)	2.86E+05	(4)	14	5	5	370.2	123.7	1448.2
12	2.67E+05	(4)	1.33E+05	(2)	15	2	3	198.7	29.9	1976.2
13	1.07E+05	(3)	3.21E+05	(9)	28	6	4	36.0	6.1	138.3
14	6.25E+05	(5)	2.50E+05	(2)	8	5	6	245.6	42.6	2287.6
15	3.33E+05	(13)	1.69E+06	(66)	39	31	8	20.8	10.4	37.6
16	6.36E+04	(7)	5.55E+05	(61)	110	10	3	12.2	4.6	26.2
17	2.62E+05	(11)	1.57E+06	(66)	42	29	7	17.6	8.3	33.2
18	8.06E+04	(5)	1.77E+05	(11)	62	3	2	48.2	12.9	146.8
19	2.97E+05	(27)	2.09E+05	(19)	91	4	2	146.6	79.1	277.0
20	1.18E+04	(1)	4.71E+04	(4)	85	1	1	28.8	0.5	259.0
21	1.00E+05	(4)	2.50E+05	(10)	40	5	3	42.7	9.6	143.5
22	4.17E+05	(10)	1.67E+05	(4)	24	3	3	250.5	74.9	1051.7
23	9.09E+04	(2)	1.36E+05	(3)	22	2	3	71.0	5.8	581.7
24	3.33E+05	(8)	2.08E+05	(5)	24	4	3	163.3	48.1	619.5
25	3.33E+05	(10)	2.33E+05	(7)	30	4	3	146.7	51.1	446.8
26	1.67E+05	(3)	2.22E+05	(4)	18	4	4	78.9	11.5	447.8
27	3.85E+05	(10)	5.38E+05	(14)	26	10	5	74.6	29.6	178.4
28	9.00E+05	(9)	3.00E+05	(3)	10	5	6	296.4	77.8	1589.1
29	1.11E+05	(2)	1.67E+05	(3)	18	3	3	71.0	5.8	581.7
30	2.00E+05	(4)	2.50E+05	(5)	20	5	4	83.8	16.6	377.6
31	8.33E+04	(3)	5.00E+05	(18)	36	9	4	18.2	3.3	59.5
32	1.56E+05	(5)	1.56E+05	(5)	32	3	2	103.7	24.0	439.3
33	1.00E+06	(6)	3.33E+05	(2)	6	6	8	292.1	55.8	2584.3
34	1.67E+05	(4)	2.50E+05	(6)	24	5	4	70.2	14.4	287.6
35	6.67E+04	(3)	3.78E+05	(17)	45	7	3	19.2	3.5	63.5
36	2.19E+05	(7)	4.69E+05	(15)	32	9	4	49.2	16.8	126.0
37	6.88E+05	(11)	1.25E+05	(2)	16	2	3	519.9	124.3	3890.6
38	2.54E+05	(15)	6.95E+05	(41)	59	13	4	38.4	19.6	70.3
39	1.25E+05	(3)	1.67E+05	(4)	24	3	3	78.9	11.5	447.8
40	1.56E+06	(14)	2.11E+06	(19)	9	38	17	76.8	35.6	160.2
41	5.00E+05	(10)	1.00E+05	(2)	20	2	2	475.0	110.4	3649.8
42	3.43E+05	(12)	1.03E+06	(36)	35	19	6	35.1	16.5	68.2
43	5.00E+05	(8)	5.63E+05	(9)	16	10	7	92.5	31.1	266.0

44	8.70E+04	(4)	2.17E+05	(10)	46	4	2	42.7	9.6	143.5
45	2.20E+05	(11)	2.00E+05	(10)	50	4	2	113.9	44.2	295.4
46	4.07E+05	(24)	2.37E+05	(14)	59	4	2	176.0	88.4	364.6
47	9.30E+04	(4)	3.02E+05	(13)	43	5	3	33.0	7.6	103.4
48	1.04E+05	(7)	6.42E+05	(43)	67	12	4	17.3	6.5	38.1
49	2.08E+05	(5)	5.83E+05	(14)	24	11	6	38.0	10.5	108.9
50	1.40E+05	(7)	1.44E+06	(72)	50	26	6	10.4	3.9	22.0
51	1.50E+05	(3)	1.00E+05	(2)	20	2	2	151.4	17.9	1648.5
52	3.33E+05	(2)	1.67E+05	(1)	6	3	5	193.6	10.9	6895.4
53	6.06E+04	(4)	2.42E+05	(16)	66	4	2	26.9	6.4	80.6
54	2.50E+05	(6)	2.92E+05	(7)	24	5	4	89.4	24.8	304.3
55	1.46E+05	(7)	2.92E+05	(14)	48	5	3	52.7	17.8	137.1
56	4.44E+05	(4)	3.33E+05	(3)	9	6	6	136.3	23.5	888.1
57	3.33E+05	(10)	3.67E+05	(11)	30	7	4	94.5	36.1	242.1
58	1.88E+05	(3)	1.25E+05	(2)	16	2	3	151.4	17.9	1648.5
59	2.50E+05	(4)	6.25E+04	(1)	16	1	2	368.6	41.2	9245.0
60	2.00E+05	(16)	4.38E+05	(35)	80	8	3	47.9	24.6	88.2
61	1.10E+06	(11)	1.70E+06	(17)	10	31	15	67.7	28.6	151.5
62	9.53E+05	(61)	1.61E+06	(103)	64	29	6	61.7	44.2	85.4
63	5.36E+04	(3)	1.96E+05	(11)	56	4	2	29.5	5.1	107.1
64	2.99E+04	(2)	3.88E+05	(26)	67	7	3	8.6	0.9	32.1
65	7.50E+04	(3)	1.00E+05	(4)	40	2	2	78.9	11.5	447.8
66	2.14E+05	(9)	1.67E+05	(7)	42	3	2	132.4	44.4	411.6
67	6.67E+05	(4)	8.33E+05	(5)	6	15	13	83.8	16.6	377.6
68	5.00E+04	(2)	1.25E+05	(5)	40	2	2	43.5	4.0	250.7
69	2.00E+05	(5)	1.20E+05	(3)	25	2	2	168.6	33.8	1035.0
70	1.67E+05	(5)	3.00E+05	(9)	30	5	4	58.6	15.3	190.3
71	2.50E+05	(2)	5.00E+05	(4)	8	9	9	54.0	4.7	355.0
72	1.67E+05	(3)	2.78E+05	(5)	18	5	4	63.7	9.7	314.8
73	4.50E+05	(9)	5.00E+04	(1)	20	1	1	785.7	129.1	12902.5
74	6.25E+05	(10)	1.69E+06	(27)	16	31	12	39.0	16.7	82.1
75	3.44E+06	(155)	2.82E+06	(127)	45	51	9	126.3	99.6	160.0
76	9.38E+04	(3)	1.25E+05	(4)	32	2	2	78.9	11.5	447.8
77	3.50E+05	(7)	2.50E+05	(5)	20	5	4	143.5	39.9	560.2
78	2.50E+05	(4)	2.50E+05	(4)	16	5	4	103.7	19.4	538.5
79	8.33E+05	(10)	1.67E+05	(2)	12	3	4	475.0	110.4	3649.8
80	3.57E+05	(5)	2.86E+05	(4)	14	5	5	128.4	28.1	627.4
81	2.00E+06	(40)	1.10E+07	(219)	20	199	27	19.1	13.3	26.8
82	4.17E+05	(10)	2.92E+05	(7)	24	5	4	146.7	51.1	446.8
83	5.00E+05	(3)	1.67E+05	(1)	6	3	5	281.7	25.1	8176.7
84	1.07E+05	(3)	4.64E+05	(13)	28	8	5	25.1	4.4	87.3
85	2.31E+05	(9)	5.38E+05	(21)	39	10	4	45.1	18.0	101.3
86	4.10E+06	(41)	1.38E+07	(138)	10	250	43	31.1	21.3	44.2
87	7.00E+05	(21)	2.67E+05	(8)	30	5	3	265.6	115.7	679.9
88	4.33E+05	(13)	4.33E+05	(13)	30	8	4	103.7	44.5	240.5
89	8.33E+05	(10)	1.67E+05	(2)	12	3	4	475.0	110.4	3649.8
90	9.17E+05	(11)	1.67E+05	(2)	12	3	4	519.9	124.3	3890.6
91	0.00E+00	(0)	1.33E+05	(4)	30	2	2	19.8	0.7	156.6
92	9.38E+05	(15)	2.25E+06	(36)	16	41	14	43.7	22.1	81.2
93	1.36E+05	(6)	1.82E+05	(8)	44	3	2	78.5	22.4	252.9
94	8.33E+04	(2)	4.17E+04	(1)	24	1	1	193.6	10.9	6895.4

OP1510 (Olympics) sedimentary bedrock, (Counted by Sarah Falkowski Oct. 2016)
EFFECTIVE TRACK DENSITY FOR FLUENCE MONITOR (tracks/cm^2): 8.250E+05
RELATIVE ERROR (%): 1.48
EFFECTIVE URANIUM CONTENT OF MONITOR (ppm): 15.00
ZETA FACTOR AND STANDARD ERROR (yr cm^2): 252.90 5.00
SIZE OF COUNTER SQUARE (cm^2): 1.000E-06

Grain no.	RhoS (cm^-2)	(Ns)	RhoI (cm^-2)	(Ni)	Squares	U+/-2s		Grain Age	Age (Ma) --95%	CI--
1	5.00E+05	(9)	4.44E+05	(8)	18	8	6	116.1	40.0	340.6
2	5.33E+05	(8)	4.67E+05	(7)	15	8	6	117.8	37.7	375.3
3	5.56E+05	(5)	8.89E+05	(8)	9	16	11	65.6	16.8	222.3
4	2.00E+06	(48)	4.21E+06	(101)	24	77	15	49.5	34.3	70.3
5	3.81E+05	(8)	3.81E+05	(8)	21	7	5	103.5	34.0	311.4
6	6.00E+05	(12)	9.50E+05	(19)	20	17	8	65.9	29.1	141.5
7	3.89E+05	(14)	5.28E+05	(19)	36	10	4	76.6	35.5	159.8
8	9.17E+05	(11)	2.92E+06	(35)	12	53	18	33.0	15.0	65.8
9	1.05E+06	(21)	2.75E+06	(55)	20	50	14	39.9	22.8	66.7
10	3.00E+05	(3)	2.00E+05	(2)	10	4	5	151.1	17.9	1645.0
11	5.33E+05	(8)	1.40E+06	(21)	15	25	11	40.1	15.2	92.8
12	2.00E+05	(14)	4.43E+05	(31)	70	8	3	47.2	23.1	90.7
13	1.15E+06	(23)	5.15E+06	(103)	20	94	19	23.4	14.1	36.8
14	2.50E+05	(6)	1.00E+06	(24)	24	18	7	26.6	8.7	65.2
15	4.17E+05	(20)	1.48E+06	(71)	48	27	6	29.5	16.9	48.7
16	3.57E+05	(10)	6.07E+05	(17)	28	11	5	61.5	25.0	140.5
17	1.25E+05	(3)	1.25E+05	(3)	24	2	2	103.5	14.0	735.5
18	4.17E+05	(10)	8.75E+05	(21)	24	16	7	49.9	20.8	109.4
19	1.56E+05	(5)	5.63E+05	(18)	32	10	5	29.6	8.4	80.5
20	3.00E+05	(6)	8.50E+05	(17)	20	15	7	37.4	11.9	97.2
21	7.69E+04	(1)	4.62E+05	(6)	13	8	7	19.4	0.4	141.8
22	4.29E+05	(18)	6.67E+05	(28)	42	12	5	66.9	34.8	124.5
23	5.33E+05	(8)	1.80E+06	(27)	15	33	13	31.3	12.1	69.6
24	2.92E+05	(7)	7.50E+05	(18)	24	14	6	41.0	14.3	101.1
25	1.44E+06	(23)	4.13E+06	(66)	16	75	19	36.4	21.5	59.0
26	4.44E+05	(4)	3.33E+05	(3)	9	6	6	135.9	23.5	886.0
27	6.67E+05	(8)	1.17E+06	(14)	12	21	11	59.9	21.6	150.6
28	1.88E+05	(3)	1.06E+06	(17)	16	19	9	19.2	3.5	63.4
29	8.75E+05	(7)	1.63E+06	(13)	8	30	16	56.5	18.9	149.8
30	9.44E+05	(17)	3.00E+06	(54)	18	55	15	33.0	17.8	57.3
31	1.22E+06	(22)	2.72E+06	(49)	18	49	14	46.9	26.9	78.5
32	1.11E+05	(2)	5.56E+04	(1)	18	1	2	193.1	10.9	6885.2
33	2.14E+05	(6)	5.00E+05	(14)	28	9	5	45.2	14.1	122.7
34	1.25E+05	(1)	1.25E+05	(1)	8	2	4	103.5	1.3	5286.0
35	5.31E+05	(17)	7.50E+05	(24)	32	14	6	73.7	37.1	142.0
36	1.67E+05	(2)	1.67E+05	(2)	12	3	4	103.5	7.6	1299.3
37	8.75E+05	(35)	8.25E+05	(33)	40	15	5	109.7	66.4	181.3
38	2.33E+05	(7)	5.33E+05	(16)	30	10	5	46.1	15.9	116.3
39	2.00E+05	(12)	1.50E+05	(9)	60	3	2	137.0	53.5	363.5
40	2.22E+05	(4)	3.33E+05	(6)	18	6	5	70.1	14.4	286.9
41	5.42E+05	(13)	1.08E+06	(26)	24	20	8	52.3	24.5	104.5
42	1.33E+05	(2)	7.33E+05	(11)	15	13	8	20.1	2.0	86.4
43	5.56E+05	(5)	1.78E+06	(16)	9	32	16	33.2	9.3	92.5
44	4.00E+05	(4)	1.20E+06	(12)	10	22	12	35.6	8.2	113.8

45	4.29E+05	(9)	8.10E+05	(17)	21	15	7	55.5	21.6	129.8
46	2.00E+05	(6)	2.67E+05	(8)	30	5	3	78.3	22.3	252.3
47	1.04E+05	(5)	6.46E+05	(31)	48	12	4	17.3	5.1	43.5
48	6.88E+05	(11)	1.31E+06	(21)	16	24	10	54.8	23.7	117.6
49	2.00E+05	(6)	1.00E+05	(3)	30	2	2	200.3	44.4	1175.7
50	6.11E+05	(11)	7.78E+05	(14)	18	14	7	81.7	33.6	191.6
51	6.67E+05	(10)	6.67E+05	(10)	15	12	7	103.5	38.8	273.5
52	5.00E+05	(30)	1.48E+06	(89)	60	27	6	35.2	22.4	53.6
53	5.00E+05	(6)	6.67E+05	(8)	12	12	8	78.3	22.3	252.3
54	5.33E+05	(8)	6.67E+05	(10)	15	12	7	83.3	28.5	230.8
55	1.33E+05	(4)	6.33E+05	(19)	30	12	5	22.6	5.4	65.8
56	7.33E+05	(11)	2.13E+06	(32)	15	39	14	36.1	16.3	72.7
57	2.86E+04	(2)	3.00E+05	(21)	70	5	2	10.6	1.1	40.5
58	2.86E+05	(4)	7.14E+05	(10)	14	13	8	42.6	9.5	143.2
59	3.25E+05	(13)	6.00E+05	(24)	40	11	4	56.6	26.4	114.5
60	8.33E+05	(15)	2.44E+06	(44)	18	44	13	35.7	18.3	64.9
61	2.67E+05	(4)	6.67E+05	(10)	15	12	7	42.6	9.5	143.2
62	5.00E+05	(6)	1.58E+06	(19)	12	29	13	33.5	10.8	85.3
63	1.68E+06	(67)	3.45E+06	(138)	40	63	11	50.5	37.1	68.0
64	4.58E+05	(11)	3.75E+05	(9)	24	7	4	125.9	47.8	339.2
65	2.22E+05	(4)	7.22E+05	(13)	18	13	7	32.9	7.6	103.1
66	1.33E+05	(4)	5.67E+05	(17)	30	10	5	25.2	6.0	74.9
67	1.67E+05	(6)	5.00E+05	(18)	36	9	4	35.3	11.3	90.9
68	1.33E+05	(2)	5.33E+05	(8)	15	10	7	27.5	2.7	129.4
69	6.67E+05	(16)	4.17E+05	(10)	24	8	5	163.8	70.8	399.1
70	1.39E+05	(5)	1.39E+05	(5)	36	3	2	103.5	24.0	438.2
71	3.33E+05	(18)	4.70E+06	(254)	54	86	11	7.5	4.3	11.9
72	1.04E+06	(52)	1.58E+06	(79)	50	29	6	68.4	47.2	98.1
73	3.33E+04	(2)	1.17E+05	(7)	60	2	2	31.3	3.0	154.7
74	3.33E+05	(5)	4.67E+05	(7)	15	8	6	74.7	18.6	267.2
75	3.33E+04	(1)	2.00E+05	(6)	30	4	3	19.4	0.4	141.8
76	1.00E+06	(10)	1.50E+06	(15)	10	27	14	69.5	27.9	163.5
77	1.07E+06	(30)	2.11E+06	(59)	28	38	10	53.0	32.9	83.2
78	1.85E+05	(5)	5.93E+05	(16)	27	11	5	33.2	9.3	92.5
79	3.14E+05	(11)	3.14E+05	(11)	35	6	3	103.5	40.9	260.2
80	1.07E+05	(6)	2.86E+05	(16)	56	5	3	39.7	12.5	104.5
81	4.44E+05	(8)	6.11E+05	(11)	18	11	7	75.8	26.4	203.9
82	4.69E+05	(15)	1.09E+06	(35)	32	20	7	44.8	22.6	83.5

OP1513 (Olympics) sedimentary bedrock, (Counted by Sarah Falkowski Oct. 2016)

Grain no.	**RhoS (cm^-2)**	**(Ns)**	**RhoI (cm^-2)**	**(Ni)**	**Squares**	**U+/-2s**		**Grain Age**	**Age (Ma) --95% CI--**	
1	3.57E+04	(1)	5.36E+05	(15)	28	10	5	7.9	0.2	45.0
2	5.00E+04	(1)	3.00E+05	(6)	20	5	4	19.4	0.4	141.6
3	8.57E+04	(3)	1.29E+06	(45)	35	23	7	7.3	1.4	21.6
4	0.00E+00	(0)	1.25E+05	(5)	40	2	2	15.5	0.5	112.8
5	1.67E+05	(1)	1.50E+06	(9)	6	27	18	13.0	0.3	83.1
6	2.00E+05	(4)	1.65E+06	(33)	20	30	10	13.1	3.2	35.4
7	1.21E+05	(4)	3.61E+06	(119)	33	66	12	3.6	0.9	9.2
8	4.88E+04	(2)	4.15E+05	(17)	41	8	4	13.1	1.4	51.5
9	8.62E+04	(5)	1.78E+06	(103)	58	32	6	5.2	1.6	12.2
10	5.00E+05	(6)	6.58E+06	(79)	12	120	27	8.1	2.8	18.0
11	3.51E+04	(2)	2.28E+05	(13)	57	4	2	17.0	1.8	70.5

12	5.00E+05	(4)	1.98E+07	(158)	8	360	58	2.7	0.7	6.9
13	7.32E+04	(3)	4.63E+05	(19)	41	8	4	17.2	3.1	55.7
14	2.78E+04	(1)	3.17E+06	(114)	36	58	11	1.0	0.0	5.2
15	6.67E+04	(2)	9.33E+05	(28)	30	17	6	8.0	0.9	29.5
16	1.05E+05	(4)	1.82E+06	(69)	38	33	8	6.3	1.6	16.2
17	7.14E+04	(2)	8.57E+05	(24)	28	16	6	9.3	1.0	34.9
18	1.25E+05	(3)	1.38E+06	(33)	24	25	9	9.9	1.9	30.1
19	9.76E+04	(4)	2.17E+06	(89)	41	40	8	4.9	1.2	12.4
20	4.00E+04	(2)	7.60E+05	(38)	50	14	4	5.9	0.6	21.2
21	7.69E+04	(6)	9.87E+05	(77)	78	18	4	8.3	2.9	18.5
22	4.88E+04	(2)	4.63E+05	(19)	41	8	4	11.7	1.2	45.3
23	8.33E+04	(3)	1.42E+06	(51)	36	26	7	6.4	1.2	18.9
24	6.38E+04	(3)	1.87E+06	(88)	47	34	7	3.7	0.7	10.7

OP1517 (Olympics) sedimentary bedrock, (Counted by Sarah Falkowski Oct. 2016)
EFFECTIVE TRACK DENSITY FOR FLUENCE MONITOR (tracks/cm^2): 8.220E+05
RELATIVE ERROR (%): 1.48
EFFECTIVE URANIUM CONTENT OF MONITOR (ppm): 15.00
ZETA FACTOR AND STANDARD ERROR (yr cm^2): 252.90 5.00
SIZE OF COUNTER SQUARE (cm^2): 1.000E-06

Grain no.	RhoS (cm^-2)	(Ns)	RhoI (cm^-2)	(Ni)	Squares	U+/-2s		Grain Age	Age (Ma) --95%	CI--
1	0.00E+00	(0)	9.68E+04	(6)	62	2	1	12.7	0.4	87.7
2	2.78E+04	(1)	1.03E+06	(37)	36	19	6	3.2	0.1	16.6
3	5.56E+04	(2)	5.56E+05	(20)	36	10	4	11.1	1.2	42.7
4	1.13E+05	(8)	8.87E+05	(63)	71	16	4	13.4	5.5	27.6
5	6.25E+04	(1)	1.31E+06	(21)	16	24	10	5.6	0.1	30.7
6	5.33E+04	(4)	1.53E+06	(115)	75	28	5	3.8	1.0	9.5
7	6.06E+04	(2)	6.36E+05	(21)	33	12	5	10.6	1.1	40.4
8	1.79E+04	(1)	9.29E+05	(52)	56	17	5	2.3	0.0	11.6
9	2.71E+05	(13)	6.67E+06	(320)	48	122	14	4.3	2.2	7.3
10	7.14E+04	(3)	2.43E+06	(102)	42	44	9	3.2	0.6	9.2
11	1.00E+05	(6)	8.67E+05	(52)	60	16	4	12.3	4.2	27.9
12	0.00E+00	(0)	9.38E+05	(15)	16	17	9	4.9	0.2	28.9
13	9.52E+03	(1)	1.52E+05	(16)	105	3	1	7.4	0.2	41.7
14	0.00E+00	(0)	1.27E+06	(38)	30	23	7	1.9	0.1	10.6
15	1.18E+04	(1)	2.24E+05	(19)	85	4	2	6.2	0.1	34.3
16	3.45E+04	(2)	5.52E+05	(32)	58	10	4	7.0	0.8	25.4
17	0.00E+00	(0)	2.50E+04	(2)	80	0	1	42.9	1.3	531.1

OP1521 (Olympics) sedimentary bedrock, (Counted by Sarah Falkowski Nov. 2016)
EFFECTIVE TRACK DENSITY FOR FLUENCE MONITOR (tracks/cm^2): 8.200E+05
RELATIVE ERROR (%): 1.48
EFFECTIVE URANIUM CONTENT OF MONITOR (ppm): 15.00
ZETA FACTOR AND STANDARD ERROR (yr cm^2): 252.90 5.00
SIZE OF COUNTER SQUARE (cm^2): 1.000E-06

Grain no.	RhoS (cm^-2)	(Ns)	RhoI (cm^-2)	(Ni)	Squares	U+/-2s		Grain Age	Age (Ma) --95%	CI--
1	8.33E+04	(2)	1.71E+06	(41)	24	31	10	5.4	0.6	19.5
2	6.00E+05	(36)	1.07E+06	(64)	60	20	5	58.2	37.5	88.6
3	4.17E+04	(4)	1.04E+05	(10)	96	2	1	42.3	9.5	142.3
4	1.00E+05	(6)	1.60E+06	(96)	60	29	6	6.6	2.3	14.6

5	5.67E+05	(17)	2.97E+06	(89)	30	54	12	19.9	11.0	33.5
6	4.12E+05	(7)	1.65E+06	(28)	17	30	11	26.3	9.5	60.5
7	0.00E+00	(0)	1.73E+05	(9)	52	3	2	8.3	0.3	52.3
8	6.00E+04	(3)	2.40E+05	(12)	50	4	2	26.9	4.7	95.4
9	5.00E+05	(6)	3.92E+06	(47)	12	72	21	13.5	4.6	31.0
10	5.00E+05	(8)	3.00E+06	(48)	16	55	16	17.6	7.1	36.8
11	6.25E+04	(1)	2.25E+06	(36)	16	41	14	3.3	0.1	17.1
12	4.38E+05	(7)	9.38E+05	(15)	16	17	9	48.8	16.7	124.9
13	4.00E+05	(10)	2.60E+06	(65)	25	48	12	16.2	7.3	31.2
14	2.92E+05	(19)	1.97E+06	(128)	65	36	6	15.5	9.0	25.0
15	1.46E+06	(35)	3.50E+06	(84)	24	64	14	43.2	28.2	64.6
16	7.50E+05	(6)	1.88E+06	(15)	8	34	17	42.0	13.2	112.2
17	5.33E+05	(16)	2.43E+06	(73)	30	45	10	22.9	12.3	39.3
18	4.58E+05	(22)	3.38E+06	(162)	48	62	10	14.2	8.6	22.0
19	0.00E+00	(0)	1.73E+06	(109)	63	32	6	0.7	0.0	3.6
20	2.94E+04	(2)	7.65E+05	(52)	68	14	4	4.3	0.5	15.1
21	3.57E+04	(1)	1.07E+05	(3)	28	2	2	37.5	0.7	416.8
22	1.79E+05	(5)	1.93E+06	(54)	28	35	10	9.9	3.0	23.8
23	6.67E+04	(2)	1.23E+06	(37)	30	23	7	6.0	0.7	21.7
24	6.67E+04	(4)	1.23E+06	(74)	60	23	5	5.8	1.5	15.0
25	3.33E+05	(8)	4.17E+05	(10)	24	8	5	82.8	28.4	229.4
26	2.40E+05	(12)	1.76E+06	(88)	50	32	7	14.3	7.0	25.9
27	5.56E+04	(1)	6.11E+05	(11)	18	11	7	10.6	0.2	64.6
28	1.17E+06	(7)	1.67E+05	(1)	6	3	5	617.1	92.5	11630.7
29	2.00E+06	(20)	7.00E+05	(7)	10	13	9	285.5	119.2	780.4
30	2.50E+05	(4)	6.88E+05	(11)	16	13	7	38.5	8.7	126.1
31	6.00E+05	(18)	2.67E+05	(8)	30	5	3	226.7	95.7	592.3
32	5.00E+04	(3)	1.13E+06	(68)	60	21	5	4.8	0.9	13.9
33	1.29E+06	(18)	3.64E+06	(51)	14	67	19	36.7	20.1	63.5
34	4.44E+05	(8)	2.89E+06	(52)	18	53	15	16.2	6.5	33.8
35	2.34E+05	(11)	9.79E+05	(46)	47	18	5	25.0	11.6	48.5
36	2.00E+05	(4)	1.25E+06	(25)	20	23	9	17.1	4.2	47.9
37	1.43E+05	(6)	4.05E+05	(17)	42	7	4	37.1	11.8	96.6
38	2.50E+05	(3)	2.42E+06	(29)	12	44	16	11.2	2.1	34.5
39	9.52E+04	(2)	8.57E+05	(18)	21	16	7	12.3	1.3	48.0
40	4.17E+04	(1)	8.33E+04	(2)	24	2	2	54.9	0.9	926.3
41	2.50E+05	(4)	3.69E+06	(59)	16	67	18	7.3	1.9	19.0
42	3.75E+05	(3)	5.00E+05	(4)	8	9	9	78.3	11.4	444.2
43	4.00E+05	(6)	1.80E+06	(27)	15	33	13	23.5	7.8	56.8
44	4.76E+04	(5)	1.90E+05	(20)	105	3	2	26.5	7.6	70.8
45	4.38E+05	(7)	2.44E+06	(39)	16	45	14	18.9	7.0	42.0
46	6.67E+05	(4)	1.67E+05	(1)	6	3	5	365.5	40.9	9203.3
47	2.92E+05	(7)	4.17E+04	(1)	24	1	1	617.1	92.5	11630.7
48	0.00E+00	(0)	2.89E+05	(11)	38	5	3	6.7	0.2	41.2
49	1.82E+05	(6)	2.82E+06	(93)	33	52	11	6.9	2.4	15.1
50	1.25E+05	(2)	8.13E+05	(13)	16	15	8	17.0	1.7	70.1
51	1.67E+05	(1)	3.33E+05	(2)	6	6	8	54.9	0.9	926.3
52	3.00E+05	(3)	4.00E+05	(4)	10	7	7	78.3	11.4	444.2
53	6.67E+05	(6)	2.56E+06	(23)	9	47	19	27.5	9.0	68.0
54	3.75E+05	(9)	1.04E+06	(25)	24	19	8	37.7	15.3	82.2
55	1.43E+04	(1)	1.57E+05	(11)	70	3	2	10.6	0.2	64.6
56	0.00E+00	(0)	2.33E+05	(17)	73	4	2	4.3	0.2	25.1
57	1.40E+05	(7)	5.20E+05	(26)	50	10	4	28.3	10.2	65.7
58	5.56E+04	(1)	3.33E+05	(6)	18	6	5	19.3	0.4	140.9

59	2.16E+05	(11)	3.33E+05	(17)	51	6	3	67.1	28.3	150.2
60	1.00E+05	(2)	9.50E+05	(19)	20	17	8	11.7	1.2	45.1
61	3.75E+05	(6)	5.00E+05	(8)	16	9	6	77.8	22.2	250.8
62	8.33E+04	(1)	8.33E+04	(1)	12	2	2	102.9	1.3	5264.1
63	1.25E+06	(15)	5.83E+05	(7)	12	11	8	215.8	84.7	614.3
64	7.32E+04	(3)	1.12E+06	(46)	41	21	6	7.1	1.3	21.0
65	2.88E+05	(19)	5.14E+06	(339)	66	94	11	5.9	3.5	9.2
66	1.43E+05	(1)	2.14E+06	(15)	7	39	20	7.8	0.2	44.8
67	6.25E+04	(1)	5.63E+05	(9)	16	10	7	13.0	0.3	82.7
68	1.50E+05	(3)	2.20E+06	(44)	20	40	12	7.4	1.4	22.0
69	4.17E+05	(10)	2.17E+06	(52)	24	40	11	20.2	9.0	39.6
70	1.39E+05	(5)	1.11E+06	(40)	36	20	6	13.3	4.0	32.8
71	9.17E+05	(11)	2.50E+05	(3)	12	5	5	356.3	99.6	1835.1
72	3.00E+05	(6)	2.55E+06	(51)	20	47	13	12.5	4.3	28.4
73	2.40E+05	(12)	2.48E+06	(124)	50	45	8	10.2	5.0	18.2
74	6.67E+05	(6)	3.33E+05	(3)	9	6	7	199.1	44.1	1169.2
75	7.50E+05	(12)	9.94E+06	(159)	16	182	29	7.9	4.0	14.1
76	1.85E+05	(5)	9.26E+05	(25)	27	17	7	21.2	6.2	55.0
77	1.00E+05	(5)	9.80E+05	(49)	50	18	5	10.9	3.3	26.4
78	2.50E+05	(2)	6.50E+06	(52)	8	119	33	4.3	0.5	15.1
79	5.56E+04	(1)	6.67E+05	(12)	18	12	7	9.8	0.2	58.2
80	1.00E+06	(6)	3.00E+06	(18)	6	55	26	35.1	11.2	90.3
81	0.00E+00	(0)	4.07E+05	(11)	27	7	4	6.7	0.2	41.2
82	4.44E+05	(8)	9.44E+05	(17)	18	17	8	49.1	18.2	118.3
83	8.33E+04	(1)	1.25E+06	(15)	12	23	12	7.8	0.2	44.8
84	1.65E+05	(13)	2.30E+06	(182)	79	42	6	7.5	3.9	13.0
85	3.33E+05	(6)	2.22E+05	(4)	18	4	4	151.8	36.8	709.1
86	1.25E+05	(3)	1.21E+06	(29)	24	22	8	11.2	2.1	34.5
87	6.00E+04	(3)	1.20E+05	(6)	50	2	2	52.9	8.4	238.4
88	2.80E+05	(14)	3.04E+06	(152)	50	56	9	9.6	5.1	16.5
89	1.88E+05	(3)	4.38E+05	(7)	16	8	6	45.6	7.4	191.9
90	8.33E+04	(2)	4.58E+05	(11)	24	8	5	20.0	2.0	85.9
91	2.22E+05	(2)	5.33E+06	(48)	9	98	28	4.6	0.5	16.5
92	1.37E+04	(1)	5.07E+05	(37)	73	9	3	3.2	0.1	16.6
93	1.50E+05	(6)	1.93E+06	(77)	40	35	8	8.3	2.9	18.4
94	4.44E+05	(12)	1.78E+06	(48)	27	33	9	26.1	12.5	49.4
95	4.17E+04	(1)	8.33E+04	(2)	24	2	2	54.9	0.9	926.3
96	1.11E+05	(4)	3.06E+05	(11)	36	6	3	38.5	8.7	126.1
97	1.25E+05	(1)	5.00E+05	(4)	8	9	9	28.5	0.5	256.9
98	2.67E+05	(4)	1.27E+06	(19)	15	23	11	22.5	5.4	65.4
99	9.17E+05	(22)	6.13E+06	(147)	24	112	19	15.6	9.4	24.4
100	3.08E+05	(12)	2.92E+06	(114)	39	53	10	11.0	5.5	19.8
101	1.50E+05	(9)	1.75E+06	(105)	60	32	6	9.0	4.0	17.5
102	6.25E+04	(1)	1.13E+06	(18)	16	21	10	6.5	0.1	36.4
103	2.50E+05	(10)	3.35E+06	(134)	40	61	11	7.9	3.6	14.7

OP1522 (Olympics) sedimentary bedrock, (Counted by Sarah Falkowski Nov. 2016)
EFFECTIVE TRACK DENSITY FOR FLUENCE MONITOR (tracks/cm^2): 8.180E+05
RELATIVE ERROR (%): 1.48
EFFECTIVE URANIUM CONTENT OF MONITOR (ppm): 15.00
ZETA FACTOR AND STANDARD ERROR (yr cm^2): 252.90 5.00
SIZE OF COUNTER SQUARE (cm^2): 1.000E-06

Grain	**RhoS**	**(Ns)**	**RhoI**	**(Ni)**	**Squares**	**U+/-2s**	**Grain**	**Age (Ma)**

no.	(cm^-2)		(cm^-2)					Age	--95% CI--	
1	5.00E+05	(12)	2.88E+06	(69)	24	53	13	18.2	8.9	33.4
2	5.00E+05	(12)	1.63E+06	(39)	24	30	10	32.0	15.1	61.8
3	3.50E+05	(7)	3.00E+05	(6)	20	6	4	119.1	34.6	420.8
4	7.14E+04	(5)	1.34E+06	(94)	70	25	5	5.7	1.7	13.3
5	6.67E+04	(3)	2.22E+04	(1)	45	0	1	278.7	24.9	8126.1
6	4.76E+04	(2)	2.38E+04	(1)	42	0	1	191.5	10.8	6849.2
7	1.55E+06	(62)	3.40E+06	(136)	40	62	11	47.1	34.2	63.9
8	5.94E+05	(19)	1.50E+06	(48)	32	28	8	41.0	22.7	70.6
9	3.70E+04	(1)	3.70E+04	(1)	27	1	1	102.6	1.3	5255.3
10	4.05E+05	(17)	3.10E+05	(13)	42	6	3	133.5	61.5	296.1
11	3.33E+04	(1)	1.67E+05	(5)	30	3	3	22.9	0.4	182.3
12	5.00E+05	(27)	2.30E+06	(124)	54	42	8	22.6	14.2	34.3
13	2.50E+04	(1)	2.50E+04	(1)	40	0	1	102.6	1.3	5255.3
14	6.00E+05	(12)	1.65E+06	(33)	20	30	10	37.8	17.7	74.4
15	1.18E+06	(71)	3.45E+06	(207)	60	63	9	35.5	27.1	46.7
16	1.00E+06	(35)	2.54E+06	(89)	35	47	10	40.7	26.6	60.6
17	1.85E+04	(1)	5.56E+04	(3)	54	1	1	37.5	0.7	415.8
18	1.48E+05	(8)	5.74E+05	(31)	54	11	4	27.0	10.6	59.1
19	2.67E+05	(8)	2.33E+05	(7)	30	4	3	116.8	37.3	372.2
20	1.39E+06	(39)	2.29E+06	(64)	28	42	11	62.8	41.0	94.7

OP1527 (Olympics) sedimentary bedrock, (Counted by Sarah Falkowski Nov. 2016)
EFFECTIVE TRACK DENSITY FOR FLUENCE MONITOR (tracks/cm^2): 8.170E+05
RELATIVE ERROR (%): 1.48
EFFECTIVE URANIUM CONTENT OF MONITOR (ppm): 15.00
ZETA FACTOR AND STANDARD ERROR (yr cm^2): 252.90 5.00
SIZE OF COUNTER SQUARE (cm^2): 1.000E-06

Grain no.	RhoS (cm^-2)	(Ns)	RhoI (cm^-2)	(Ni)	Squares	U+/-2s		Grain Age (Ma) Age	--95% CI--	
1	1.19E+05	(5)	1.19E+06	(50)	42	22	6	10.6	3.2	25.7
2	1.14E+05	(4)	1.60E+06	(56)	35	29	8	7.7	1.9	20.0
3	2.50E+05	(5)	3.00E+06	(60)	20	55	14	8.9	2.7	21.2
4	1.22E+05	(11)	8.22E+05	(74)	90	15	4	15.5	7.3	29.1
5	5.00E+04	(3)	5.00E+05	(30)	60	9	3	10.8	2.0	33.2
6	1.29E+05	(9)	1.50E+06	(105)	70	28	5	9.0	3.9	17.5
7	7.20E+05	(36)	1.76E+06	(88)	50	32	7	42.2	27.8	62.7
8	1.67E+05	(8)	1.83E+06	(88)	48	34	7	9.6	3.9	19.3
9	1.79E+05	(5)	1.96E+06	(55)	28	36	10	9.7	2.9	23.2
10	4.38E+05	(14)	1.13E+06	(36)	32	21	7	40.3	20.0	75.9
11	2.14E+05	(6)	8.21E+05	(23)	28	15	6	27.4	9.0	67.8
12	5.00E+05	(6)	1.58E+06	(19)	12	29	13	33.1	10.7	84.5
13	2.00E+05	(4)	3.35E+06	(67)	20	62	15	6.4	1.6	16.5
14	2.50E+05	(8)	2.63E+06	(84)	32	48	11	10.0	4.1	20.3
15	7.50E+04	(3)	2.13E+06	(85)	40	39	9	3.8	0.7	11.0
16	3.57E+04	(1)	4.29E+05	(12)	28	8	4	9.7	0.2	58.0
17	5.56E+04	(2)	1.33E+06	(48)	36	24	7	4.6	0.5	16.4
18	8.57E+04	(3)	3.49E+06	(122)	35	64	12	2.7	0.5	7.6
19	4.69E+05	(15)	2.56E+06	(82)	32	47	10	19.0	10.1	33.0
20	1.88E+05	(15)	1.08E+06	(86)	80	20	4	18.2	9.7	31.4
21	2.33E+05	(7)	4.47E+06	(134)	30	82	14	5.5	2.1	11.4
22	8.33E+04	(2)	2.42E+06	(58)	24	44	12	3.8	0.4	13.5
23	2.00E+05	(4)	3.50E+05	(7)	20	6	5	59.7	12.7	228.2

24	3.50E+05	(7)	2.00E+06	(40)	20	37	12	18.4	6.8	40.7
25	2.50E+05	(4)	2.31E+06	(37)	16	42	14	11.6	2.9	31.0
26	1.67E+05	(2)	8.33E+04	(1)	12	2	2	191.3	10.7	6844.0
27	1.25E+05	(5)	1.58E+06	(63)	40	29	7	8.4	2.6	20.1
28	1.57E+05	(11)	1.61E+06	(113)	70	30	6	10.2	4.9	18.7
29	1.20E+05	(3)	3.00E+06	(75)	25	55	13	4.3	0.8	12.5
30	4.00E+05	(24)	2.60E+06	(156)	60	48	8	16.0	9.9	24.5
31	3.75E+04	(3)	1.09E+06	(87)	80	20	4	3.7	0.7	10.8
32	1.00E+05	(1)	1.00E+05	(1)	10	2	3	102.5	1.3	5250.9
33	6.67E+05	(12)	5.56E+04	(1)	18	1	2	1012.1	180.8	14321.3
34	3.33E+05	(8)	2.13E+06	(51)	24	39	11	16.5	6.6	34.3
35	0.00E+00	(0)	7.14E+04	(1)	14	1	2	102.5	2.6	3130.2
36	2.14E+05	(6)	2.68E+06	(75)	28	49	11	8.5	2.9	18.8
37	8.33E+04	(2)	4.17E+04	(1)	24	1	1	191.3	10.7	6844.0
38	2.22E+05	(2)	1.22E+06	(11)	9	22	13	19.9	2.0	85.5
39	8.33E+04	(2)	1.29E+06	(31)	24	24	8	7.1	0.8	26.2
40	4.00E+05	(8)	5.80E+06	(116)	20	106	20	7.3	3.0	14.5
41	4.67E+05	(7)	8.27E+06	(124)	15	152	28	6.0	2.3	12.4
42	1.00E+05	(1)	1.40E+06	(14)	10	26	14	8.4	0.2	48.3
43	6.80E+05	(34)	3.72E+06	(186)	50	68	10	18.9	12.7	27.3
44	2.50E+05	(3)	3.67E+06	(44)	12	67	20	7.4	1.4	22.0
45	4.17E+05	(5)	6.58E+06	(79)	12	121	27	6.7	2.1	15.9
46	1.07E+05	(3)	1.39E+06	(39)	28	26	8	8.3	1.6	25.0
47	6.67E+05	(20)	8.27E+06	(248)	30	152	20	8.4	5.0	13.2
48	6.00E+05	(6)	1.05E+07	(105)	10	193	38	6.1	2.1	13.3
49	3.33E+05	(2)	1.50E+06	(9)	6	28	18	24.3	2.4	110.0
50	8.33E+04	(2)	4.17E+04	(1)	24	1	1	191.3	10.7	6844.0
51	1.00E+05	(2)	2.35E+06	(47)	20	43	13	4.7	0.5	16.8
52	5.00E+05	(3)	5.00E+05	(3)	6	9	10	102.5	13.8	728.8
53	2.50E+05	(5)	1.15E+06	(23)	20	21	9	23.0	6.7	60.2
54	2.50E+05	(2)	3.25E+06	(26)	8	60	23	8.5	0.9	31.7
55	1.67E+05	(3)	1.72E+06	(31)	18	32	11	10.5	2.0	32.0
56	3.33E+05	(3)	1.11E+05	(1)	9	2	3	278.4	24.8	8120.4
57	1.33E+05	(2)	1.40E+06	(21)	15	26	11	10.5	1.1	40.2
58	1.27E+06	(19)	2.00E+06	(30)	15	37	13	65.3	34.7	119.1
59	0.00E+00	(0)	3.00E+05	(6)	20	6	4	12.6	0.4	87.2
60	5.56E+04	(2)	1.72E+06	(62)	36	32	8	3.6	0.4	12.6
61	1.83E+05	(11)	2.77E+06	(166)	60	51	8	6.9	3.3	12.6
62	2.59E+05	(7)	2.37E+06	(64)	27	44	11	11.5	4.4	24.6
63	3.78E+05	(17)	1.96E+06	(88)	45	36	8	20.1	11.1	33.7
64	3.33E+05	(2)	2.00E+06	(12)	6	37	21	18.3	1.9	76.9
65	5.00E+05	(3)	1.33E+06	(8)	6	24	17	39.9	6.6	159.5
66	3.75E+05	(21)	1.46E+06	(82)	56	27	6	26.6	15.5	43.1
67	4.17E+04	(1)	1.13E+06	(27)	24	21	8	4.4	0.1	23.2
68	1.67E+05	(2)	2.67E+06	(32)	12	49	17	6.9	0.7	25.3
69	3.33E+05	(8)	1.75E+06	(42)	24	32	10	20.0	8.0	42.3
70	1.85E+05	(5)	1.15E+06	(31)	27	21	8	17.1	5.1	43.1
71	4.29E+05	(6)	2.50E+06	(35)	14	46	15	18.1	6.1	42.4
72	2.83E+05	(17)	2.00E+06	(120)	60	37	7	14.7	8.2	24.4
73	1.88E+05	(3)	1.50E+06	(24)	16	28	11	13.5	2.5	42.4
74	6.67E+04	(1)	1.20E+06	(18)	15	22	10	6.5	0.1	36.3
75	8.89E+05	(8)	4.67E+06	(42)	9	86	26	20.0	8.0	42.3
76	2.50E+05	(3)	5.00E+05	(6)	12	9	7	52.8	8.4	237.5
77	4.08E+04	(2)	8.98E+05	(44)	49	16	5	5.0	0.6	18.0

78	2.20E+05	(11)	1.60E+05	(8)	50	3	2	139.8	51.8	394.7
79	3.33E+04	(2)	6.67E+04	(4)	60	1	1	53.3	4.7	350.8
80	4.17E+05	(15)	6.39E+05	(23)	36	12	5	67.3	32.6	133.5
81	6.25E+05	(20)	1.50E+06	(48)	32	28	8	43.1	24.1	73.6
82	5.43E+05	(38)	2.29E+05	(16)	70	4	2	239.4	132.1	455.2
83	6.67E+04	(2)	2.00E+05	(6)	30	4	3	36.1	3.4	189.8
84	1.00E+05	(2)	3.30E+06	(66)	20	61	15	3.4	0.4	11.8
85	1.67E+05	(2)	1.25E+06	(15)	12	23	12	14.7	1.5	59.0
86	2.14E+05	(9)	1.05E+06	(44)	42	19	6	21.4	9.1	43.7
87	5.56E+04	(2)	4.17E+05	(15)	36	8	4	14.7	1.5	59.0
88	3.50E+05	(7)	1.05E+06	(21)	20	19	8	34.9	12.3	83.6
89	9.26E+04	(5)	2.93E+06	(158)	54	54	9	3.4	1.0	7.8
90	8.33E+04	(3)	3.61E+05	(13)	36	7	4	24.8	4.4	86.2
91	2.00E+05	(6)	1.87E+06	(56)	30	34	9	11.3	3.9	25.6
92	2.50E+05	(6)	3.08E+06	(74)	24	57	13	8.6	3.0	19.1
93	2.86E+05	(6)	1.81E+06	(38)	21	33	11	16.7	5.6	38.8
94	8.33E+04	(1)	1.58E+06	(19)	12	29	13	6.2	0.1	34.1
95	2.00E+05	(12)	2.13E+06	(128)	60	39	7	9.8	4.9	17.5
96	0.00E+00	(0)	1.94E+05	(7)	36	4	3	10.7	0.4	71.3
97	2.08E+04	(1)	2.29E+05	(11)	48	4	2	10.6	0.2	64.3
98	3.67E+05	(11)	2.13E+06	(64)	30	39	10	18.0	8.4	33.9
99	9.68E+04	(3)	1.77E+06	(55)	31	33	9	5.9	1.1	17.3
100	8.33E+05	(15)	2.17E+06	(39)	18	40	13	39.9	20.3	73.4
101	6.60E+05	(33)	5.54E+06	(277)	50	102	13	12.4	8.3	17.7
102	2.00E+05	(3)	3.00E+06	(45)	15	55	16	7.2	1.4	21.4
103	7.41E+04	(4)	8.15E+05	(44)	54	15	5	9.7	2.4	25.8

OP1528 (Olympics) sedimentary bedrock, Counted by Sarah Falkowski May 2017
EFFECTIVE TRACK DENSITY FOR FLUENCE MONITOR (tracks/cm^2): 9.280E+05
RELATIVE ERROR (%): 1.51
EFFECTIVE URANIUM CONTENT OF MONITOR (ppm): 15.00
ZETA FACTOR AND STANDARD ERROR (yr cm^2): 261.20 6.80
SIZE OF COUNTER SQUARE (cm^2): 1.000E-06

Grain no.	RhoS (cm^-2)	(Ns)	RhoI (cm^-2)	(Ni)	Squares	U+/-2s		Grain Age	Age (Ma) --95%	CI--
1	1.20E+05	(3)	1.20E+06	(30)	25	19	7	12.7	2.4	38.9
2	2.00E+05	(2)	1.00E+05	(1)	10	2	3	223.9	12.6	7536.3
3	0.00E+00	(0)	3.33E+05	(2)	6	5	7	50.0	1.5	615.2
4	8.33E+04	(4)	1.02E+06	(49)	48	17	5	10.3	2.6	27.0
5	3.13E+04	(1)	8.13E+05	(26)	32	13	5	5.3	0.1	28.3
6	1.71E+05	(6)	1.40E+06	(49)	35	23	6	15.2	5.2	34.6
7	0.00E+00	(0)	2.89E+06	(101)	35	47	9	0.8	0.0	4.5
8	0.00E+00	(0)	3.27E+06	(157)	48	53	9	0.5	0.0	2.9
9	3.70E+04	(1)	5.93E+05	(16)	27	10	5	8.6	0.2	48.6
10	1.25E+05	(2)	8.13E+05	(13)	16	13	7	19.8	2.0	81.9
11	8.33E+04	(3)	2.50E+05	(9)	36	4	3	41.7	7.0	160.0
12	2.50E+05	(7)	1.54E+06	(43)	28	25	8	20.1	7.5	44.1
13	1.20E+05	(3)	2.16E+06	(54)	25	35	10	7.1	1.3	20.7
14	2.33E+05	(7)	3.73E+06	(112)	30	60	12	7.7	3.0	16.1
15	4.25E+05	(17)	4.30E+06	(172)	40	70	11	12.1	6.8	19.7
16	2.29E+05	(8)	4.49E+06	(157)	35	73	12	6.3	2.6	12.5
17	1.25E+05	(5)	2.23E+06	(89)	40	36	8	7.0	2.2	16.5
18	4.00E+04	(1)	4.80E+05	(12)	25	8	4	11.4	0.2	67.9

19	0.00E+00	(0)	1.25E+05	(5)	40	2	2	18.0	0.6	131.0
20	6.67E+04	(4)	2.83E+06	(170)	60	46	7	3.0	0.8	7.4
21	6.67E+04	(2)	5.00E+05	(15)	30	8	4	17.2	1.8	69.2
22	1.00E+05	(5)	9.00E+05	(45)	50	15	4	13.8	4.2	33.8
23	1.00E+05	(5)	3.94E+06	(197)	50	64	9	3.2	1.0	7.3
24	6.90E+04	(6)	2.69E+06	(234)	87	43	6	3.2	1.1	6.9
25	0.00E+00	(0)	7.30E+05	(73)	100	12	3	1.2	0.0	6.3
26	4.17E+04	(1)	1.00E+06	(24)	24	16	7	5.7	0.1	30.9
27	0.00E+00	(0)	2.22E+05	(10)	45	4	2	8.7	0.3	53.9
28	8.33E+04	(3)	2.69E+06	(97)	36	44	9	3.9	0.8	11.3
29	1.11E+05	(2)	5.00E+06	(90)	18	81	17	2.9	0.3	10.0
30	7.50E+04	(3)	2.18E+06	(87)	40	35	8	4.4	0.8	12.6
31	6.25E+05	(20)	1.05E+07	(335)	32	169	19	7.3	4.4	11.4
32	7.14E+04	(5)	1.07E+06	(75)	70	17	4	8.3	2.5	19.7
33	2.50E+04	(1)	3.00E+05	(12)	40	5	3	11.4	0.2	67.9
34	2.08E+05	(5)	2.71E+06	(65)	24	44	11	9.6	2.9	22.9
35	1.00E+05	(3)	2.37E+06	(71)	30	38	9	5.4	1.0	15.6
36	1.25E+05	(3)	2.50E+06	(60)	24	40	10	6.4	1.2	18.6
37	1.25E+05	(7)	3.59E+06	(201)	56	58	8	4.3	1.7	8.9
38	6.67E+04	(2)	8.00E+05	(24)	30	13	5	10.8	1.2	40.6
39	2.50E+05	(5)	3.40E+06	(68)	20	55	13	9.2	2.8	21.8
40	3.33E+04	(3)	4.33E+05	(39)	90	7	2	9.8	1.8	29.3
41	5.00E+05	(10)	7.55E+06	(151)	20	122	20	8.1	3.8	15.2
42	0.00E+00	(0)	9.52E+04	(4)	42	2	1	22.9	0.8	181.1
43	4.00E+05	(8)	8.65E+06	(173)	20	140	22	5.7	2.4	11.3
44	3.75E+05	(21)	2.20E+06	(123)	56	36	6	20.8	12.3	33.0
45	4.17E+04	(2)	8.33E+05	(40)	48	13	4	6.5	0.7	23.3

OP1531 (Olympics) sedimentary bedrock, (Counted by Sarah Falkowski Nov. 2016)
EFFECTIVE TRACK DENSITY FOR FLUENCE MONITOR (tracks/cm^2): 8.150E+05
RELATIVE ERROR (%): 1.48
EFFECTIVE URANIUM CONTENT OF MONITOR (ppm): 15.00
ZETA FACTOR AND STANDARD ERROR (yr cm^2): 252.90 5.00
SIZE OF COUNTER SQUARE (cm^2): 1.000E-06

Grain no.	RhoS (cm^-2)	(Ns)	RhoI (cm^-2)	(Ni)	Squares	U+/-2s		Grain Age	Age (Ma) --95%	CI--
1	9.60E+05	(24)	6.40E+05	(16)	25	12	6	152.3	78.3	304.3
2	3.00E+05	(12)	1.55E+06	(62)	40	29	7	20.1	9.8	37.3
3	1.44E+05	(13)	6.11E+05	(55)	90	11	3	24.5	12.2	45.0
4	4.00E+05	(20)	1.06E+06	(53)	50	20	5	39.0	22.0	65.9
5	4.69E+04	(3)	1.56E+05	(10)	64	3	2	32.0	5.5	119.0
6	4.94E+04	(4)	1.48E+05	(12)	81	3	2	35.2	8.1	112.4
7	3.13E+04	(1)	5.94E+05	(19)	32	11	5	6.2	0.1	34.0
8	2.86E+04	(2)	7.14E+04	(5)	70	1	1	42.9	3.9	247.1
9	1.09E+06	(76)	7.37E+06	(516)	70	136	13	15.2	11.9	19.5
10	1.67E+05	(4)	9.58E+05	(23)	24	18	7	18.5	4.5	52.3
11	2.50E+05	(3)	1.08E+06	(13)	12	20	11	24.7	4.3	86.0
12	4.79E+05	(23)	3.23E+06	(155)	48	59	10	15.4	9.4	23.8
13	8.89E+04	(8)	1.11E+05	(10)	90	2	1	82.3	28.2	228.1
14	1.07E+05	(6)	1.59E+06	(89)	56	29	6	7.1	2.5	15.7
15	2.50E+05	(6)	4.54E+06	(109)	24	84	16	5.8	2.0	12.7
16	2.14E+05	(6)	2.04E+06	(57)	28	37	10	11.1	3.8	25.1
17	4.00E+04	(4)	1.80E+05	(18)	100	3	2	23.6	5.6	69.2

18	8.57E+04	(6)	1.39E+06	(97)	70	26	5	6.5	2.3	14.4
19	2.50E+05	(25)	2.57E+06	(257)	100	47	6	10.1	6.4	15.1
20	1.83E+05	(11)	1.93E+06	(116)	60	36	7	9.9	4.7	18.1
21	3.40E+05	(17)	1.00E+05	(5)	50	2	2	333.9	122.8	1113.3
22	1.67E+04	(1)	2.83E+05	(17)	60	5	2	6.9	0.1	38.6
23	1.10E+06	(22)	1.30E+06	(26)	20	24	9	86.7	46.9	158.2
24	2.83E+05	(17)	2.15E+06	(129)	60	40	7	13.7	7.7	22.6
25	2.50E+04	(1)	3.50E+05	(14)	40	6	3	8.3	0.2	48.2
26	4.60E+05	(23)	7.02E+06	(351)	50	129	14	6.8	4.2	10.3
27	9.00E+04	(9)	3.30E+05	(33)	100	6	2	28.4	11.8	59.8
28	5.67E+05	(34)	5.47E+06	(328)	60	101	11	10.7	7.3	15.2
29	4.44E+04	(4)	3.89E+05	(35)	90	7	2	12.2	3.0	32.9
30	3.75E+05	(15)	3.23E+06	(129)	40	59	11	12.1	6.5	20.5
31	6.67E+04	(4)	1.17E+05	(7)	60	2	2	59.6	12.6	227.7
32	7.50E+04	(6)	2.50E+05	(20)	80	5	2	31.4	10.1	79.4
33	4.00E+04	(4)	6.70E+05	(67)	100	12	3	6.4	1.6	16.5
34	1.00E+05	(8)	1.34E+06	(107)	80	25	5	7.8	3.2	15.7
35	1.11E+05	(10)	9.00E+05	(81)	90	17	4	12.9	5.9	24.6
36	3.88E+05	(31)	3.53E+06	(282)	80	65	8	11.4	7.5	16.5
37	5.00E+04	(4)	2.88E+05	(23)	80	5	2	18.5	4.5	52.3
38	2.50E+05	(20)	1.11E+06	(89)	80	20	4	23.3	13.5	37.9
39	5.75E+05	(23)	2.60E+06	(104)	40	48	9	22.9	13.8	36.0
40	1.25E+05	(2)	2.50E+05	(4)	16	5	4	53.2	4.7	350.0
41	1.58E+06	(19)	2.50E+05	(3)	12	5	5	596.6	189.2	2759.8
42	5.25E+05	(21)	2.15E+06	(86)	40	40	9	25.3	14.8	40.8
43	5.50E+05	(11)	8.65E+06	(173)	20	159	25	6.6	3.2	12.0
44	2.00E+05	(16)	2.19E+06	(175)	80	40	6	9.5	5.3	15.7
45	1.70E+05	(17)	1.50E+06	(150)	100	28	5	11.8	6.6	19.3
46	5.75E+05	(23)	1.80E+06	(72)	40	33	8	33.0	19.6	53.1
47	1.67E+05	(10)	2.02E+06	(121)	60	37	7	8.6	4.0	16.2
48	1.20E+05	(3)	3.60E+05	(9)	25	7	4	35.4	6.0	136.3
49	1.04E+05	(5)	1.04E+06	(50)	48	19	5	10.6	3.2	25.7
50	9.38E+04	(3)	1.56E+05	(5)	32	3	2	62.8	9.6	310.3
51	3.67E+05	(22)	6.67E+05	(40)	60	12	4	56.6	32.0	97.1
52	1.43E+05	(3)	2.86E+05	(6)	21	5	4	52.6	8.3	237.0
53	5.00E+05	(15)	3.00E+05	(9)	30	6	4	168.3	70.0	430.7
54	1.80E+05	(9)	1.44E+06	(72)	50	27	6	13.1	5.7	25.8
55	4.08E+04	(2)	5.51E+05	(27)	49	10	4	8.2	0.9	30.3
56	6.67E+04	(2)	5.00E+05	(15)	30	9	5	14.6	1.5	58.8
57	9.00E+04	(9)	1.30E+06	(130)	100	24	4	7.3	3.2	14.0
58	6.50E+05	(13)	1.40E+06	(28)	20	26	10	48.0	22.7	94.8
59	1.22E+05	(11)	8.89E+05	(80)	90	16	4	14.3	6.8	26.7
60	2.00E+05	(9)	1.27E+06	(57)	45	23	6	16.5	7.1	33.1
61	1.40E+05	(14)	3.50E+05	(35)	100	6	2	41.4	20.4	78.2
62	1.11E+05	(4)	3.61E+05	(13)	36	7	4	32.5	7.5	101.9
63	5.71E+04	(4)	1.86E+05	(13)	70	3	2	32.5	7.5	101.9
64	7.14E+04	(3)	1.05E+06	(44)	42	19	6	7.4	1.4	21.9
65	5.71E+05	(40)	6.47E+06	(453)	70	119	12	9.1	6.4	12.6
66	1.25E+05	(9)	3.33E+05	(24)	72	6	2	39.0	15.8	85.6
67	6.25E+04	(2)	2.81E+05	(9)	32	5	3	24.2	2.4	109.8
68	6.25E+04	(1)	6.25E+04	(1)	16	1	2	102.2	1.3	5242.1
69	3.93E+05	(11)	8.57E+05	(24)	28	16	6	47.4	20.8	99.5
70	3.33E+05	(12)	1.11E+06	(40)	36	20	6	31.1	14.7	59.9
71	1.00E+05	(10)	9.50E+05	(95)	100	17	4	11.0	5.0	20.8

72	1.67E+05	(2)	1.58E+06	(19)	12	29	13	11.6	1.2	44.8
73	1.50E+05	(6)	4.00E+05	(16)	40	7	4	39.2	12.4	103.2
74	1.88E+05	(15)	5.13E+05	(41)	80	9	3	37.9	19.3	69.3
75	2.89E+05	(13)	3.49E+06	(157)	45	64	10	8.6	4.4	15.0
76	5.83E+05	(35)	1.55E+06	(93)	60	29	6	38.8	25.4	57.6
77	2.50E+04	(1)	2.75E+05	(11)	40	5	3	10.6	0.2	64.2
78	5.40E+05	(27)	4.56E+06	(228)	50	84	11	12.3	7.9	18.2
79	2.08E+05	(10)	2.06E+06	(99)	48	38	8	10.6	4.8	19.9
80	2.50E+05	(6)	8.33E+04	(2)	24	2	2	288.0	55.0	2553.3
81	4.81E+05	(13)	1.33E+06	(36)	27	25	8	37.4	18.1	71.5
82	3.33E+05	(2)	5.00E+05	(3)	6	9	10	70.0	5.7	573.6
83	1.25E+05	(4)	9.38E+04	(3)	32	2	2	134.3	23.2	876.0
84	3.29E+05	(23)	1.47E+06	(103)	70	27	5	23.1	13.9	36.4
85	1.02E+05	(5)	2.24E+05	(11)	49	4	2	47.5	12.7	144.7
86	4.17E+04	(3)	2.78E+05	(20)	72	5	2	16.1	2.9	51.9
87	1.35E+06	(27)	6.60E+06	(132)	20	121	21	21.1	13.4	32.0
88	1.00E+05	(9)	3.67E+05	(33)	90	7	2	28.4	11.8	59.8
89	4.94E+04	(4)	5.19E+05	(42)	81	10	3	10.2	2.6	27.0
90	4.00E+04	(4)	3.20E+05	(32)	100	6	2	13.3	3.3	36.2
91	1.60E+06	(64)	9.25E+05	(37)	40	17	6	175.5	115.9	269.5
92	1.60E+06	(64)	6.38E+06	(255)	40	117	15	26.0	19.7	34.2
93	4.00E+05	(12)	2.83E+06	(85)	30	52	11	14.7	7.2	26.7
94	3.33E+05	(10)	3.33E+04	(1)	30	1	1	854.2	144.9	13355.4
95	1.11E+06	(30)	2.11E+06	(57)	27	39	10	54.2	33.5	85.4
96	3.50E+05	(7)	1.45E+06	(29)	20	27	10	25.3	9.2	57.8
97	2.00E+05	(4)	1.60E+06	(32)	20	29	10	13.3	3.3	36.2
98	6.25E+04	(5)	4.25E+05	(34)	80	8	3	15.6	4.6	38.9
99	2.00E+05	(2)	1.00E+06	(10)	10	18	11	21.8	2.2	96.0
100	4.00E+05	(28)	4.36E+06	(305)	70	80	9	9.5	6.2	14.0

OP1533 (Olympics) sedimentary bedrock, (Counted by Sarah Falkowski Nov. 2016)
EFFECTIVE TRACK DENSITY FOR FLUENCE MONITOR (tracks/cm^2): 8.130E+05
RELATIVE ERROR (%): 1.48
EFFECTIVE URANIUM CONTENT OF MONITOR (ppm): 15.00
ZETA FACTOR AND STANDARD ERROR (yr cm^2): 252.90 5.00
SIZE OF COUNTER SQUARE (cm^2): 1.000E-06

Grain no.	RhoS (cm^-2)	(Ns)	RhoI (cm^-2)	(Ni)	Squares	U+/-2s		Grain Age	Age (Ma) --95%	CI--
1	9.09E+03	(1)	3.45E+05	(38)	110	6	2	3.1	0.1	16.0
2	2.00E+04	(2)	8.80E+05	(88)	100	16	3	2.5	0.3	8.7
3	4.41E+04	(3)	5.44E+05	(37)	68	10	3	8.7	1.6	26.3
4	1.89E+05	(17)	5.50E+06	(495)	90	101	10	3.6	2.0	5.7
5	1.48E+05	(4)	1.04E+06	(28)	27	19	7	15.2	3.7	41.9
6	1.00E+05	(6)	2.02E+06	(121)	60	37	7	5.2	1.8	11.4
7	5.56E+04	(2)	1.56E+06	(56)	36	29	8	3.9	0.4	13.9
8	3.33E+04	(2)	6.50E+05	(39)	60	12	4	5.7	0.6	20.3
9	2.50E+04	(1)	7.25E+05	(29)	40	13	5	4.0	0.1	21.4
10	7.00E+04	(7)	1.28E+06	(128)	100	24	4	5.7	2.2	11.9
11	1.00E+04	(1)	1.50E+05	(15)	100	3	1	7.8	0.2	44.4
12	3.06E+04	(3)	2.04E+05	(20)	98	4	2	16.1	2.9	51.8
13	1.00E+05	(5)	1.66E+06	(83)	50	31	7	6.4	2.0	15.0
14	8.33E+04	(2)	2.54E+06	(61)	24	47	12	3.6	0.4	12.7
15	2.19E+05	(7)	4.34E+06	(139)	32	80	14	5.3	2.0	11.0

16	1.00E+05	(2)	2.05E+06	(41)	20	38	12	5.4	0.6	19.3
17	1.43E+05	(5)	4.71E+06	(165)	35	87	14	3.2	1.0	7.4
18	5.19E+04	(4)	6.10E+05	(47)	77	11	3	9.1	2.3	23.9
19	5.00E+04	(5)	3.40E+05	(34)	100	6	2	15.5	4.6	38.8
20	9.23E+04	(6)	6.92E+05	(45)	65	13	4	14.0	4.8	32.2

OP1539 (Olympics) sedimentary bedrock, (Counted by Sarah Falkowski Nov. 2016)
EFFECTIVE TRACK DENSITY FOR FLUENCE MONITOR (tracks/cm^2): 8.120E+05
RELATIVE ERROR (%): 1.48
EFFECTIVE URANIUM CONTENT OF MONITOR (ppm): 15.00
ZETA FACTOR AND STANDARD ERROR (yr cm^2): 252.90 5.00
SIZE OF COUNTER SQUARE (cm^2): 1.000E-06

Grain no.	RhoS (cm^-2)	(Ns)	RhoI (cm^-2)	(Ni)	Squares	U+/-2s		Grain Age	Age --95%	(Ma) CI--
1	2.50E+04	(2)	3.25E+05	(26)	80	6	2	8.5	0.9	31.5
2	3.33E+04	(1)	8.00E+05	(24)	30	15	6	4.9	0.1	26.2
3	8.33E+04	(6)	2.50E+06	(180)	72	46	7	3.5	1.2	7.6
4	8.33E+04	(4)	7.08E+05	(34)	48	13	4	12.5	3.1	33.8
5	8.33E+04	(2)	1.21E+06	(29)	24	22	8	7.6	0.8	27.9
6	5.56E+04	(2)	2.50E+05	(9)	36	5	3	24.1	2.4	109.4
7	7.50E+04	(3)	1.45E+06	(58)	40	27	7	5.6	1.1	16.3
8	4.00E+05	(6)	2.40E+06	(36)	15	44	15	17.5	5.9	40.9
9	6.25E+04	(2)	2.00E+06	(64)	32	37	9	3.4	0.4	12.1
10	6.25E+04	(2)	2.50E+05	(8)	32	5	3	27.1	2.7	127.4
11	1.67E+05	(2)	3.17E+06	(38)	12	58	19	5.8	0.6	20.9
12	1.56E+05	(7)	2.42E+06	(109)	45	45	9	6.7	2.6	14.0
13	6.67E+04	(2)	5.00E+05	(15)	30	9	5	14.6	1.5	58.6
14	5.00E+05	(3)	1.67E+06	(10)	6	31	19	31.8	5.4	118.6
15	4.00E+04	(2)	8.60E+05	(43)	50	16	5	5.1	0.6	18.3
16	1.00E+05	(5)	1.40E+06	(70)	50	26	6	7.6	2.3	17.9
17	1.79E+05	(5)	2.89E+06	(81)	28	53	12	6.5	2.0	15.4
18	6.00E+04	(6)	1.00E+06	(100)	100	18	4	6.3	2.2	13.9
19	1.25E+05	(3)	1.71E+06	(41)	24	32	10	7.9	1.5	23.5
20	7.50E+04	(3)	6.50E+05	(26)	40	12	5	12.4	2.3	38.6
21	3.33E+04	(2)	2.67E+05	(16)	60	5	2	13.7	1.4	54.4

OP1542 (Olympics) sedimentary bedrock, (Counted by Sarah Falkowski May 2017)
EFFECTIVE TRACK DENSITY FOR FLUENCE MONITOR (tracks/cm^2): 9.330E+05
RELATIVE ERROR (%): 1.51
EFFECTIVE URANIUM CONTENT OF MONITOR (ppm): 15.00
ZETA FACTOR AND STANDARD ERROR (yr cm^2): 261.20 6.80
SIZE OF COUNTER SQUARE (cm^2): 1.000E-06

Grain no.	RhoS (cm^-2)	(Ns)	RhoI (cm^-2)	(Ni)	Squares	U+/-2s		Grain Age	Age --95%	(Ma) CI--
1	8.89E+04	(4)	2.67E+05	(12)	45	4	2	41.6	9.5	132.7
2	5.17E+04	(3)	1.33E+06	(77)	58	21	5	5.0	1.0	14.4

3	1.22E+05	(11)	1.68E+06	(151)	90	27	4	9.0	4.3	16.3
4	1.44E+05	(13)	8.22E+05	(74)	90	13	3	21.6	10.9	38.8
5	8.75E+04	(7)	1.19E+06	(95)	80	19	4	9.2	3.5	19.2
6	2.80E+05	(28)	1.32E+06	(132)	100	21	4	25.9	16.5	39.0
7	3.17E+04	(2)	4.92E+05	(31)	63	8	3	8.4	0.9	30.8
8	6.19E+05	(26)	1.93E+06	(81)	42	31	7	39.2	24.1	61.3
9	5.71E+04	(2)	2.97E+06	(104)	35	48	9	2.5	0.3	8.7
10	4.00E+04	(4)	6.00E+05	(60)	100	10	2	8.4	2.1	21.9
11	1.33E+05	(12)	1.81E+06	(163)	90	29	5	9.1	4.5	16.1
12	3.10E+05	(31)	3.26E+06	(326)	100	52	6	11.6	7.7	16.8
13	4.00E+04	(2)	3.20E+05	(16)	50	5	3	16.2	1.7	64.5
14	7.41E+04	(6)	1.72E+06	(139)	81	28	5	5.4	1.9	11.7
15	1.00E+05	(7)	1.23E+06	(86)	70	20	4	10.1	3.9	21.3
16	1.00E+05	(2)	6.50E+05	(13)	20	10	6	19.9	2.1	82.3
17	1.60E+05	(8)	6.00E+04	(3)	50	1	1	307.4	77.5	1667.1
18	5.00E+04	(5)	1.38E+06	(138)	100	22	4	4.6	1.4	10.6
19	2.00E+04	(2)	4.30E+05	(43)	100	7	2	6.1	0.7	21.7
20	3.33E+04	(2)	3.83E+05	(23)	60	6	3	11.3	1.2	42.8

OP1551 (Olympics), counted by Sarah Falkowski July 2017
EFFECTIVE TRACK DENSITY FOR FLUENCE MONITOR (tracks/cm^2): 9.420E+05
RELATIVE ERROR (%): 1.51
EFFECTIVE URANIUM CONTENT OF MONITOR (ppm): 15.00
ZETA FACTOR AND STANDARD ERROR (yr cm^2): 256.80 5.00
SIZE OF COUNTER SQUARE (cm^2): 1.000E-06

Grain no.	RhoS (cm^-2)	(Ns)	RhoI (cm^-2)	(Ni)	Squares	U+/-2s	Grain Age	Age (Ma) --95%	CI--
1	1.49E+04	(1)	3.73E+05	(25)	67	6 2	5.5	0.1	29.5
2	0.00E+00	(0)	2.62E+05	(11)	42	4 2	7.9	0.3	48.0
3	2.50E+05	(3)	3.42E+06	(41)	12	54 17	9.3	1.8	27.7
4	4.00E+04	(2)	9.60E+05	(48)	50	15 4	5.4	0.6	19.2
5	1.00E+04	(1)	3.00E+05	(30)	100	5 2	4.6	0.1	24.2
6	3.13E+04	(1)	5.63E+05	(18)	32	9 4	7.6	0.2	42.4
7	5.77E+04	(3)	9.42E+05	(49)	52	15 4	7.8	1.5	22.9
8	5.56E+04	(1)	5.56E+05	(10)	18	9 5	13.6	0.3	84.5
9	3.00E+04	(3)	3.10E+05	(31)	100	5 2	12.3	2.3	37.4
10	2.67E+05	(4)	2.07E+06	(31)	15	33 12	16.1	4.0	44.0
11	2.50E+04	(2)	1.15E+06	(92)	80	18 4	2.8	0.3	9.8
12	1.11E+05	(1)	1.00E+06	(9)	9	16 10	15.1	0.3	96.3
13	1.50E+05	(6)	1.63E+06	(65)	40	26 6	11.4	4.0	25.6
14	2.78E+04	(1)	4.72E+05	(17)	36	8 4	8.1	0.2	45.3
15	0.00E+00	(0)	8.33E+04	(2)	24	1 2	49.9	1.5	614.1
16	1.43E+05	(5)	3.57E+06	(125)	35	57 10	5.0	1.5	11.6
17	4.76E+04	(1)	1.52E+06	(32)	21	24 9	4.3	0.1	22.6
18	2.38E+05	(10)	7.38E+06	(310)	42	118 14	4.0	1.9	7.3
19	2.50E+05	(5)	5.05E+06	(101)	20	80 16	6.2	1.9	14.4
20	2.56E+04	(1)	3.33E+05	(13)	39	5 3	10.5	0.2	61.7
21	2.19E+05	(7)	2.44E+06	(78)	32	39 9	11.1	4.2	23.4

OP1573 (Olympics), counted by Sarah Falkowski July 2017
EFFECTIVE TRACK DENSITY FOR FLUENCE MONITOR (tracks/cm^2): 9.410E+05
RELATIVE ERROR (%): 1.51

EFFECTIVE URANIUM CONTENT OF MONITOR (ppm): 15.00
ZETA FACTOR AND STANDARD ERROR (yr cm^2): 256.80 5.00
SIZE OF COUNTER SQUARE (cm^2): 1.000E-06

Grain no.	RhoS (cm^-2)	(Ns)	RhoI (cm^-2)	(Ni)	Squares	U+/-2s	Grain Age	Age (Ma) --95%	CI--
1	8.33E+05	(10)	6.00E+06	(72)	12	96 23	17.0	7.7	32.6
2	2.00E+04	(2)	2.50E+05	(25)	100	4 2	10.3	1.1	38.7
3	3.75E+05	(3)	4.13E+06	(33)	8	66 23	11.5	2.2	34.9
4	5.00E+04	(2)	5.00E+05	(20)	40	8 4	12.9	1.4	49.6
5	1.00E+06	(1)	2.60E+07	(26)	1	414 162	5.3	0.1	28.2
6	2.50E+05	(10)	6.48E+06	(259)	40	103 13	4.7	2.2	8.7

OP1582 (Olympics) sedimentary bedrock, (Counted by Sarah Falkowski Nov. 2016)
EFFECTIVE TRACK DENSITY FOR FLUENCE MONITOR (tracks/cm^2): 8.100E+05
RELATIVE ERROR (%): 1.48
EFFECTIVE URANIUM CONTENT OF MONITOR (ppm): 15.00
ZETA FACTOR AND STANDARD ERROR (yr cm^2): 252.90 5.00
SIZE OF COUNTER SQUARE (cm^2): 1.000E-06

Grain no.	RhoS (cm^-2)	(Ns)	RhoI (cm^-2)	(Ni)	Squares	U+/-2s	Grain Age	Age (Ma) --95%	CI--
1	1.67E+05	(5)	2.23E+06	(67)	30	41 10	7.9	2.4	18.7
2	4.17E+04	(2)	1.35E+06	(65)	48	25 6	3.4	0.4	11.8
3	1.25E+05	(2)	1.44E+06	(23)	16	27 11	9.5	1.0	36.0
4	6.00E+04	(3)	4.60E+05	(23)	50	9 4	14.0	2.6	44.1
5	6.67E+03	(1)	2.73E+05	(41)	150	5 2	2.9	0.1	14.7
6	0.00E+00	(0)	1.67E+05	(3)	18	3 3	26.6	0.9	243.3
7	2.78E+04	(2)	2.50E+05	(18)	72	5 2	12.1	1.3	47.4
8	1.17E+05	(7)	3.00E+06	(180)	60	56 8	4.1	1.6	8.4
9	2.03E+05	(13)	3.58E+06	(229)	64	66 9	5.9	3.0	10.1
10	1.94E+04	(3)	1.87E+05	(29)	155	3 1	11.1	2.1	34.1
11	4.17E+04	(2)	4.17E+05	(20)	48	8 3	10.9	1.2	42.1
12	3.00E+05	(9)	7.03E+06	(211)	30	130 18	4.4	2.0	8.5
13	1.16E+04	(1)	3.95E+05	(34)	86	7 3	3.4	0.1	17.9
14	5.71E+04	(4)	3.14E+05	(22)	70	6 2	19.2	4.7	54.6
15	1.78E+05	(8)	2.91E+06	(131)	45	54 10	6.4	2.6	12.7
16	1.11E+05	(10)	1.59E+06	(143)	90	29 5	7.3	3.4	13.6
17	1.43E+05	(5)	1.17E+06	(41)	35	22 7	12.8	3.8	31.5
18	3.25E+05	(13)	6.68E+06	(267)	40	124 16	5.0	2.6	8.7
19	1.51E+05	(8)	1.62E+06	(86)	53	30 7	9.7	4.0	19.6
20	4.00E+04	(2)	4.20E+05	(21)	50	8 3	10.4	1.1	39.8
21	1.00E+05	(11)	2.05E+06	(226)	110	38 5	5.1	2.5	9.1
22	4.29E+04	(3)	9.29E+05	(65)	70	17 4	5.0	0.9	14.4

B.4 Zircon fission track single grain analyses

Table DR4: Zircon fission track Single grain ages listed for each sample.

```
==================ZetaAge Program v. 4.8 (Brandon 8/13/02)==================
Zr_OP1513-1 sedimentary bedrock, (counted by Lorenz Michel Sep. 2017)
EFFECTIVE TRACK DENSITY FOR FLUENCE MONITOR (tracks/cm^2):      5.410E+05
                                        RELATIVE ERROR (%):      1.58
               EFFECTIVE URANIUM CONTENT OF MONITOR (ppm):     50.00
                 ZETA FACTOR AND STANDARD ERROR (yr cm^2):    109.00    11.00
                             SIZE OF COUNTER SQUARE (cm^2):      1.000E-06
Grain     RhoS      (Ns)      RhoI     (Ni)  Squares  U+/-2s     Grain  Age (Ma)
 no.     (cm^-2)            (cm^-2)                             Age     --95% CI--
   1   4.50E+06 (  72)  5.44E+06 (  87)    16     503 109   24.4    17.6   33.7
   2   2.44E+06 (  22)  1.89E+06 (  17)     9     175  84   38.0    19.3   76.2
   3   3.88E+06 (  31)  6.75E+06 (  54)     8     624 170   16.9    10.5   26.8
   4   6.75E+06 (  81)  5.92E+06 (  71)    12     547 130   33.5    24.1   46.8
   5   5.25E+06 (  21)  6.50E+06 (  26)     4     601 234   23.8    12.7   43.9
   6   4.29E+06 (  60)  3.86E+06 (  54)    14     356  97   32.7    22.2   48.1
   7   9.50E+06 (  38)  5.50E+06 (  22)     4     508 215   50.6    29.3   89.9
   8   5.78E+06 (  52)  3.78E+06 (  34)     9     349 119   44.9    28.6   71.4
   9   1.12E+07 ( 112)  5.40E+06 (  54)    10     499 136   60.8    43.6   85.8
  10   1.00E+07 ( 120)  8.33E+06 ( 100)    12     770 156   35.3    26.8   46.5
  11   4.70E+06 (  47)  2.70E+06 (  27)    10     250  95   51.0    31.2   85.2
  12   1.09E+07 (  87)  6.38E+06 (  51)     8     589 165   50.0    35.1   72.2
  13   4.43E+06 (  31)  3.43E+06 (  24)     7     317 128   37.9    21.6   67.5
  14   2.00E+07 (  60)  7.00E+06 (  21)     3     647 280   83.3    50.3  144.3
  15   8.13E+06 (  65)  8.75E+06 (  70)     8     809 194   27.3    19.2   38.9
  16   3.67E+06 (  11)  3.00E+06 (   9)     3     277 180   35.8    13.6   97.7
  17   5.80E+06 (  58)  6.10E+06 (  61)    10     564 145   28.0    19.2   40.8
  18   9.67E+06 (  58)  1.00E+07 (  60)     6     924 239   28.4    19.5   41.5
  19   9.40E+06 (  47)  8.40E+06 (  42)     5     776 239   32.9    21.2   51.1
  20   3.00E+06 (  36)  2.17E+06 (  26)    12     200  78   40.6    23.9   70.1
  21   1.10E+07 (  99)  7.67E+06 (  69)     9     709 171   42.1    30.7   58.2
  22   6.40E+06 (  64)  5.80E+06 (  58)    10     536 141   32.4    22.4   47.1
  23   5.40E+06 (  54)  5.40E+06 (  54)    10     499 136   29.4    19.8   43.7


Zr_OP1517-2 sedimentary bedrock, (counted by Lorenz Michel Sep. 2017)
EFFECTIVE TRACK DENSITY FOR FLUENCE MONITOR (tracks/cm^2):      5.420E+05
                                        RELATIVE ERROR (%):      1.58
               EFFECTIVE URANIUM CONTENT OF MONITOR (ppm):     50.00
                 ZETA FACTOR AND STANDARD ERROR (yr cm^2):    109.00    11.00
                             SIZE OF COUNTER SQUARE (cm^2):      1.000E-06
Grain     RhoS      (Ns)      RhoI     (Ni)  Squares  U+/-2s     Grain  Age (Ma)
 no.     (cm^-2)            (cm^-2)                             Age     --95% CI--
   1   7.33E+06 (  88)  5.33E+06 (  64)    12     492 124   40.5    29.0   56.8
   2   1.55E+07 ( 155)  8.50E+06 (  85)    10     784 171   53.6    40.9   70.8
   3   7.86E+06 ( 165)  7.14E+06 ( 150)    21     659 109   32.4    25.8   40.8
   4   4.88E+06 (  39)  3.00E+06 (  24)     8     277 112   47.7    28.1   83.0
   5   1.08E+07 ( 130)  6.67E+06 (  80)    12     615 138   47.8    35.9   64.0
   6   9.00E+06 ( 144)  6.81E+06 ( 109)    16     628 122   38.9    30.1   50.4
   7   8.07E+06 ( 121)  5.00E+06 (  75)    15     461 107   47.4    35.3   64.2
   8   7.25E+06 (  87)  5.42E+06 (  65)    12     500 124   39.4    28.2   55.2
   9   5.81E+06 (  93)  4.63E+06 (  74)    16     427 100   37.0    27.0   51.0
  10   8.00E+06 (  72)  7.11E+06 (  64)     9     656 165   33.1    23.3   47.2
  11   1.47E+07 ( 176)  1.09E+07 ( 131)    12    1007 179   39.6    31.3   50.1
```

12	1.15E+07	(138)	9.00E+06	(108)	12	830	162	37.6	29.0	48.9
13	4.24E+06	(89)	2.90E+06	(61)	21	268	69	42.9	30.7	60.5
14	1.37E+07	(41)	1.10E+07	(33)	3	1015	352	36.6	22.6	59.7
15	7.75E+06	(93)	8.33E+06	(100)	12	769	155	27.4	20.4	36.8
16	4.44E+06	(40)	2.89E+06	(26)	9	267	104	45.2	27.0	77.2
17	1.13E+07	(45)	5.75E+06	(23)	4	530	219	57.3	34.1	99.4
18	1.26E+07	(189)	8.80E+06	(132)	15	812	143	42.1	33.5	53.1
19	8.00E+06	(64)	6.88E+06	(55)	8	634	171	34.3	23.5	50.1
20	2.03E+07	(61)	1.20E+07	(36)	3	1107	368	49.8	32.5	77.4
21	4.00E+06	(32)	3.25E+06	(26)	8	300	117	36.2	20.9	63.3
22	2.22E+06	(20)	1.78E+06	(16)	9	164	81	36.8	18.1	75.8
23	1.30E+07	(78)	8.83E+06	(53)	6	815	224	43.3	30.2	62.6
24	5.50E+06	(33)	4.33E+06	(26)	6	400	156	37.3	21.7	65.0
25	8.93E+06	(134)	6.47E+06	(97)	15	597	122	40.7	31.1	53.4

Zr_OP1533-2 sedimentary bedrock, (counted by Lorenz Michel Sep. 2017)

EFFECTIVE TRACK DENSITY FOR FLUENCE MONITOR (tracks/cm^2): 5.430E+05
RELATIVE ERROR (%): 1.58
EFFECTIVE URANIUM CONTENT OF MONITOR (ppm): 50.00
ZETA FACTOR AND STANDARD ERROR (yr cm^2): 109.00 11.00
SIZE OF COUNTER SQUARE (cm^2): 1.000E-06

Grain no.	RhoS (cm^-2)	(Ns)	RhoI (cm^-2)	(Ni)	Squares	U+/-2s	Grain Age	Age (Ma) --95%	CI--
1	5.27E+06	(79)	5.40E+06	(81)	15	497 111	28.8	20.8	39.8
2	2.17E+06	(65)	1.33E+06	(40)	30	123 39	47.8	31.8	72.9
3	4.92E+06	(118)	2.88E+06	(69)	24	265 64	50.4	37.1	68.9
4	1.93E+06	(77)	1.53E+06	(61)	40	140 36	37.2	26.3	53.0
5	1.94E+06	(31)	2.00E+06	(32)	16	184 65	28.6	16.9	48.4
6	4.04E+06	(109)	1.85E+06	(50)	27	171 48	64.1	45.5	91.6
7	3.96E+06	(95)	3.46E+06	(83)	24	318 70	33.8	24.9	46.0
8	5.58E+06	(134)	3.38E+06	(81)	24	311 70	48.7	36.7	65.1
9	6.89E+06	(186)	5.19E+06	(140)	27	477 82	39.2	31.3	49.2
10	7.67E+06	(46)	5.83E+06	(35)	6	537 181	38.7	24.4	62.0
11	1.36E+07	(272)	3.75E+06	(75)	20	345 80	106.3	82.1	139.3
12	1.03E+07	(164)	6.06E+06	(97)	16	558 114	49.8	38.5	64.8
13	4.08E+06	(98)	3.25E+06	(78)	24	299 68	37.1	27.2	50.6
14	7.97E+06	(255)	4.09E+06	(131)	32	377 67	57.2	42.9	76.4
15	8.25E+06	(99)	5.08E+06	(61)	12	468 120	47.8	34.4	67.0
16	3.20E+06	(64)	2.80E+06	(56)	20	258 69	33.7	23.2	49.2
17	4.21E+06	(101)	2.08E+06	(50)	24	192 54	59.4	42.0	85.2
18	1.06E+07	(212)	3.65E+06	(73)	20	336 79	85.3	65.1	113.0
19	4.95E+06	(99)	3.00E+06	(60)	20	276 72	48.6	34.9	68.2
20	1.66E+06	(73)	1.68E+06	(74)	44	155 36	29.1	20.8	40.8
21	9.59E+06	(307)	4.78E+06	(153)	32	440 72	59.0	44.7	77.9
22	8.50E+06	(153)	4.67E+06	(84)	18	430 94	53.6	40.8	71.0
23	5.73E+06	(86)	4.47E+06	(67)	15	411 101	37.9	27.2	53.0

Zr_OP1539-2 sedimentary bedrock, (counted by Lorenz Michel Sep. 2017)
EFFECTIVE TRACK DENSITY FOR FLUENCE MONITOR (tracks/cm^2): 5.440E+05
RELATIVE ERROR (%): 1.58
EFFECTIVE URANIUM CONTENT OF MONITOR (ppm): 50.00
ZETA FACTOR AND STANDARD ERROR (yr cm^2): 109.00 11.00
SIZE OF COUNTER SQUARE (cm^2): 1.000E-06

Grain no.	RhoS (cm^-2)	(Ns)	RhoI (cm^-2)	(Ni)	Squares	U+/-2s	Grain Age (Ma)	--95% CI--	
							Age		
1	2.33E+06	(56)	4.46E+06	(107)	24	410 80	15.5	11.0	21.6
2	1.59E+06	(43)	4.37E+06	(118)	27	402 75	10.8	7.4	15.4
3	2.75E+06	(33)	7.33E+06	(88)	12	674 145	11.1	7.2	16.8
4	5.71E+05	(12)	1.48E+06	(31)	21	136 49	11.6	5.4	23.0
5	2.80E+06	(56)	5.95E+06	(119)	20	547 102	14.0	9.9	19.3
6	1.83E+06	(11)	3.00E+06	(18)	6	276 129	18.2	7.7	40.4
7	5.00E+05	(12)	1.50E+06	(36)	24	138 46	10.0	4.7	19.4
8	7.14E+05	(15)	2.24E+06	(47)	21	206 60	9.5	4.9	17.2
9	3.25E+06	(39)	7.33E+06	(88)	12	674 145	13.2	8.8	19.4
10	1.89E+06	(68)	4.00E+06	(144)	36	368 62	14.0	10.3	18.8
11	3.94E+06	(63)	6.69E+06	(107)	16	615 120	17.5	12.5	24.1
12	1.25E+06	(15)	4.33E+06	(52)	12	398 111	8.6	4.5	15.4
13	5.05E+06	(106)	1.16E+07	(243)	21	1064 140	12.9	10.2	16.3
14	2.50E+06	(15)	5.33E+06	(32)	6	490 173	14.0	7.0	26.4
15	5.71E+05	(12)	1.76E+06	(37)	21	162 53	9.7	4.6	18.8
16	1.31E+06	(21)	3.88E+06	(62)	16	356 91	10.1	5.8	16.7
17	4.76E+05	(10)	1.33E+06	(28)	21	123 46	10.7	4.6	22.4
18	1.13E+06	(27)	3.83E+06	(92)	24	352 74	8.7	5.4	13.5
19	5.00E+06	(60)	8.08E+06	(97)	12	743 152	18.3	13.0	25.6
20	3.50E+05	(7)	1.25E+06	(25)	20	115 46	8.4	3.0	19.7
21	1.69E+06	(27)	5.50E+06	(88)	16	506 109	9.1	5.7	14.1

Zr_OP1551-1 sedimentary bedrock, (counted by Lorenz Michel Sep. 2017)
EFFECTIVE TRACK DENSITY FOR FLUENCE MONITOR (tracks/cm^2): 5.470E+05
RELATIVE ERROR (%): 1.58
EFFECTIVE URANIUM CONTENT OF MONITOR (ppm): 50.00
ZETA FACTOR AND STANDARD ERROR (yr cm^2): 109.00 11.00
SIZE OF COUNTER SQUARE (cm^2): 1.000E-06

Grain no.	RhoS (cm^-2)	(Ns)	RhoI (cm^-2)	(Ni)	Squares	U+/-2s	Grain Age (Ma)	--95% CI--	
							Age		
1	1.11E+06	(40)	1.78E+06	(64)	36	163 41	18.6	12.2	28.1
2	1.63E+06	(39)	2.54E+06	(61)	24	232 60	19.1	12.4	28.9
3	1.83E+06	(44)	3.33E+06	(80)	24	305 69	16.4	11.1	24.0
4	2.00E+06	(72)	2.67E+06	(96)	36	244 50	22.3	16.2	30.7
5	1.25E+06	(20)	8.13E+05	(13)	16	74 40	45.5	21.7	99.6
6	5.42E+05	(13)	1.50E+06	(36)	24	137 46	10.8	5.2	20.8
7	5.83E+05	(28)	1.00E+06	(48)	48	91 26	17.4	10.5	28.3
8	1.08E+06	(27)	2.48E+06	(62)	25	227 58	13.0	7.9	20.7
9	6.25E+05	(15)	1.67E+06	(40)	24	152 48	11.2	5.7	20.7
10	5.56E+05	(10)	2.00E+06	(36)	18	183 61	8.4	3.7	17.0
11	2.75E+06	(44)	4.56E+06	(73)	16	417 98	18.0	12.0	26.5
12	1.17E+07	(117)	1.21E+07	(121)	10	1106 204	28.8	22.1	37.5
13	6.10E+06	(61)	6.40E+06	(64)	10	585 147	28.4	19.6	40.9
14	3.33E+05	(10)	9.00E+05	(27)	30	82 31	11.1	4.8	23.5

15	9.71E+05	(34)	1.20E+06	(42)	35	110	34	24.1	14.9	38.8
16	2.14E+06	(77)	1.42E+06	(51)	36	129	36	44.8	31.1	65.2
17	2.58E+06	(62)	1.33E+06	(32)	24	122	43	57.4	37.0	90.9
18	5.83E+05	(21)	8.06E+05	(29)	36	74	27	21.6	11.7	39.1
19	1.08E+06	(39)	2.89E+06	(104)	36	264	52	11.2	7.5	16.3
20	2.50E+06	(40)	4.25E+06	(68)	16	388	95	17.5	11.5	26.3
21	1.15E+06	(23)	2.40E+06	(48)	20	219	63	14.3	8.3	23.9
22	6.54E+06	(157)	3.83E+06	(92)	24	350	74	50.6	38.9	66.3
23	1.72E+06	(62)	3.47E+06	(125)	36	317	58	14.8	10.7	20.2

Zr_OP1552-1 sedimentary bedrock, (counted by Lorenz Michel Sep. 2017)
EFFECTIVE TRACK DENSITY FOR FLUENCE MONITOR (tracks/cm^2): 5.480E+05
RELATIVE ERROR (%): 1.58
EFFECTIVE URANIUM CONTENT OF MONITOR (ppm): 50.00
ZETA FACTOR AND STANDARD ERROR (yr cm^2): 109.00 11.00
SIZE OF COUNTER SQUARE (cm^2): 1.000E-06

Grain no.	RhoS (cm^-2)	(Ns)	RhoI (cm^-2)	(Ni)	Squares	U+/-2s		Grain Age	Age (Ma) --95%	CI--
1	1.00E+06	(45)	1.82E+06	(82)	45	166	37	16.4	11.1	23.9
2	1.00E+06	(40)	1.83E+06	(73)	40	167	39	16.4	10.8	24.4
3	9.05E+05	(38)	1.83E+06	(77)	42	167	38	14.8	9.7	22.0
4	2.18E+06	(122)	2.52E+06	(141)	56	230	39	25.8	20.0	33.2
5	4.88E+06	(78)	4.25E+06	(68)	16	388	95	34.2	24.3	48.0
6	5.25E+05	(21)	1.08E+06	(43)	40	98	30	14.6	8.2	25.1
7	8.10E+05	(34)	1.36E+06	(57)	42	124	33	17.8	11.3	27.7
8	1.69E+06	(27)	1.81E+06	(29)	16	165	61	27.8	15.8	48.5
9	7.38E+05	(31)	1.48E+06	(62)	42	135	34	15.0	9.4	23.3
10	7.19E+06	(115)	5.63E+06	(90)	16	513	109	38.0	28.6	50.8
11	5.83E+05	(21)	1.42E+06	(51)	36	129	36	12.3	7.0	20.8
12	1.20E+06	(67)	2.34E+06	(131)	56	213	38	15.3	11.2	20.7
13	7.50E+05	(24)	1.78E+06	(57)	32	163	43	12.6	7.5	20.6
14	1.02E+06	(49)	2.48E+06	(119)	48	226	42	12.3	8.6	17.3
15	6.90E+05	(29)	1.29E+06	(54)	42	117	32	16.1	9.8	25.6
16	5.71E+05	(12)	1.29E+06	(27)	21	117	45	13.4	6.1	27.1
17	1.43E+06	(43)	3.87E+06	(116)	30	353	66	11.1	7.6	15.8
18	5.52E+06	(138)	4.60E+06	(115)	25	420	79	35.7	27.7	46.2
19	4.22E+05	(27)	1.27E+06	(81)	64	115	26	10.0	6.2	15.6
20	6.90E+05	(69)	1.37E+06	(137)	100	125	22	15.0	11.1	20.2
21	6.61E+05	(37)	1.43E+06	(80)	56	130	29	13.8	9.1	20.6
22	1.07E+06	(30)	2.00E+06	(56)	28	182	49	16.0	9.9	25.3
23	1.07E+06	(48)	2.87E+06	(129)	45	262	47	11.1	7.8	15.6
24	1.29E+06	(31)	2.21E+06	(53)	24	201	55	17.5	10.8	27.7

Zr_OP1582-1 sedimentary bedrock, (counted by Lorenz Michel Sep. 2017)
EFFECTIVE TRACK DENSITY FOR FLUENCE MONITOR (tracks/cm^2): 5.450E+05
RELATIVE ERROR (%): 1.58
EFFECTIVE URANIUM CONTENT OF MONITOR (ppm): 50.00
ZETA FACTOR AND STANDARD ERROR (yr cm^2): 109.00 11.00
SIZE OF COUNTER SQUARE (cm^2): 1.000E-06

Grain no.	RhoS (cm^-2)	(Ns)	RhoI (cm^-2)	(Ni)	Squares	U+/-2s		Grain Age	Age (Ma) --95%	CI--
1	4.77E+06	(143)	2.33E+06	(70)	30	214	51	60.3	45.0	81.6
2	5.50E+06	(165)	3.50E+06	(105)	30	321	63	46.5	36.2	60.0

3	7.72E+06 (139)	8.11E+06 (146)	18	744	125	28.2	22.2	35.9
4	6.09E+06 (67)	2.64E+06 (29)	11	242	89	68.1	43.6	109.3
5	3.17E+06 (95)	2.13E+06 (64)	30	196	49	43.9	31.7	61.3
6	5.31E+06 (85)	2.31E+06 (37)	16	212	70	67.7	45.7	102.6
7	5.62E+06 (118)	5.81E+06 (122)	21	533	98	28.7	22.0	37.3
8	8.56E+06 (231)	4.74E+06 (128)	27	435	78	53.4	42.8	66.9
9	4.12E+06 (198)	3.77E+06 (181)	48	346	53	32.4	24.4	43.0
10	4.50E+06 (54)	2.17E+06 (26)	12	199	77	61.2	37.8	101.9
11	2.57E+06 (54)	1.43E+06 (30)	21	131	48	53.1	33.5	86.1
12	3.36E+06 (121)	1.67E+06 (60)	36	153	40	59.5	43.4	82.7
13	9.05E+05 (19)	7.62E+05 (16)	21	70	34	35.1	17.1	73.0
14	2.75E+06 (33)	2.92E+06 (35)	12	268	90	28.0	16.8	46.3
15	4.12E+06 (99)	2.08E+06 (50)	24	191	54	58.5	41.3	84.0
16	2.42E+06 (29)	1.58E+06 (19)	12	145	66	45.1	24.5	85.1
17	1.74E+06 (61)	1.77E+06 (62)	35	163	41	29.2	20.1	42.2
18	6.40E+06 (96)	3.07E+06 (46)	15	281	83	61.6	43.0	89.6
19	8.92E+06 (107)	6.08E+06 (73)	12	558	131	43.4	31.9	59.3
20	6.67E+05 (20)	6.33E+05 (19)	30	58	26	31.2	15.8	61.7
21	2.50E+06 (50)	2.20E+06 (44)	20	202	61	33.7	22.0	51.7
22	2.56E+06 (92)	2.03E+06 (73)	36	186	44	37.3	27.1	51.5
23	7.38E+06 (155)	4.90E+06 (103)	21	450	90	44.5	34.5	57.8

Appendix C

Additional data tables of section 3.3

The following pages contain supplementary data tables for the manuscript "Frictional transition leaves a permanent mark in Cascadia." presented in section 3.3.2.

These tables include the estimates of long-term denudation rates from thermochronometry and cosmogenic nuclides used in the analysis of the paper (Table S1, section C.1). Furthermore, the displacements related to episodic tremor and slip as derived from literature sources is reported (Table S2, section C.2).

C.1 Long-term denudation rates

Table S1: Published long term denudation rates, based on cosmogenic nuclide dating (Adams and Ehlers, 2018) and based on thermochronometric dating (Michel et al., 2018). Location of the samples is given in Latitude/Longitude and the rate at the respective sample location.

Rates based on cosmogenic nuclides

Sample	Latitude (°N)	Longitude (°E)	Denudation rate (mm/yr)	Denudation rate 2 SD (mm/yr)
WA1501	47.810972	-123.44503	0.638	0.118
WA1502	47.948389	-123.56092	0.718	0.134
WA1503	47.969639	-123.59908	0.93	0.183
WA1519	47.878306	-123.70736	2.511	0.618
WA1520	47.885139	-123.75147	0.61	0.112
WA1522	47.976972	-123.68797	0.432	0.09
WA1523	47.876735	-123.69469	1.881	0.442
WA1524	47.876161	-123.69537	3.117	0.782
WA1525	47.916688	-123.24247	1.451	0.301
WA1526	47.67787	-124.11701	0.224	0.037
WA1527	47.62844	-123.6316	0.564	0.104
WA1537	47.615017	-123.47443	1.213	0.256
WA1538	47.739067	-123.17657	0.635	0.116
WA1539	47.951718	-123.81862	0.318	0.055
U-EFMC	47.685616	-124.23868	0.171	0.034
L-EFMC	47.653568	-124.24006	0.129	0.02
U-WC	47.738694	-124.04432	0.158	0.025
L-WC	47.728534	-124.03657	0.199	0.031
DEN104	47.55637	-124.28191	0.223	0.176
DEN106	47.644947	-124.24263	0.114	0.043
DEN101	47.642348	-124.23752	0.237	0.11

Rates based on thermochronometry

Sample	Latitude (°N)	Longitude (°E)	Denudation rate (mm/yr)
OP1502	47.90796	-122.92804	0.25
OP1504	47.93233	-123.19509	0.329
OP1505	47.96524	-123.11056	0.257
OP1507	47.98305	-123.61359	0.522
OP1510	48.09852	-123.62231	0.256
OP1513	47.96015	-123.57273	0.695
OP1515	47.81031	-123.44630	0.93
OP1516	47.88040	-123.47196	0.914
OP1517	47.93891	-123.51376	0.816
OP1518	48.05061	-123.83886	0.253
OP1521	48.04832	-124.08702	0.25
OP1522	48.00530	-124.41620	0.25
OP1523	48.12315	-124.22835	0.25
OP1527	47.82500	-124.05184	0.254
OP1529	47.78265	-124.14257	0.25
OP1530	47.73081	-124.26813	0.25
OP1531	47.63659	-124.34966	0.25
OP1532	47.87025	-123.88135	0.386
OP1533	47.87572	-123.69427	0.867
OP1534	47.88536	-123.75552	0.749
OP1536	47.48917	-124.03370	0.25
OP1539	47.64151	-123.65870	0.897
OP1540	47.59012	-123.54913	0.828
OP1542	47.56001	-123.37533	0.527
OP1545	47.51918	-123.32442	0.311
OP1547	47.44632	-123.11424	0.25
OP1548	48.02186	-123.34295	0.306
OP1565	47.91644	-123.24616	0.515
OP1580	47.73972	-123.17929	0.568
OP1582	47.95595	-123.83732	0.309

C.2 Vertical displacement due to ETS

Table S2: GPS-based vertical displacement due to episodic tremor and slip (ETS) at the respective GPS station. The reported displacment corresponds to the average displacment for a single ETS event, and is based on eight ETS events during 2000 to 2014. Data is from Bruhat and Segall (2016).

Station name	Latitude (°N)	Longitude (°E)	Vertical displacement (mm)	Vertical displacement 1SD (mm)
ALBH	48.389781	-123.487471	1.05	0.54
ARLI	48.174067	-122.141860	-0.53	0.70
BAMF	48.835329	-125.135105	5.37	0.82
BELI	48.755269	-122.478998	-0.62	0.75
BLYN	48.016058	-122.927540	-1.61	1.68
BRNB	49.275056	-123.021821	2.91	1.24
CHCM	48.010618	-122.775867	-1.44	0.72
CHWK	49.156608	-122.008427	0.57	0.64
CLRS	48.820300	-124.130800	1.76	0.98
CUSH	47.423344	-123.219924	5.51	1.13
DWH1	47.774104	-122.080156	-0.40	1.36
GRP4	48.194668	-122.127286	-0.32	1.10
KTBW	47.547319	-122.795418	-0.67	0.56
LKCP	47.944379	-121.830853	-0.74	0.66
NANO	49.294810	-124.086480	0.26	0.57
NEAH	48.297855	-124.624907	1.58	0.65
P064	47.969846	-123.487705	2.07	1.35
P398	46.925785	-123.916145	1.83	0.72
P399	47.433920	-123.612960	4.66	0.93
P400	47.513349	-123.812450	7.56	1.55
P401	47.937188	-124.557020	1.59	0.61
P402	47.766221	-124.305897	2.29	0.74
P403	48.062322	-124.140875	3.44	0.89
P418	47.236645	-123.407814	5.53	0.75
P423	47.287903	-122.941210	1.36	0.72
P426	47.802725	-122.514585	-0.83	0.80
P435	48.059549	-123.503279	5.30	0.91
P436	48.045302	-123.134348	0.58	0.74
P437	48.001809	-122.459158	-0.54	0.83
P438	48.419148	-122.670263	-1.05	0.72
P439	48.708192	-122.909304	-0.96	0.68
P440	48.856193	-122.493341	-0.47	0.77
P441	48.915970	-122.139640	0.09	1.09
P442	48.260480	-121.615550	1.38	0.82
PABH	47.212799	-124.204582	1.55	0.51
PCOL	47.172057	-122.570806	-0.94	0.69
PFLD	47.898507	-122.282183	-0.09	0.71
PGC5	48.648533	-123.451129	-1.84	0.54
PTAL	49.256329	-124.860956	1.77	0.57
PTRF	48.544100	-124.412900	1.99	1.09
PUPU	47.499559	-122.008081	-4.30	1.40
RPT1	47.387506	-122.374767	-1.74	0.96
SC02	48.546195	-123.007611	-2.38	0.55
SC03	47.816587	-123.705738	8.66	0.73
SC04	48.923164	-123.704130	-0.99	0.65
SEAT	47.653977	-122.309476	-1.04	0.66
SEDR	48.521558	-122.223848	-1.21	0.66
TWHL	47.015905	-122.922876	1.93	0.59
UCLU	48.925637	-125.541641	2.81	0.61
VERN	48.417854	-122.337203	1.29	0.91
WHD1	48.312716	-122.696144	-5.41	1.21

Appendix D

Location of important files on the group server

This appendix indicates, where important files created during the PhD project are located on the server of the Earth Surface Dynamics group.

D.1 Manuscripts

All papers and manuscripts presented in chapter 3 can be found under

`/esd/esd01/docs/lmichel/papers`

Here, sub folders for the different manuscripts exist (`/paper_1`,`/paper_2`, ...). In the folder of the respective manuscript the text (submitted .docx-files), figures (submitted .pdf-files or .tif-files along with the original .ai-files) and the correspondence during the review process (where available) are located in subfolders: `/text`, `/figures`, `/review`. The most up-to-date version (i.e., the submitted version of the respective files) can be found in these, along with earlier versions (in sub folders).

D.2 Datasets

Several datasets have been generated during the PhD project. All data from thermochronometric dating available as spreadsheets and categorized into results from (U-Th)/He and fission-track methods, are located in

`/esd/esd01/docs/lmichel/data_small/thermochronometry`

Data from the flux calculations section 3.2 along with the matlab scripts used for calculation are located in

`/esd/esd01/docs/lmichel/data_small/flux_calculations`

The results (i.e., the calculated thermochronometer ages from section 3.1 and section 3.4 or the exhumation histories from section 3.2) from the different modelling approaches are summarized in the respective sub folders in

`/esd/esd01/docs/lmichel/data_small/modelling_results`

D.3 Modelling

A large number of thermo-kinematic models using Pecube have been run during the PhD project. The data of all these simulations (i.e., modelled thermochronometer ages, goodness of fit) along with the respective Pecube .in-files used to define the models are available on the group server. For a better overview, the different simulations have been categorized into groups. Initial test runs investigating various physical parameters and different ellipse shapes are located in

`/esd/esd01/data/lmichel/model_runs/pecube/test`

All data from the final simulations of the first manuscript (section 3.1) are located at

`/esd/esd01/data/lmichel/model_runs/pecube/ellipse`

The Monte-Carlo simulations of the manuscript presented in section 3.2 are located at

`/esd/esd01/data/lmichel/model_runs/pecube/monte_carlo`

Results from the simulations of section 3.4 investigating changes of topography are located at

`/esd/esd01/data/lmichel/model_runs/pecube/topography_changes/steady_simulations`

D.4 ArcGIS

Variable ArcGIS files have been created during the course of the PhD project. The folder structure for categorizing these is oriented along the varies tasks, that emerged during the PhD. If ArcGIS was used in order to create a figure presented in any of the manuscripts or papers, the corresponding .mxd-file is located in the respective figure folder (see appendix D.1). Shapefiles created from various datasets during the PhD are located at

`/esd/esd01/share/arc/extreme/pecube/Cascades/lmichel/shape_files`

Any data prepared with ArcGIS in order to import it into Pecube (e.g., topography from DEMs) is located in

`/esd/esd01/share/arc/extreme/pecube/Cascades/lmichel/pecube`

Files used during planning the field work can be found under

`/esd/esd01/share/arc/extreme/pecube/Cascades/lmichel/fieldwork`

D.5 Thesis writing

Files involved in creating this thesis can also be found on the server, the .tex-files are located in

`/esd/esd01/docs/lmichel/thesis_writing/text`

and the figure files (.pdf-files or .tif-files included in the figure) and the original .ai-files are located at

`/esd/esd01/docs/lmichel/thesis_writing/figures`